UNIVERSITY OF SOUTHAMPTON

FACULTY OF NATURAL AND ENVIRONMENTAL SCINCES

Chemistry

Volume 1 of 1

Electrodeposition and characterisation of nickel, germanium and tin thin films

by

Mahboba Mohammed Hasan

Thesis for the degree of

Doctor of Philosophy

March 2017

UNIVERSITY OF SOUTHAMPTON

ABSTRACT

FACULTY OF NATURAL AND ENVIRONMENTAL SCINCES

Chemistry

Thesis for the degree of Doctor of Philosophy

ELECTRODEPOSITION AND CHARACTERISATION OF NICKEL, GERMANIUM AND TIN THIN FILMS

Mahboba Mohammed Hasan

The electrodeposition and characterisation of metals, Ni, Ni-B and Sn and a semi-conductor, Ge are the objectives of this study. Electrodeposition is an important metal surface coating technique as it can smoothly coat large and complex objects in a convenient and economically viable way. We are examining the microstructure of the films electrodeposited in this work using a variety of X-ray diffraction techniques, scanning electron microscopy, energy dispersive X-ray spectroscopy, wavelength dispersive X-ray spectroscopy, and X-ray photoelectron spectroscopy.

Nickel coatings have wide applications in decorative and functional applications as hard, corrosion resistant surfaces. Boron is often incorporated into electrodeposited Ni using the standard Watt's bath (nickel chloride/nickel sulphate/boric acid) and adding dimethylamine borane as the source of boron, the electrodepositions are achieved by chronopotentiometry.

Germanium is an important semi-conductor, its widest application areas are optoelectronics and photonics. Ge films have been electrodeposited from tetrabutylammonium chlorogermanate $[^{n}Bu_4N][GeCl_3]$ in tetrabutylammonium chloride $[^{n}Bu_4N]Cl$ dichloromethane solution, using chronoamperometry. The as-deposited Ge is amorphous. High temperature thermal annealing under anaerobic condition is applied to the films to crystallise.

Tin is a soft, pliable and highly crystalline element with wide range of applications including decoration, electronic, and optical areas. Electrodeposition of tin is achieved from an electrolyte containing tetrabutylammonium chlorostannate $[^{n}Bu_4N][SnCl_3]$ and tetrabutylammonium chloride $[^{n}Bu_4N]Cl$ in dichloromethane solution, using chronoamperometry. Flat tin films on Au sputtered on glass substrates, nanowire tin in phosphonate grafted anodic alumina and un-grafted AAO membranes were produced. Electrodepositions on Au substrate were obtained at various temperatures.

Ni was electrodeposited in a highly crystalline form. The addition of B to the Ni matrix has reduced the degree of crystallinity and raised the amount of stress in the films. These effects were enhanced by increasing the amount of added B. Great influence on the preferred orientation of the Ni crystals was observed with the variations in the thickness and current density. In the Ge electrodeposition, modifications to the electrolyte composition and the substrate resulted in various morphologies and quality of adhesions in the Ge films, which was effective in the adhesion in the films after the annealing. Sn films were produced in a high crystalline form, electrodeposition at various temperature developed effects on the morphology and the texture of the electrodeposited Sn film. Characterisation on the Sn inside the anodic alumina templates indicates various diameter wires grown inside the membranes.

Table of Contents

DECLARATION OF AUTHORSHIP

I, Mahboba Mohammed Hasan

declare that this thesis and the work presented in it are my own and has been generated by me as the result of my own original research.

Electrodeposition and characterisation of nickel, germanium and tin thin films

I confirm that:

1. This work was done wholly or mainly while in candidature for a research degree at this University;
2. Where any part of this thesis has previously been submitted for a degree or any other qualification at this University or any other institution, this has been clearly stated;
3. Where I have consulted the published work of others, this is always clearly attributed;
4. Where I have quoted from the work of others, the source is always given. With the exception of such quotations, this thesis is entirely my own work;
5. I have acknowledged all main sources of help;
6. Where the thesis is based on work done by myself jointly with others, I have made clear exactly what was done by others and what I have contributed myself;
7. Parts of this work have been published as:

[C. Cummings, P. N. Bartlett, D, Pugh, G. Reid, W. Levason, M. M. Hasan, A. L. Hector, J. Spencer, D. Smith, J. Electrochem. Soc. 2015, 162, D619]

[C. Cummings, P. N. Bartlett, D, Pugh, G. Reid, W. Levason, M. M. Hasan, A. L. Hector, J. Spencer, D. Smith, S. Marks, ChemElectrochem. 2016, 3, 726]

Signed: ....

Date: ....

Acknowledgements

This PhD thesis could not have been completed without help and support from many people, who contributed in some way in this work. I would like to take the opportunity to thank them all individually. First of all I wish to express my sincerest gratitude and appreciation to my supervisor Professor Andrew L Hector for accepting me into his group and for all his support and encouragement during the long period of my work with him as a PhD student, and for the freedom to work in my own way. He has always been happy to offer all help needed and advice in learning new experiments, understanding and interpreting results. He has also provided insightful discussions about the research. He is a nice, kind and patient person, it has been my pleasure to know him and to work with him. I would like to thank my co-supervisor Professor Philip N Bartlett for providing help whenever asked. I am grateful to him for efficiently involving me in the group meetings he held on the projects, which have been an opportunity to exchange useful ideas between the members of the projects and to hold scientific discussions.

The efficient contribution from a number of postdoctoral researchers has resulted in the smooth progression in my work. Here I would like to express my appreciation to every one of them. Many thanks to Dr. Gabriela P Kissling, who patiently taught me her method of germanium electrodeposition and for allowing me to use her equipment to carry out the experiments. I would like to express my appreciation to her for being always available to provide advice and for her valuable scientific knowledge and many insightful discussions and suggestions. She is a very helpful, nice and cheerful person. My gratitude to Dr. Charles Cummings for his help in running electrodeposition experiments, FEG-SEM instrument training and insightful scientific discussions. Many thanks, to Dr. Pete Richardson for his help in using the potentiostat instrument, and for being always happy to provide scientific knowledge and discussions. Thanks to Dr. David Cook for helping me to remove the overgrowth from AAO membranes, and for his knowledge in scientific electrochemical discussions. I would like to thank Dr. Marek Jura and Dr. Gavin Stenning from ISIS in Diamond light sources for their help with running thin film XRD measurements and also I am thankful to Dr. Reza Kashtiban, University of Warwick for the TEM measurements. I would like to express my gratitude to Dr. Mark Light for the Smartlab instrument training. I always received his aid in running different measurements and when struggling with the technical issues, using the instrument. He has been always helpful and patient person with the users. Dr. Andrew Jolleys has provided me with the precursor for germanium electrodeposition, and Dr. Jennifer Burt with the precursor for the tin electrodeposition I would like to thank them both. The dried dichloromethane solvent was provided by Dr. David Pugh, thanks to him. I also thank Dr. Ruomeng Huang for his contribution in the research by fabricating the silica sputtered TiN on

silicon substrate. I received my training to use the XPS instrument from Dr. Zakaria Moktadir, who I would like to acknowledge. Special sincere thanks to Dr. Andrew Lodge for the proofreading of my thesis, sharing his knowledge in scientific writing, and for his contribution in this research by providing the grafted AAO membranes. Thanks to Zondy Webber for gold sputtered AAO work, and thanks to Dr. Vinita Mittal for her help with the XPS instrument. I have received a training session on high resolution SEM instrument from Dr. Richard Beanland from the University of Warwick, for which I am grateful. I am very thankful to Mr. Alistair Clark for training me on the SEM instrument to learn EDX and WDX measurement and for providing the gold sputtered on glass substrates. This work could have not been accomplished in a smooth, successful way without the support and the perfect work environment provided by the members of Hector group. I am very grateful to the current members of Hector group and the past members of the group who I shared the same working and writing up places with. The friendly share of the place and the equipment has decreased the struggles and difficulties during my PhD work.

I especially thank my mother and father for the huge lifelong love and support they have given me and for all the sacrifices they have made for me and my brothers and sisters. My husband and my two children have given me so much love and support that I cannot find the right words to thank them, so I thank them very much indeed, and love them very much.

I dedicate this thesis to
my parents, my husband, Shafiq
my beloved children, Shad and Anosha
for their constant support and unconditional love.

Definitions and Abbreviations

Abbreviations	Meaning
AAO	Anodic aluminium oxide
BE	Binding energy
CA	Chronoamperometry
CE	Counter electrode
CD	Current density
CP	Chronopotentiometry
CV	Cyclic voltammetry
CTAB	Cetyl trimethylammonium bromide
DCM	Dichloromethane
DMAB	Dimethylamine borane
ED	Electrodeposition
EDX	Electron dispersive X-ray spectroscopy
GC	Glassy carbon
GIXRD	Grazing incidence X-ray diffraction
ICSD	Inorganic crystal structure database
OAm	Olyleamine
OCP	Open circuit potential
PF	Pole figure
RE	Reference electrode
SCF	Supercritical fluid
SCFED	Supercritical fluid electrodeposition
SEM	Scanning electron microscopy
SSTiN	Silica sputtered titanium nitride
TEM	Transmission electron microscopy
WE	Working electrode
WDX	Wavelength dispersive X-ray spectroscopy
XRD	X-ray diffraction

Physical terms, their definition, and units

Physical term	Definition	Unit
A	atomic weight	g mol^{-1}
a	area	m^2
C	concentration of analyte in solution	mol cm^{-3}
d-spacing	inter-atomic spacing	Å
D	diffusion coefficient	cm^2 s^{-1}
E	potential	V
Ɛ	Young's modulus	MPa
F	Faraday constant (96485.3)	C mol^{-1}
ϕ	angle between the planes (h,k,l)	degrees (°)
h	Plank's constant (6.626 e^{-24})	m^2 Kg s^{-1}
I	current	A
L	thickness	m
λ	wavelength of X-ray beam	Å
ν	frequency of radiation	Hz
P	density	g cm^{-3}
Q	electric charge	C
R	gas constant (8.314)	J K^{-1} mol^{-1}
σ	direct stress	MPa
T	temperature	K or °C
θ	angle between incident /scattering beam	degrees (°)
W	weight	g
V	primary beam voltage (SEM)	kV

Chapter 1 Introduction

1.1 Electrodeposition

Surface degradation processes such as wear, oxidation, and corrosion under varied conditions are a serious problem in many engineering applications.[1] Hence surface treatment of materials used in such applications is vital.[2] There are many methods to coat materials, but selecting any method for coating purposes depends on the desired type and property of the coated material. Physical vapour deposition involves evaporation or sputtering of a material then condensing it to form a solid film on the substrate. The method allows the deposition of pure metals or alloys, or deposition directly from the target.[3] Chemical vapour deposition (CVD) involves transfer of a reactant in the form of vapour to the substrate surface on which a chemical reaction occurs and the crystal growth takes place. In evaporation techniques, the material is transferred atom by atom from the source to the film growth surface, that has been deposited onto a substrate.[4] Electrolytic deposition (ELD) techniques are generally used in ceramic production. In ELD an electro-generated base is used to hydrolyse the metal ions or complexes to form deposits of oxide, hydroxide or peroxide on the substrate. Thermal treatment can be used to convert the hydroxide and peroxide deposits into corresponding oxides.[5, 6] Electrodeposition is an important technique in metal surface coating[7] as it is a convenient and economically viable technique,[2] and able to deposit on large areas and curved surfaces. Growing deposits with different sizes of crystallites from nanometres up to macroscopic dimensions is effectively achieved with electrodeposition.[7, 8] Metals deposited by electrodeposition often have smooth surfaces and minimum lattice defects at ambient and lower temperatures. By using other physical methods achieving these properties can be difficult.[9]

Products of metal electrodeposition have very wide utilization in industry including in engineering, nanotechnology, sensors and microsystems, and the electronics industry. [10-12] Also they have roles in oil and gas installation, the automobile, agro-allied and aeronautical industries.[11] Examples of these applications are the electrodeposited materials in thin film magnetic recording heads,[13] electrodeposited copper to replace aluminium and its alloys in integrated circuits[14] and in nanostructured films.[10, 15] Protection and decoration of surfaces are wide range of applications for electrodeposits.[16]

There are specific cases where combinations of two deposition techniques are used to obtain better results. For instance electrophoretic deposition (EPD) and electrolytic deposition (ELD) may be combined in ceramic production,[5] and the fabrication of a multilayer Laue lenses combines pulsed laser deposition and focused ion beam machining.[17] Damascene-copper wafers can be used to make chip interconnects.[18] The dual damascene process is an additive modified patterning process, used to fill submicron structures without defects and to combine them without voids. A dielectric layer is deposited and etched to produce patterned trenches, and then a thick layer of copper is deposited to fill the trenches. The next step is the removal of the copper layer on the surface leaving the copper filled inside the trenches (Figure 1.1). In the following step a metallic barrier and copper seed layer are deposited using PVD, then in the last step copper is deposited by CVD.[14, 19]

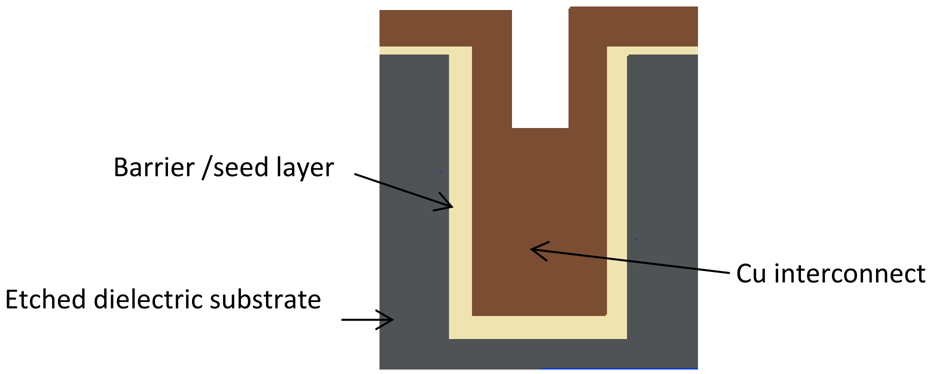

Figure 1.1 A schematic figure showing a trench of dielectric substrate filled with Cu interconnect.

Electrodeposition processes consist of applying pure materials by reduction of an electrolyte solution on top of the base material using a passage of current.[20, 21] Other terms used to describe electrodeposition or electroplating techniques include metal reduction, electrometallurgy or electroforming, depending on the type and the form of the deposit. Mostly the deposited metal has a crystalline form, which made the Russian chemist Kistiakovski call the process electrocrystallization.[12] Electrodeposition from an electrolyte source by passing a current through an electrochemical cell was first described in the scientific literature by Alessandro Volta in 1800,[16] but electroless deposition was discovered centuries before.[16] Electroless deposition involves using a strong reducing agent such as borohydride, hydrazine borane, pyridine borane or dimethylamine borane to deposit the material.[22] Electrodeposited coatings often exhibit higher surface stability than the same material deposited by electroless deposition. In general the electroless deposited materials are less porous and more corrosion resistant, but cost more. One of the other differences is the higher deposition rates in electrodeposition.[23]

An important aspect of electrodeposition today is to provide an environmentally safe process, especially as the technique has a wide range of applications. After Volta's discovery many developments on decorative plating of silver and gold by electrolytic deposition took place, where the electrolytes used in these processes were mostly toxic and contained large amount of cyanide.[16]

Two electrochemical quantities affect the deposition potential at which the metal deposition occurs. One is the standard electrode potential E°, and is characteristic of the metals, it is the measure of energy per unit charge from an oxidation/reduction reaction. The second quantity is the activity of the ion in the electrolyte. The amount of the metal deposited on the cathode is determined by Faraday's law, stating that the amount of electrochemical reaction on an electrode in an electrochemical cell is proportional to the quantity of electric charge passed through the cell.

$$W = ZQ \qquad (1)$$

Where W is the product weight in grams, Q is the quantity of electric charge in Coulombs and Z is the electrochemical equivalent. Z can be defined as the mass of the ion deposited by passing one Coulomb of electricity, its unit is g C^{-1}.

When an electrical current is passed through an electrochemical cell, the electrode potential will differ from the equilibrium potential by a value called overpotential. There are different rate controlling steps in an electrochemical cell, indicated by four partial reactions occurring in the cell. The partial reactions are charge transfer, diffusion, chemical reaction and crystallization.[24] The overpotential is to overcome the partial reactions in the cell. The substances consumed or produced in the overall reactions are transported to and from the electrode surfaces to/from the bulk, by a process called mass transfer.[22] The value of the overpotential determines the deposition rate, the structure and the property of the deposit. The Ni deposition overpotential magnitude is of the order of hundreds of millivolts.[12] A desired thickness of a deposit can be determined by using a known area of the substrate to deposit on.

By using Faraday's law, the time in seconds required to deposit a film of a desired thickness can be determined using the following relation.[22]

$$t\ (s) = \frac{Lad}{nI} \qquad (2)$$

Where I is the electric current in A, L is the thickness of the film in m, a is the area of the electrode (substrate) in m^2, d is the density of the deposited metal in g m^{-3} and n is the number of electrons required per metal ion.

The crystal structure and microstructure of the deposited metal determine many of its chemical and physical properties. A number of factors determine the nature of an electrodeposit, and by controlling some of these factors in electrodeposition process modifications can be produced in the electrodeposited surface. These factors include the composition of the electrolyte solution, pH, temperature, current density and the potential applied to the electrochemical cell.[20] In addition current distribution determines the morphology of the deposited surface producing surface roughness, surface defects, and overgrowth in small areas.[12] The substrate material can also affect the nature of the deposit through epitaxial growth, which results from any interfacial structural kinship between the deposit and the atomic lattices of the substrate. Another phenomenon related to the nature of substrate is pseudomorphism in which the deposit exhibits similar geometric features and grain boundaries to those of substrate.[24]

Deposition of materials can be applied to different substrates such as carbon steels, iron, aluminium and aluminium alloys etc.[25] The nature of the substrate affects the texture of the deposit in electrodeposition, such that in deposition on single crystal substrates the growth process can show strong epitaxial influences. Using randomly oriented polycrystalline substrates it is still possible to develop preferred orientation or texture in the deposition. Using amorphous substrates typically a randomly oriented deposit is obtained.[22]

Electrodeposition uses a cell containing the electrolyte and a counter electrode. The electrochemical cell is connected to an external power supply to obtain current flow, the object to be coated is the negative electrode, so that the metal ions are reduced and deposited on the surface. The formation of bubbles on the surface of the substrate is due to hydrogen evolution produced from the hydrolysis of the electrolyte which occur in parallel to metal deposition.[12] Gas bubbles on the cathode are a common problem, and can cause defects in the coating by producing voids in the deposited layers and porous films with poor adhesion.[26, 27]

1.1.1 Electrodeposition of metals

Metals have a fixed lattice of positive ions (atomic core) packed with free electrons (electron gas). The electron distribution of a metal always includes at least one valance electron (negative charge) that can move freely and randomly within the volume of the metal. The strong metallic bonds result from the interaction between the free electrons and the metal ion. The electron gas of the metal is the sum of the valance electrons from each atom within the lattice. In the presence of an electric field the valence electrons move towards the positive direction of the electric field. Thus metals are good electric and thermal conductors, which is theoretically described by the classical free-electron theory and Wiedemann-Franz law.[24] Wiedemann-Franz law states that the ratio of thermal conduction to the electric conduction is directly proportional to absolute temperature, the proportionality constant is called the Lorentz number. It indicates that the electric and thermal current are carried by the same fermionic particles.[28]

Metals and metal alloys are largely deposited by electrodeposition method. Electrodeposition of metals takes place in an electrolyte containing a precursor providing metal ions, which adsorb on the electrically conducting substrate that is immersed in the electrolyte. The ions are then reduced by electrons supplied from an external source through the conducting substrate and bond to the substrate's surface forming a metallic coating.[29]

1.1.2 Electrodeposition of semiconductors

Electrochemical properties of semiconductors are compared to those of metals by examining the electronic energy bands. Metals do not have band gap (the difference in energy level between the conduction band (CB) and the valence band (VB)), allowing free movement of electrons. This gap in dielectric materials is large, thus there is no chance for electrons to move from the valance band to the conducting band. The band gap in semiconductors is not as big as in insulators and electrons can be excited from the valence band to the conduction band.[30] The changeable optical and electronic properties of semiconductors especially in their nanostructure forms have received great interest.[31] Thermal or photochemical excitation of electrons from the VB to the CB can be achieved in semiconductors. More developed techniques have been used to obtain the electron excitation, for instance by doping. There are 2 types of doped semiconductors n-type, in which excess electrons from the dopant are the dominant charge carriers, and p-type semiconductors, in which electrons from the semiconductor are utilized in bonding with the dopant leaving holes as dominant charge carriers.[32]

Semiconductor electrodeposition faces challenges due to the low electric conductivity. Hence once the initial layers are deposited a passivation layer will form on the surface of the substrate causing difficulties in the charge transfer.[33]

1.1.3 Supercritical fluid electrodeposition (SCFED)

Electrodeposition from supercritical fluids (SCFs) was recently developed to deposit reactive materials and amorphous thin films.[8] One important aspect is that these non-aqueous solvents can often have a wide potential window, and so deposition of reactive elements like germanium may be feasible without the cost and high viscosity issues associated with ionic liquids. Supercritical fluids have been described as a "fourth state of matter"[34] (Figure 1.1). In SCF the substance has intermediate physical properties between those of liquids and gases. Liquid substances under certain conditions of temperature and pressure, convert to SCF state. By applying a critical heating temperature to a liquid under a constant pressure, a dynamic equilibrium can be obtained. The particles gain energy to leave the liquid and an equal number of particles lose energy to leave the gas phase, this point is known as the critical point.[35, 36]

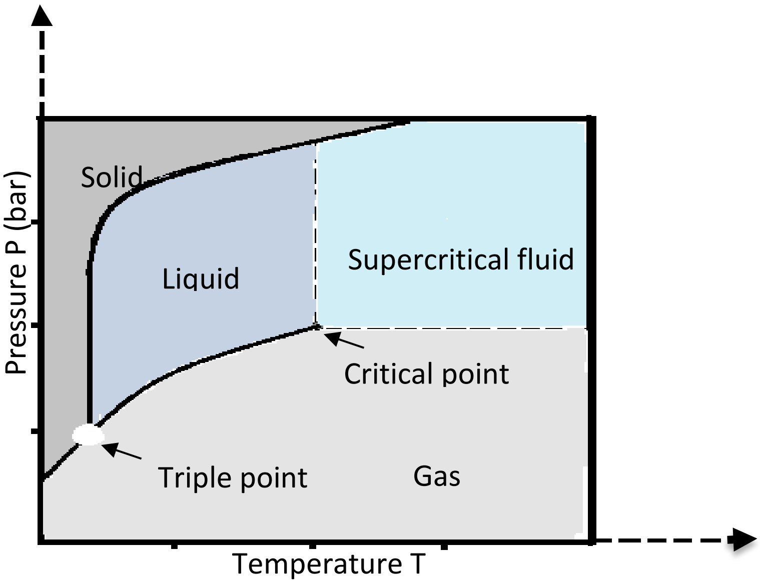

Figure 1.2 A chart for material states according to the temperature and pressure.

Solvents in supercritical phase exhibit interesting properties such as high diffusion and dissolving power, improved mass transport compared to liquids, low surface tension allowing electrodeposition onto fragile substrates, and low viscosity.[37] Electrodeposition from supercritical fluids has the potential to directly fill nano-scale features. With smaller length scales, SCFs can ease the process due to the penetration ability of SCFs to nanopores with diameters as small as 4 nm.[8] Other advantages of using SCFs in electrodeposition are in the depositions at high temperature and high deposition current densities.

The most used SCF is CO_2, which exhibits good mass transport, wide electrochemical window, a relatively low critical temperature of 31.2 °C and pressure of 7.38 MPa, and is non-toxic compound.[8, 38] In SCFED it is typically necessary either to use CO_2 with a co-solvent such as acetonitrile to increase its dielectric constant,[39] or to use more polar solvents such as CH_2F_2.[40]

In this thesis aqueous and non-aqueous electrodeposition was examined in parallel with a wider study into the SCFED of various materials. Some characterisation work on the SCFED materials is also included. Growth on flat substrates and in anodic alumina templates is reported and the systems studied are nickel, nickel-boron, germanium and tin. The crystallographic and microstructural properties of the deposits are examined in detail.

Chapter 2 Experimental techniques

2.1 Electrodeposition

A 3-electrode electrochemical cell consists of the working, reference and counter electrodes. The electrochemical reactions take place on the working electrode (WE) surface which should be electrochemically inert. The reference electrode (RE) has an important role in the cell, it has a constant potential and allows the potentiostat to independently control the potential of the working electrode. The basic reference electrode is the standard hydrogen electrode, but due to the difficult practical use of this electrode other reference electrodes are used and are called secondary reference electrodes. The role of the counter electrode (CE) is to pass the same current as on the working electrode to be measure through the potentiostat,[41] (Figure 2.1) shows a schematic of a 3-electrode electrochemical cell.

Electrodeposition is the electrochemical process of reducing a metal from an electrolyte to grow a film on a conducting surface.[12] Different electrochemical techniques are associated with metal electrodeposition. Chronopotentiometry and chronoamperometry methods were used to deposit materials in this work.

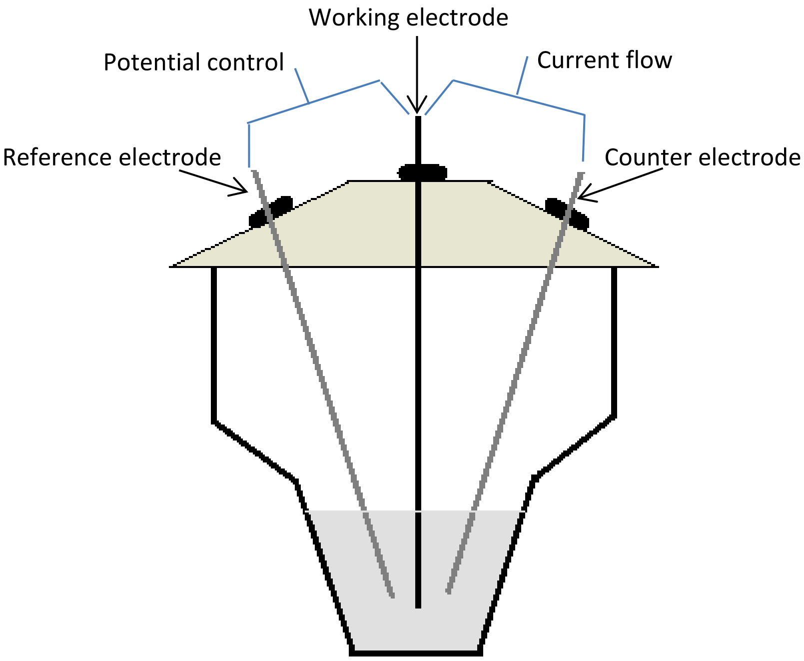

Figure 2.1 A 3-electrode electrochemical cell

There are cases where the RE consists of a metal wire having a constant potential and is called pseudo reference electrode acting as reference and counter at the same time. Hence the cell composed of 2-electrodes, the WE and the pseudo RE. In a 2-electrode setup the potential across the whole cell is measured, thus it's applicable in electrochemical experiments with no requirement of precise potential control at the WE interface. Figure 2.2 shows a schematic 2-electrode cell setup, applied for nickel electrodeposition, the anode is a piece of Ni foil acting as pseudo RE and CE.

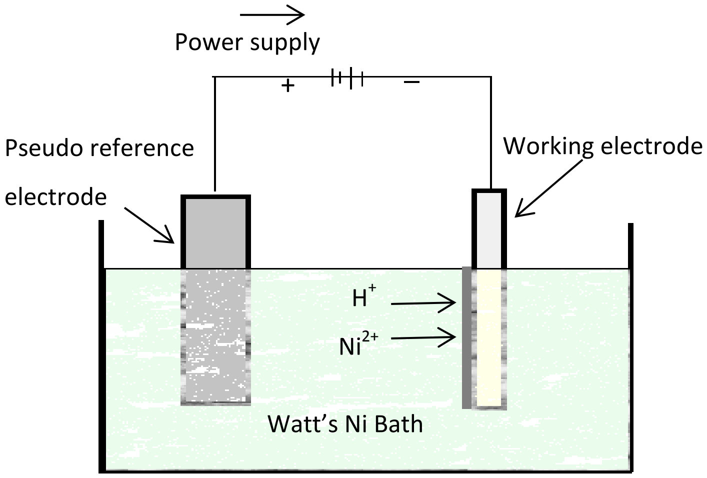

Figure 2.2 A 2 electrode electrochemical cell shown in a schematic cell for Ni electrodeposition.

2.1.1 Chronopotentiometry

Chronopotentiometry (CP) is a voltammetric method, in which the current is controlled and the potential of the working electrode is monitored with time. Hence chronopotentiometry can also be referred to as a galvanostatic (constant current) method.

In our work the CP technique was used to deposit Ni and Ni-B electrochemically on substrates of gold (sputtered on glass with a Cr wetting layer). A fixed current density of 0.01 or 0.02 A cm^{-2} was applied, which was expected to control the amount of B in the deposit according to the recipe published by K. Krishnaveni and co-workers.[1] The change in potential was then monitored. The deposition time was calculated according to the required thickness in the deposit. 2-electrode cells were used consisting of a nickel foil anode and the gold film substrate sized ~ 2.5 cm length and 1 cm width as cathode, around 1 cm of the length left out of the cell (uncoated).

A Biologic SP 150 potentiostat was used for the deposition.

Transition time (τ) is the time required for the concentration of the oxidized species at the electrode surface to reach zero and its value depends on the applied current. The relation between τ and *i* is described by the Sand equation.[42] The transition time is proportional to the bulk concentration of the species reacting at the electrode surface, and inversely proportional to the current.[43]

$$\tau^{1/2} = \frac{\left[nFA(\pi D_{ox})^{\frac{1}{2}}(C_a)_{ox}\right]}{2i} \qquad (3)$$

Where *i* is the constant current in amperes, $(C_a)_{ox}$ is the cell concentration of the analyte in mol dm^{-3}, D_{ox} is the diffusion coefficient of the analyte in $cm^2\ s^{-1}$, *A* is the electrode area in cm^2, *F* is the Faraday constant (96485.3 C mol^{-1}) and *n* is the number of electrons transfered. From this mathematical relationship, the transition times can show great change with variations of current density. The Sand equation is applied to a stationary electrode when the mass transfer is diffusion controlled, in our experiment of nickel electrodeposition, the solution is kinetically controlled and not diffusion controlled. Hence a negative deviation of τ is expected, due to the preceding reaction at the electrode surface which limits the species concentration at the electrode surface, so the transition time value will be smaller. The diffusion coefficient (D) can be calculated by measuring τ for several values of applied current and find the average D value using the equation.[44]

$$\mathrm{D} = \frac{4\ \mathrm{i}^2\ \tau}{\pi(\mathrm{nAF}(C_a\,)_{ox})^2} \qquad (4)$$

Where *D* is the diffusion coefficient, *τ* is the transition time, and *C* is the concentration of the analyte in the cell.

In chronopotentiometry the time chosen is important, so that the diffusion process determines the potential and the limiting current is low. At mass transfer limited currents the concentration of the electroactive species becomes zero at the electrode surface. The applied current reduces the oxidised species at the electrode surface, this produce a concentration gradient of the oxidised species between the bulk and the electrode surface, an equation relative to the technique is a potential-time relation shown below.

$$\mathrm{E} = \mathrm{E}^{\circ} + \frac{\mathrm{RT}}{\mathrm{nF}}\ln\frac{\tau^{\frac{1}{2}} - \mathrm{t}^{\frac{1}{2}}}{\mathrm{t}^{\frac{1}{2}}} \qquad (5)$$

Where *E* is the potential, *E°* is the formal potential of the electrode, *t* is the time, *R* is the gas constant (8.314 J $K^{-1}\ mol^{-1}$) and *T* is the temperature in Kelvin.[45]

2.1.2 Chronoamperometry

Chronoamperometry (CA) is a technique in which the potential is controlled and the current is measured as a function of time. Typically chronoamperometry is applied for a planar electrode in an unstirred solution, in which the reaction at the electrode surface is extremely fast compared to mass transfer.[46] The Cottrell equation (Equation 6) describes the current response in chronoamperometry.

$$i = \frac{nFAD_{ox}^{\frac{1}{2}}\, C_{ox}^{b}}{\pi^{\frac{1}{2}}\, t^{\frac{1}{2}}} \qquad (6)$$

Where C^{b}_{ox} is the concentration of the oxidized species in the bulk and t is time. D_o can be calculated from the (I vs $t^{-1/2}$) slope. (Figure 2.3) illustrates the steps in chronoamperometry, of potential stepping (a), current variation with time (b), and concentration profiles (c). Showing the current decrease with time, following the potential step, and the concentration profiles from zero oxidation to a value where the oxidation is diffusion controlled.[47, 48]

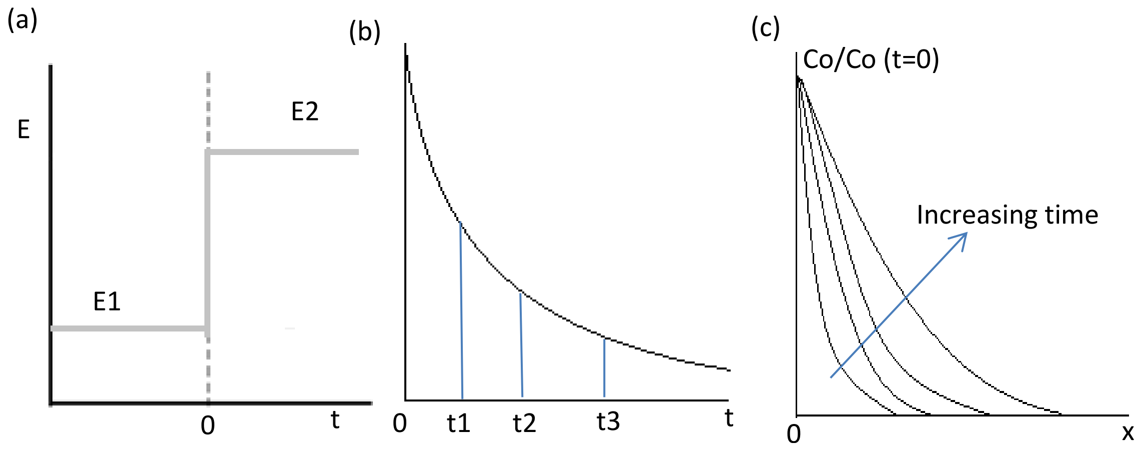

Figure 2.3 The schematic representation for a CA in an unstirred solution, of the potential step (a), the variation of current with time (b) and the concentration profile of the active species o in the solution with the distance X (c).

CA is a convenient technique to deposit materials that have various reduction potentials such as Ge, where a specific reduction potential can be selected to deposit at. In this work thin Ge films were deposited on a patterned TiN substrates at different various reduction potentials.

The electrochemistry of the Ge precursor was studied on glassy carbon (GC) disc electrodes by cyclic voltammetry, using Ag/AgCl in 0.1 M [^{n}Bu$_4$N]Cl in DCM as the reference electrode and a Pt gauze as the counter electrode. A similar test was repeated using the patterned TiN substrates as the working electrode. The reduction potential of Ge^{+2} to Ge^{0} was determined. Potential values between -1.25 to -2 V were used in CA experiments, for each applied potential the current was monitored for a specific time range between 5 minutes and 2 hours. The electrochemical processes were carried out inside the glove box under nitrogen atmosphere, as some of the precursors are moisture and air sensitive. A MicroAutolab 3 potentiostat and Nova software were used for the electrochemical measurements.

2.1.3 X-ray diffraction

When an X-ray beam of an appropriate wave length is scattered from the lattice planes of atoms in a crystal, which are aligned at an angle θ to the beam, constructive interference can occur, due to the regular arrangement of the atoms in crystalline materials. Hence well-defined X-ray beams will leave the sample in various directions (Figure 2.4).[49]

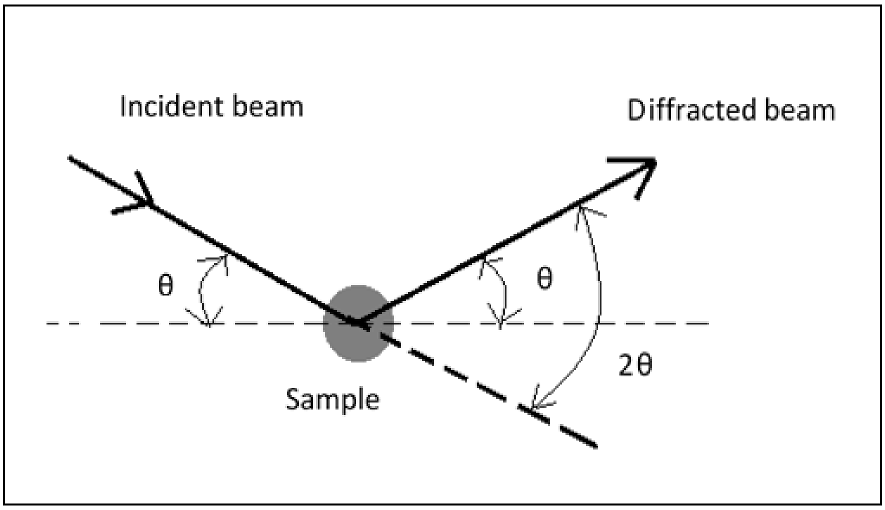

Figure 2.4 X-ray diffraction by a material sample.

The conditions under which constructive interference occurs are described by the Bragg equation.[50]

$$n\lambda = 2d_{hkl}\sin\theta \qquad (7)$$

Where *n* is an integer, λ is the wavelength of the incident X-rays in Å, *d* is the spacing between the planes in the atomic lattice in Å, and θ is the angle between the incident beam and the scattering planes. The use of X-ray powder diffraction data with standard crystallographic databases to identify a phase in a mixture of unknown phases has been possible since the 1930s.[51]

2.1.3.1 Thin film diffraction geometry

The grazing incidence X-ray diffraction (GIXRD) technique is based on irradiating the sample with X-rays at small incidence angles, such that the travelling path of X-ray photons is maximised. Path length is determined by $L = t[(1 / \sin \alpha+1)/(\sin 2\theta-\alpha)]$, where L is the path length, t is the layer thickness, α and θ are the incidence and Bragg angle respectively in degrees. It has been developed to provide diffraction patterns with depth-resolved information about the surface layers of materials,[52, 53] (Figure 2.5). Very small X-ray incidence angles result in total external reflection from the surface. Hence optimum GIXRD measurements are performed around the critical angle, which is the incident angle below which total external reflection occurs. The critical angle is a function of the X-ray wavelength and the density of the matter.[54] GIXRD (Figure 2.5-a) enhances the scattering contribution sensitivity from the film and decreases the observed substrate scattering.[52]

The geometry of a symmetric (θ, 2θ) X-ray diffraction measurement includes incident angle that is equal to the diffracted angle, causing deeper penetration of the X-ray beam into the sample. This geometry only observes crystal lattice planes that are parallel to the sample surface (Figure 2.5-b). Although the diffraction peak intensities for thin films scanned using symmetric X-ray measurement can be weak and may be obscured by the high peak and background intensities for the substrate, a symmetric XRD measurement is a powerful tool when applied to thin films to determine the crystallite orientations, as the reflections are from lattice planes parallel to the sample surface.[55]

In-plane XRD measurement involves both the incident and diffracted beams being kept at grazing angles, and hence measurement of the X-ray intensities that are diffracted from lattice planes normal to the sample surface (Figure 2.5-c). It is a very useful technique in thin film characterisation, as the measurement geometry minimises the diffraction and background intensities for the substrate.[56] It also gives good information on crystallite orientation.

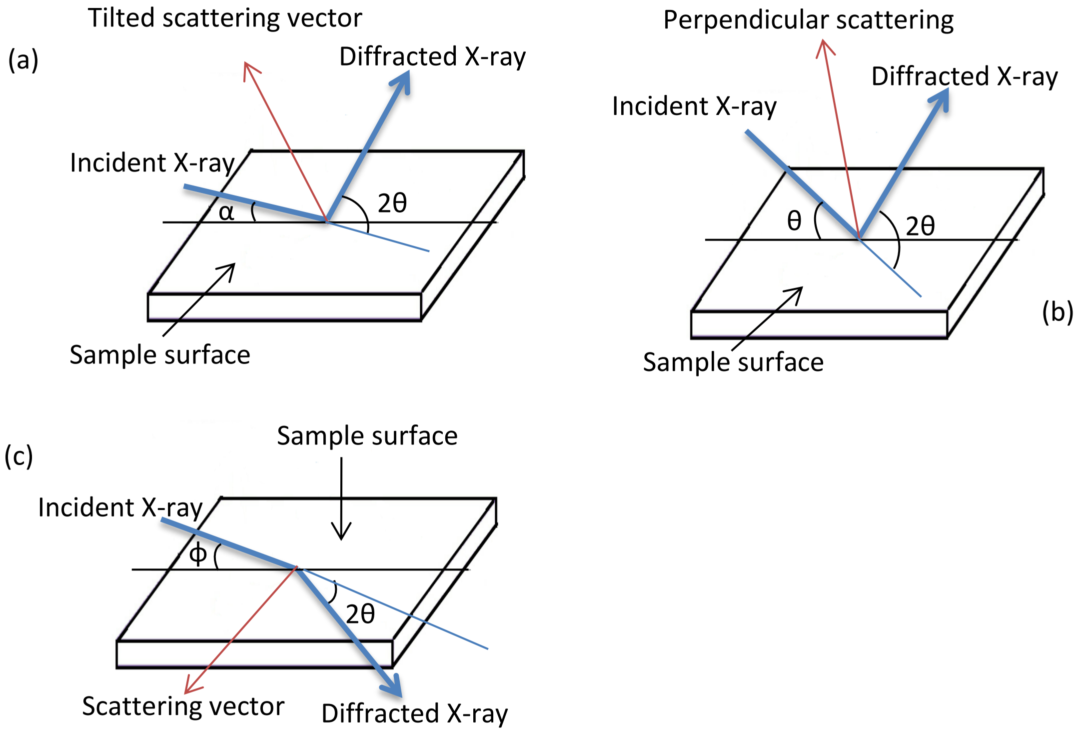

Figure 2.5 Schematic representation of grazing incidence X-ray diffraction measurement from a flat surface (a), a symmetric diffraction measurement (b), and an in-plane diffraction measurement, in which the diffraction vector is kept in the plane of the sample surface (c).

Parallel beam (PB) optics are usually used in thin film X-ray diffraction (Figure 2.6), since at grazing incidence a divergent beam could not be used to illuminate just the sample. A parallel incident X-Ray beam is obtained using extra-fine slits and the diffracted X-rays from the sample are also parallelised using parallel slit analyser (PSA). Using PB causes reduced intensities, as the incident X-rays come from a divergent light source.

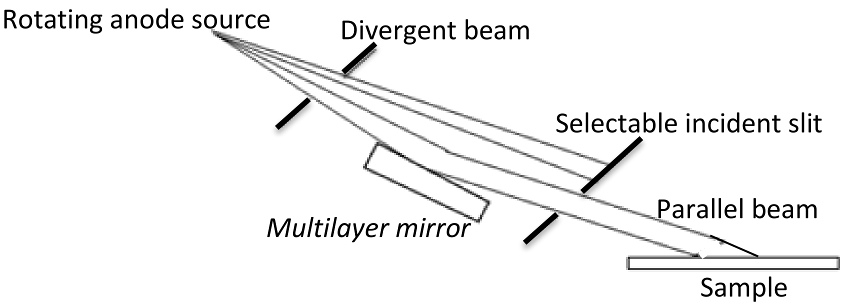

Figure 2.6 A sketch representing the CBO optics on Smartlab and how parallel beam is obtained for thin film studies.[55]

GIXRD has a wide application range in the characterisation of thin films, and in the measurement of strain and relaxation in thin layers. Although GIXRD improves the signal to noise ratio, its usage is limited, because small angles of incidence are limited to flat surfaces. At a critical angle of 0.3°, any variation in the surface normal (long or short variation), results in large parts of the surface moving out of the reflection area.[54] Hence good sample alignment is needed, the Smartlab X-ray diffractometer does the sample alignment such that the direct half beam cut is aligned to the sample.

To characterise the films, several different X-ray techniques were employed. To determine the phase information, preferred orientation, shifts in lattice parameters and to perform Rietveld refinement, out of plane symmetric and grazing-incidence X-ray diffraction measurements were collected for the samples. All the measurements were collected with the thin film (Smartlab) X-ray diffractometer. The optical device used was medium resolution parallel beam (PB). The optics used are 5° incident and receiving Soller slits, and the one-dimensional DTex 250 detector (1D). (θ/2θ) were collected for the samples in the 2θ range of 20-80°. The collection duration was varied. Using similar geometry and 2θ range, grazing incidence (2-theta) scans for the films were collected at an incidence angle of 1°. The incidence angle was adjusted using the tilt-adjustment axis Ry (i.e. tilting the stage towards the X-ray source). In-plane 2-θ/χ measurements were collected on flat samples to confirm the orientation distributions in the films. The optical device used was PB. The optics used were in-plane 0.05° incident and in-plane 5° receiving Soller slits, 0.5° parallel-slit analyser (PSA) and the one-dimensional detector (1D). The patterns were collected in the 2θ range of 20-80°. A collection duration of 30 minutes was typically applied.

2.1.3.2 Rietveld refinement

Rietveld refinement is named after the person who developed the method in 1969.[57] It provides whole pattern fitting, including lattice parameters, profile parameters, atomic positions and background parameters.[51] Information obtained from Rietveld refinement includes crystallographic structure determination, quantification of amounts of crystalline phases, residual stress, crystallite size, preferred orientation and lattice constant determination. Different programs are used to carry out Rietveld refinement, GSAS (general structure analysis system)[58] was used in this work. GSAS can be used to fit crystallographic and magnetic structural models to the X-ray and neutron diffraction data for single crystal or powder materials.

The Rietveld method considers the number of X-ray photons counted at a point across the entire powder diffraction pattern, the method is described in the Rietveld equation.[59]

$$M(S_i\,,\ X) = \mathrm{b}(S_i,\ X) + \sum_{k=k_1}^{k_2} I_k(X_s)\,\emptyset(S_i - S_k\,,\ X_P) \qquad (8)$$

The terms X_b, X_s, and X_p (p is the momentum transfer) are background, structure, and peak shape parameters respectively: $S_i = 2\ Sin\ \theta_i/\lambda$; $B\ (S_i, X)$ is a background function; $I_k\ (X_s)$ is the integrated intensity of Kth Bragg reflection; and $\emptyset\ (S_i - S_k, X_p)$ is a peak shape function.

The structure factor equation (shown below) describes how the atom arrangement (x, y, and z) affects the scattered beam.

$$F_K = \sum_j N_j F_j\ e^{2\pi i(hx_j + ky_j + lz_j)}\ e^{\left(\frac{-B_j \sin^2\theta}{\lambda^2}\right)} \qquad (9)$$

Where: F_K = structure factor of a specific peak; N_j = site occupancy; F_j = atomic form factor; h, k and l = Miller indices; x, y and z = fractional atomic coordinates; and B_j = thermal displacement parameter.

Peak intensity is affected by many factors such as atom location, Lorentz polarization, temperature or atomic displacement factor, with respect to absorption, preferred orientation, extinction and multiplicity factors.[58] Different factors produce peak broadening, the two major types of broadening observed in powder diffraction data are strain broadening and crystallite size broadening. Strain broadening can be estimated using the equation described below, the instrumental contribution can be subtracted.

$$S = \frac{\pi}{18000}\sqrt{(8\ln 2)(U - U_i)}\ \ 100\% \qquad (10)$$

Where U is the profile coefficient and U_i is the instrumental contribution function

Hence the strain component can be expressed as

$$S = \frac{\pi}{18000}(Y - Y_i)100\% \qquad (11)$$

Where Y is the Lorentzian component from the fit (Ly), and Y_i is the instrumental contribution function.

The second broadening is crystallite size broadening, which can be estimated from this broadening effect using the equation below.

$$P = \frac{18000\, K\lambda}{\pi X} \qquad (12)$$

Where: *K* is the Scherrer constant, with a value of ~ 0.9; λ is the wave length in Å; and *X* is the Lorentzian broadening.

The preferred orientation has important effects on the physical and chemical properties in crystalline materials. There are two functions in GSAS to correct the preferred orientation (O_{ph}) effect in powder diffraction. These are the March-Dollase function and the spherical harmonic function. The March-Dollase function gives a complete correction in samples having cylindrical symmetry along the diffraction vector. The function is able to deal with both needle and plate-shaped crystals, and with data obtained in Debye Scherrer geometry in neutron diffraction and Bragg-Brentano geometry in X-ray diffractometers. Assuming the sample has a preferred orientation axis lying normal to the diffraction plane, the preferred orientation can be detected from the refinable coefficient (R_o), whose value is obtained from the equation given below:

$$O_{ph} = \frac{1}{M_p}\sum_{j=1}^{M_p}\left(R_o \cos^2 A_j + \frac{\sin^2 A_j}{R_o}\right) \qquad (13)$$

Where O_{ph} is the preferred orientation correction (ph indicates the set of each phase in each histogram), and A_j is the angle between the preferred orientation axis and the diffraction vector.

A value of 1 for R_o means no preferred orientation in the sample. Whilst a value greater than 1 means the sample is cylindrical, in which the plate-like crystals are expected to be normal to the diffraction plane. R_o will be less than 1 if the sample was a flat plate, hence normal packing of the crystals to diffraction vector is expected. For parallel orientation of cylindrical symmetric distribution, the March-Dollase formula is given by:[60]

$$O_{ph} = \frac{1}{M_p}\sum_{j=1}^{M_p}\frac{1}{N}\sum_{k=1}^{N}\left(R_O B_{kj}^2 + \frac{1-B_{kj}^2}{R_o}\right)^{\frac{-3}{2}} \qquad (14)$$

Where $(B_{kj} = cos\, A_j\, sin\,\theta + sin\,\Delta k\, sin\, A_j\, cos\,\theta)$ and $(0 \leq \Delta\, k \leq 2\pi)$

The goodness of the fit can be estimated through the R- weighted profile (R_{wp}) by taking into account that each estimated parameter reduces the sum by 1, hence each weighted square between an observation and an estimated model is a term, a sum of n terms with p parameters.

$$R_{wp} = \left\{ \sum_{i=1}^{n} w_i \,[y_i(obs) - y_i(calc)]^2 \bigg/ \sum_{i=1}^{n} w_i \,(y_i(obs))^2 \right\}^{1/2} \qquad (15)$$

Where y_i is the numerical intensity value and w_i is = $1/y_i$.

Rietveld refinement was performed on the X-ray diffraction data from electrodeposited samples, using the GSAS package. To obtain the instrumental peak shape parameters, standard powder patterns were also collected on the Smartlab diffractometer, using identical geometries and collection conditions of the samples. Patterns for SiO_2 and LaB_6 powders were refined, and the U, V, and W values were extracted from the fits and used as found values in the sample refinements. This allowed L_x and L_y to be refined freely in the sample data to obtain the crystallite size and strain as independent variables without correlation to the instrumental peak shape.

2.1.3.3 Texture and pole figure measurements

Texture or preferred orientation represents the orientation of the crystallites, with respect to the sample reference frame. The distribution of grain orientations directly affects the physical properties of polycrystalline materials,[52] for example anisotropic properties such as Remnant polarization, dielectric constant, and elastic moduli. The orientation distribution function (ODF) can fully describe the texture. However simplified techniques are normally used in texture analysis for thin films, including pole figures, rocking curves and Φ scans. The texture of thin films is mostly fibre texture, in which most of the crystallites contain preferred orientation with respect to one direction in the sample reference frame (fibre axis). In biaxial texture, the crystallites are oriented preferentially along two fixed directions in the sample frame,[52] this is normally observed in rolled metal foils and epitaxially grown films.

Pole figure (PF) analysis is applied on polycrystalline samples to determine the distribution of crystal orientation.[61] In a PF measurement, evaluation of all the grains' reflections I_m (where m is hkl) is needed to obtain average texture at the surface. The position of the poles is described by two angular parameters, tilt angle from sample surface (α) and the rotation angle (β) around sample surface normal direction. The PF is applied by using a fixed (2θ) angle of diffraction and varying the two geometrical parameters α and β, to collect diffraction intensities under various orientations (Figure 2.7). [52, 61] Tilting angle is varied and the intensities of the peaks are measured.

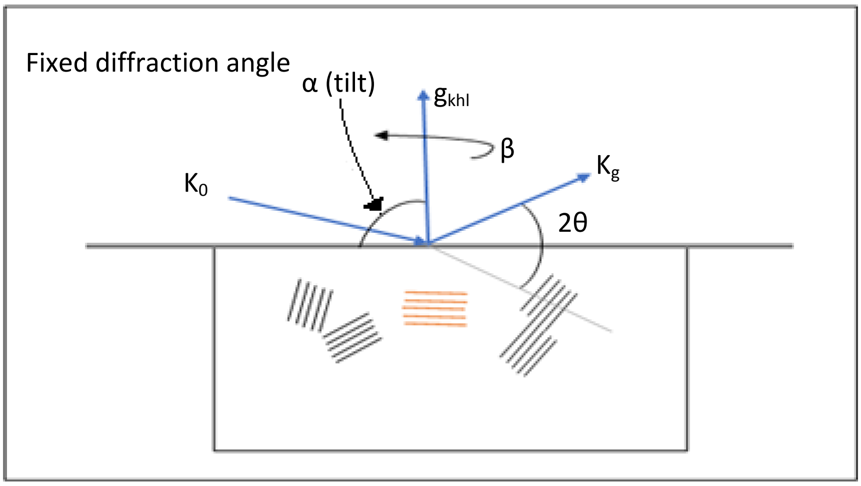

Figure 2.7 Schematic representations for pole figure measurement geometry, scan directions of preferred orientation axes β and α.

α=0 (lattice plane normal is parallel to the sample surface normal) is the outer end, and α=90 (lattice plane normal is perpendicular to the sample surface normal) is the centre of the pole figure,[62] (Figure 2.8).

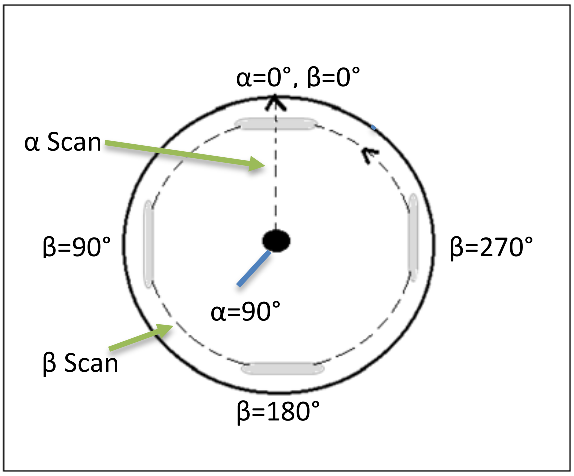

Figure 2.8 Schematic definition for α and β, α is the tilt angle from surface normal direction of the sample, and β is the angle (rotation) around surface normal direction of the sample.

The precision of PF measurement depends on crystal symmetry and the resolution. On other hand complete PF information cannot be obtained, due to the absence of the information from some tilting angles. At α=0° the Bragg peak intensities are not evaluated, caused by geometric restrictions. The missing information about orientation at α =0° and close to 0° is assessed from other Bragg peaks.[52]

Pole figure measurements were applied in the characterisation of Ni, Ni-B films, to determine the texture and the orientation distribution information, and consequently to determine the effect of B content and thickness change on the texture and preferred orientation. The measurements were performed using a fixed diffraction angle 2θ, and collecting β scans at a series of α values. Pole figures were collected at values corresponding to the Ni (200), Ni (220), and Ni (222) planes. The reflection method was applied, in which the sample is set to reflection geometry and two rotations of the χ axis (tilt=α) and ϕ axis (in-plain rotation=β) are used. Pole figure analysis (in-plane) was also performed on Sn nanowire samples to examine the texture within the wires. In-plane PFs are performed by combining the 2θχ, ϕ, 2θ and ω axes in the measurement. The detector is fixed at the 2θ position of interest (Sn 200 or Sn 101) and β is scanned with ϕ motion at each α angle. The α axis is controlled with the combination of 2θ and 2θχ, hence the measurements are performed without the requirement to tilt the sample.

2.1.3.4 Stress measurement

Residual stress in thin films is usually anisotropic, consisting of a mechanical force caused by several factors. It is called residual stress because it is mostly measured after the film production.[4] Stress distributes in the film after the growth on the substrate or on the adjacent layers. This type of stress is called growth stress, it depends on the material properties and the substrate temperature. An external factor such as the change in the physical environment for the film material produces induced stress.[4, 52]. Thermal stress is produced due to a rapid heating or cooling of materials. In thin films the thermal stress is due to the temperature differences between the material sections and/or the different thermal expansion/contraction rates between the film material and the substrate.

The external force can be a positive (tensile) or negative (compressive) (Figure 2.9). The former tends to increase the interatomic distances, while the compressive force (stress) tends to shorten the interatomic distances.[63] Hence lattice parameter measurements are a sensitive probe of film stress.

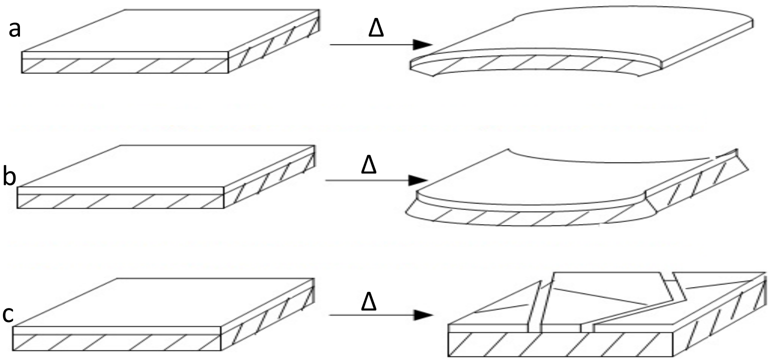

Figure 2.9 Representative figure for the types of stress in thin films, according to thermal expansion differences between the deposit and the substrate, (a) higher thermal expansion coefficient of the deposit vs. the substrate, (b) lower thermal expansion coefficient of the deposit vs. the substrate, and (c) interfacial stress, any substrate thermal expansion cause cracks and poor adhesion.

Different methods are used to measure the residual stress in thin films, X-ray diffraction is one of the methods. It covers the type of stress referred to as macrostress, depending on the linear attenuation coefficient (μ) of the material. The X-ray diffraction measurements are on a consistent length scale of a few hundred micrometres. Other types of stress on length scales below the X-ray penetration depth are called microstress. In case of very thin films it is crucial to use in-plane grazing-incidence diffraction to measure the residual stress. Various tilt (ψ) angles need to be chosen, with small steps of Δψ to run a symmetric ψ mode lattice spacing depth profiling. A very small penetration depth is obtained by following the described measurement setup, hence the thickness t remains always smaller than ψ.[52] From the facts mentioned above the lattice spacing (d) value is proportional to the generated stress. The stress measurement (iso-inclination) method works on the basis of choosing one lattice plane (hkl) and varying the X-ray incidence angle, then the residual stress is obtained from the d-spacing value. The relation between the stress value σ, ψ, and 2θ is described in the formula below:

$$\sigma = -\frac{\varepsilon}{2(1+V)} . \cot\theta_0 . \frac{\pi}{180} . \frac{\Delta\,(2\theta)}{\Delta(\sin^2\psi)} = K . \frac{\Delta\,(2\theta)}{\Delta(\sin^2\psi)} \qquad (16)$$

Where σ is stress in MPa,w2 K is the stress constant, $\mathcal{E}$ is the Young’s modulus in MPa, V is the Poisson’s ratio, and θ_0 is the diffraction angle in stress-free conditions.

In our work iso-inclination, fixed-psi method measurements were performed on Ni and Ni-B films to determine the stress. The instrument was the Smartlab X-ray diffractometer, the geometry used was medium resolution parallel beam/parallel-slit analyser (PB/PSA), with a 0.5° PSA and zero dimensional detector (0D, also called a point detector). Figure 2.10 shows the measurement geometry. Other stress evaluations were done using Rietveld refinements and from the observations of the shifts in Bragg-Brentano reflections.

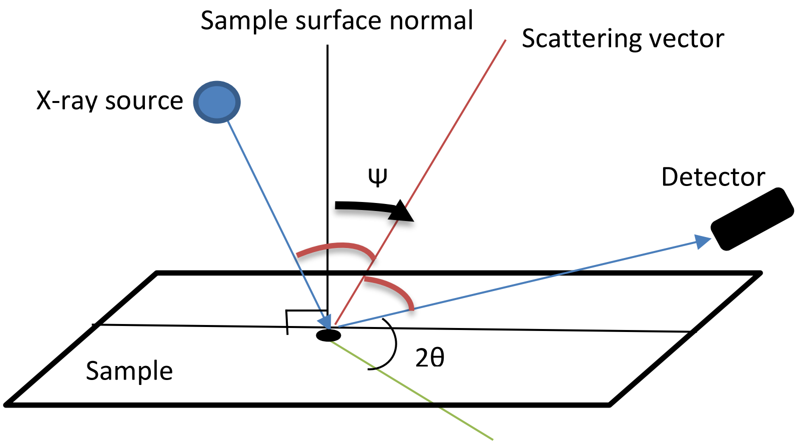

Figure 2.10 Representative diagram showing the iso-inclination measurement method.

2.2 SEM, EDX and WDX

2.2.1 Scanning electron microscopy (SEM)

Scanning electron microscopy (SEM) is a high resolution surface investigation technique with the ability to resolve surface structure down to nanometre scale.[64] SEM has a large depth of field, it's able to image rough surfaces in focus over a large change in vertical height, and hence to obtain low or high magnification images for large non-flat samples.[65] The technique is based on accelerating electrons in range of 0.1- 5 KeV (low voltage SEM) or high voltage up to 50 KeV, from a filament, or field-emission cathode.[66] The SEM column parts are an electron gun, two condenser lenses, an objective lens, an electron detection system, and a set of deflectors (Figure 2.11). [67] The electron lenses are used to de-magnify the beam cross-section at the gun, which is of magnitude 10 to 100 times in the case of a beam emission gun. The aim of the beam demagnification is to obtain electron-probe currents of 10^{-9} -10^{-12} A on the sample surface, where the diameter of the probe is 1-10 nm.[66] The total demagnification from the source to the specimen is typically 1000 to 64000 times.[67]

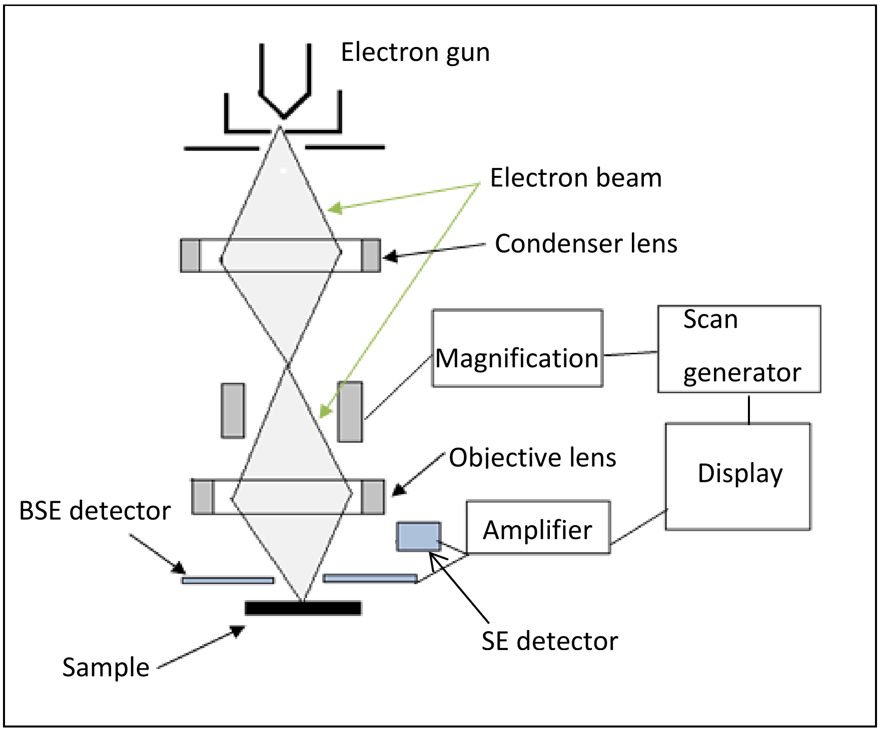

Figure 2.11 Schematic diagram for SEM system

Applying an electric voltage between the electron gun and a conductive sample results in emission of electrons from the electron gun towards the surface of the sample.[64] In the design of most SEM instruments the beam enters the specimen chamber through the final lens, where it interacts with the surface of the specimen by approximately 10 nm to 10 µm of interaction depth.[67] The interaction depth has a teardrop shape (Figure 2.12), and its volume is determined by the electron energy and the density of the sample. At high beam energy, the width of the interaction volume (R) which easily can be wider than the diameter of the electron probe, will limit the SEM resolution. The value of R can be estimated from the following formula derived by Kanaya and Okayama in 1972.[68]

$$R\ (\mu_m) = \frac{0.0276\, A\, V^{1.67}}{Z^{0.889}\ P} \qquad (17)$$

Where V is the primary beam voltage in kV, A is the atomic weight in g mol^{-1}, P is the mass density in g cm^{-3}, and Z is the atomic number. Various electron interactions result, which cause diffusion in electrons due to gradual loss in the electron’s energy and lateral spreading due to multiple large-angle elastic scattering events. The scattered electrons are from different depths, accordingly different scattered electrons are produced in terms of their energy. The most informative scattered electrons in SEM imaging are secondary electrons (SE). These electrons have energy less than 50 eV and escaped from the top surface of the specimen as a result of inelastic collision, hence provide an image of the topology. While back-scattered electrons (BSE) have broad energy range from 50 eV up to the primary beam energy, they are back scattered from deeper levels in the sample as a result of multiple elastic collisions.[66, 67] BSE images have greater sensitivity to the density of the material under study.

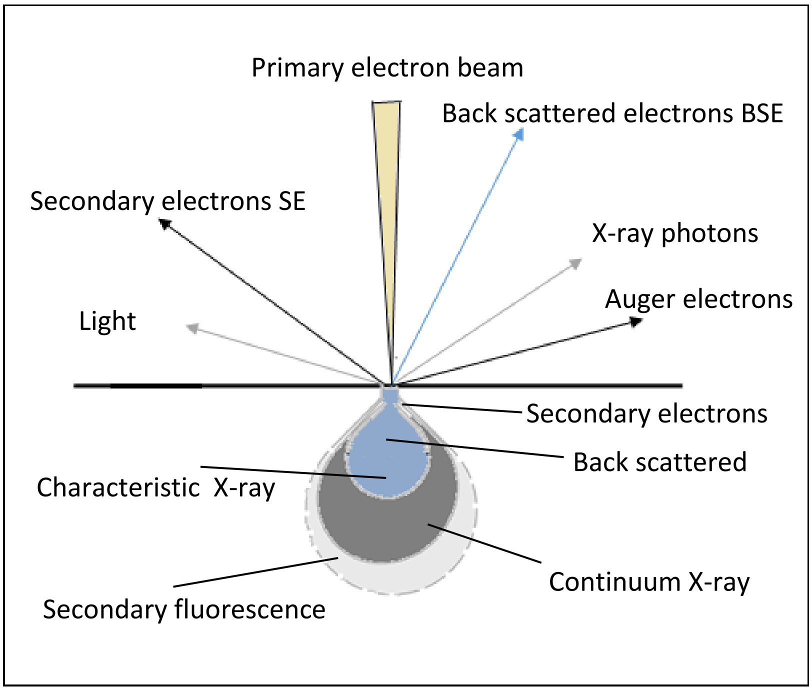

Figure 2.12 Teardrop shape penetration and interaction of the incidence beam current within the sample surface.

In SEM, depth of focus is a distance (D), and can be defined as the focusing distance that includes the highest variation on the specimen. The expression below describes the depth of focus.

$$D = \frac{\delta}{\alpha_\circ} \qquad (18)$$

Where δ is the probe resolution at the specimen, and α_o is the semi-angle of the beam.[67]

High vacuum SEM is applied to conductive samples, so that the electric current has an electrical path to ground through the sample. The high vacuum is to increase the travel distance of the electrons,[69] the vacuum environment is between 10^{-6} and 10^{-10} Torr.[64] The sample bombardment with electric current is a continuous process in SEM, hence dielectric or low conductivity samples eventually get negatively charged. Carbon tape or a conductive material is used to make good conductivity between the specimen and the sample stub. The Ni and Ni-B films were characterised by an FEI XL30 ESEM, the samples were mounted on SEM stubs using carbon dots. To provide the conductivity between the stub and the film carbon tape was used between the film surface and the stage, because the substrate is a gold sputtered on glass, hence the back of the substrate (the glass) is dielectric. All imaging was carried out under vacuum of around 1 x 10^{-6} mBar, accelerating beam voltage between 5 -20 kV. Ge films were also characterised by SEM, similarly to Ni in the preparation process the samples were mounted on SEM stubs using carbon dots and conductivity between the sample surface and the stub was by using carbon tapes. The SE was utilized to image the sample surfaces. To determine the actual film thicknesses cross-section images were collected on each of Ni, Ni-B, and Ge films. Sn samples electrodeposited on Au substrate and in AAO template were characterised for their morphologies using a JEOL JSM 6500F field emission scanning electron microscope. The sample preparation was similar to that in Ni imaging.

2.2.2 Energy dispersive X-ray spectroscopy (EDX)

Energy dispersive X-ray spectroscopy is an analytical technique used to detect and determine the elemental composition of a component. It is among the most frequently employed analytical techniques. The measurements are based on the determination of the energy distribution of the X-ray photons. EDX is integrated with SEM, bombarding a surface with an electron beam results in atomic excitations and releasing energy in the form of X-rays. The signals emitted from the sample which contain fingerprint information about each element, are collected using an energy dispersive X-ray detector. The mechanism of this energy release is by removal of electrons from atoms at the sample surface. The removed electrons leave vacancies, which are filled with electrons from higher shells. This last process results in emission of energy in the form of X-rays or Auger electrons. The latter is used in high spatial and depth resolution detection techniques (Figure 2.13).[70, 71]

When an electron drops from higher energy level to a lower energy shell for instance from L to K, the X-ray energy is determined as, $EK_{\alpha} = EL - EK$. Figure 2.14 shows energy levels for K and L-shells for electron movements in EDX.

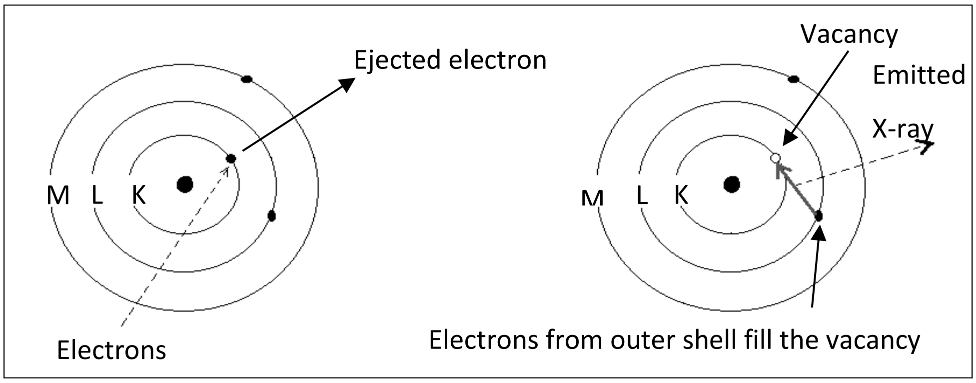

Figure 2.13 Schematic diagram showing the electron activity and X-ray characteristic in EDX.

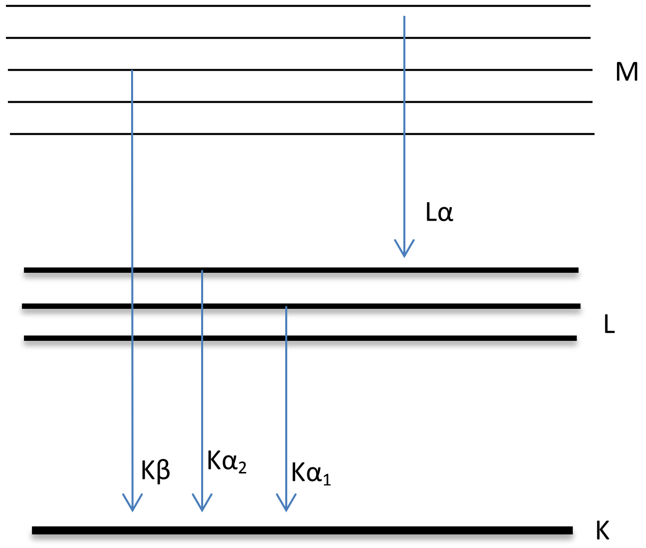

Figure 2.14 Representative figure for some electron transitions in the K, L and M shells for EDX.

To combine EDX with SEM, it requires an X-ray detector, pulse processor, and an analyser system. A histogram of X-ray energy versus intensity is the detection output in EDX created by the detector. The detector is an important part of EDX, it converts the incoming X-ray photons to proportional amplitude of electronic pulses.[72] There is limitation in EDX to determine low density elements. Elements below carbon in atomic number are not detected and elements below sodium are not very quantitative.[71, 73] Although EDX suffers from a lack of lateral and spatial resolution, depth resolution, and sensitivity, it is a powerful analytical technique.[70] EDX is capable of detecting elements in compositions down to 0.1% atomic concentration or 1 wt %. The high detection ability makes EDX a unique technique in detecting and quantifying small concentrations of elements in very small volume.

In this work the EDX spectra for the samples were collected using a Thermo Scientific Noran System 7 (NNS), with a Thermo Scientific Ultradry silicon drift EDX detector on the XL30 SEM. At high magnifications of around 1000x the spot size was increased from the SEM monitor until a detector counts on the EDX monitor showed a value of above 10,000, with the dead time below 25%. In the EDX experiments the live time limit was set to the default value of 30 s. In general the emission current was between 50 – 100 µA. Whole area EDX spectra for Ni and Ni-B were collected. For the Ge films, spectra for whole area and for specific points across the sample were recorded. EDX spectra were collected for Sn electrodeposited on flat Au and in AAO templates using a JEOL JSM 6500F field emission scanning electron microscope, collection times over 1 minute.

2.2.3 Wavelength dispersive X-ray spectroscopy (WDX)

In place of the energy dispersive semiconductor in EDX, WDX spectrometers use diffraction from a single crystal to measure X-ray intensity at specific wavelengths/photon energies. The wavelength measured by a specific crystal orientation is described by the Bragg equation.[73] Therefore the method is called wavelength dispersive X-ray spectroscopy. However, similarly to EDX spectra WDX data are usually displayed on an energy scale (KeV).[70] To obtain a measured X-ray intensity as a function of wavelength, continuous changes in the incidence angle of the crystal are required (Figure 2.15).

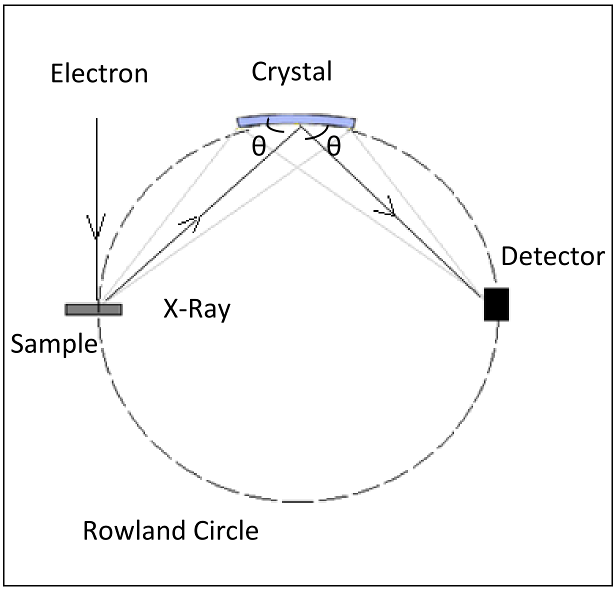

Figure 2.15 The sample, analytical crystal and detector configuration on the Rowland circle in a WDX spectrometer.

WDX detectors provide higher resolution (about 10 eV) than the EDX detector, but are more expensive and complex.[70] WDX is very effective in analysing low Z elements or low concentration elements. As the peaks are narrow, an improvement in signal/noise ratio is obtained and overlapping signals can be resolved. The detection limit of WDX is ~ 200 ppm and some special cases can be as low as 1 ppm.[73]

The WDX spectrometer used in this work was a Thermofisher MagnaRay WDX analyser operated from the Noran system 7 analysis system. It has the ability to move from element to element in short time (0.5 s) and has a very good peak-to-background ratio and high X-ray collection rates. With MagnaRay the WDX data is automatically combined with EDX, so that during the EDX data collection the spectrometer automatically determine the elements to analyse and perform all the WDX operations. It exhibits high resolution and sensitivity to trace elements. High throughput for all elements is obtained by a single low-energy capable sealed Xenon proportional counter, joined to the focusing optic. It exhibits an angular precision of better than 0.001°, which ensures the correct location of WDX peaks.

WDX was applied to the samples in this work to determine the quantitative elemental ratios, especially in the case of Ni-B, to determine the B wt. % in the samples. Qualitative WDX were collected for the present elements in Ni and Ni-B samples to detect the peaks, high and low background positions. The settings are similar to that of EDX, with the importance of using very high magnifications to prevent WDX signal dropping. Quantitative WDX measurements were by using standards for each element to determine the exact weight percentages.

2.3 X-ray photoelectron spectroscopy (XPS)

X-ray photoelectron spectroscopy (XPS), also known as X-ray photoemission spectroscopy is a non-destructive surface and near surface analytical technique used to determine the composition and electronic structure of atoms within the sample under study. XPS is a technique that focusses on the surface, applied to a large area with the ability to analyse several nanometres depth (less than 10 nm).[74] In XPS the sample is irradiated with monochromatic photons. Some of these photons collide with electrons in the core shells of the atoms, causing electron ejection (Figure 2.16).[75-77] These are of low energy and bonding inactive.

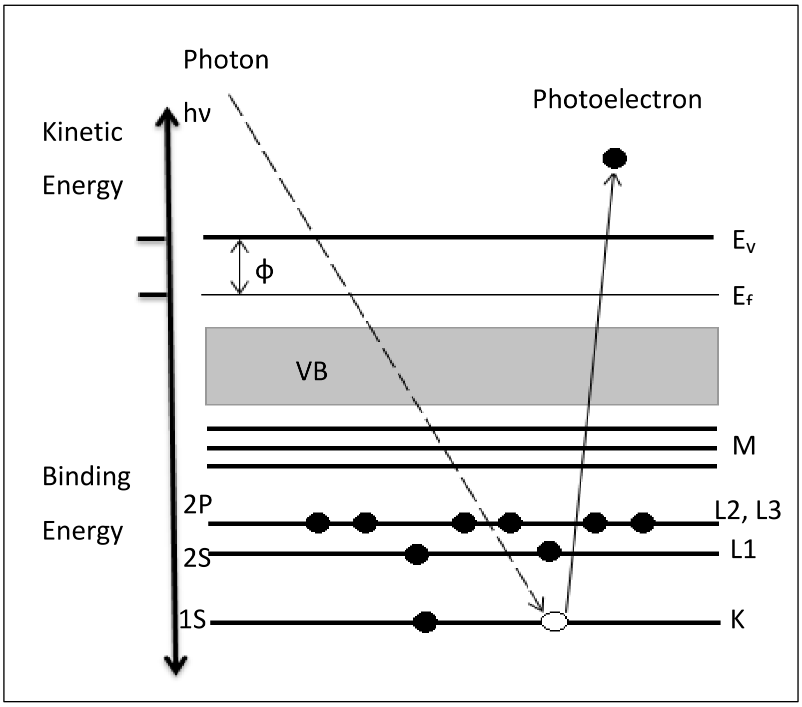

Figure 2.16 A diagram of photon energy, as a core level electron is promoted to the above vacuum level.

Figure 2.16 shows a K shell electron collided by a photon beam and ejected to above the conduction band of the element. The ejected electron obtains a kinetic energy which is dependent on the photon beam energy of the source and the chemical state of the element in the material. Hence kinetic energy (KE) which is measurement relative to the vacuum level (E_v) is determined by subtracting the binding energy (BE) which is allied to the fermi level (E_f) from the photon energy of the source.[75, 78]

$$KE = h\nu - (BE + \phi) \qquad (19)$$

Where *h* is Plank's constant (6.626 e^{-24} m^2 Kg s^{-1}), *v* is the frequency of the radiation, *BE* is the binding energy of the electron, and ϕ is the work function of the material, which is defined as the energy required to detach an electron from a solid.[79]

The binding energy remains unaffected by changing the energy of the photon source, it is an essential property of the material. Variation in the chemical environment of an atom including its oxidation state, leads to slight altering in the BE known as chemical shift, and assists the determination of the chemical, valence or charge state of an element in a compound. [74, 75] The XPS spectra contain characteristic peaks for ejected core shell electrons overlaying a background arising from inelastic scattered electrons, accompanied by induced Auger transitions. XPS peaks are identified by the number (1, 2, 3,..) and denotations (s, p, d, f,…) of the core level from which the electron is emitted as well as the spin quantum number of the electron (s= ±½).[79]

The energy loss during inelastic scattering at higher energy levels , which appear as a background feature in the XPS spectra, need to be corrected to obtain a correct identification for the kinetic energy related peaks. Three methods are typically used to correct background, placing them in simplicity order are: linear, Shirley, and Tougaard background correction methods.[74] An XPS instrument consists of a radiation source, a vacuum environment, an electron energy analyser, an electron detector and a data system (Figure 2.17).[74]

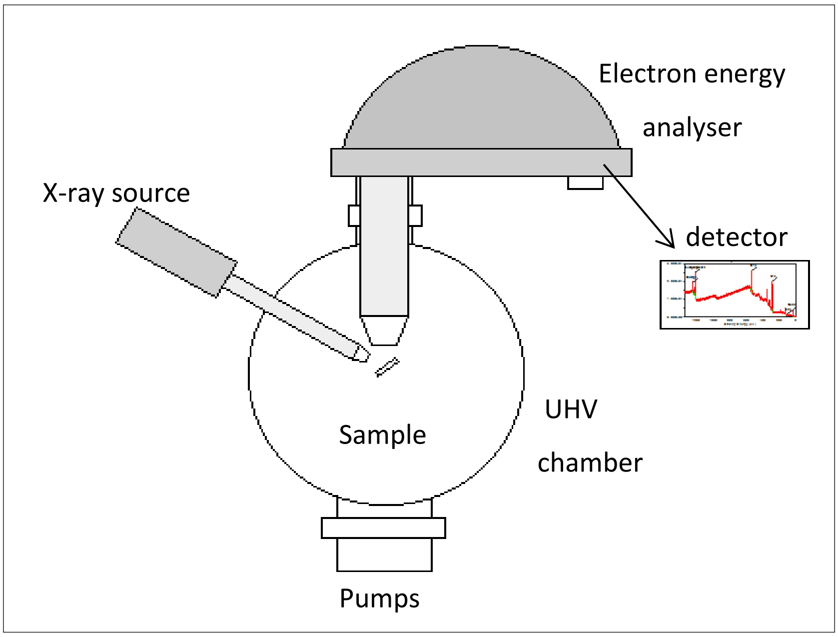

Figure 2.17 A schematic diagram for a typical XPS system.

The X-ray and the filament in XPS processing require relatively high vacuum (10^{-7} Torr) to operate, and operating the analysis under high vacuum pressure also prevents surface contamination. The inelastic free path is the mean distance that an electron can travel without being scattered. Hence ultra-high vacuum (10^{-9} Torr) is applied to deliver the low pressure required in obtaining the high mean free path for the electrons.[79]

Al K_α (hv= 1486.6 eV) and Mg K_α (hv= 1253.6 eV) are the most used anode materials in XPS instruments. The cathode is a filament which irradiates the anode with thermal electrons as a result of heating, and applying high voltage to the anode causes electron emission with characteristic spectrum.[80] The kinetic energy of the photoelectrons is measured by the energy analyser, which consists of a hemispherical electron energy analyser. A high resolution energy analyser is essential in XPS, to ensure the peak detection of every chemical state of the elements in the material. Two types of detectors are used with XPS instruments, a channel electron multiplier or a position sensitive detector. [74, 79]

With dielectric and semiconductor samples charging can occur during XPS experiments. Photoelectrons are ejected from the surface and positive charge will be built up on the surface, as less electrons return to the surface compared to the leaving electrons. Hence electrons are ejected with less kinetic energy causing higher binding energy, known as charging shift. An electron flood gun is mostly used to correct the charging, the gun is utilised to bombard the surface with electrons to neutralize the accumulated positive charge.[79]

To characterise the electronic state of thin Ge films produced in our work, XPS was applied to the as-deposited samples and the annealed samples. A Thermofisher Theta Probe Angle-Resolved X-ray Photoelectron Spectrometer was used, with a monochromated, micro-focused Al K-Alpha source. To avoid atmosphere contact the samples were transferred inside sealed vials under N_2, except for a short time period during sample loading into the instrument.

Chapter 3 Electrodeposition and characterisation of Ni and Ni-B

3.1 Introduction

Coating processes are generally used to modify material surfaces in order to improve the performance and to increase their lifetimes, including to increase the hardness, and wear and corrosion resistance.[81] Ni coating is considered an important process due to the wide application areas of this material. The applications include decorative, functional and electroforming areas.[82] Iron-group metals (Ni, Co and Fe) exhibit unique magnetic and thermophysical properties, which put them in the position of interest as electroplating materials.[83] Nickel is a ferromagnetic material, nanostructured Ni and Ni alloys are very useful in magnetic sensors and memory devices and the data storage industry.[9, 84] Making nickel alloys with other metals often causes enhancements in the properties of these metal coatings, for example zinc is used to coat steel for protective purposes and by using Ni-Zn alloy a significant improvement in corrosion resistance and mechanical wear have been achieved.[85] Surfaces coated using pure Ni or using Ni alloys exhibit superior hardness and high corrosion, abrasion and erosion resistance and good resistivity against high temperature oxidation.[86, 87] Ni exhibits high catalytic activity in the oxidation reactions of small organic compounds such as glucose, carbohydrates and more especially methanol and ethanol [88]. Nickel-based alloys including Ni-B, Ni-S, and Ni-P are used as catalysts for fuel cells and storage batteries, in which amorphous Ni-alloys show better performance than the crystalline state.[89] The composite coating materials have found industrial applications in aircraft, automobile and many other engineering industries.[87]

The coverage of the surface in nickel electroplating is very good.[84, 85] Ni electrodeposition is achieved in a cell consisting of an anode and a cathode suspended in a conductive solution containing Ni^{+2} ions, these ions are reduced to metallic Ni on the cathode by passing current between the two electrodes. The anode often consists of the metal being deposited so as to replace the reduced Ni^{+2} in the solution, an immediate transfer of the metal ions to the solution occur by dissolution. The applied current in electrodeposition is either direct current (DC) or pulsed current (PC). In direct current deposition a constant current is applied, while in pulsed electrodeposition a cyclic current wave form is applied. PC electrodeposition is effective when a nanocrystalline deposit is required.[12, 90]

The deposited Ni layer is bound to the surface of the substrate by covalent, ionic, polar, or other types of bonds produced from the interatomic forces between the Ni-layer and the substrate surface.[82] The rate of deposition is proportional to the current density.[82] Many factors have effects on the stress and the texture of the electrodeposited films like hydrogen gas, plating time, current density, organic additives in the electrolyte composition.[1]

The Ni deposit has a face-centred-cubic crystal structure.[91]A single layer of nickel is often applied in the decorative applications. However in the case of specific surfaces that are exposed to severe corrosive conditions, multi-layered nickel coatings are applied with the same thicknesses of a single layer.[91] Nickel coated carbon fibres are utilized in electronic devices.[92]The electrochemical reaction mechanism of Ni deposition has the general form as described in the following three steps, however several factors determine the mechanism of Ni deposition such as pH, concentration, electrode material and bath additives.

$$Ni^{+2} + X^- \longrightarrow NiX^+$$

$$NiX^+ + e^- \longrightarrow NiX\ ads$$

$$NiX\ ads + e^- \longrightarrow Ni + X^-$$

The X^- is assumed to be Cl^- in the case of the commonly used Watts bath[83].

There is a great interest in nickel and nickel alloy plating, a large number of publications are available on nickel deposition. The studies include the effects of impurities,[93] additives,[94] process variables,[11] surfactant,[27] crystallite structure and size,[84, 95-97] deformation,[98] and electrochemical mechanism.[9, 85]. Many studies have been carried out on the effect of impurities of various metals on Ni electrodeposition. For example Mohanty and co-workers have studied the effect of Cd^{+2} on nickel electrodeposition from sulphate bath, their observations shows that Cd^{+2} effects on the current efficiency and crystallite orientation when added at concentrations above 500 mg dm^{-3}. [93] Solving the hydrogen evolution problems, which is due to the electrolysis of aqueous electrolytes is one of the study subjects in this area. Researchers have found supercritical phase of the electrolytes can be used to overcome the hydrogen evolution problem.[99] Variation of the deposition temperature and the current density was studied by Luo and co-workers to determine the effect on the microstructure of the deposit. The results show production of dense material with high tensile stress when deposited at a high current density of about 30 mA cm^{-2}, and less dense material with small compressive stress when deposited using low current density of about 2 mA cm^{-2}. [100]

Further studies on evaluation of morphology, structure and mechanical properties of Ni films electrodeposited from supercritical carbon dioxide were produced by Chang, Nagoshi, Rahman and their co-workers.[101-103] Parameter variation was applied in Ni electrodeposition from supercritical electrolyte when Lee and co-workers deposited Ni from post supercritical CO_2 mixed with Watt's bath. In comparison with supercritical electrolyte and conventional deposition, the film contained less pinholes, smoother surface and higher hardness. This is explained by the presence of dissolved CO_2 in the sc-CO_2 electrolyte compared to the conventional methods. On the other hand, they have measured internal stress of the deposits and determined its correlation with the grain size. Their observations indicate an inverse relation slip between the grain size and the internal stress.[104]

Composite coatings are a blend of two or more substances that are deposited together in a homogeneous form, in which any of the substances is kept chemically separated in the coating structure. Composite Ni-B plating can be achieved using electrodeposition or electroless (autocatalytic) depositions or other techniques such as flame-spraying (thermo mechanical methods).[21, 87] Nickel atoms are 33.6% bigger than boron atoms, this indicates the weak possibility for solid solutions to be formed in the Ni-B system, but is possible with nonequilibrium systems like electrodeposition.[105] The presence of boron in the composition of Ni coatings increases the hardness and results in better wear resistance.

Many papers have reported Ni, Ni alloys and composite coatings on various substrates, using different techniques. In 1973 Gorbunora and co-workers described the electroless deposition of Ni-B alloys, from a plating bath consisting of a Ni-salt, NaOH, a complexing agent and a stabilizer. Samples with 4.5 % B consisted of two Ni-B phases, a solid solution of B and hydrogen in Ni and an amorphous Ni-B, while the samples prepared with higher B contents consisted of only an amorphous phase of Ni-B.[106] Electroless deposition and electrodeposition of Ni-B from borohydride bath have been reported by Rajacopal in 1983.[87] Krishnaveni and his co-workers have produced electrodeposited Ni-B from a modified Watt's Ni bath. They studied the texture of Ni-B composite deposits using XRD and selected area diffraction (SAD) patterns, and all the patterns show preferred orientation along the Ni <111> axes.[1] One year after their publication, Yu-ching and Tse-chaun Chou published a paper about the fabrication of Ni-B thin films for ethanol sensor on Pt/Ti on alumina (Al_2O_3) substrates, using Ni Watt's bath. They detected high sensitivity of the prepared Ni-B to the concentration of ethanol, ranging from 100 to 600 ppm, which is dependent on the weight ratio of Ni-B and the ED time.[107] Diplas and co-workers have worked on the deposition of amorphous Ni-B alloy, using electrodeposition technique on polycrystalline Ni substrate.[89] Nano-crystalline Ni-B electrodeposition on a stainless steel substrate has been achieved by Lee and co-workers, using a Ni bath containing the compositional chemicals of Watt’s bath, with the difference of using trimethylamine borane as the B source and sodium lauryl sulphate.[108] They have shown changes in the morphology of the films surfaces from a dull and rough to a smooth and bright surface by adding B to Ni deposits, as shown in other studies.[1] Their study also examined the stress in the films, and concluded it to be tensile and to undergo an increase by increasing the B content. Wen and Szpunar have successfully electrodeposited 50 and 12 nm in diameter nickel nanowires into nanoporous alumina template films on silicon wafers coated with gold.[109]

Electroless deposition involves using a strong reducing agent such as borohydride, hydrazine borane, pyridine borane or dimethylamine borane to deposit the material from the solution on top of the substrate. Electroless means the process does not involve any external electric current from electrodes, but the process does include charge transfer.[82] In electrodeposition the reduction of the material in the electrolyte is achieved by passing an electric current from an electrode.[21]

In the electrodeposition of Ni-B using Watt’s bath dimethylamine borane (DMAB) is used as a source of boron and the reduction of the elements is by applying current. Here to prevent the electroless deposition of the material the electrolyte solution needs conditioning by controlling temperature and pH.[110] According to the literature the amount of B in the electrodeposition of Ni-B films from DMAB added Watt’s nickel bath is controlled[1]. This was by relying on the fact of increased Ni reduction by increasing the current density and that the contribution of B in the deposit comes from DMAB complex decomposition. So a higher current density means increased Ni reduction relative to the DMAB decomposition, hence less B contribution in the deposit.[1] Ni-B compositions of 1% and 3% of boron content were produced in this work using current density variation to control the amount of B in the deposits.

3.2 Experimental

Ni and Ni-B films of various thickness and B content were deposited from Watt’s Ni bath by chronopotentiometry (CP), with various thicknesses and B contents. The films are characterised using X-ray diffraction methods, SEM, EDX and WDX.

3.2.1 Preparation of Watt’s nickel bath

The recipe used by Krishnaveni *et.al.* was followed,[1] aqueous electrolyte (Watt’s nickel bath) mixture was prepared by dissolving nickel sulphate hexahydrate (12 g, Sigma Aldrich), nickel chloride hexahydrate (2.25 g, Sigma Aldrich) and boric acid (1.5 g, Sigma Aldrich) in deionised water (50 cm^3). In the deposition of Ni-B films dimethylamine borane (DMAB) (0.15 g, Sigma Aldrich) was added as the source of B. In the deposition of some of the 5 µm thick films, sucrose (0.1 g) was added to the bath composition. The pH of the solution was fixed to be 3.5 by adding few drops of 10 % HCl solution and the pH was monitored using pH meter.

3.2.2 Electrodeposition process

The electrochemical cell consists of 2 electrodes, the cell was surrounded by a glass jacket allowing water circulation to keep the temperature of the bath at a specified value. A 200 nm gold film was the working electrode (sputtered on glass with a 30 nm Cr wetting layer) and nickel foil acted as both the working electrode and as the pseudo reference. 50 cm^3 of the nickel bath solution was used in the experiments, the size of gold electrodes were around 1 cm width and 2.5 cm length. Before the start the solution was degassed using nitrogen gas flow for 30 minutes. The technique used in the deposition was chronopotentiometry using a Biologics SP 150 potentiostat. A constant current density of 0.01 A cm^{-2} and 0.16 A cm^{-2} was applied for a fixed time period, during which time the change in potential across the cell was monitored. The temperature was maintained at 45±1 °C. The charge passed during the film formation was calculated in advance to obtain fixed thicknesses of 0.5, 1.3, 5 and 13 µm. The amount of B content was targeted via the applied current density,[1] and the thickness of the films was controlled by the deposition time (i.e. amount of charge passed).

3.2.3 XRD experiments

The XRD patterns were collected on the Smartlab X-ray diffractometers at ISIS, in Diamond light source and at the University of Southampton, with Cu K_α or Cu $K_{\alpha1}$ radiation, using 2θ scans in the range between 20-100°. In-plane measurements in the 2θ range of 20-100° were carried out on some of the films using 2 θ/χ measurements.

Pole figure measurements were performed using the reflection method in which two rotations on the χ and ϕ axes are applied. A high resolution parallel beam, reflection method was used, the detector position was fixed at the 2θ diffraction angles for the Ni 200, 220, and 222 reflections. α-step and β-rotation scans were performed on the samples to obtain pole figure data.

3.2.4 SEM, EDX and WDX experiments

Scanning electron microscopy (SEM) was carried out to examine surface morphologies and the elemental peak positions for Ni and B were determined using electron dispersive spectroscopy (EDX). The B content percentage in the Ni-B films was determined by wavelength dispersive spectroscopy (WDX). The WDX detector was aligned by maximizing the Ni L_α line intensity and the

Ni L_α and B K_α lines were used to analyse Ni and B. Elemental standards of Ni and B from a standard block were used to quantify Ni and B in the deposits.

3.3 Results and discussion

Characterisation techniques including a number of X-ray diffraction techniques, SEM, EDX and WDX, were applied to the deposits to determine properties including composition, crystallite size, morphology and stress. Quantitative evaluation of boron distributed in Ni matrix was also performed. Hydrogen bubbling from the electrolysis of the aqueous bath was observed in the cell during the deposition process. To decrease the effect of stress and to improve the adhesion between the deposit and the substrate, some of the samples were produced with the addition of 2 g dm^{-3} of sucrose to the bath composition, Sucrose helps to refine the grain size of the deposit,[111] as the adsorbed molecules or ions, causing surface chare modification and prevent agglomeration of the deposited particles.

3.3.1 Chronopotentiometric deposition of Ni films

3.3.1.1 Electrochemistry (chronopotentiometric data)

In chronopotentiometry the ohmic drop from the solution resistance is constant, since the applied current is constant.[42] Hence the initial voltages in the films deposited at same current density are expected to be similar.

The potential-time transients recorded for 0.5 µm Ni film (Figure 3.1), consist of three major regions; a large negative potential in the initial steps of the deposition due to double layer charging and the start of Ni nucleation. After a few seconds in which the growth of the Ni nuclei starts, the potential becomes more negative due to diffusion limitation, in which reduction of Ni and release of Ni ions from the oxidation of the anode Ni foil into the electrolyte takes place. Bubble formation on the cathode's surface starts roughly at this time, hence the increased negativity in the potential could be caused by bubbles accumulations. As the growth of the layers continues the potential shows a gradual decrease in magnitude, and this could be due to hydrogen evolution process (release of the bubbles from the surface) along with the film growth, and also probably due to surface roughness. For the 5 µm Ni (Figure 3.1), when the film continues to grow for longer time a gradual decrease in the potential with time is observed, it might be due to accumulation of H_2 bubbles on the deposit's surface, which results in reducing the electroactive surface area.

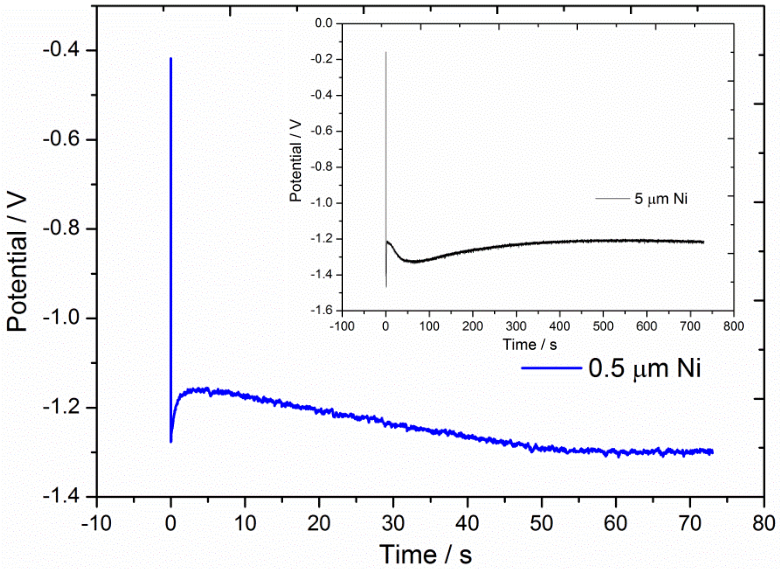

Figure 3.1 Chronopotentiograms for growth of 0.5 µm thick and 5 µm thick (the inset graph) Ni films from Ni Watt's bath. The applied current density was 20 mA cm^{-2}, the temperature was 45 °C and the pH was 3.5.

3.3.1.2 SEM and EDX measurements

SEM was applied to examine the surface morphology of the films and to study the effect of thickness and sucrose additive on the morphology. Figure 3.2 shows SEM micrographs for Ni films electrodeposited at different thicknesses, with sucrose added to some of them. In general the Ni films had rough and dull surfaces. The electrodeposited Ni surfaces without the additive have dull and pyramidal crystallite morphologies, by adding sucrose to the electrolytes composition this morphology is switched to a brighter surface morphologies with spherical particle growth, and this is more obvious in the thicker (13 µm) films. Studies show similar effect of additives on Ni morphology when saccharine was added to the Ni electrodeposition bath.[2, 111] The surface of the very thin (0.5 µm) films is less rough with a more uniform distribution of particles compared to the thicker films. This indicates increased roughness and particle agglomeration with increasing the thickness of the deposit.

Cross-section SEM was used to determine whether the real thicknesses matched the intended ones from the deposition duration calculations. The SEM images confirm the exact thicknesses of every film, and Figure 3.3 is an example of cross-section SEM on two different Ni thicknesses.

EDX analysis showed peaks for Ni and only small quantities of O and C, the films composition are free from Cl and S elements sourced from the electrolyte's components (Figure 3.4). At this stage quantification of Ni using WDX was not applied, which was used in Ni-B deposit's characterisation, Full detail on this is in following Ni-B deposition sections.

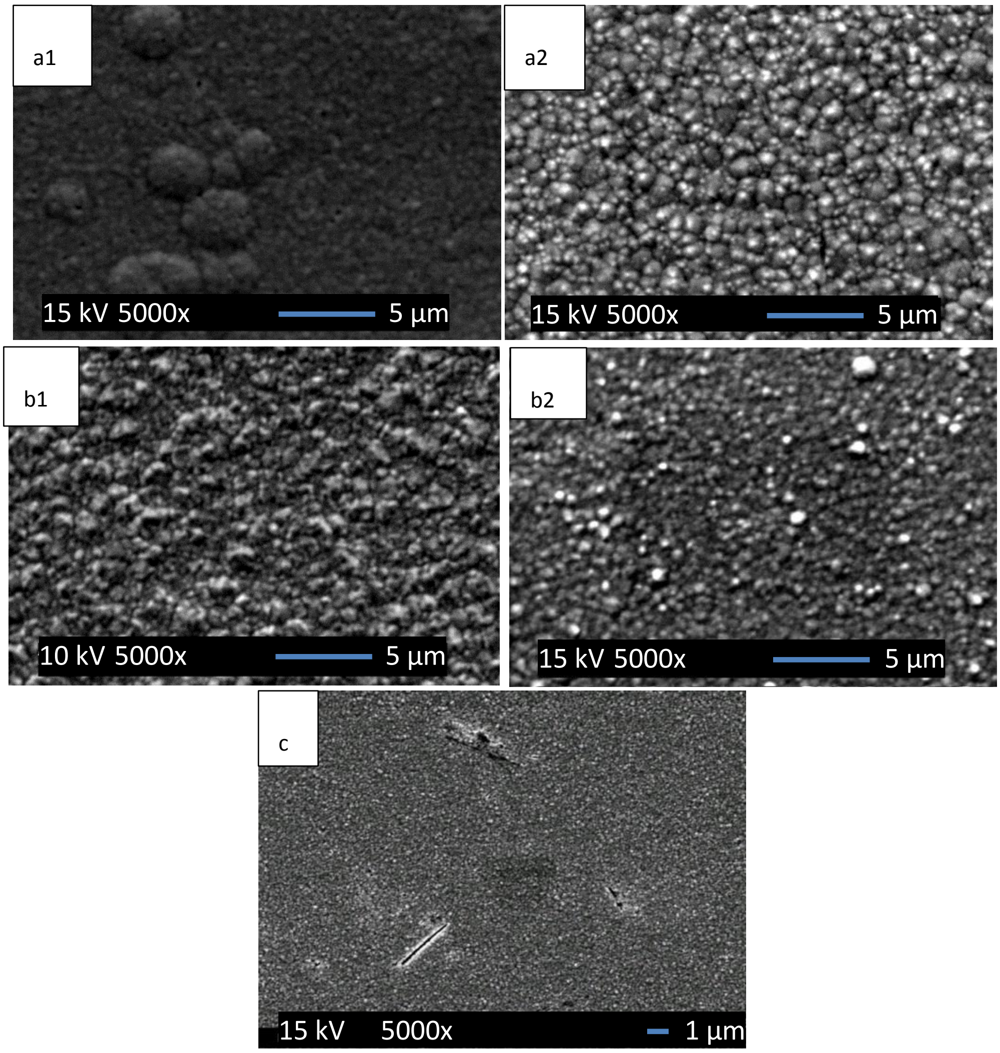

Figure 3.2 SEM micrographs for 13 µm thick Ni film without sucrose (a1), with sucrose (a2), 5 µm thick Ni film without sucrose (b1) with sucrose (b2), and 0.5 µm thick Ni film without sucrose (c).

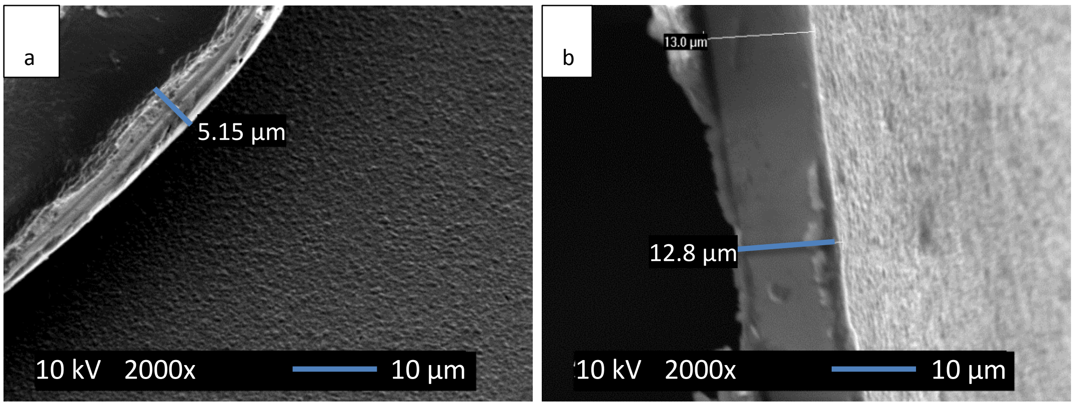

Figure 3.3 SEM micrograph (cross-section) for (a) 5 µm, and (b) 13 µm Ni films electro deposited from Ni Watt's bath with sucrose added.

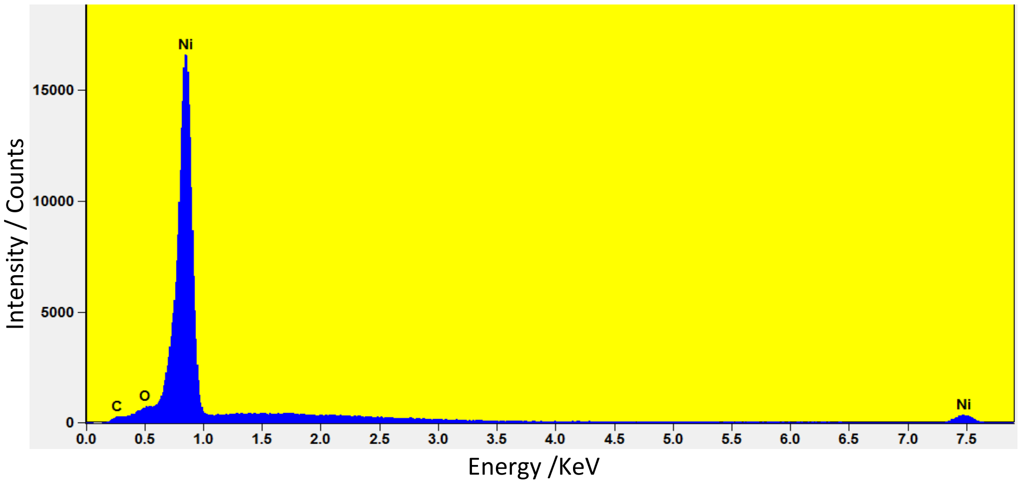

Figure 3.4 EDX spectrum for 5 µm thick Ni film electro deposited from Ni Watt's bath.

Hence by increasing the thickness of the deposits, the surface of the deposits become rougher and less uniform in the particle distributions is observed. Adding sucrose to the electrolyte resulted in improved uniformity and brighter Ni surface. The shape of the grown crystallites was switched to spherical from pyramidal shapes by adding sucrose. Peaks for Ni and minor impurities of C and O were detected in the EDX spectra.

3.3.1.3 XRD characterisation

Symmetric and grazing incidence X-ray diffraction scans were run on the Ni films to determine the structural parameters including the phase information, lattice parameter, crystallite orientation and strain. Grazing incidence scans produce the largest contribution from the films (strongest patterns, Figure 3.5) relative to the substrate, whereas symmetric scans allow observation of preferred orientation. XRD patterns for Ni films include peaks for Ni 111, 200, 220, 311 and 400, and for Au 111, 200, 220, 311 and 222.

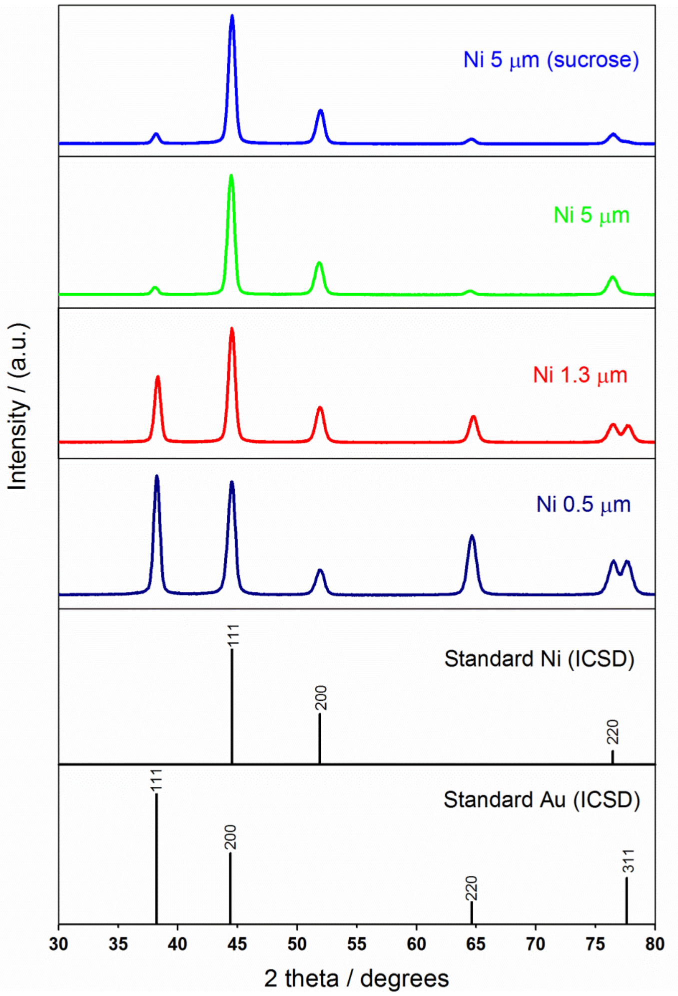

Figure 3.5 XRD plots of grazing incidence scans for Ni films having different thicknesses, electrodeposited from the Watt's bath by chronopotentiometry at 45° C, pH 3.5 and the stirring rate of 600 rpm. Comparison patterns come from the Inorganic Crystal Structure Database (ICSD).[112]

Rietveld refinements were performed to understand the effect of thickness on structural and texture properties of the Ni sample (Figure 3.6). Symmetric XRD scans of the Ni films were utilized to perform the refinements (Figure 3.7), although symmetric scans contain larger substrate contribution, they provide better peak shapes, as the peaks are narrower and less asymmetric compared to the grazing incidence (GI) XRD patterns. The parameters extracted from Rietveld fits are the crystallite size, isotropic strain and lattice constant (Table 1). Further measurements using XRD like strain measurement, in-plane grazing incidence XRD, and pole figures, were carried out to quantify the stress and to determine the crystallographic orientation in the films.

Table 1 Crystallographic parameters for Ni films extracted from Rietveld refinement

Ni film composition	wRp/Rp/ %	Strain% (isotropic)	(111) peak position / 2θ degree	Lattice parameter/ Å	Crystallite size / nm
Ni/ 0.5 µm	9.4 / 5.7	0.22(2)	44.51	3.510(2)	64.7(2)
Ni/ 1.3 µm	19.5/ 9.3	0.41(13)	44.53	3.5140(3)	72.4(2)
Ni/ 5 µm	10.4/6.3	0.252(7)	44.55	3.5163(3)	73.3(11)
Ni/ 5 µm (sucrose)	10.3/6.3	0.109(3)	44.57	3.51527(9)	56.7(4)
Ni/ 13 µm (sucrose)	25.9/19.2	0	44.50	3.52186(13)	68.1(4)

The internal strain in the films is estimated from changes in lattice parameter (variation in lattice parameter), the values were extracted from the final refinement fits of the films (see Table 1), the goodness of the fits called the reliability factors show accepted values, except for the 13 µm thick Ni in which the reliability factors (wRp/Rp) are a little high. Ni films showed an increase in lattice parameter with increasing the thickness, except in the films produced from sucrose containing bath. From the lattice constant observations, the Ni films are under compressive stress. The bulk value of Ni lattice parameters is a = 3.52394(8) Å,[113] this value for the thin Ni films is lower due to the stress effect between the deposit and the substrate, caused by the difference in thermal expansion coefficient between the two metal. By increasing the thickness the lattice parameter value increases, the 13 µm Ni show the closest lattice parameter value to the bulk value, this indicates reduction in the stress in the films by growing them thicker, studies in this area have shown similar relation between the stress and the thickness, by means of more defects in thinner films causes higher stress. [114-116] Moridi et.al have reported in a study that the residual stress variation with the thickness is mainly caused by interface misfit dislocations.

Isotropic strain measured from the Lorentzian Ly profile coefficients extracted from the refinements, show very low values for the 0.5 µm Ni films. The low isotropic strain values may be related to the small difference in the thermal expansion coefficient values of nickel (α=12.7x10^{-6} °C^{-1}) and gold (α =14.2×10^{-6} °C^{-1}) at room temperature.[100, 117] While by growing the films thicker the isotropic strain begins to increase indicating increased strain between the growing layers of Ni. The 5 µm Ni film show less isotropic strain percentage, which is due to delamination effects within the deposit, reduction in this value was also observed in the 5 µm film deposited with sucrose and this shows the effect of sucrose addition on strain.

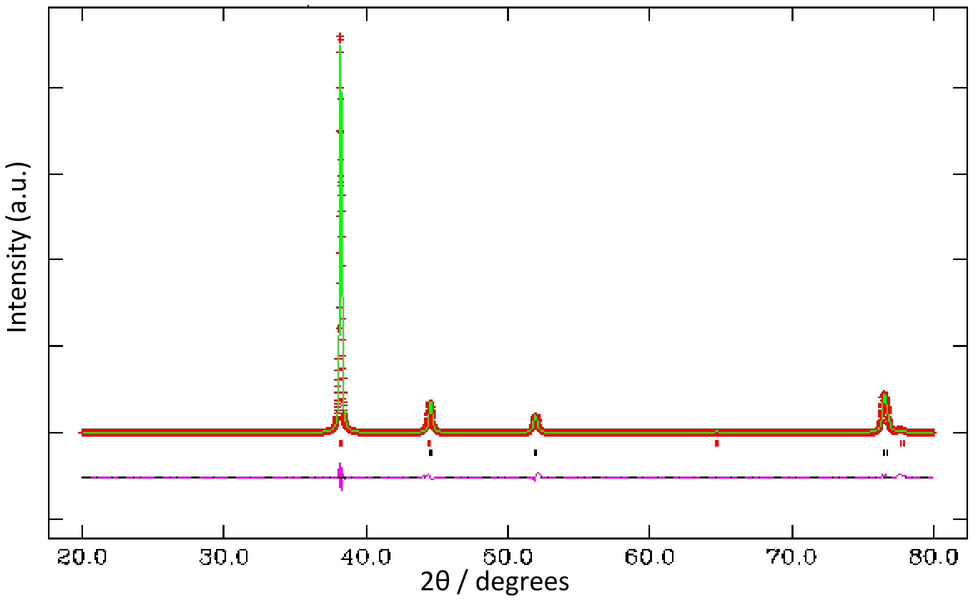

Figure 3.6 Rietveld fit to the XRD pattern from a 5 µm Ni film (symmetric scan). Crosses are the observed intensities and the solid line is the calculated intensities, straight horizontal line is the difference (obs. - calc.) and the vertical bars are the reflection position marks for Au (top) and Ni (bottom).

The crystallite size measurements from the Lx parameter extracted from the refinements on Ni films (Table 1) indicates particle sizes between 64.7 and 70.4 nm for the films produced in additive free Watt's bath, while the value is lower than this range for the films fabricated in sucrose added bath. In a paper by Rashidi and Amadeh, effects of an additive (saccharin) on grain size were investigated. They showed that adding saccharin at concentrations up to 3 g dm^{-3} caused a regular decrease in grain sizes, and beyond this concentration the grain size was independent of the saccharin concentration. This was explained by the possibility of saturation of adsorption sites, or overpotential levelling off.[2] In our work, sucrose was added at a concentration of 2 g dm^{-3} and this concentration was fixed for all the experiments, hence constant effect of sucrose is expected in all sucrose added Ni films.

Symmetric XRD patterns (Figure 3.7) showed Ni <111> orientation at 0.5 µm thickness <111> and polycrystalline film at 1.3 µm, <200> orientation at (sucrose free) 5 µm thickness, while at 5 µm thickness with sucrose <220> orientation was observed, strong <220> orientation at (sucrose free) 13 µm and absolutely <220> orientation at 13 µm sucrose added Ni. This result matches the literature outcomes in this area, as many previous studies have shown similar results. The direction of growing planes of crystallites in thin films matches that for the substrate, as a preferred orientation on favourably oriented grains comes after the nucleation stage.[1] The results are showing great influence from sucrose addition on the preferred orientation, along with the effect from increasing the thickness. In Rashidi and Amadeh's paper which is about the effects of experimental variables, it was found that increasing the additive which was saccharin in their case, has effect on grain orientation by switching the preferred orientation from <200> to random.[2] They postulated that H_2 bubbles adsorbed on the deposit's surface inhibit the growth of <110> orientation,[1] and increasing the concentration of saccharin means that the adsorbed H_2 are replaced by adsorbed saccharin molecules. In our work sucrose was added to the deposits at 5 µm thickness and over, and caused an enhancement in <220> orientation in every case (Figure 3.7).

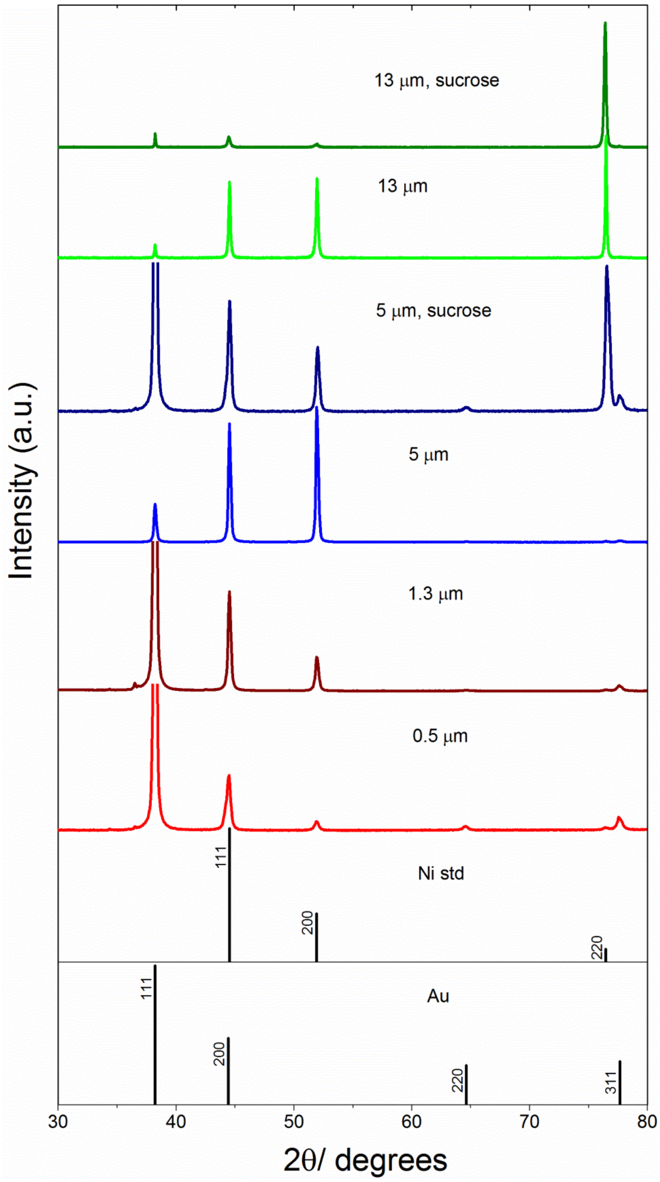

Figure 3.7 XRD plots of symmetric scans for Ni films, electrodeposited at different thicknesses, from Watt's bath.

In-plane measurements applied to Ni films to confirm the preferred orientation and the effect of the changes in the thickness. In-plane X-ray diffraction enhances the peak intensity of the thin films and minimises the intensity and background ratio of the substrate. From the in-plane measurements preferred orientation in the films can be confirmed, looking at (Figure 3.8), the ratio of <200> intensity to <111> of (0.4/0.6)is increased for the 5 µm thick film compared to the 0.5 µm one which is (0.3/0.7), as the diffraction from lattice planes normal to the surface of the sample can be detected on Ni films when in-plane XRD is applied.[56] In the thinner deposits the 0.5 µm and 1.3 µm films the patterns are showing rather polycrystalline film.

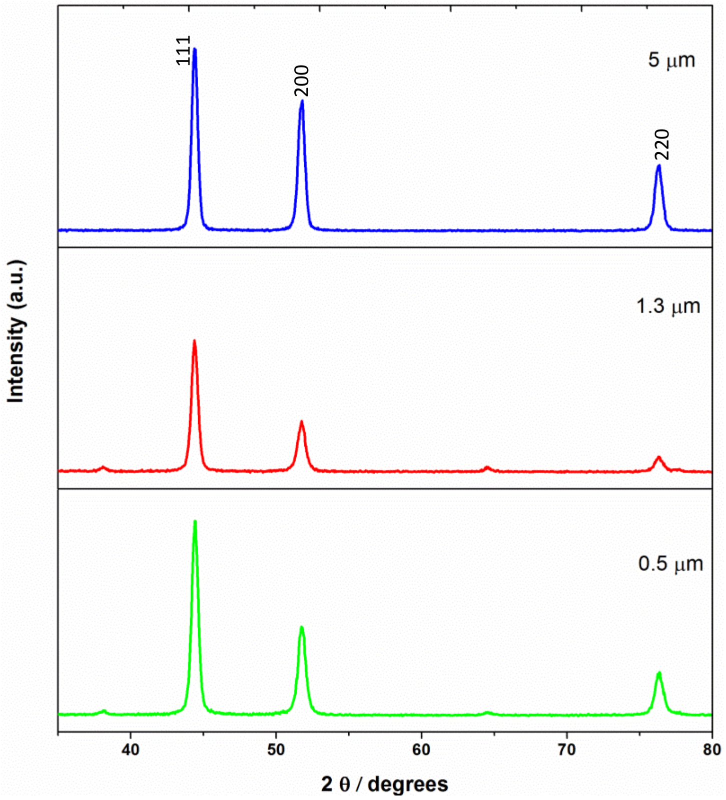

Figure 3.8 In-plane XRD plots for Ni films, electrodeposited at different thicknesses, from Watt's bath.

In summary the electrodeposited films are under compressive stress, which shows higher values in the thin films and increases with increasing the thickness. While the isotropic strain increases by increasing the film thicknesses, the thick films produced with sucrose possess lower isotropic strain compared to the additive free films with the same thickness. The crystallite size was reduced for the films produced from the sucrose added electrolyte. The thin Ni films (0.5 µm) showed preferred orientation on the Ni <111> diffraction plane, this was changed to polycrystalline with <111> the slightly dominant plane in the 1.3 µm, <200> in the additive free 5 µm film and <220> in the sucrose derived 5 µm and the 13 µm Ni films.

3.3.1.4 Pole figure measurements

To obtain a full texture determination of the films, pole figure (PF) measurements were applied to electrodeposited Ni films (Figure 3.9). Angles between planes within the crystallographic structure of a cubic system are determined using Equation 20.[118]

$$\cos \emptyset = \frac{h_1 h_2 + k_1 k_2 + l_1 l_2}{\sqrt{(h_1^2+k_1^2+l_1^2)(h_2^2+k_2^2+l_2^2)}} \qquad (20)$$

Where $\emptyset$ is the angle between the planes, *(h,k,l)* are the miller indices.

The calculations show interplanar angles of 54.74° between the Ni <111> and <200>, 35.28° between the Ni <220> and <111>, and 45.03° between the Ni <200> and <220> planes. These angles are compared to the values of alpha observed in the PF measurements, which represent the angles between the diffraction vectors of the planes. The observations resulting from the PF measurements on the films are listed in Table 2.

Table 2 Texture for Ni films of different thicknesses with and without sucrose

Film thickness/ µm	Observations in <200> PF	Observations in <220> PF	Observations in <222> PF
0.5	90° peak, <200> 54.8° peak, <111>	35.3° peak, <111>	90° peak , <111> 54.8° peak, <200>
1.3	90° peak, <200> 54.8° peak, <111>	90° peak, <220> 35.3° peak, <111> 45° peak, <200>	90° peak, <111> 54.8° peak, <200>
5	90° peak, <200> 45° peak, <220>	90° peak, <220> 45° peak, <200>	90° peak, <111> 54.8° peak, <200>
5 with sucrose	90° peak, <200> 45° peak, <220>	90° peak, <220> 45° peak, <200>	90° peak, <111> 35.3° peak, <220>
13 with sucrose	90° peak, <200> 45° peak, <220>	90° peak, <220> 45° peak, <200>	90° peak, <111> 35.3° peak, <220> 54.8° peak, <200>

From the pole figure results, thin Ni films of 0.5 µm have mixed <111> and <200> orientation with dominant <111> growth direction. By increasing the thickness to 1.3 µm the <111> orientation is less dominant, due to increased preferred orientation along <200>. Growing the films thicker to

5 µm produced with sucrose has resulted in stronger <200> orientation and a further decrease in <111> preferred orientation (Figure 3.9), and some preferred orientation along <220> is observed. The PF on thick film of 13 µm Ni with sucrose showed a switch in orientation to strong <220>. The pole figure results are in agreement with the symmetric XRD results. We have detected that adding sucrose has a great effect on further switching the orientation from <111> to <220>, when the films grow thicker.

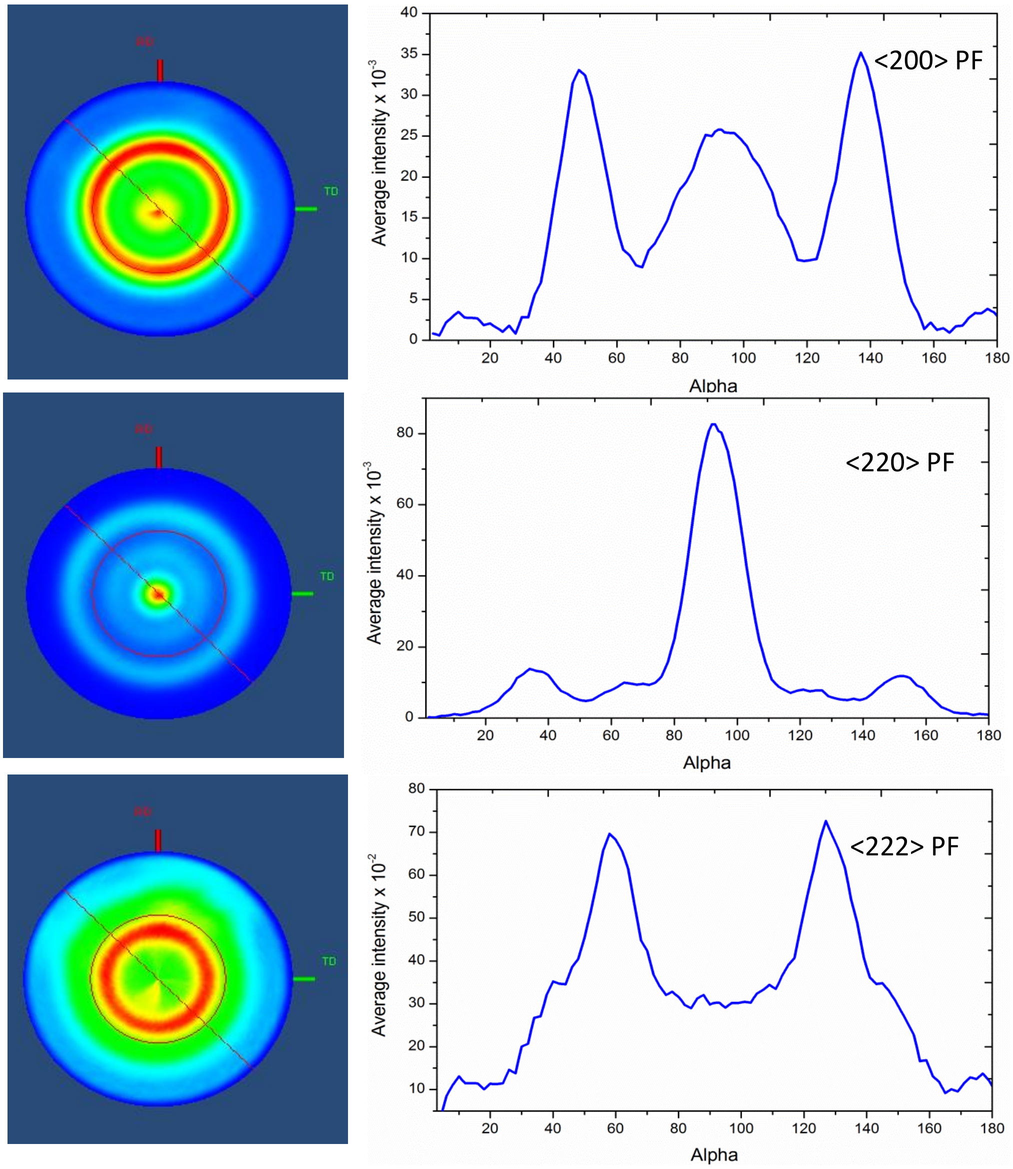

Figure 3.9 2D projection and cut-line pattern for pole figure measurement collected on 5 µm Ni film, electrodeposited from sucrose containing Watt's bath.

3.3.1.5 Residual stress measurements

The stress in Ni thin films in this work originated from internal intrinsic and thermal forces, i.e. the external (mechanical) force of the bath temperature and the non-equilibrium method (electrodeposition) fabricating the films.[119, 120] To determine the stress in the films using XRD the iso-inclination method was applied to the Ni films. The stress measurement processing was not easy, as samples with very flat surfaces are needed for good sample alignment and also high 2θ reflections of Ni with minimal overlap with the substrate reflections had to be selected. To choose a suitable Ni reflection, wide range symmetric scan were carried out on the films in 2θ ranges between 80-120° (Figure 3.10).

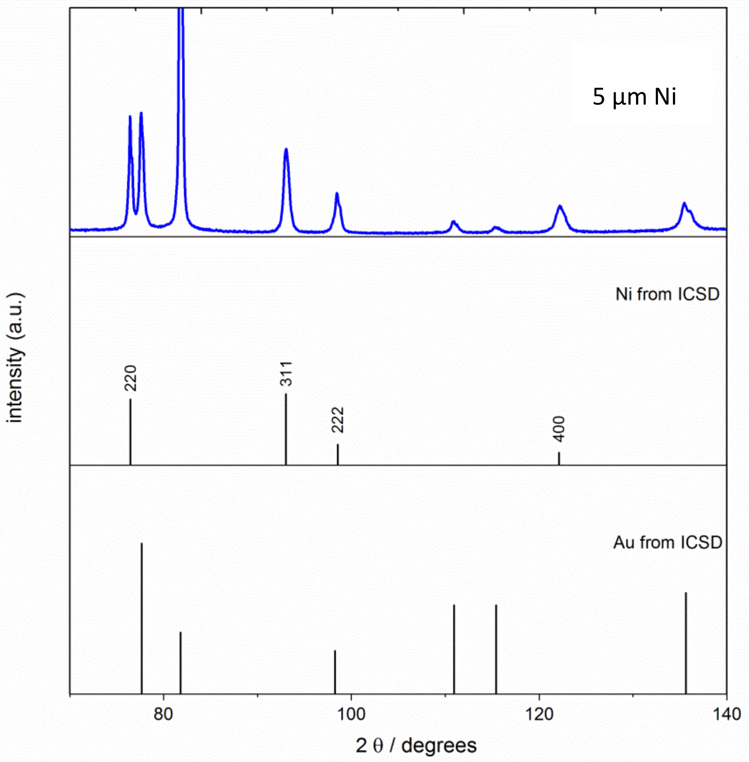

Figure 3.10 XRD pattern (symmetric scan) using high angle 2 θ ranges, on 5 µm Ni film electrodeposited from Ni bath.

Due to the Ni 222 diffraction peak overlap with Au 400, the Ni 311 peak (Figure 3.10) was selected for the measurements. The Ni 400 peak was also used in stress measurements but this was not successful due to the weak diffraction intensity. The XRD pattern for the 311 reflection at each Ψ point was collected. From the profile shifts in the peaks towards lower 2θ angles away from surface normal (higher d-spacing) is observed and this indicates that the stress in the films is tensile. The stress value is determined by multiplying the slope from $\mathrm{Sin}^2\psi$ and 2θ by the stress constant.

Figure 3.11 shows the stress measured for a 0.5 µm Ni film, and the value is 95 ±15 MPa. Residual stress measured on 5 µm Ni indicates a stress value of 110 ±5 MPa, from these results the 5 µm thick Ni is under higher stress compared to the 0.5 µm one. Hence stress increases with thickness. For 13 µm thick Ni film electrodeposited with sucrose the residual stress value was 66 ±10 MPa, which is lower than those for the 5 and even 0.5 µm films. Two factors are expected to be responsible for this result, firstly the presence of sucrose during film formation inhibits relaxation during the film growth, and secondly due to the fact that by growing the film thicker the interfacial strain between the deposit and the substrate will decrease, and hence less stressed deposited layer will form, the later can be supported by observations in previous studies on Ni.[115]

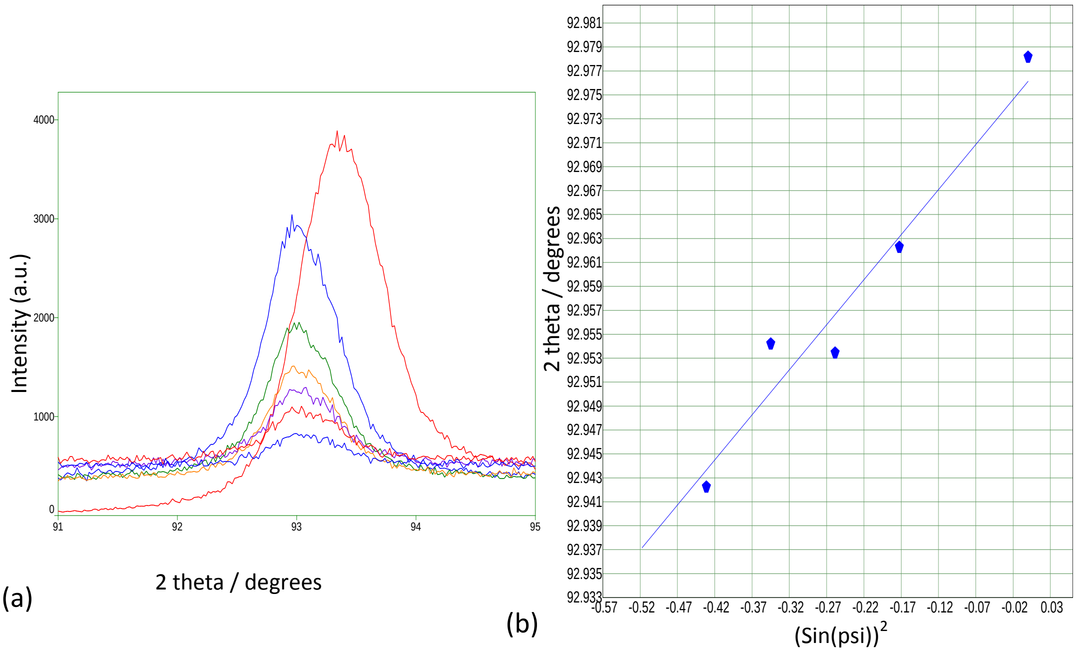

Figure 3.11 XRD Stress measurement profile (variation in 2θ position for Ni 311 reflection vs the intensity of the reflection at each 2θ position) for 0.5 µm Ni film deposited on Au substrate from Ni bath. (a), and $\sin^2 \Psi$ line chart (b). The measurement method applied was iso-inclination, fixed psi. The stress ± reliability from the slope is 95 ± 15 MPa.

Studies report the effect of experimental parameters such as bath temperature and boric acid concentration on stress,[100, 121] as for the effect of temperature it has been shown that at low electrolyte temperatures the films possess compressive stress which turns to tensile stress by increasing the electrolyte's temperature. In our work these parameters and other parameters such as stirring rate and electrolyte volume are kept constant. The bath temperature applied in this work was 45 °C and the residual stress measurements showed tensile stress in all the films. Nguyen suggested that sucrose addition causes decreases in the stress on the films, while increasing its concentration has no effect on the stress.[104] Thus in the deposits produced with sucrose less stressed films are expected.

3.3.2 Ni-B films electrodeposited at different thicknesses and B contents

The electrolyte compositions used in electrodepositing Ni-B films was similar to that used with B free Ni films, under the same conditions of pH and bath temperature. DMAB was used as B source. The concentration of B source has a big role on the electrodeposition process, as DMAB is a reducing agent and excessive quantities of this compound would lead to electroless deposition of Ni-B. Electrolyte pH is also one of the critical parameters in Ni-B electrodeposition, as previous research has shown that B content increases with increasing the pH, as the DMAB can decompose at low electrolyte pHs and thus less B contribution is expected with the deposition in acidic electrolyte.[122]

3.3.2.1 Electrochemistry (chronopotentiometric data)

Electrochemistry plots of potential-time transient for the 0.5 and 5 μm thick Ni-B films with 1% B content show similar initial step shape (Figure 3.12) and similar final (steady state) potentials. However, between these two steps different potential-time transient shapes are observed, possibly due to different nucleation processes. Sucrose reduces the magnitude of the potential applied to achieve the same current density to the 1% B containing Ni-B films. In the sucrose containing electrolyte, increased number of adsorbed species are expected, as the sucrose molecule alongside the H_2 molecules are adsorbed on the cathode surface. Thus the electroactive surface area is reduced.

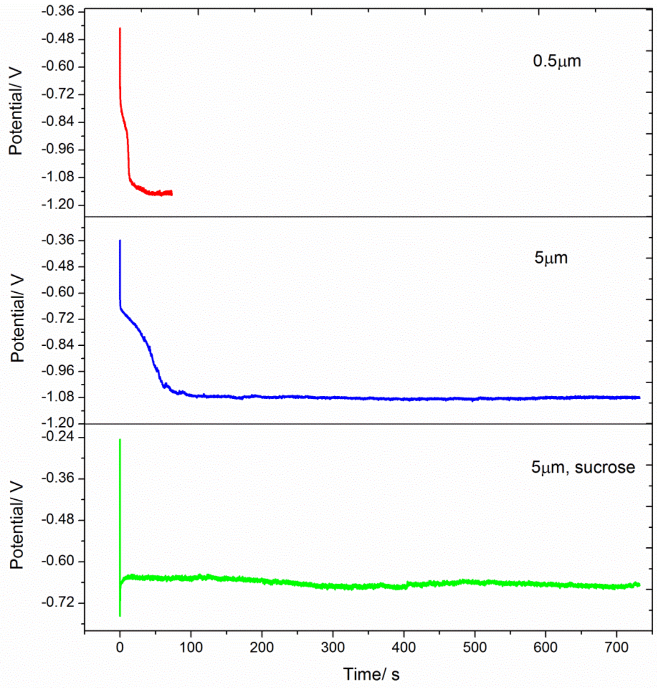

Figure 3.12 Chronopotentiometric graph, for Ni-B containing 1% B, deposited at 0.02 A cm^{-2} and at two different thicknesses, with and without sucrose addition. Au is the substrate. A Ni bath was used as electrolyte.

In the experimental section the assertion from the literature that the B content in the films is determined by the value of the applied current density was mentioned.[1] In electrodeposition (ED) of 3 wt. % B smaller current density is required, hence in response a smaller potential is expected. In the formation of 5 µm film after a certain time a gradual increase in the potential value was observed, which then showed a jump in value to about -1 V, where the potential time response showed a steady state (Figure 3.13). In the additive free thick films peeling around edges in the electrodeposit is observed during the electrodeposition process, which can explain the unsteady potential time response discussed in the 5 µm film. After deposition layers of the deposit were observed on the back of some peeled areas. Another factor is the increased hydrogen bubbling in the 3% B films as the electrodeposition time elapsed. Similarly to the 3% B films, the chronopotentiometric data on 1% B films show that adding sucrose to the bath composition has resulted in smaller potential response.

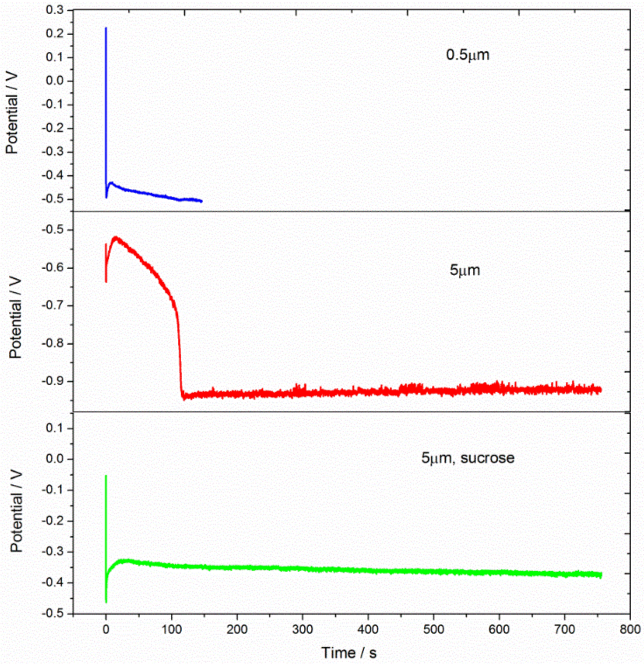

Figure 3.13 Chronopotentiometric graph, for Ni-B, 3% B content. The electrodepositon was on Au substrate from Ni bath, at different thicknesses with and without sucrose.

3.3.2.2 SEM, EDX and WDX measurements

SEM images for Ni-B films indicate smooth and bright surfaces with pinholes on the Ni-B surfaces, the number of which varied with the B content and thicknesses of the deposits. Increasing the amount of B has resulted in increased smoothness but also more pinholes. By growing the films thicker, the number of pinholes was reduced, suggesting some of them are filled in. Figure 3.14 is SEM micrographs for various Ni-B films, showing the effect of thickness, B content and sucrose addition on the morphology. 0.5 µm thick Ni-B film show increased brightness in the 3 wt. % B content film with obvious appearance of number of pinholes if compared to the 1 wt. % B containing film. Increased pinhole density was found in 1.3 µm thick Ni-B films, with less pinholes in the 1% B content Ni films. This morphology is possibly caused by the B source (DMAB) used in the bath, as a lot of bubbles were observed in the bath with higher DMAB concentration during the deposition process. Pinholes and bubbles are present in the surface of 3 wt. % B content 5 µm thick Ni-B films, the morphology of the 5 µm film produced by adding sucrose shows reduction in the number of the holes and minimised bubbles. Smooth surfaces are observed for the 1 wt. % B, 5 µm thick Ni-B films with or without sucrose, with the observation of decreased bubbles in case of the film produced with sucrose. The 13 µm Ni-B film with 1 and 3 wt. % B are produced from Ni bath containing sucrose and show small number of pinholes and spherical particle growth.

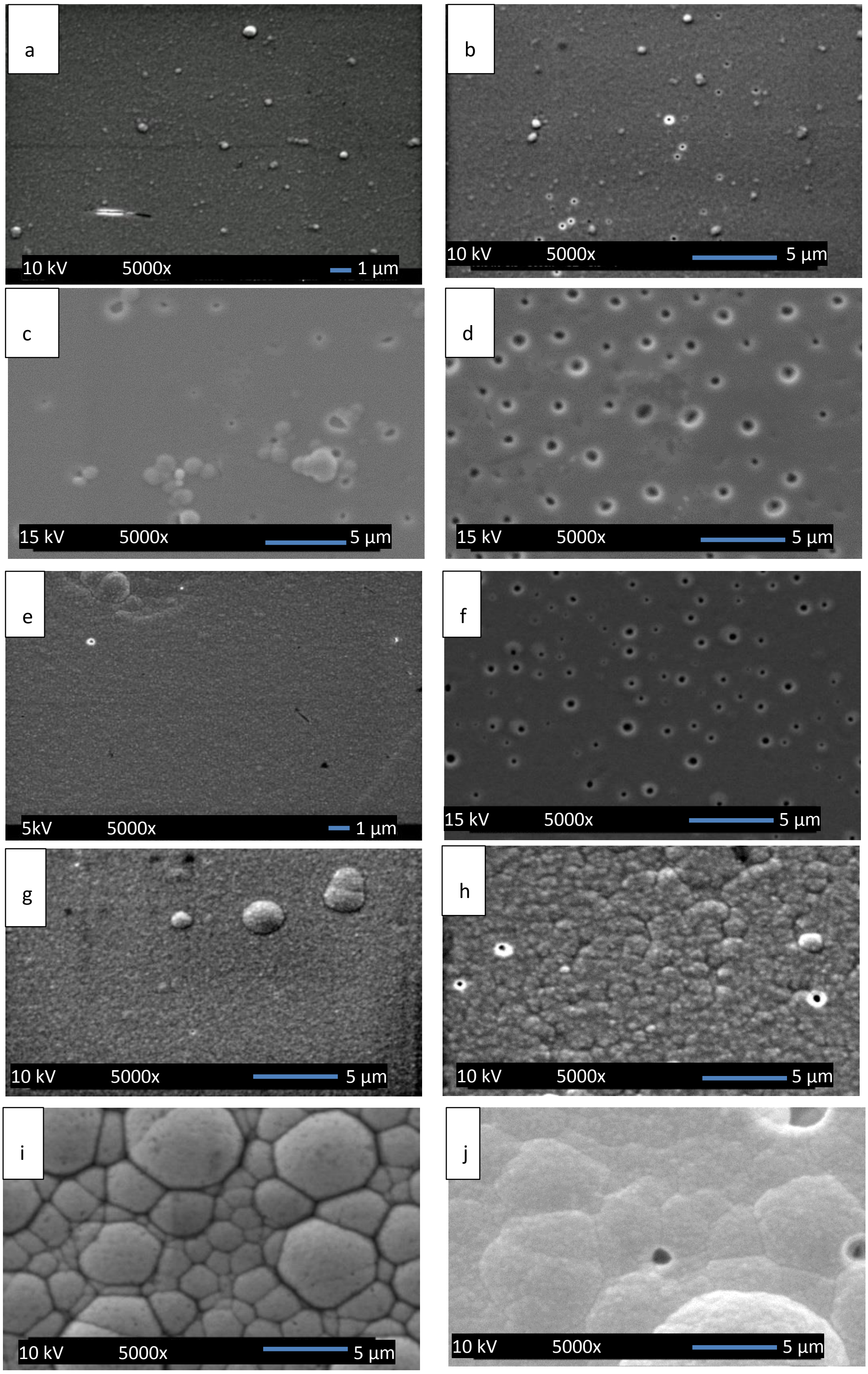

Figure 3.14 SEM micrograph for Ni-B film containing (a) 0.5 µm 1% B, (b) 0.5 µm 3% B, (c) 1.3 µm 1% B, (d) 1.3 µm 3% B, (e) 5 µm 1% B, (f) 5 µm 3% B, (g) 5 µm 1% B (sucrose), (h) 5 µm 3% B (sucrose), (i) 13 µm 1% B (sucrose) and (j) 13 µm 3% B (sucrose). The films are electrodeposited on Au from Watt's Ni bath.

The cross-section SEM on 0.5 and 5 µm Ni-B film containing 1 wt. % B show thicknesses similar to the target values (Figure 3.15), EDX and WDX were applied to Ni-B films to determine the qualitative EDX peaks, quantitative elemental ratios and the purity of the films.

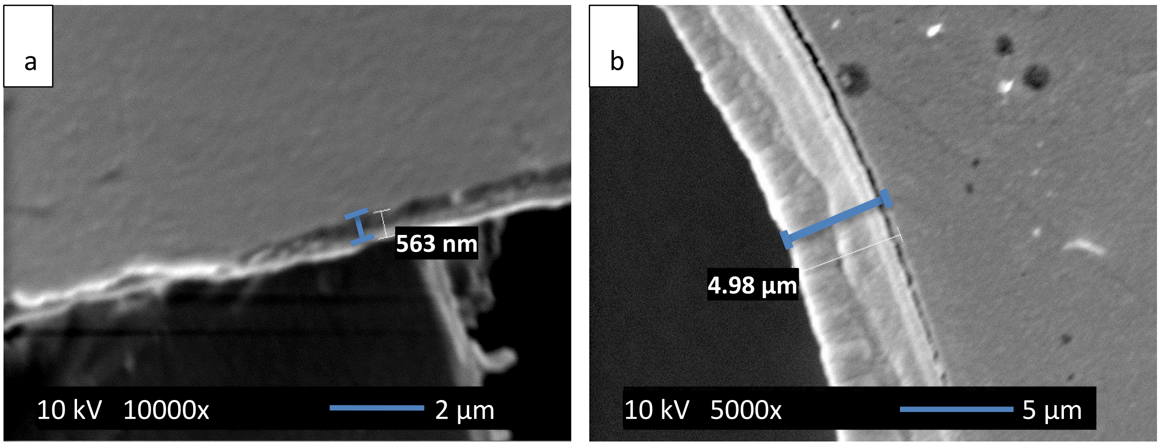

Figure 3.15 Cross-section SEM micrograph showing the thickness for 1% B containing Ni-B film with thickness (calculated based on the charge passed) of (a) 0.5 µm and (b) 5 µm , electrodeposited on Au from sucrose added Watt's Ni bath.

EDX spectra for the Ni-B films showed the presence of Ni and contaminations of O and C (Figures 3.16), in this energy range no peak was detected for B, as the element fluoresces at energy below the detector cut-off. Hence qualitative WDX scans were run on the films to detect the presence of B, the qualitative WDX results show stronger B peaks for the samples that were expected to contain 3 wt. % B compared to samples intended to contain 1 wt. % B (Figure 3.16). However the B content in the films determined using quantitative WDX measurement show around 2 wt. % B for the films aimed to contain 1 wt.% B and around 2.8 wt.% for the 3% intended films (Table 3). This difference in B content with applied current density is smaller than previously observed by K. Krishnaveni *et al.*, in which B content in the Ni matrix was evaluated using atomic absorption spectrophotometry.[1] A study states that the distribution of B atoms across the film thickness is non-uniform, and the B contribution ratio decrease by increasing the thickness, hence the WDX signal for B may decrease for the thicker films.[123] The data in table 3 contain the weight and atomic ratios for both the Ni and B elements measured quantitatively by WDX, B and Ni standards were used to conduct the measurements. The presented results are normalised to the total percentage of the two elements as variation in the values was detected, which might be due to changes in the beam current of the SEM instrument.

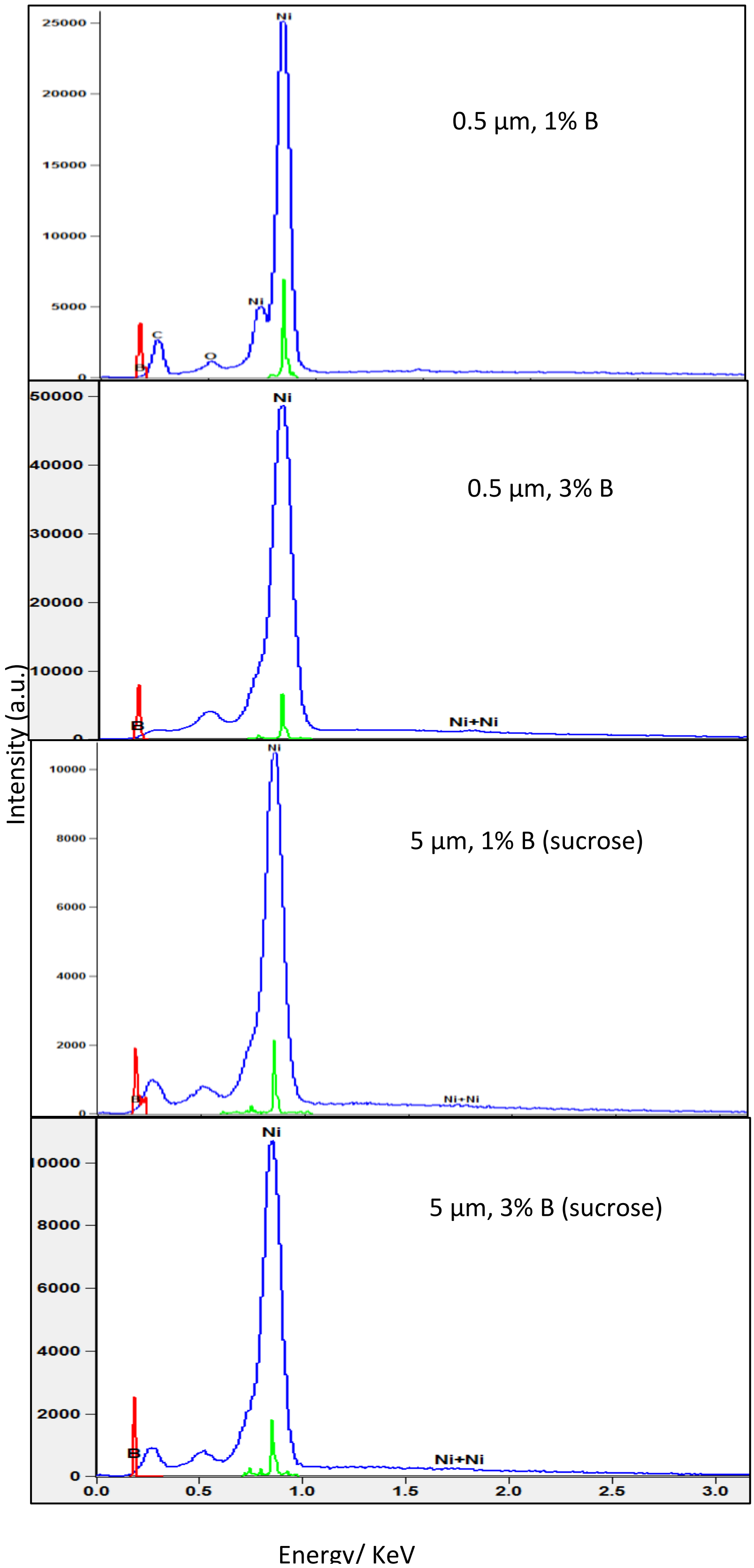

Figure 3.16 EDX and WDX scans for Ni-B films, prepared by chronopotentiometry from Watt's Ni bath. The blue is the EDX pattern for the film, the red is the WDX scan for B and the green is the WDX scan for Ni. With indicated thicknesses, B content and additive content in each plot.

Table 3 Quantitative estimation for the B % in the electrodeposited Ni-B film using WDX analysis.

Film composition	Element line	Source	Element Wt. %/ Error	Normalised Wt.%	Atom % (calculated from normalised)
0.5 µm, 3% B	B K+	WDS	2.66/ ±0.09	2.50	12.2
	Ni L+	WDS	103.66/ ±1.05	97.5	87.7
5 µm, 1% B	B K+	WDS	1.96/ ±0.08	1.97	9.8
	Ni L+	WDS	97.50/ ±0.83	98.0	90.2
5 µm, 1% B (sucrose)	B K+	WDS	2.04/ ±0.06	1.90	9.5
	Ni L+	WDS	105.10/ ±1.05	98.1	90.5
5 µm, 3% B	B K+	WDS	2.25/ ±0.07	2.32	11.4
	Ni L+	WDS	94.84/ ±0.95	97.7	88.6
5 µm, 3% B (sucrose)	B K+	WDS	2.76/ ±0.07	2.55	12.4
	Ni L+	WDS	105.31/ ±1.05	97.5	87.6

The morphology of µm Ni-B exhibit smooth surface with pinholes, the numbers of pinholes are higher in the 0.5 and 1.3 µm films and gradually decrease by increasing the thickness of the deposited films. Ni-B with 3 wt. % B contains more pinholes on their surfaces compared to the 1 wt. % B films and sucrose addition has resulted in less pinholes. The qualitative WDX scan on the 3 wt. % B film show stronger B peak and less strong B peak for the 1 wt. % B, however the quantitative B measurement has revealed higher quantities of B in the films intended to contain 1 wt. % B and quantities close to the intended amount in the 3 wt. % B.

3.3.2.3 XRD characterisation

Unlike the B free Ni films the XRD patterns for Ni-B film show only a broad peak for Ni 111 and the other Ni peaks are not observed (figure 3.17), further broadening in the peak is observed by increasing the thickness of the films. The broadening diffraction comes from both the crystallite size and the strain. Crystallite size broadening increases with 2θ whereas strain broadening decreases with 2θ, so it is most likely that this change is due to a reduced crystallite size. Quantitative estimations for the crystallite size and strain resulting in the peak broadening are determined from the Rietveld refinement. Texture information was not obtained from the symmetric scans, as Ni 111 was the only indicated Ni peak in all the patterns, and a hump in the position of Ni 200 peak was observed for some of the patterns (Figure 3.18).

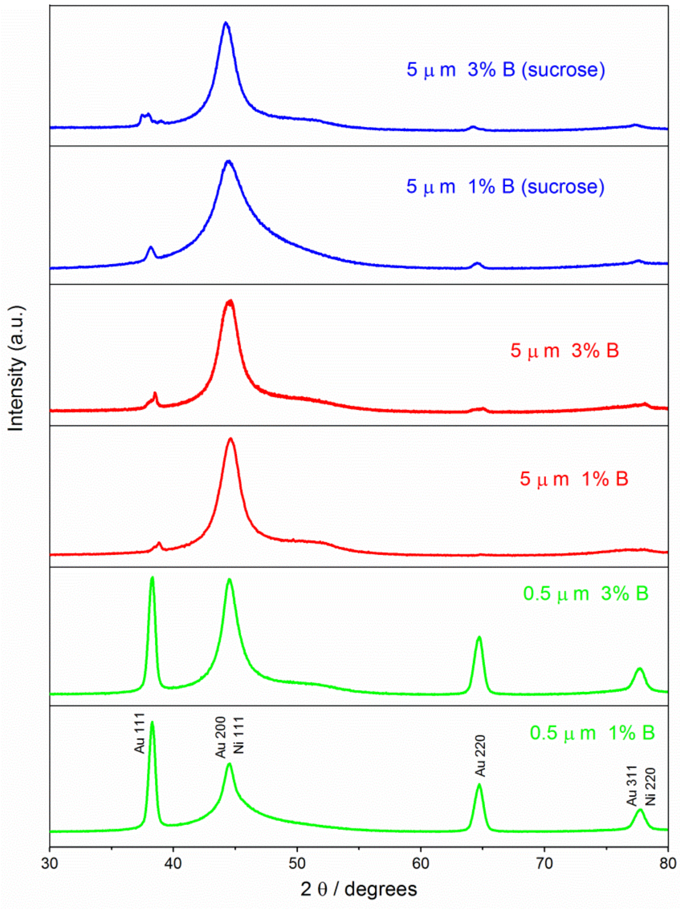

Figure 3.17 XRD plot of grazing incidence scans for Ni-B films electrodeposited from the Watt's bath. Having different thicknesses, B contents and bath additives stated on each pattern.

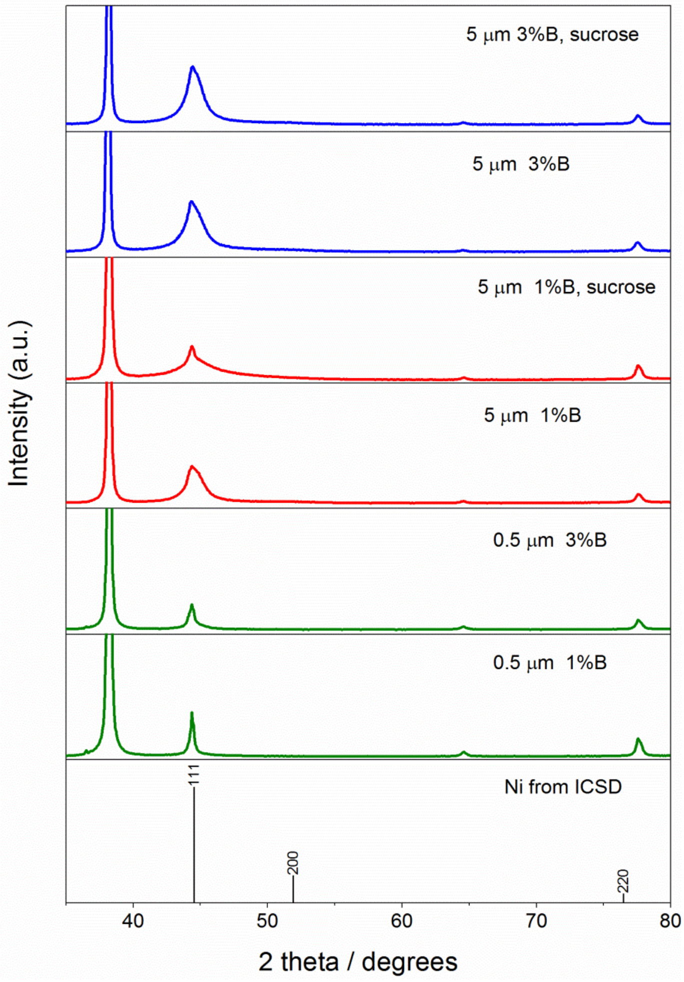

Figure 3.18 XRD plot of symmetric scans for Ni-B films electrodeposited from the Watt's bath. The thicknesses, B contents and bath additives stated on each pattern.

Rietveld refinement was applied to the symmetric scans of all the Ni-B films (Figure 3.19). A number of parameters are extracted from the final fits on the films (Table 4). Lattice constants for Ni-B films extracted from the Rietveld fits for the XRD data, have shown values higher than B free Ni films, indicating that the Ni-B films are under larger tensile stress compared to the B free Ni films. This tends to decrease by increasing the thickness and B amount with noticeable few scattering in the values that might be caused by experimental variable. As discussed in Ni section growing the films thicker reduce the stress caused by lattice mismatch between the deposit and the substrate. The effects coming from increasing the B content are due to an increase in the number of smaller size B atoms replacing the large Ni atoms.[105] Adding sucrose into the electrolyte's composition has its own effect on the lattice parameter variations, where the decrease in the values for the individual films having same composition is observed. The shift in Ni 111 peak positions does not follow a gradual trend, due to dual variation effect, the thicknesses variation along with the variations in B contents, hence other factors such as instrumental broadening and sample imperfections might be responsible in the XRD peak shifts.

Isotropic strain calculated from the Lorentzian Ly values from the final Rietveld fits show an increase in value with increasing the thickness and B content, this value was decreased when sucrose was added, especially in the case of thickest films (13 µm).

The crystallite sizes of Ni have shown massive decrease by adding B and decrease further by adding sucrose. From (Table 3) crystallite sizes between 6-15 nm were obtained for the films produced with 1 wt. % B and 3 wt. % B. Crystallite size calculation was by employing the Lorentzian component (Lx) from the refinements as the value X in equation (12). Generally smaller crystallite sizes were obtained for the higher B containing films compared to the lower B containing ones. In both film compositions, the crystallite size shows a gradual decrease with increasing the thickness. This determines that the effect of B addition on crystallite size in thick films is greater than in thin films. On another hand the effect of sucrose on further reduction in crystallite sizes is obvious.

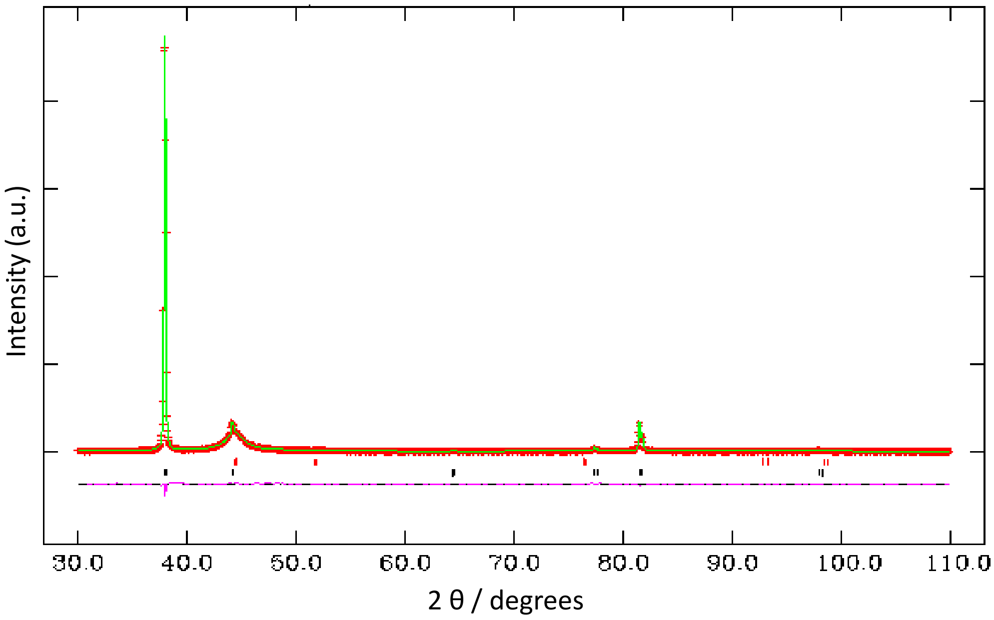

Figure 3.19 Rietveld fit of Ni-B 5 µm and 1% B film (symmetric scan). (-) marks are the observed intensities and the solid line is the calculated intensities, straight horizontal line is the difference (obs. – calc.) and the vertical bars are the reflection position marks (the top bars are for Au and the bottom for Ni).

Table 4 Crystallographic parameters for Ni-B films extracted from Rietveld refinement.

Film composition (symmetric)	wRp/Rp	(111) peak position / 2θ degree	Lattice parameter	Crystallite size / nm	Isotropic / strain %
Ni-B/0.5 µm, 1 % B	10.1/5.8	44.43	3.5313(42)	21.0(7)	0.003(5)
Ni-B/0.5 µm, 3 % B	5.7/4.0	44.38	3.5372(44)	12.8(2)	0.01(5)
Ni-B/1.3 µm, 1 % B	9.1/6.2	44.56	3.5261(14)	15.2(1)	0.32(17)
Ni-B/1.3 µm, 3 % B	7.9/5.5	44.59	3.5244(15)	12.0(8)	1.5(5)
Ni-B/5 µm, 1% B	5.7/4.0	44.60	3.5185(47)	12.5(2)	3.29(5)
Ni-B/5 µm, 1 % B (sucrose)	8.1/5.4	44.58	3.5204(55)	6.4(1)	3.16(9)
Ni-B/5 µm, 3 % B	8.7/ 5.6	44.56	3.5152(59)	7.1(1)	3.93(5)
Ni-B/5 µm, 3 % B (sucrose)	5.7/4.1	44.58	3.5192(35)	6.2(1)	0.07(3)
Ni-B/13 µm, 1 % B	6.0/4.1	44.37	3.5169(32)	14.50(4)	5.61(6)
Ni-B/13 µm, 1 % B (sucrose)	7.8/5.6	44.59	3.5188(10)	8.0(1)	0.29(14)
Ni-B/13 µm, 3 % B	8.7/6.4	44.46	3.5144(48)	6.1(1)	2.95(8)
Ni-B/13 µm, 3 % B (sucrose)	8.4/ 6.2	44.65	3.5178(14)	8.2(1)	0.65(2)

In-plane measurement and the out of plane (the symmetric) XRD results on Ni-B films (Figure 3.20), indicates <111> preferred orientation, these observations are not reliable as the only identified peak is the Ni 111. Hence collecting pole figures on these films was essential to ensure these observations. Adding B to the Ni matrix has removed the effect of the thickness on the preferred orientation, from (Figure 3.18) the Ni <111> remained the dominant orientation on increasing the thickness of the film in both 1% and 3% B containing Ni-B films.

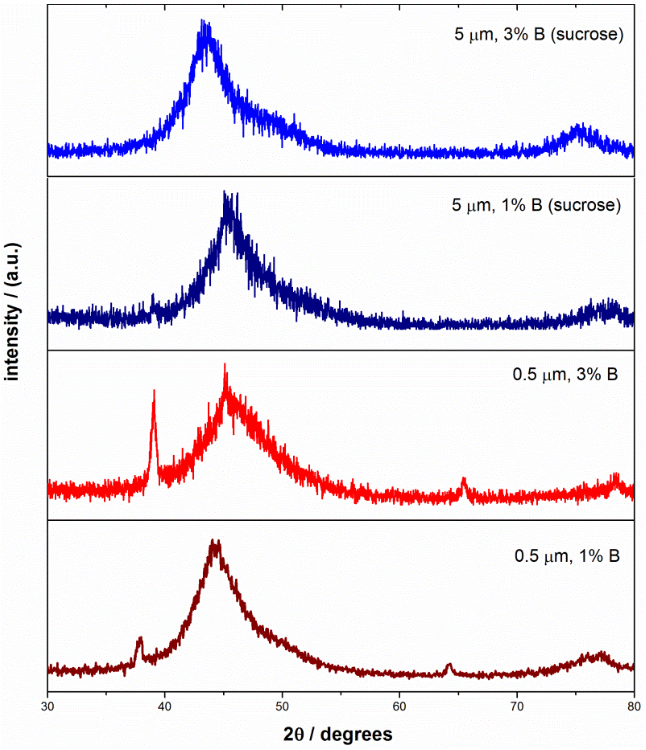

Figure 3.20 XRD plot (in-plane) for Ni-B films electrodeposited from the Watt's bath. Having different thicknesses, B contents and bath additives stated on each pattern.

Stress investigations from XRD analysis indicate tensile stress in the films, which is higher in amount compared to the stress in the Ni films. Increasing the thickness of the deposits and increasing the amount of B content independently, lead to decrease the amount of the stress. Similarly the isotropic strain calculations show reduction in the amount of the strain in the films with increasing either the thickness or the amount of B content. Ni-B films consist of crystallites much smaller in size compared to the Ni films, hence B has great effect in the crystallinity of Ni. The reduction was evolved with the amount of B content, smaller crystallites were measured in the thicker films compared to the thin ones of the same B content.

3.3.2.4 Pole figure measurements

More detailed information about the texture of the films is obtained from the PF results (Figure 3.21), information about how the PF data is interpreted is produced in PF part in Ni electrodeposition section (Section 3.3.1.4). Results for texture analysis on all different Ni-B compositions from the measurements are tabulated and presented in Table 5.

Table 5 Texture for 1 wt. % and 3 wt. % B containing Ni-B films of different thicknesses with and without sucrose.

Film thickness/ µm, composition / wt. % of B	Observations in <200> PF	Observations in <220> PF	Observations in <222> PF
0.5, 1%	90° peak, <200>	35.3° peak, <111> 35.3° peak, <111> 60° peak, <-220>	90° peak , <111> 54.8° peak, <200>
0.5, 3%	90° peak, <200>	90° peak, <220> 35.3° peak, <111> 60° peak, <-220>	90° peak , <111> 54.8° peak, <200>
5, 1%	54.8° peak, <111>	No discernible peak	90° peak , <111> 54.8° peak, <200>
5, 3%	No data		
5, 1% with sucrose	90° peak, <200>	90° peak, <220> 35.3° peak, <111> 60° peak, <-220>	90° peak , <111> 54.8° peak, <200>
5, 3% with sucrose	90° peak, <200>	90° peak, <220> 35.3° peak, <111> 60° peak, <-220>	90° peak , <111> 54.8° peak, <200>

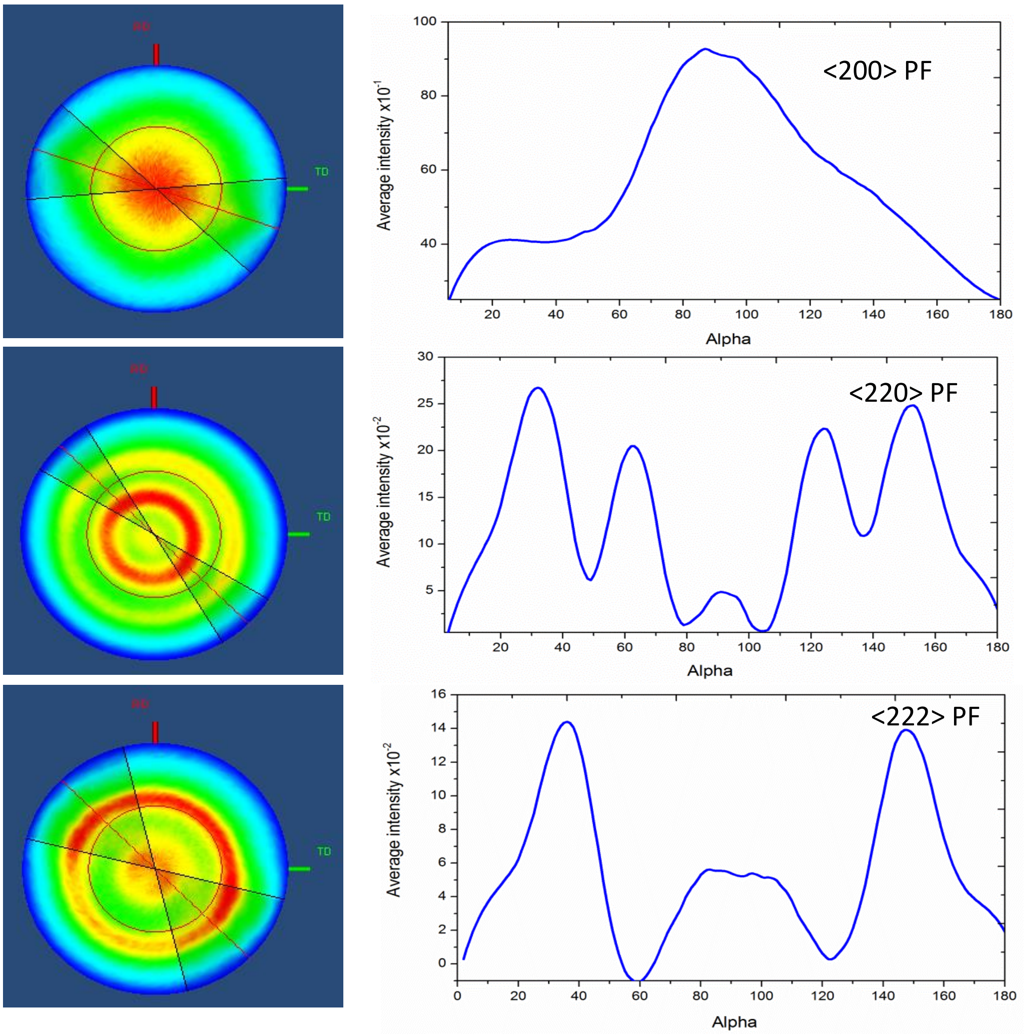

Figure 3.21 2D projection and cut-line pattern for Ni-B film (0.5 µm 1% B) electrodeposited from the Watt's bath.

In the PF analysis performed on the Ni-B samples, the features are much broader due to small crystallite sizes, hence fewer distinct orientation effects. From the above analysis in table 5, the orientation along <200> plane is dominant in both 1 and 3% Ni-B for the thin (0.5 µm) films, the <200> orientation has been reported in literature for Ni-B films electrodeposited at current densities above 10 mA cm^{-2}, the Ni-B films in this work were obtained at 10 mA cm^{-2} and above.[122] In the thick Ni-B film, orientation along <111> is indicated for the low B content (1 wt. %) film deposited without the addition of sucrose. While for the same composition that produced with sucrose and also for 3 wt. % Ni-B having 5 µm, the PF measurement has revealed a texture similar to that observed for the thin films.

3.3.2.5 Stress measurements

B addition to Ni matrix has resulted in obtaining more stressed films, detected from the greater tendency for delamination observed for the Ni-B films compared to B free ones. Studies including stress evaluation for thicker (~ 20 µm) Ni-B films show tensile stress in the films and an increase in the value by increasing the amount of B content[108]. Increased stress in the films is likely to be due to incorporation of B atom in the lattice structure of the Ni, which leads to dislocations within the crystal structure. Evaluating the stress in the electrodeposited Ni-B films, using the technique applied to the Ni (section 3.3.1.4) was not possible, as the high angle peaks have too low an intensity to be measured. However a decrease in lattice parameter values for Ni-B films compared to the Ni ones is an indicator of increased stress in the former films. Varied stress in Ni-B is expected by varying the composition and thickness, more stressed deposits are expected by increasing the amount of B and the thickness.

3.3.3 Variation of current density in Ni deposition

Ni films of 5 µm thickness were deposited at different current density using deposition method and Ni bath composition similar to the ones used in Ni and Ni-B depositions (sections 3.1 and 3.2). The rate of deposition is increased by increasing current density, hence more aggressive nucleation and growth of the deposited layers. Here we aim to determine the effect on the properties of the deposit.

3.3.3.1 Electrochemistry (chronopotentiometric data)

The chronopotentiograms mainly follow similar trends of slightly increased negative potential in the start of the deposition (the nucleation), and slightly smaller potential after a certain time of deposition in each chrononopotentiogram, then followed by a steady potential-time response. The value of potential is variable for each film according to applied current density. Figure 3.22 show the potential-time response for Ni film electrodeposition using different current densities, apparently the CP plots show sharper nucleation along with a higher level of bubble generation (noise) features by increasing the current densities, as the Ni deposited at 80 mA cm^{-2} exhibit sharpest and noisiest CP.

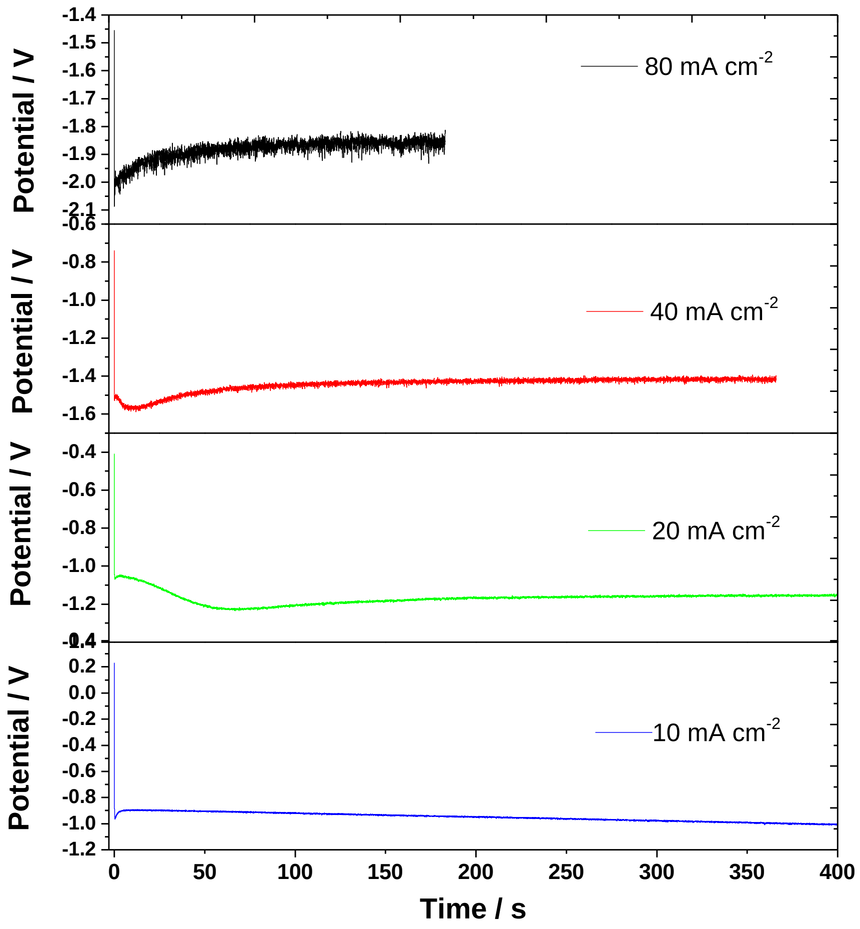

Figure 3.22 Chronopotentiometric graphs, for 5 µm Ni, electrodeposited on Au from Ni bath, the applied current densities were varied (stated on each plot), by chronopotentiometry at 45 °C, pH 3.5, and stirring rate 600 rpm.

3.3.3.2 SEM measurements

The morphology of the film surfaces are similar to B-free and additive-free Ni films in section (3.3.1.2). Ni films electrodeposited at different current densities share a uniform rough morphology. Only the Ni film electrodeposited at 80 mA cm^{-2} shows a different morphology, as it exhibits agglomerations of spherical particles (Figure 3.23).

Ul-Hamid *et.al* deposited Ni on Al-Cu alloy substrate, their results show change in morphology from more uniform with high coverage capacity to lower coverage and non-uniform deposits by decreasing the current density from 50 to 25 mA cm^{-2},[124] in this work the substrate is gold sputtered on glass, such an effect was not observed.

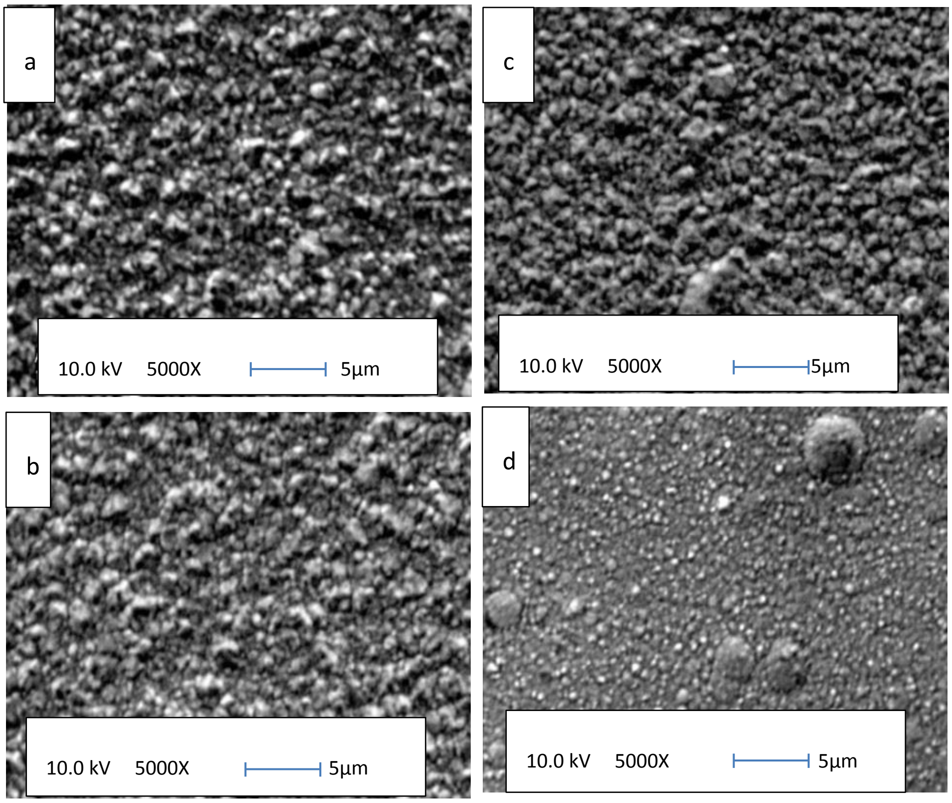

Figure 3.23 SEM micrograph for 5 µm thick Ni film electrodeposited from Ni Watt's bath. At different applied current densities (a) 0.01 A cm^{-2}, (b) 0.02 A cm^{-2}, (c) 0.04 A cm^{-2}, (d) 0.08 A cm^{-2}.

3.3.3.3 XRD characterisation and Rietveld refinements

The symmetric scans (Figure 3.24), show that <200> orientation is dominant for 5 µm Ni films deposited at 0.01 and 0.02 A cm^{-2}. A polycrystalline texture in the film deposited at 0.04 A cm^{-2} is switched to dominant <220> for the film deposited at 0.08 A cm^{-2} and totally <220> orientation in Ni deposited at 0.16 A cm^{-2}. This was determined by measuring the intensity ratios between the <200> and <220> (I <200>/I <220>), the values were compared to this ratio in the standard polycrystalline Ni from ICSD.[112] the ratio between the intensities of these two reflections (I <200>/I <220>) is ~ 0.83/0.17 in standard Ni XRD pattern. Variation in this ratio was observed in every film, most obviously in the films electrodeposited at current densities of and exceeding 0.08 A cm^{-2}, the ratio for the Ni ED at 0.08 A cm^{-2} is ~ 0.02/0.98 showing <220> orientation.

Symmetric scan data were refined using Rietveld refinement to determine the effect of current density variation on the crystallographic and structural parameters, (Figure 3.25). Table 6 shows the measured parameters for the films from the final fits. The lattice parameters are close in value between the films, and the strain shows irregular changes with applied current densities.

Non-regular strain variation might be due to delamination in the film edges. Ni 111 peak position detected from the Rietveld fit, shifts to higher 2θ XRD angle with increasing the current density except in the case of the film deposited at 0.08 A cm^{-2}, which show the lowest 2θ angle for Ni 111 peak position, possibly caused by different growth mechanism at this deposition rate. In general the Ni 111 peak position variation is an indication of increased strain in the films.

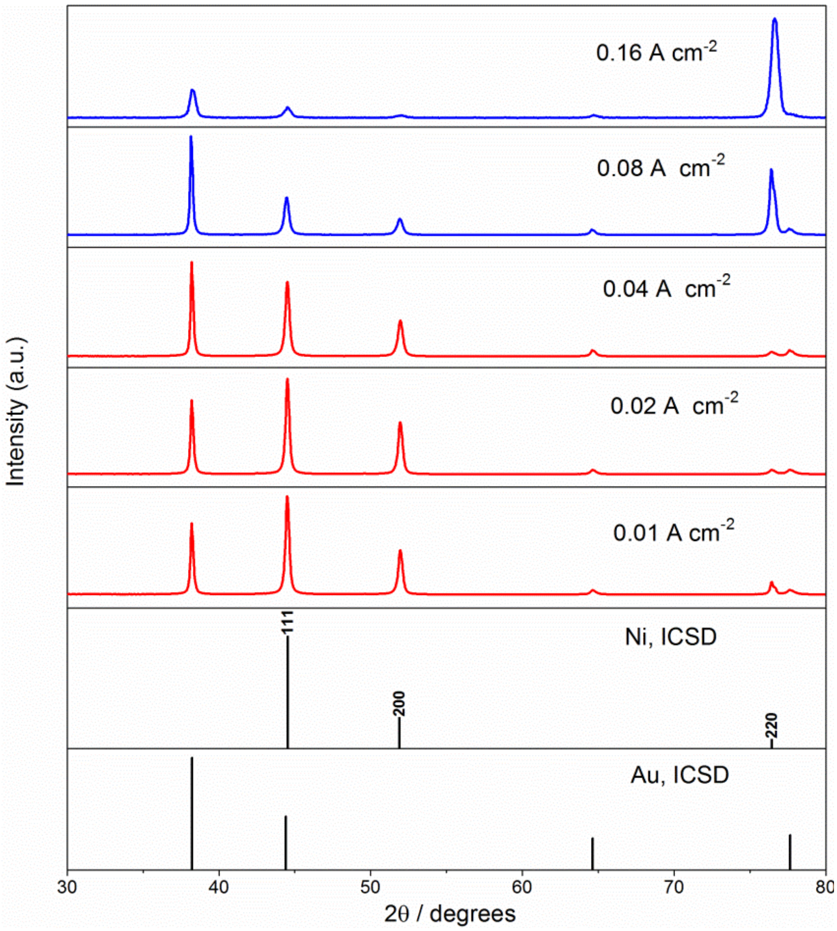

Figure 3.24 XRD plots of symmetric scans for Ni films, electrodeposited at different current densities, from the Watt's bath. Comparison patterns come from the Inorganic Crystal Structure Database (ICSD).

The crystallite size varies with current density. The smallest crystallite size is 32.3 nm for the film deposited at 0.16 A cm^{-2}, and the largest is 49.8 nm for the film deposited at 0.01 A cm^{-2} (Figure 3.26) show crystallite size variation with current density. The crystallite size is gradually reduced by increasing the deposition rate, this result is in agreement with previous studies about the effect of current density on crystallite size in Ni deposit[124, 125]

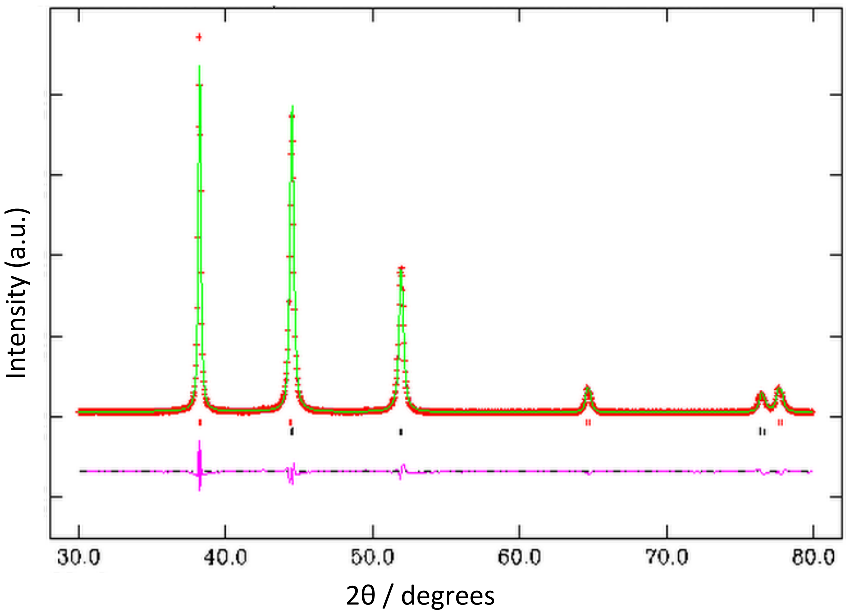

Figure 3.25 Rietveld fit of Ni 5 μm deposited at current density of 0.04 A cm^{-2} (symmetric scan). crosses are the observed intensities and the solid line is the calculated intensities, straight horizontal line is the difference (obs. – calc.) and the vertical bars are the allowed reflection position marks (the top bars are for Au and the bottom for Ni).

Table 6 Crystallographic parameters extracted from Rietveld refinement for Ni films electrodeposited at different current densities.

Current density of 5 μm Ni film (symmetric scan)	wRp/Rp	Strain% (isotropic)	111 peak position / 2θ degree	Lattice parameter	Crystallite size / nm
Ni/ 0.01 A cm^{-2}	10.5/7.2	0.1	44.56	3.5192(2)	49.8(6)
Ni/ 0.02 A cm^{-2}	9.8/7.4	0.1	44.58	3.5179(2)	46.2(5)
Ni/ 0.04 A cm^{-2}	12.3/8.8	0.2	44.59	3.5197(2)	44.6(8)
Ni/ 0.08 A cm^{-2}	10.5/7.0	0	44.54	3.51995(17)	39(4)
Ni/ 0.16 A cm^{-2}	17.3/13.0	0	44.62	3.5140(5)	32.3(4)

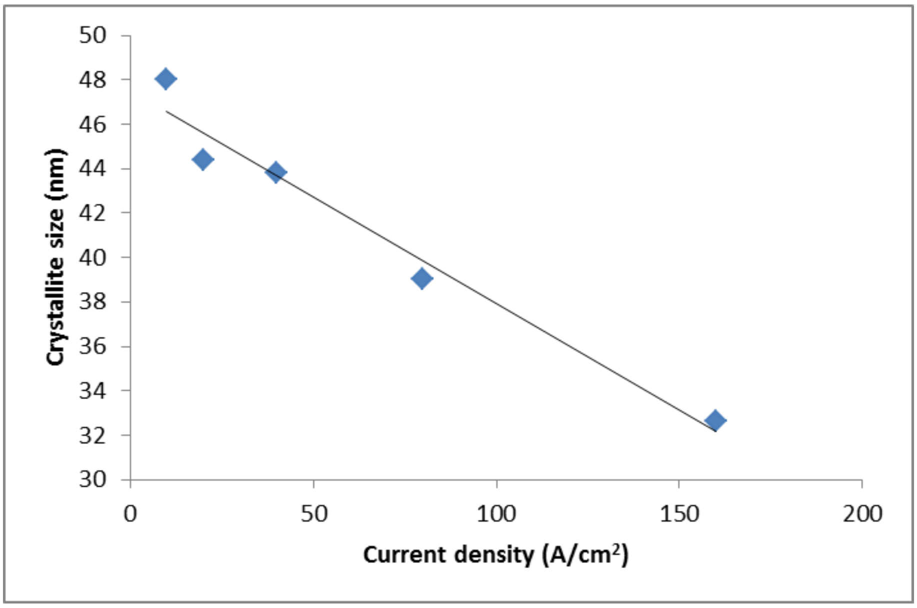

Figure 3.26 A plot of crystallite size vs. current density, fitted to a linear line.

Symmetric XRD characterisation show Ni <200> alignment in the films electrodeposited at current densities of 0.01 and 0.02 A cm^{-2}, rather polycrystalline structure at 0.04 A cm^{-2} and Ni <220> alignment at current densities of 0.08 A cm^{-2} and 0.16 A cm^{-2}. Isotropic strain predominantly increases by increasing the current density. Gradual reduction in the crystallite size with increase in current densities is detected in the samples.

3.3.3.4 Pole figure measurements

The outcomes from pole figure examinations on Ni films deposited at 10, 20, 40, 80 and 160 mA cm^{-2} are presented in Table 7. Figure 3.27 is the PF on Ni deposited at 80 mA cm^{-2}.

Using high current densities of 80 and 160 mA cm^{-2} has a great effect on the texture of the deposits. Ul-Hamid *et.al* have varied the current density in electrodepositing Ni between 25 and 50 mA cm^{-2}, and reported the peak intensity ratio of 111>200 for the lower current density and 200>111 for the higher current density,[124] similarly we observed switch in orientation from 111 to 200 with increasing the current density, increasing the current density in this work has resulted in more texture developments and complete domination of 220 orientation. Pathak *et.al* have reported the change in texture in Ni very thick (90 µm) electrodeposits from 110 orientation to 200 orientation,[115] thus an opposite observation was obtained in their work. To explain this we have discovered in section 3.1 of this work, the switch in preferred orientation from 200 to 110 by increasing the thickness from 5 µm to 13 µm. Hence the two parameters (thickness and current density), independently affect the texture within the deposit.

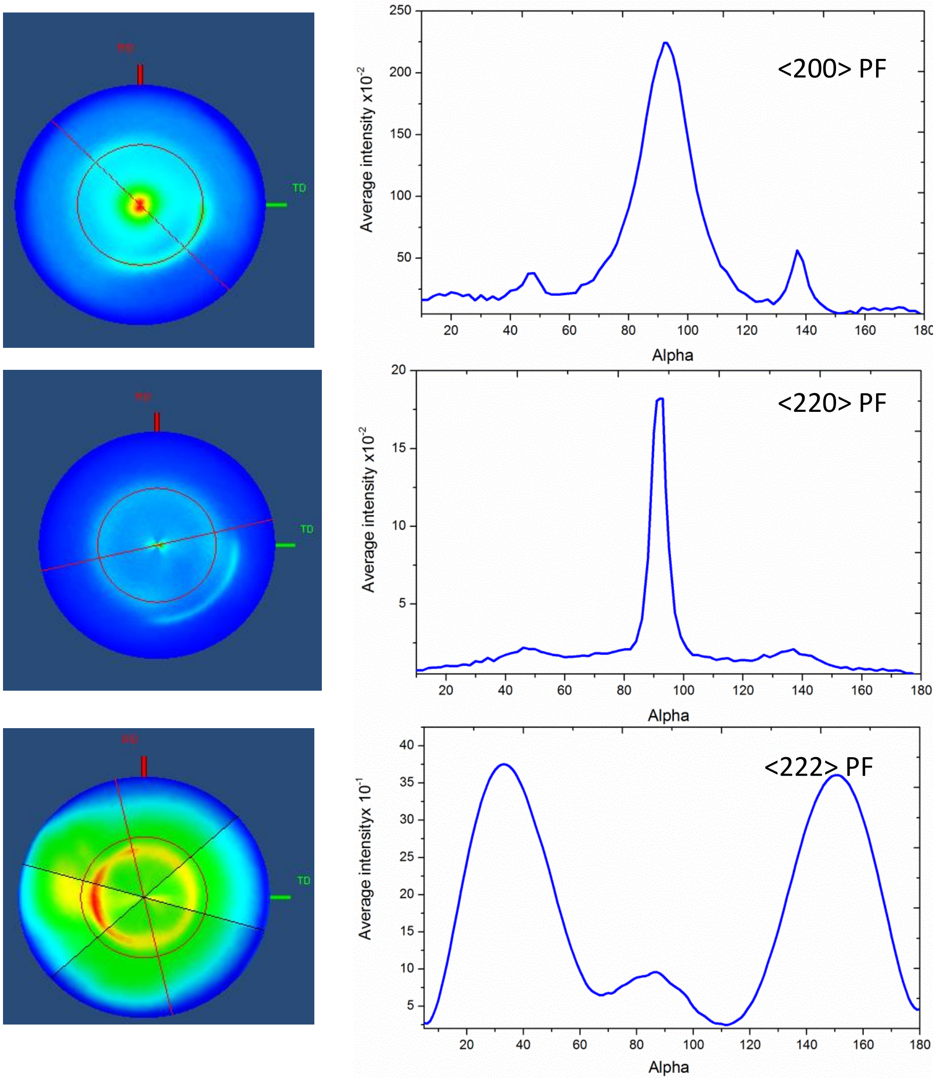

Figure 3.27 2D projections and cut-line patterns for 5 µm Ni film electrodeposited at 80 mA cm $^{-}$, from the Watt's bath.

Table 7 Texture for Ni films electrodeposited from Watt's Ni bath at different current densities.

Current density/ mA cm^{-2}	Observations in <200> PF	Observations in <220> PF	Observations in <222> PF
10	90° peak, <200>	90° peak, <220> 35.3° peak, <111>	90° peak , <111> 54.8° peak, <200>
20	90° peak, <200>	45° peak, <200>	90° peak , <111> 54.8° peak, <200>
40	90° peak, <200>	90° peak, <220> 45° peak, <200>	90° peak , <111> 54.8° peak, <200>
80	90° peak, <200> 45° peak, <220>	90° peak, <220>	90° peak , <111> 54.8° peak, <200>
160	90° peak, <200> 45° peak, <220>	90° peak, <220>	35.3° peak, <220>

3.3.3.5 Residual stress measurements

Residual stress measured for 5 µm Ni films deposited at different current densities, using iso-inclination method adapted with Young's modulus. Previous studies show increasing stress on the electrodeposited Ni film by increasing the deposition current density.[114] In a study by Lou *et al.*, at high current densities, the deposits are under high tensile stress, similar to the that observed in this work. While when they used low current densities of (2 mA cm^{-2}) deposits exhibiting low compressive stress were obtained, current density values as low as theirs were not applied in this work.[100] The Ni films deposited here are under tensile stress, indicated from the shift in XRD peak reflections and the measured residual stress, which show increase in value by increasing the current density (Table 8 and Figure 3.28) show stress measurement on Ni film electrodeposited at 40 mA cm^{-2}.

Table 8 Residual stress measured for 5 µm Ni films deposited at different current densities, using iso-inclination method adapted with Young's modulus.

Deposition current densities/ A cm^{-2}	Stress/ MPa
0.01	383 ± 68
0.02	502 ± 56
0.04	903 ± 54

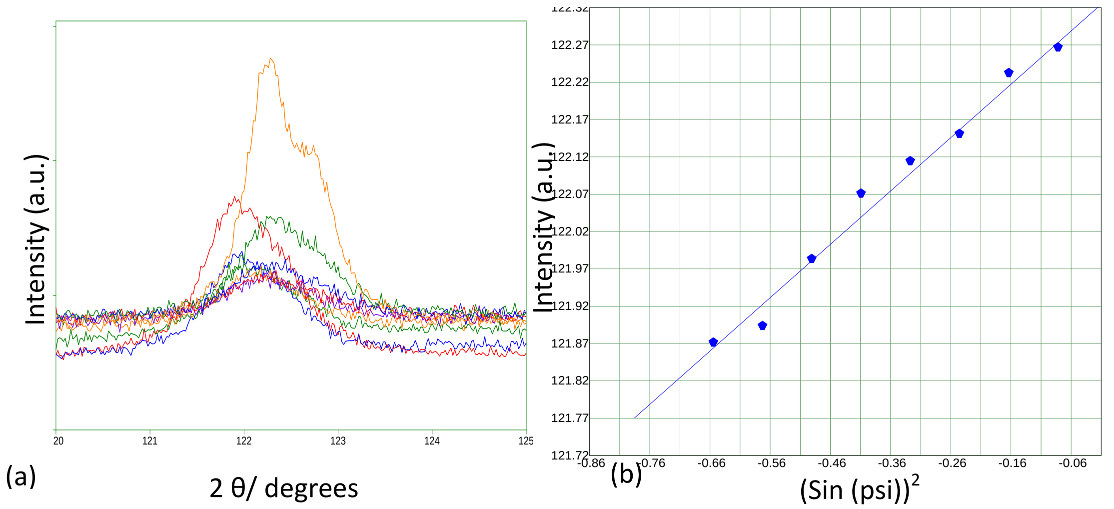

Figure 3.28 XRD Stress measurement profile for 5 µm Ni film deposited on Au substrate at 40 mA cm^{-2} from Ni bath (a), and Sin^2 Ψ line chart (b). The measurement method applied was iso-inclination, fixed psi. The stress ± reliability from the slope using the equation (Y =0.71X+122.332) is 903 ± 54 MPa.

3.4 Conclusion

Ni and Ni-B films having thicknesses between 0.5 and 13 µm were electrodeposited (ED) from Watt's Ni bath with and without addition of sucrose, using a chronopotentiometry (CP) method. The B content in Ni-B films was targeted at 1 or 3 wt. %. To study the effect of current density on the deposited Ni, experiments were adapted to deposit Ni of a constant thickness (5 µm), at varied current densities between 0.01 and 0.16 A cm^{-2}. Characterisation of the morphology, composition, crystallite size, stress, strain and texture was carried out on the films. For Ni films deposited at different thicknesses, the electrochemistry (CP) data show similar trends of potential-time transients for the films, in the films ED with sucrose added to the electrolyte, a decrease in the value of the potential passed in the system was observed. Morphology investigation of the films (section 3.3.1.2) indicates rough and dull surfaces with pyramidal growth of particles, an increase in the roughness was observed by increasing the thickness of the electrodeposits with an increase in particle agglomeration on the surface. Sucrose addition in some of the electrolytes has resulted in more uniform deposits with change in particle shapes to spherical rather than pyramidal particles. EDX shows small quantities of O and C contamination.

XRD patterns show peaks associated with Ni, and Au peaks from the substrate. Rietveld refinement outcomes were used to determine films properties. Strain and stress in the films were evaluated from both the lattice constant variations and the shift in 2θ angles, Ni XRD reflections show changes in strain from compressive in thin films to tensile and increase in value of stress and strain with increase in the thickness of the deposit, except some cases where the thick film was produced with sucrose or where delamination of the deposit from the substrate has occurred. Film thicknesses show almost no effect on their crystallite size (Table 1), while the presence of sucrose in the deposition bath has resulted in decrease in the size of the crystallites. Symmetric XRD scans indicate variation in the film texture by varying the thicknesses, in which the <111> orientation for the 0.5 µm film is switched to mixed <111> and <200> in 1.3 µm film, and then to <200> orientation in 5 µm ones and finally to <220> orientation for the thickness of 13 µm. In-plane XRD measurements show similar texture variation to the one observed from the symmetric scans, as 200/111 peak ratio show an increase with increasing the thickness. Pole figure results are supporting the estimated texture from both the symmetric and in-plane XRD scans. <111> texture in 0.5 µm Ni is changed to mixed <111> and <200> texture for the 1.3 µm film, further change in texture to <200> orientation in 5 µm ones, and complete <220> orientation for the 13 µm Ni. Residual stress in the films was measured by iso-inclination method, increasing with thickness from 0.5 to 5 µm, but then falling again on increasing the thickness to 13 µm.

Boron was added by using procedures expected to deliver 1 wt. % and 3 wt. % B in the Ni matrix. DMAB was used as the B source, and the concentration of DMAB and the pH were kept constant to prevent electroless Ni-B deposition. The B content in the films was varied by controlling the applied current density. CP plots for Ni-B film with different B contents at various thicknesses show different initial steps due to different nucleation mechanisms in every case, but similar potentials resulted in similar current densities. In the films that peeled on the edges as the result of the strained deposit, the value of the potential has shown a gradual increase due to increased electroactive surface area.

Various surface morphologies were found depending on parameter variations. 0.5 µm Ni-B surfaces are smooth, bright and uniform with increased brightness and pinholes numbers by increasing the B content. The 1.3 µm films possess higher numbers of pinholes especially in the case of 3 % B one. 5 µm Ni-B were produced with and without sucrose, the films fabricated without sucrose have agglomeration of particles on the surfaces along with pinholes, an obvious decrease in pinholes and more uniform deposits were observed in the films containing sucrose. Spherical particles with decreased pinholes are the characteristics of 13 and 5 µm Ni-B films ED with sucrose. EDX analysis shows only peaks for Ni and small amount of C and O, no signal for B from the EDX scans, as B is a light element and requires low energy EDX. On this basis qualitative and quantitative WDX scans were run on the films to detect the presence of B in the Ni matrix as well as to evaluate the amount of Ni and B in each deposit. The qualitative scans show stronger peaks of B for the films aimed to contain 3 wt. % B over the ones aimed to have 1 wt. % B. while from the quantitative WDX results (normalised), the values of B contents differ from the aimed for values by a small amount.

XRD data for the Ni-B films contain only the Ni 111 reflection, which is due to broadening in the peaks by adding B to Ni matrix. Broadening in XRD peaks comes from the crystallite size and strain, however in Ni-B films the broadening is mostly due to crystallite size reduction. By increasing the amount of B further broadening in the peak was observed. Information on texture could not be obtained from the symmetric scans, as Ni 111 is the only identified peak for Ni. Rietveld refinement was applied, higher lattice constants were observed for Ni-B compared to Ni films. Hence larger tensile stress which tends to decrease by increasing the thickness and the amount of B, sucrose addition has caused further reduction in the value of lattice constant. Strain calculated from extracted Ly value showed increase in value by increasing the thickness and again decrease by adding sucrose. Great reduction in crystallite sizes of Ni was observed by adding sucrose and more reduction by increasing the amount of B. Pole figure measurements indicate <200> orientation in the 0.5 µm films and polycrystalline structure for the 5 µm films deposited with sucrose regardless the composition (the amount of B), but the 5 µm thick film with 1 wt. % deposited without sucrose, possess a preferred orientation similar to the thin Ni-B films.

Ni films were deposited at various current densities, the chronopotentiograms follow similar trends, and in the films deposited at higher CDs the CP plots show sharper nucleation along with a higher level of bubble generation (noise) features. Morphology examination shows uniform rough surfaces, and increased particle agglomeration by increasing the current density.

Symmetric XRD scans contain peaks for Ni and Au. The texture observed from the symmetric scans and PF measurements, indicated <200> orientation in the films deposited at 0.01 and 0.02 A cm^{-2}, and polycrystalline texture in the film deposited at 0.04 A cm^{-2}, and then <220> orientation in the films deposited at 0.08 and 0.16 A cm^{-2}. Increased strain and reduction in crystallite sizes by increasing the current density was observed from the extracted parameters in Rietveld refinement. Stress measurements using the iso-inclination method revealed a sharp increase in the stress with increased current density.

Chapter 4 Electrodeposition and characterisation of germanium

4.1 Introduction

Germanium is an important semi-conductor, its widest application areas are optoelectronics and photonics including electronic devices, sensors, and photovoltaic cells.[126] In nanoelectronic devices Ge nanowires have great and promising use. The Bohr exciton radius for Ge is 24.3 nm,[127] hence Ge is a good candidate for quantum applications. Including size dependent photoluminescence.[39, 128] Larger quantum confinement effects are found in Ge relative to silicon, due to the larger dielectric constant and smaller electron and hole effective masses of Ge.[129] Ge electron mobility is about twice that for Si and the hole mobility is about four times greater, with a smaller band gap of 0.67 eV.[130] It exhibits a high refractive index ($n = 4.12$ at $\lambda = 2$ µm) and the highest dielectric constant ($\varepsilon = 16$) among all transparent materials in the near infrared regime.[130, 131] These aspects have driven significant work with Ge, despite the limited availability and high cost compared to Si.[132] The photonic band gap of Ge increases with the dielectric contrast, hence it exhibits promising properties for IR range photonic applications.[131] Nanoparticles of Ge and Si can be utilized as substitutes for heavy metal based semiconductors in many applications, taking advantage of the environmentally friendly nature of the two elements.[133] Ge nanowires are great materials in many significant applications, they have quasi one-dimensional structure, high carrier mobility compared to the bulk materials and quantum confinement effect.[134] Germanium alloy with silicon ($SixGe_{1-x}$) is a promising compound in technological applications such as the formation of heterojunction bipolar transistors (HBT) for radio-frequency applications, in photonics this compound fills the gap between the low cost, low frequency Si chips and the high cost, high frequency chips such as gallium arsenide.[128] Photodiodes based on Ge are sensitive to visible and infrared radiation, SiGe single crystal layers are utilized very successfully in integrated electronics.[39] $Ge_xSb_yTe_z$ (GST) is another important compound that contains Ge, GST is a phase-change material with great interest, owing to its high storage capacity, data rate, reading, writing and erasing. GST has a promising use in the composition of next generation data storage materials.[130]

In the last decade huge attention has been paid to Ge, which has resulted in development of several well-established techniques in its deposition. The techniques include chemical vapour deposition, electron-beam evaporation, pulsed laser deposition, ion implantation, molecular beam epitaxy and sputtering.[135] Germanium deposition in a high quality form for commercial devices is usually achieved by chemical or physical vapour deposition methods. Nonetheless CVD and PVD are conducted with high cost, difficult conditions (high vacuum), and slow deposition rates,[126] moreover these methods are top down techniques and very challenging to use in filling high aspect ratio structures.[136] Hence thoughts were and still are on other deposition techniques.

Electrodeposition is a promising technique in Ge deposition due the cost effectiveness and viability.[137] Electrodeposition of Ge has been achieved in various electrolyte media, and some successfully being used in Ge electrodeposition include organic baths of ethylene glycol and propylene glycol,[138-141] ethylenediamine,[135],dichloromethane,[136] ionic liquids,[126, 128, 131, 137, 142] aqueous solutions,[130, 143] and supercritical fluids.[132, 144] Electrodeposition of Ge from aqueous solution is very challenging due to the high reduction potential required and low hydrogen overpotential of Ge. Thus the hydrogen evolution from the aqueous solvent hydrolysis takes place on the cathode, competing with the Ge ion reduction, which prevents the growth of the film.[132] Ionic liquids are very good substitutes for aqueous solvents, having high electrical conductivity and their reduction potential much higher than that of water. Good dried ionic liquids with low levels of water (few ppm) can solve the hydrogen evolution problem.[126] $GeCl_4$ is the most used reagent in Ge electrodeposition. [128, 131, 138, 145, 146]

Endres has worked on the electrodeposition of Ge on single crystal Au (111), depositing Ge from a room temperature ionic liquid using GeI_4 as the source of Ge [147]. Electrochemical oxidation of the film has been observed on the timescale of 2 hours, coupled with chemical oxidation by the chemical attack from GeI_4. In another paper Endres and El- Abdin have carried out an *in-situ* scanning tunnelling microscope (STM) study for the germanium phase formation[142]. The deposition has been carried out using nanoscale electrodeposition of Ge on Au (111) substrate from ionic liquid. Alteration in the growth of Ge was observed for different applied overpotentials. One of the important observations in this work is the formation of a rough layer on the gold substrate at open circuit potential. The paper concludes the variation in Ge growth mechanism with the potential variation. Wu *et al.* have selected a relatively low viscosity ionic liquid 1-butyl-1-methylpyrrolidinium dicyanamide ([BMP][DCA]) as electrolyte to electrodeposit Ge using $[GeCl_4(BuIm)_2]$ (BuIm =N-butylimidazole) as the Ge source, the motivation was increased mass transfer and conductivity as well as high solubility of metal salts in DCA based ionic liquid.[126] Macroporous Ge film has been produced and studied by Vugt *et al.*, the film was formed onto a templated gold substrate (with a dried suspension of silica spheres) using electrodeposition technique. The paper shows a successful filling of the template pores with the deposit down to the gold surface, and the ease of selective removal of the template.[141] Al-Salam *et al.* have synthesised Ge nanowires from ionic liquid, by potentiostatic electrodeposition at room temperature, using template.[134] Three-dimensionally ordered macroporous nanostructures of Ge have been formed and studied for photonic applications by Meng and co-workers. They have produced the material using direct template-assisted electrodeposition in ionic liquids.[131] In a paper by Gu *et al.* the performance of Ge nanowire films as anodes for Li^+ batteries was examined, and was found to have a stable discharge at a rate of 973 mA h g^{-1}. The nanowires were electrodeposited in a crystalline form using a metallic liquid (so called ‘flux’), which is the electrode platform for the ED and dissolves GeO_2 to produce Ge particles at the same time. The substrate employed in that work was inert electrode substrates decorated with <100 nm, individual indium nanoparticles.[148] Recently Lai *et al.* have synthesized high-density Ge nanowire arrays in anodic alumina templates (AAO) using a supercritical fluid-liquid-solid method.[144] Chandrasekharan and Sevov have deposited Ge films, anodically from ethylenediamine solutions of deltahedral Ge_9^{-4} Zintl ions. They have shown a number of advantages of using Ge_9^{-4} clusters, including high current efficiency, minimization of hydrogen evolution when using organic solvents, and overcoming the high viscosity problem associated with other non-aqueous liquids like ionic liquids.[135]

Generally Ge electrodeposits tend to form in amorphous or polycrystalline structure, when deposited on solid substrate, hence a crystallisation process is typically required. Fahrenkrug *et al.* deposited single crystal Ge nanowires, on liquid Ga nanodroplet seeds on a conductive wafer of Si or Ge, using electrochemical liquid-liquid-solid process. Ge was electrodeposited from dissolved GeO_2 in an aqueous solution, their characterisations have showed that every Ga droplet has seeded a nanowire of a single Ge <111> crystal.[143] Various crystallisation procedures have been followed with Ge so far, for instance Zainal Abidin *et al.* have used a process called rapid thermal annealing, at 980 °C for 1 s.[149] Regardless of the sensitivity of Ge to surface oxidation Khan *et al.* have used annealing in air at temperature range between 100 to 500 °C, reporting nanocrystalline Ge at the annealing temperatures of 400 and 450 °C.[150] Relatively high intensity laser illumination was used by Bartlett *et al.* to obtain a crystalline phase from amorphous Ge electrodeposited by supercritical fluid electrodeposition (SCFED).[39]

In our work the electrodeposition of Ge was on patterned titanium nitride (TiN) on silicon substrates. TiN makes an excellent substrate for metal and semi-metal electrodeposition, due to its metallic conductivity, wear and corrosion resistance and high hardness.[151] Many Ge containing compounds used as precursors for Ge electrodeposition possess sensitivity towards water, thus traces of water left in organic electrolytes may lead to oxide formation when used with water sensitive precursors. Halometallate complexes of metals have been determined to behave as excellent precursors in electrodeposition from organic electrolyte.[136] In our work the precursor was tetrabutylammonium chlorogermanate $[^nBu_4N][GeCl_3]$, which can be prepared in high yield as an easy to handle powder. Due to the contribution of the ligand as well as the central element (Ge) from the precursor in the electrochemistry,[152] the selection of the supporting electrolyte was based on the ligand from the Ge precursor, and was tetrabutylammonium chloride ([^{n}Bu$_4$N]Cl). The organic solvent, dichloromethane (DCM) has low viscosity and high electric conductivity with an appropriate salt, besides [^{n}Bu$_4$N][GeCl$_3$] is well known for high solubility in organic solvents.[136] DCM was selected in the electrolyte preparation, the whole process was performed under an inert condition (N_2 atmosphere) to prevent oxides in the composition of the deposit.

4.2 Experimental

The deposition method was initially developed by Dr. Gabriela Kissling (Chemistry, University of Southampton). The precursor [^{n}Bu$_4$N][GeCl$_3$] was synthesized by Dr. Andrew Jolleys (Chemistry, University of Southampton), and the TiN substrates were made by Ruomeng Huang (Electronics and Computer Sciences (ECS), University of Southampton).

4.2.1 Preparation of the electrolyte

0.0421 g of tetrabutylammonium chlorogermanate [^{n}Bu$_4$N][GeCl$_3$] and 0.2779 g of tetrabutylammonium chloride [^{n}Bu$_4$N]Cl (Fluka, > 99.0%) were dissolved in 10 cm^3 of dry dichloromethane DCM. The process was carried out under an inert atmosphere inside glove box.

4.2.2 Cyclic voltammetry experiments

The electrochemical processes were carried out inside the glove box. A glassy carbon (GC) rod was used as the working electrode, Ag/AgCl in (0.1 mol dm^{-3}) [^{n}Bu$_4$N]Cl in DCM was used as the reference electrode and a Pt gauze was used as the counter electrode. The cyclic voltammetry (CV) was recorded in the potential range -2 to 1 V at a scan rate of 50 mV s^{-1}.

The TiN electrodes were made by depositing a thin layer of TiN on Si wafer patterned with a grid structure of resist in the first step. The resist was removed and a second layer of resist was applied to the electrode to protect the contact area and the non-relevant areas were masked by adding a layer of silica (SiO_2), the steps are described in Figure 4.1. The same conditions and parameters as for GC electrode were used to record a cyclic voltammogram on titanium nitride (TiN) electrode.

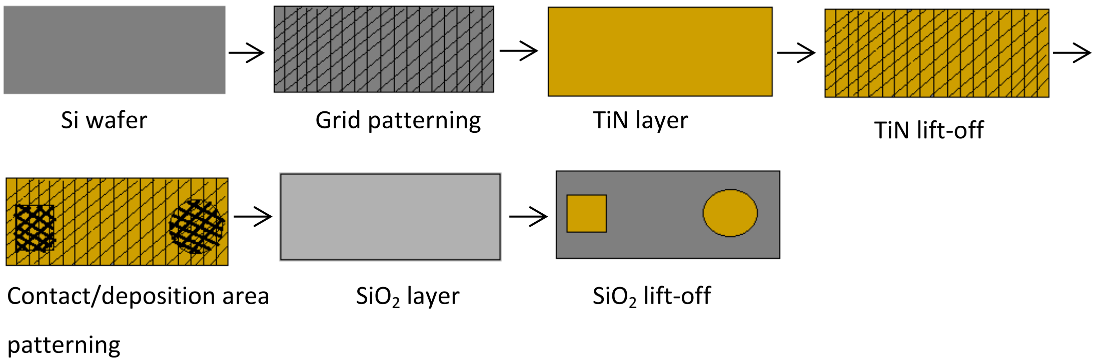

Figure 4.1 Cartoon representing the steps in the TiN substrate formation.

4.2.3 Electrochemical deposition of Ge

The deposition process was under similar conditions (inside glove box), potential step chronoamperometry was used for the deposition. The TiN substrate acted as the working electrode. The active part of the electrode was immersed in the electrolyte. A Pt gauze was the counter electrode and the Ag/AgCl in (0.1 mol dm^{-3}) [^{n}Bu$_4$N]Cl in DCM was the reference electrode. Films were produced using reduction potential singular values of-1.25, -1.3, -1.75, -1.78 and -2 V. A Micro Autolab 3 potentiostat and Nova software were used for the electrochemical measurements.

4.2.4 High temperature annealing of Ge films

Aiming to obtain crystalline Ge phase from the as-deposited amorphous phase, the samples were annealed at various temperatures of 500 to 800 °C and various durations. To avoid air exposure samples were transferred into a furnace tube inside the glove box, and put inside a tube furnace. The process was carried out under either flowing Ar or vacuum, with a 20 minute vacuum or argon flushing period prior the heating. The furnace was then heated at various rates, and the heating duration was varied between 30 minutes to 1 hr.

4.2.5 XRD, SEM, EDX and XPS experiments

The XRD patterns were collected using a Smart lab X-ray diffractometer, with Cu K$_\alpha$ radiation, using 2θ values in the range between 10-80°. After annealing the furnace tube was opened in the glove box and the sample was loaded into the air-sensitive sample holder. Grazing incidence and symmetric scans were collected. Grazing incidence scans were collected using a 1° incident angle. All sample handling was anaerobic by loading a sealed sample cell with a hemi cylindrical Kapton window in the glove box.

Scanning electron microscopy (SEM) was carried out using a Philips XL30 ESEM microscope to examine surface morphologies. All SEM imaging was under high vacuum mode. EDX spectra were recorded with an accelerating voltage of 10 kV.

The X-ray photoelectron spectroscopy measurements were conducted using a Theta Probe angle-resolved X-ray photoelectron spectrometer from Thermofisher Scientific. The system uses a monochromated, micro-focused Al K-alpha source. The peaks are calibrated using C1s peak for a known configuration. All XPS spectra were collected using 400 µm spot under UHV conditions, charge neutralisation was by combined electron/ion flood source fitted with low-energy spread electron source. XPS survey spectra scans were collected over the binding energy range 0-1100 eV, at the pass energy of 200 eV, and 1 eV energy step size, generally 3 scans were collected for 50 ms dwell time. High resolution data to examine the Ge 2p and Ge 3d peaks were collected at 50 or 200 eV pass energy over the binding energies 24-38 eV and 1200-1280 eV respectively, 3-10 scans were collected each time depending on the pass energy, the dwell time used was between 100-120 ms and the step size between 0.01-0.4 eV. Depth profiling experiments were performed to remove the surface oxide to examine the composition of the Ge layers in the deeper levels, with an Ar ion beam source with an energy of 1 µA at 3 kV used to etch the surface. The etch profile comprises 3 levels of etching, for the start level the gun was off, so no etch was done, and then for the next two levels a 10 s etch was applied in each level, developing a total final etch time of 20 s on the surface.

4.3 Results and discussion

This chapter comprises electrodeposition, crystallisation and characterisation of Ge thin films. Ge films were electrodeposited on TiN coated Si wafers (two defined areas of the substrate were left un-coated for the electrode and the deposition area), the TiN layer was sputtered with SiO_2 then a 4 mm diameter circle to deposit Ge on and a 5x5 mm square for electric contact were etched back. Hence the conducting area (TiN) on the substrate is well defined, Figure 4.2 shows a standard TiN electrode used in this work. A carton representation of the electrode build and how the electro-conductive areas work is found in section 4.2.2.

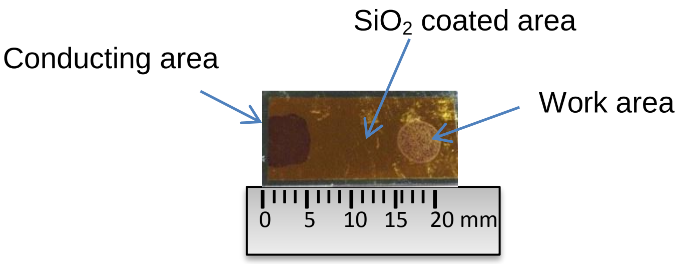

Figure 4.2 SiO_2 sputtered TiN coating on Si wafer, with the conducting and working areas etched back and Ge electrodeposited on the work area (the circle). The image is for the electrode after the Ge was electrodeposited.

The Ge electrolyte composition consisted of a tetrabutylammonium salt Ge precursor ($[^nBu_4N][GeCl_3]$), and the supporting electrolyte tetrabutylammonium chloride ($[^nBu_4N]Cl$), dissolved in dichloromethane (DCM). The shared cation and ligand between the precursor and the electrolyte increases the probability of compatibility of the two reagents, reducing likelihood of contamination and balancing solvation rates.

The electrochemistry was conducted using cyclic voltammetry (CV) and chronoamperometry (CA) techniques. A potential window of -2 to 1 V was used in the CV experiments. Ge reduction requires a high overpotential, and high stability is expected for DCM when high cathodic potentials are required in the electrochemical processes, thus it makes a good factor in choosing DCM as a solvent. DCM has a dielectric constant of $\epsilon = 9.08$ at 20 °C[153] so is a relatively low polarity organic solvent, but it has been successfully used as a solvent for electrochemical experiments.[154] Initially Ge was deposited in an amorphous form, determined from broad humps in the XRD patterns run on the postdeposition substrates, the humps were matching the positions of cubic Ge phase peaks. Thermal crystallisation at temperatures in the range of 600 to 800 °C and under anaerobic conditions was applied to the films. Characterisation techniques were applied to study the morphology, purity, composition, thickness and crystallinity of the films. Thin layers of Ge were obtained. The experimental variables examined include drying of the electrolyte, adding various surfactants to the electrolyte composition, changing substrate preparation method and variation of the deposition mechanism by applying a nucleation pulse overpotential followed by growth overpotential.

4.3.1 Ge electrodeposition under potentiostatic conditions

Electrodepositions initially used the supporting electrolyte tetrabutylammonium chloride as purchased. To determine the best electrodeposition conditions cyclic voltammetry experiments were recorded for the Ge species in the electrolyte. Cyclic voltammetry is a standard technique to study electrochemical reactions, and for determinations within these reactions, such as electrode reaction mechanisms, electron transfer constant and diffusion coefficients, electrode and electrolyte properties.[155, 156] Ge was present in the electrolyte as Ge^{+2}, as the Ge precursor consists of a Ge^{+2} salt complex.

Initially CVs were recorded on GC disc electrodes, with electroactive area of ~0.5 cm^2, using the potential window between -2 and 1 V starting from 0 V (vs. Ag/Ag$^+$), towards the cathodic direction (Figure 4.3 Peak A). The main feature in the CV is the reduction peak at a potential of -1.25 V corresponding to the reduction of Ge^{+2} to Ge^0, which is clearly defined on the first scan and becomes less defined on the subsequent scans, owing to the absence of stripping peaks in the anodic scan. Hence the Ge layer formed on the electrode from scan 1 remains and forms a semiconductor electrode surface for the second and the other following scans, resulting in a reduction in the Ge^{+2} reduction peak intensities. This peak on the TiN surface (Figure 4.3), is shifted to a more negative potential (-1.6 V) compared to the CV on GC, and is totally missing in the subsequent scans.

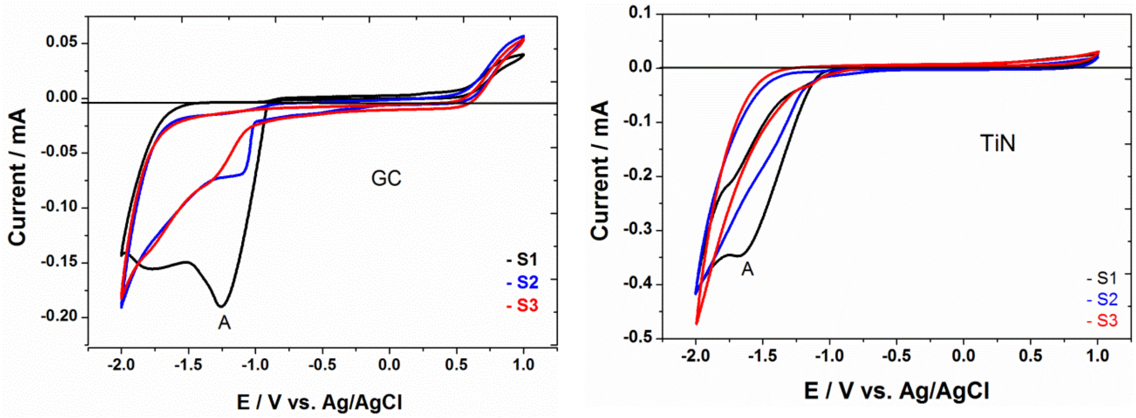

Figure 4.3 Voltammetry of 10 mmol dm^{-3} [^{n}Bu$_4$N][GeCl$_3$] in 0.1 mol dm^{-3} [^{n}Bu$_4$N]Cl in DCM vs. Ag/AgCl reference electrode, using potential window of -2, 1 V and the scan rate of 50 mV s^{-1}, on GC (left) and TiN (right) electrodes, S1, S2 and S3 indicate scans 1, 2 and 3.

Chronoamperometry is a powerful technique that can be used to study the electrode surface having high compatibility with cyclic voltammetry in electrodeposition processes. Since mass transport to the surface is particularly dependent on the geometry of the electrode,[157] the very well defined electroactive area of the TiN substrates used in this work makes them ideal to study the deposition of Ge. Ge films were obtained by potentiostatic electrodeposition (chronoamperometry), which is a process of applying constant potential and monitoring the current with time. Referring to the CVs, various potentials between -1.25 and -2 V were used to deposit Ge. The current-time transient for Ge films deposited at -1.72 V for 2 h (Figure 4.4) shows a sharp increase in the current in the initial period of the process (double layer charging), then reduces in a short time as Ge deposition takes place. The current then shows a decrease over a short time (~10 minutes) to a steady value close to zero (~ -0.01 mA). Consequently a thin deposit is expected.

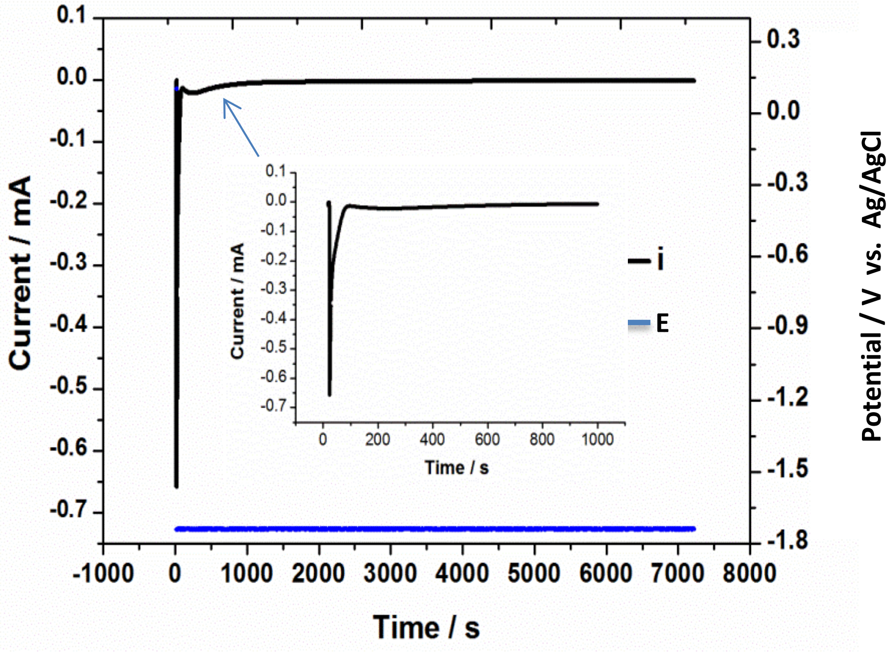

Figure 4.4 Chronoamperometric plot for Ge deposited from [^{n}Bu$_4$N][GeCl$_3$] in DCM on TiN (4 mm diameter circle) at -1.72 V deposition potential and with a deposition duration of 2 h. The black line is the current response and the blue line is the potential applied in the deposition. The inset graph represents the initial 1000 s of the chronoamperogram.

During the test to choose an optimal overpotential for Ge electrodeposition, films with different morphologies were obtained (Figure 4.5). Electrodeposited Ge films at potentials between -1.25 and -2 V exhibit a network of cracks, but the individual regions between the cracks vary in size from ~ 50 µm at -1.25 V to ~ 10 µm at -2 V with more delamination at more negative potential.

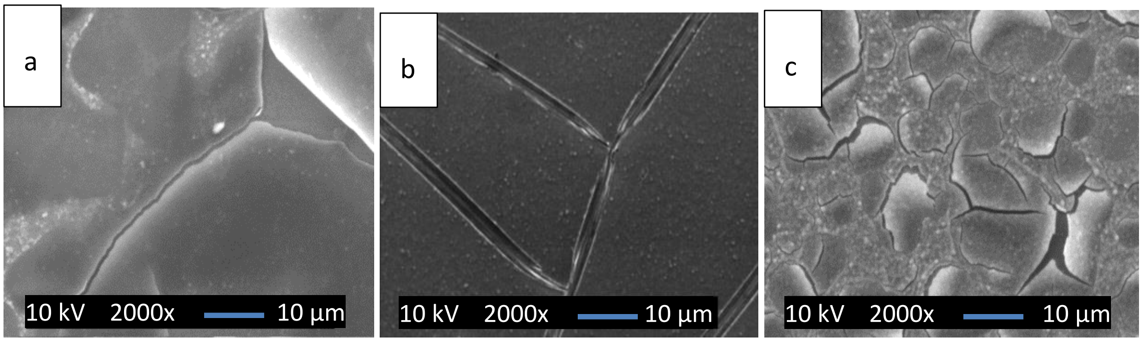

Figure 4.5 SEM images for Ge films deposited from [^{n}Bu$_4$N][GeCl$_3$] in DCM on TiN (4 mm diameter circle), with a deposition duration of 20 min, at deposition potentials of -1.25 V (a), -1.65 V (b) and -2 V (c).

The charge passed in the process can be utilized to estimate a rough thickness of the deposit. Assuming 100% Faradaic efficiency, we can detect the effect of applied overpotential on the deposit's thicknesses. In the deposition of three Ge films for 20 minutes at applied potentials of -1.25, -1.65 and -2 V, the total charges (Q) passed were 0.012, 0.024 and 0.083 Coulomb (C) respectively. The thicknesses calculated from the charge passed are 112, 136, and 469 nm for the films deposited at potentials listed above, respectively, assuming the density to be close to that of bulk Ge. The estimated thicknesses extracted from the charge passed during the depositions for films produced by variating the bath compositions and substrates are presented in table (1) at the end of the sections.

Table 1 Thicknesses estimated for Ge electrodeposited at various conditions from the charge passed during the electrodepositions.

Electrolyte and ED condition	ED potential	Substrate	ED period	Estimated thickness
As-purchased [^{n}Bu$_4$N]Cl, single potential	-1.65 V	TiN on silicon	20 min	136 nm
As-purchased [^{n}Bu$_4$N]Cl, single potential	-1.7 V	TiN on silicon	2 h	222 nm
Dried [^{n}Bu$_4$N]Cl, single potential	-1.7 V	TiN on silicon	2 h	354 nm
Dried [^{n}Bu$_4$N]Cl, nucleation and growth	-1.7 , -1.18 V	TiN on silicon	5 ms, 2 h	473 nm
Dried [^{n}Bu$_4$N]Cl, nucleation and growth	-1.95, -1.2 V	TiN foil	5 ms, 1 h	2.5 µm
Dried [^{n}Bu$_4$N]Cl, nucleation and growth	-1.5 V	Pre-heated TiN	1 h	359 nm

The thickness of the crack layers on the surface of Ge deposits from Figure 4.5 is measured by expanding the SEM images, and found to be ~116, 157 and 100 nm for the films at -1.25, -1.65 and -2 V respectively (Figure 4.6). These data were gathered using a standard resolution SEM instrument, which was not ideal for the semiconductor Ge cross-sectioning. A cross-section SEM on a higher resolution instrument of a sample of Ge electrodeposited under similar conditions Figure (4.6 d) can be used to understand our predicted thicknesses. The cross-section SEM on 20 minute deposited Ge film showed a thickness of ~100 nm, while the charge passed during the deposition of this film was 0.016 C, resulting in an estimated thickness of 90.4 nm. The cross-section image shows a uniform thin layer of Ge.

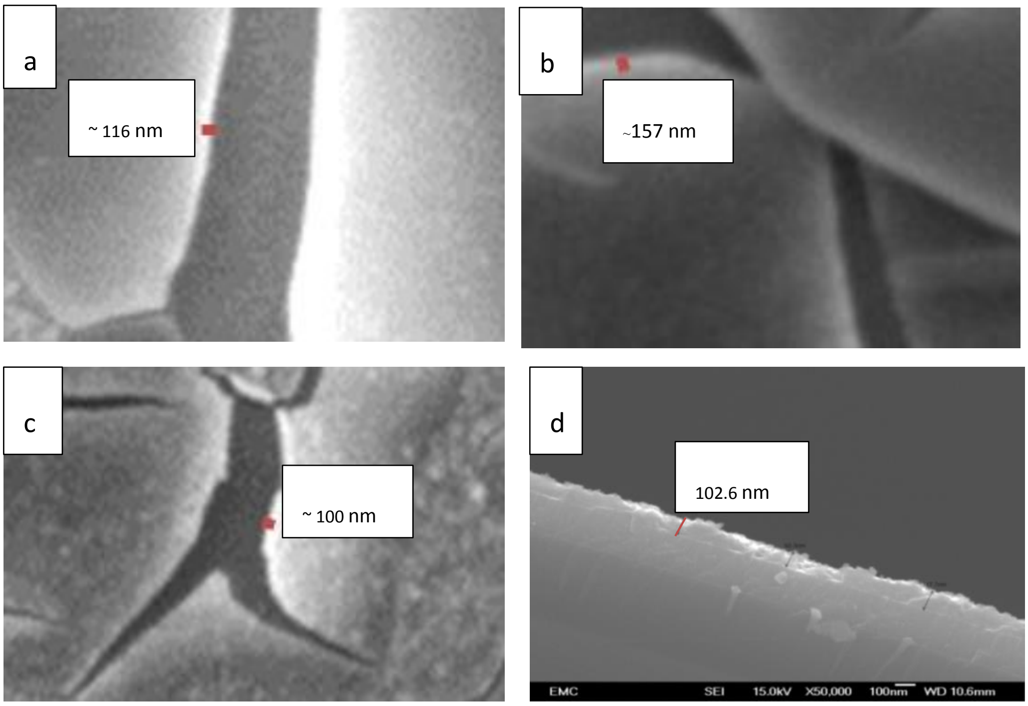

Figure 4.6 Thickness measured for the expansions on the cracked and peeled regions on the SEM figures in Figure 4.5 for Ge deposited at (a) -1.25 V, (b) -1.65, (c) -2 V and (d) is the Cross-section SEM image for Ge film deposited from [^{n}Bu$_4$N][GeCl$_3$] in DCM on TiN (4 mm diameter circle), with a deposition duration of 20 min, at -1.85 V.

EDX spectra (Figure 4.8) show Ge deposition at all potentials, with a stronger signal for the films deposited at -1.65 and -2 V, compared to the film deposited at -1.25 V. Less Cl was detected on the surface of the -1.65 V film than the one deposited at -2 V, which is not surprising as -2 V is the potential at which the electrolyte break down starts. Consequently, at this high overpotential part of the current is likely to be utilized in the electrolyte decomposition and the projected film thickness is likely to be an overestimate. The depth in the Ge sample from which X-rays are observed can be estimated using Castaing's formula and in cases where the X-ray absorption is not too strong it can be considered similar to the depth of X-ray emission by the specimen.[158]

$$\mathrm{Z_m} = 0.033\ (\mathrm{E_0^{1.7}} - \mathrm{E_c^{1.7}})\frac{\mathrm{A}}{\rho \mathrm{Z}} \qquad (21)$$

Where Z_m: sampling depth (µm), E_0: accelerating voltage (kV), E_c: critical excitation energy (keV), A: atomic mass, ρ: density (g /cm^3), and Z: atomic number.

Here an accelerating voltage of 10 kV was applied during acquisition of the EDX spectra, accordingly the estimated sampling depth using the emission energy for Ge is ~ 680 nm.

Quantitatively the atomic percentage (At.%) ratio between Si and Ge from the EDX are 4.34:1, 2.00:1 and 3.26:1 for Ge obtained at -1.25 V, -1.65 V and -2 V, these values were used in a graph between the thickness of the deposit and Si:Ge At.% ratio (Figure 4.7). The thicknesses used here are the measured from SEM in the discussion above.

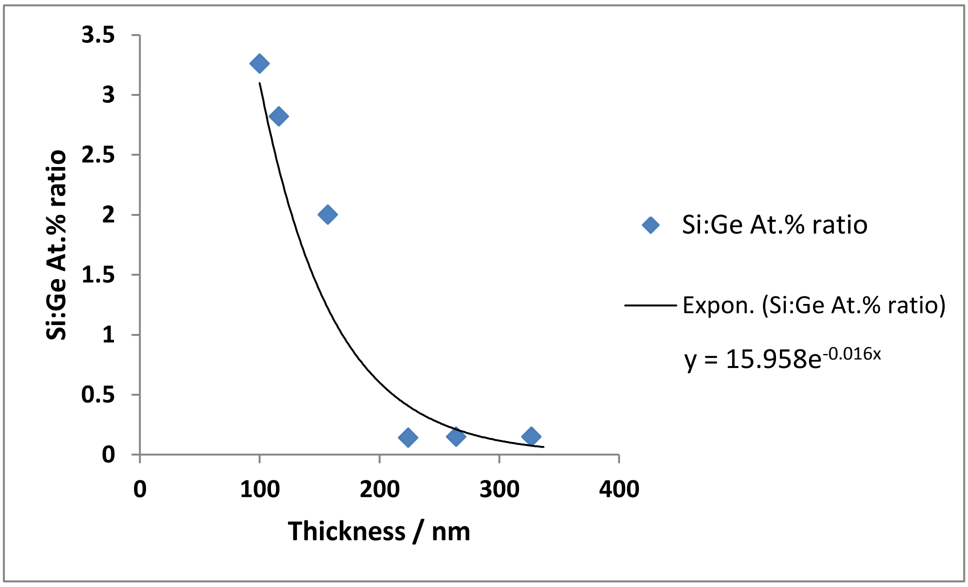

Figure 4.7 A plot of EDX measured Si:Ge At. % ratio vs. the thickness measured by SEM, the data is from Ge samples presented in figures 5, 10 and 13. The line is fitted with an exponential curve.

Relating the estimated sampling depth to the intensity ratio between Ge and Si signals from EDX (Figure 4.8), in the film deposited at -1.25 V about 0.2 of the estimated sample depth represents Ge (~ 136 nm). Herein, intensity ratios for Si and Ge (Si/Ge) were calculated in the EDX results for every sample. Consequently the peak intensity ratio (Ge/Si) in the EDX spectra for Ge deposited at -1.65 and -2 V are 0.64 and 0.56, hence their thicknesses from the measured sampling depth are estimated as 431 and 380 nm respectively. This outcome might be an indication of strong X-ray emission from the specimen at that particular accelerating voltage, thus the actual thicknesses are probably of orders of half the estimated sampling depth.

The sampling depth in EDX is finite and in case of thin films the X-rays may be generated entirely from the deposit or from the deposit plus the substrate. Electrons penetrate the surface and define an excitation volume, but some of the emitted X-rays are absorbed, and this especially applies to those from the substrate. Accordingly an overestimated thickness for the deposit is expected by applying Castaing's formula, and was observed in our calculations. We have studied the relation of Si:Ge atomic ratio from the EDX with the calculated thickness from the SEM, Figure 4.7 is the plot between Si:Ge At. % ratio and the calculated thickness in each case, and an inverse relation is found from the plot between the two variables.

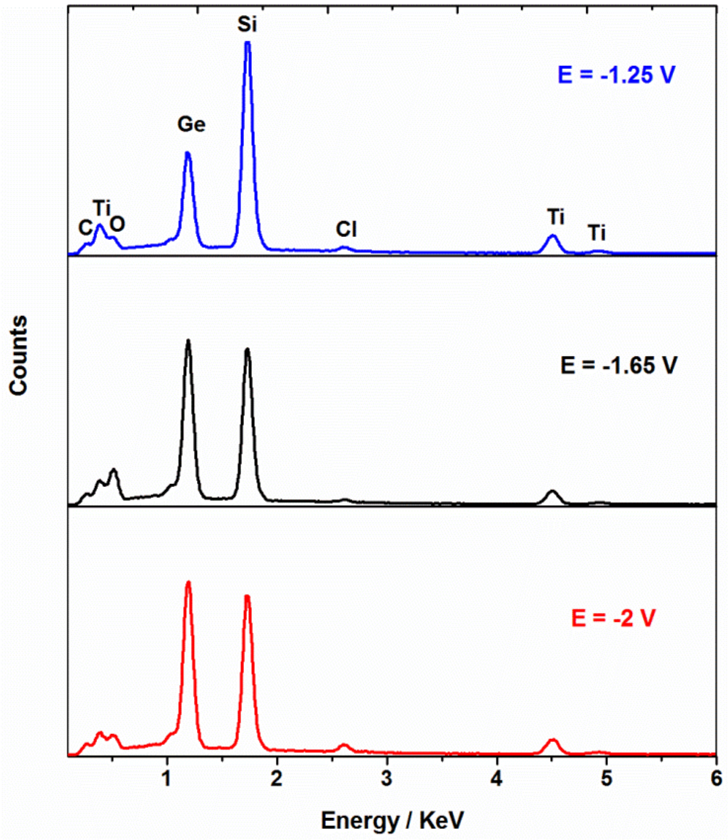

Figure 4.8 EDX spectra for Ge films deposited from [^{n}Bu$_4$N][GeCl$_3$] in DCM on TiN (4 mm diameter circle), with a deposition duration of 20 min, at different deposition potentials of -1.25 V (a),-1.65 V (b) and -2 V (c). These were collected full frame at the magnifications shown in Figure 4.5.

Ge electrodeposition is highly likely to be affected by the presence of water, as Ge^{+2} reduction takes place at a strongly cathodic potential, consequently the reduction of H$^+$ will compete with Ge^{+2} reduction resulting in hydrogen evolution on the electrode surfaces. The CA data from the as-purchased [^{n}Bu$_4$N]Cl electrolyte exhibited a rapid drop in the current to a low steady state of about -0.01 mA (Figure 4.4). Water content in the system could contribute to this rapid current drop, if precursor hydrolysis led to some GeO$_2$ content in the deposit, which would act as a more effective passivation layer than the Ge electrodeposit. Hereafter the supporting electrolyte [^{n}Bu$_4$N]Cl used in the electrodepositions was further dried. The drying was at 50 °C under vacuum overnight (21 h), and stored inside a glove box under N$_2$ atmosphere. The amount of the reagents and deposition conditions in the deposition process remained unchanged.

The CVs of Ge in dried [^{n}Bu$_4$N]Cl on GC and TiN electrodes are shown in Figure 4.9 and can be compared with the CVs recorded using the as-purchased supporting electrolyte (Figure 4.3). In the CV recorded on GC a very slight shift in the reduction peak by ~ 0.1 V towards positive direction is observed, comparably the shift in the CV on TiN electrode was by ~ 0.03 V. Otherwise the electrochemical behaviour was very similar.

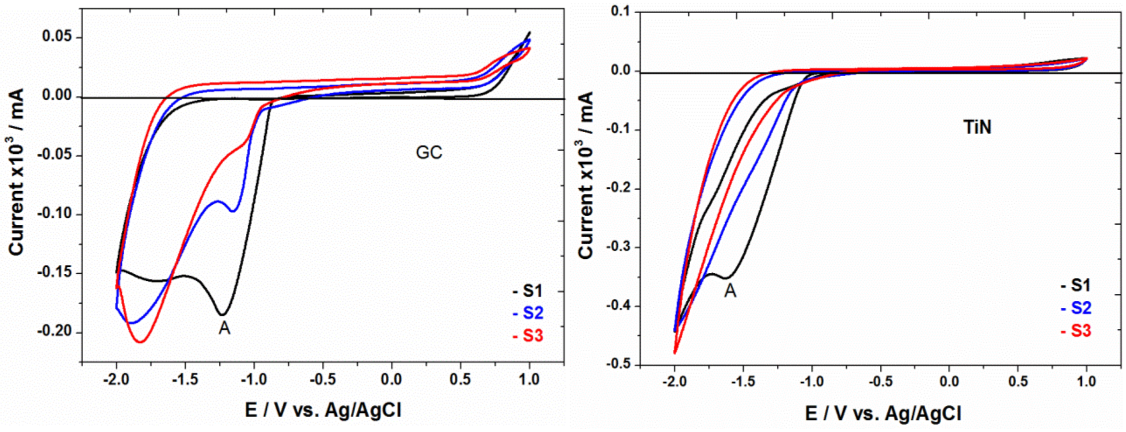

Figure 4.9 Voltammetry of 10 mmol dm^{-3} [^{n}Bu$_4$N][GeCl$_3$] in 0.1 mol dm^{-3} dried [^{n}Bu$_4$N]Cl in DCM vs. Ag/AgCl reference electrode, using potential window of -2, 1 V and the scan rate of 50 mV s^{-1}, on GC (left) and TiN (right) electrodes, S1, S2 and S3 indicate scans 1, 2 and 3.

The steady state current from the current-time transient in the experiment conducted with dried [^{n}Bu$_4$N]Cl (Figure 4.10) is bigger compared to the CA recorded with the as-purchased electrolyte (Figure 4.4), nevertheless it still exhibits a gradual decrease of the current over time. Reaching the steady state current takes almost 30 minutes. A larger total charge (0.240 C) was observed in a 2 hour deposition experiment, compared to that observed (0.164 C) in the same duration deposition experiment with as purchased electrolyte. The thickness estimated from that charge is ~ 1.35 µm. The charge passed in for a 20 minute deposition was 0.0637 C, resulting in a thickness of 358 nm (Table 1), on the other hand the thickness observed from cross section SEM in Figure 4.11 c indicates similar thickness for Ge deposited for 20 minutes using dried supporting electrolyte.

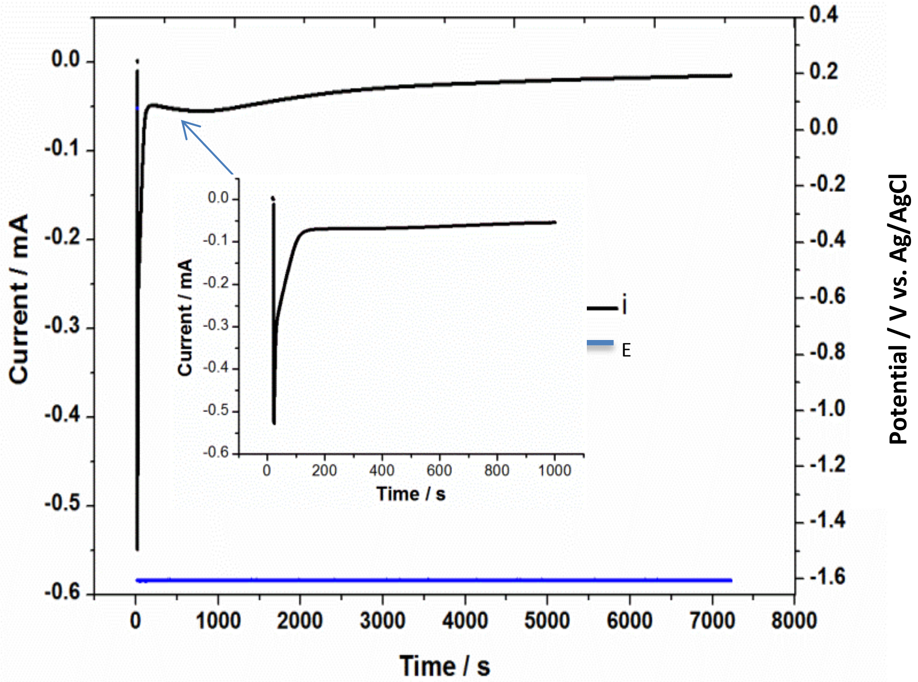

Figure 4.10 Chronoamperometric plot for Ge deposited from [^{n}Bu$_4$N][GeCl$_3$] in DCM on TiN (4 mm diameter circle) at -1.6 V deposition potential and deposition duration of 2 h, the supporting electrolyte [^{n}Bu$_4$N]Cl was previously dried. The black line is the current response and the blue line is the potential applied in the deposition. The inset graph represents the initial 1000 s of the chronoamperogram.

Figure 4.11 shows the morphology of Ge films deposited from as-purchased and the dried [^{n}Bu$_4$N]Cl. Surface morphologies for the two films share circular islands and peeled patches which is more drastic in the dried electrolyte derived Ge. As the Ge has grown thicker it appears some of the cracked regions observed with dried supporting electrolyte have fallen off and new growth has occurred in the space left behind.

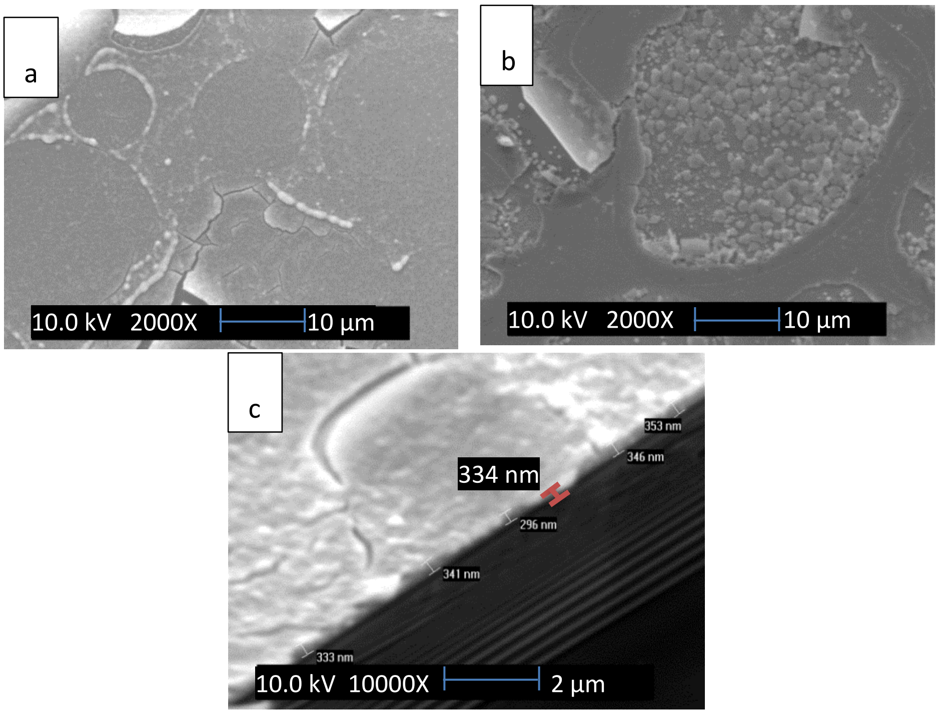

Figure 4.11 SEM images for Ge films deposited from $[^nBu_4N][GeCl_3]$ in DCM on TiN (4 mm diameter circle), the deposition duration of 20 min, at -1.6 V using $[^nBu_4N]Cl$ as purchased (a), at -1.7 V from dried $[^nBu_4N]Cl$ (b) and cross-section SEM for Ge deposited at -1.7 V using dried $[^nBu_4N]Cl$ (c).

Despite the slowing in the rate of Ge growth after 20 minutes deposition time, from the EDX spectra observations (Figure 4.12) the thickness of the deposit has grown significantly after this time. The quantitative EDX has indicated 26.8 and 61.8 At. % Ge in the 20 minutes and 2 h deposited films respectively, this also shows higher Ge content in the 20 minute deposit compared to the best condition 20 minute deposit using as-supplied supporting electrolyte . In addition the EDX spectra of Ge deposited for 2 h exclude any signal from the substrate, this indicates that X-ray emission is fully from the Ge layer, so the sample depth is estimated to exceed the 680 nm calculated from the Castaing's formula as the EDX sampling depth for Ge at this accelerating voltage. On the other hand 20 minute deposited Ge still shows a Si signal, although this is weak compared to the film deposited from as-supplied $[^nBu_4N]Cl$ (Figure 4.8, black spectrum) again suggesting a thicker deposit with the dried supporting electrolyte.

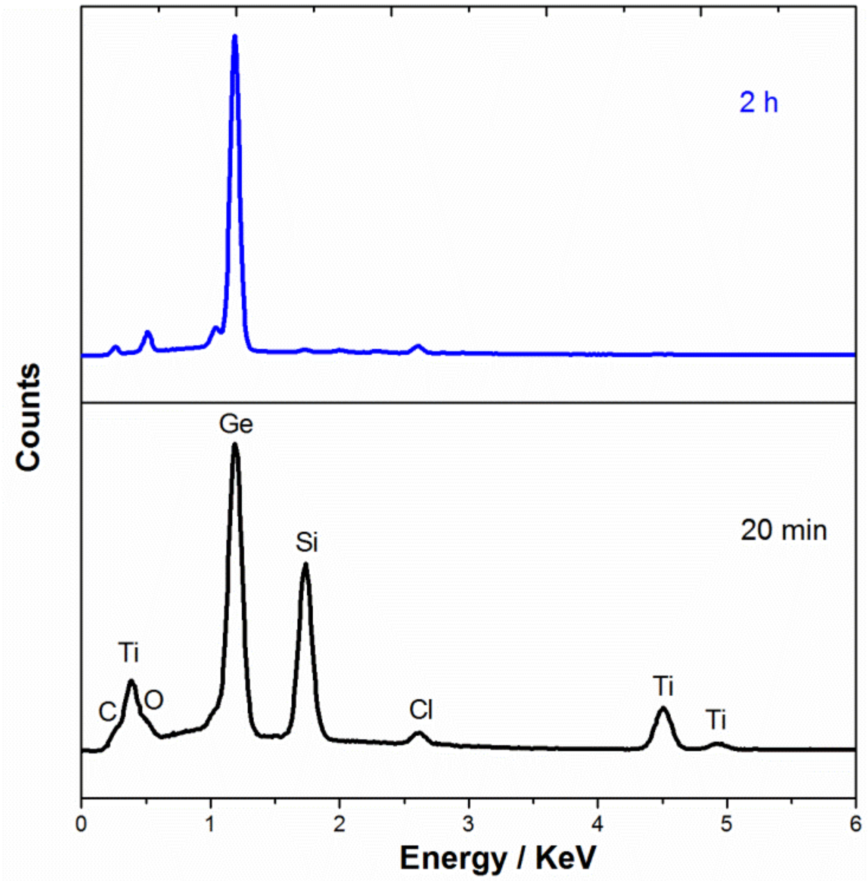

Figure 4.12 EDX spectra for Ge films deposited from dried [^{n}Bu$_4$N]Cl in DCM on TiN (4 mm diameter circle), at -1.7 V for the deposition duration of 20 min and 2 h.

4.3.2 Ge electrodeposition using nucleation and growth potentials

Nucleation is the initial and very important step in electrodeposition, the nucleus is a 2D or 3D cluster of deposited atoms of a new phase formed on a foreign surface (the substrate). The number of the nuclei increases and onset deposition will be reached, and then followed by steady state growth. In the first step of nucleation the ions or atoms reach the surface of the electrode, forming adions or adatoms. The individual adsorbed ions initially exhibit low binding energy to the surface, which increases with the arrival of more adions or adatoms to form a cluster. The rate determining process is the charge transfer, described by the Butler-Volmer equation, in Butler-Volmer equation it is assumed that the anodic and the cathodic reactions occur on the same electrode, the equation is used to determine the current depends on the potential on an electrode.[159] Accordingly one of two steps determines the rate of growth of nuclei, the lattice incorporation step or the diffusion of electrodeposited ions into the nucleus. When the former is the rate determining step, then the growth will be either as independent nuclei or as interacting nuclei. The simultaneous nucleation and growth of nuclei generally depends on the model of nuclei (2D, 3D) and the type of nucleation (instantaneous, progressive). The rate of nucleation and its competition with the growth process determines the structure and final look of the film.[24, 160] Hence controlling the rate of one of the two processes results in alterations in the structure and the grain size of the final deposit, and this has effects on the adhesion between the deposit and the substrate.

Here the electrodeposition was set up in such a way that a high nucleation rate was applied for a very short time by applying a high overpotential for 5 ms, and then followed by a slow growth rate by applying a second smaller overpotential for the rest of deposition duration. A comparison of the current-time response in the chronoamperograms for fixed potential deposition with that for nucleation and growth potential deposition was found. An obvious change in the current response in the nucleation and growth overpotential experiment (Figure 4.13) is observed compared to the single overpotential experiment (Figure 4.14). For more understanding we have plotted the first 2 minutes onset current-time response (Figure 4.13 and Figure 4.14 inset graphs), and found slower and steadier current decay with time for the constant potential route, in contrast to the nucleation and growth route which exhibited sharper current decay with time. But by the end of this onset time the current difference between the two routes is decreased to a closer value in both routes.

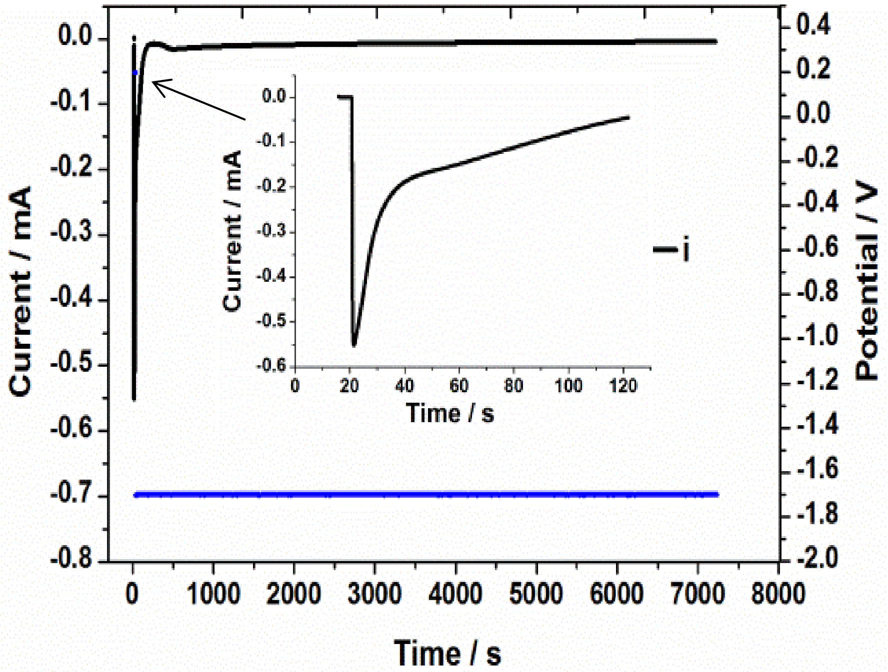

Figure 4.13 Chronoamperometric plot for Ge deposited from [^{n}Bu$_4$N][GeCl$_3$] in DCM on TiN (4 mm diameter circle), using dried [^{n}Bu$_4$N]Cl at a constant potential of -1.7 V), the deposition duration was 2 h. The blue lines represent the potential plot vs. time and the inset graphs are the onset current-time transient. The black line is the current response and the blue line is the potential applied in the deposition.

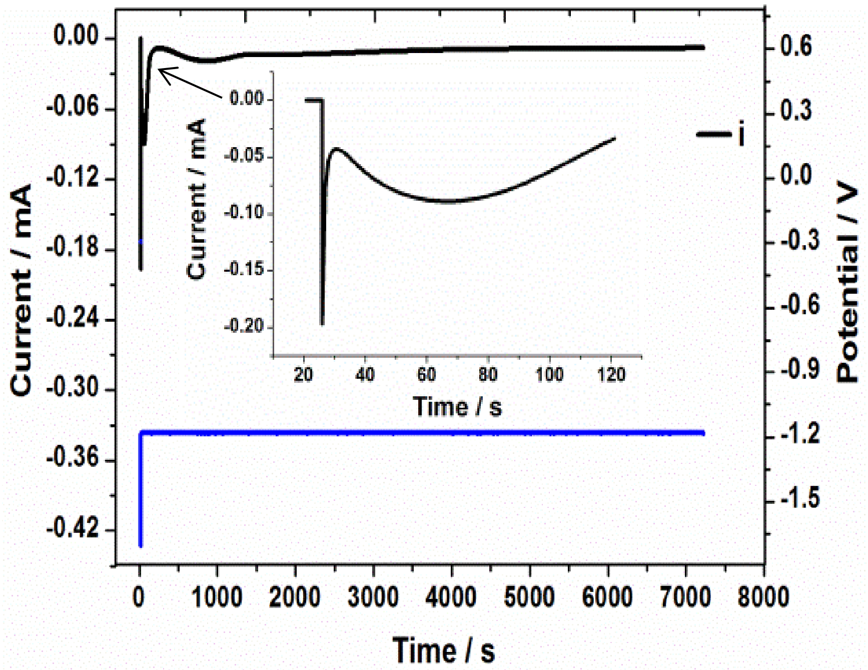

Figure 4.14 Chronoamperometric plot for Ge deposited from [^{n}Bu$_4$N][GeCl$_3$] in DCM on TiN (4 mm diameter circle), using dried [^{n}Bu$_4$N]Cl at -1.7 V for 5 ms, followed by -1.18 V, for the rest of the deposition (right), the deposition duration was 2 h. The blue lines represent the potential plot vs. time and the inset graphs are the onset current-time transient. The black line is the current response and the blue line is the potential applied in the deposition.

The SEM images (Figure 4.15) for the film produced by nucleation and growth experiment, show a non-smooth surface with deep cracks, but less delamination from the surface is seen hence it is assumed to be better adhered compared to the film produced by fixed potential growth. The single potential derived Ge film exhibited thin circular peelings, and in the spaces left behind new growth was seen to have occurred. New spherical growth particles formed rings of beads like agglomerations around the edges of the areas under the peelings.

Results from quantitative EDX analysis show higher Si:Ge atomic percentage ratio of 0.30:1 in the films produced from single potential experiment compared to that (0.14:1) in the film from the nucleation and growth experiments, and this suggests thicker deposits in the nucleation and growth deposition. The EDX spectra in Figure 4.16 confirm this observation, as stronger Ge signal was detected for the nucleation and growth derived sample compared to the single potential derived sample. The stronger Si peak in the EDX collected on the nucleation and growth sample compared to the single potential sample is possibly due to the deep cracks in that sample, allowing access of the electron beam to the substrate through the cracks. A small Cl peak is observed in both films. The total charge passed in each case matches with the EDX analysis, as the charge passed in the two systems was 0.063 and 0.084 C suggesting thicknesses of 354 and 473 nm for the single potential and nucleation and growth respectively (Table 1). The actual thickness from dried electrolyte is presumably close in value to the estimated ones from the charge referring back to the SEM measured thickness for a sample deposited under similar condition for 20 minutes (Figure 4.11) and the measured thickness matched the estimated one from the charge passed during the deposition. Hence we can say for similar ED setup and bath compositions, the charge is mostly utilized in Ge^{+2} /Ge^0 reduction.

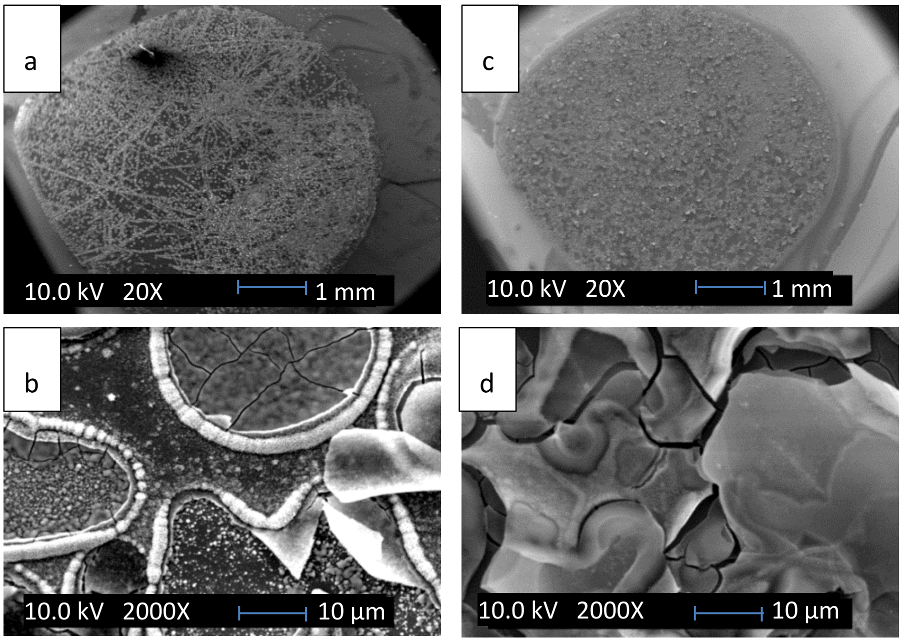

Figure 4.15 SEM images for Ge films deposited from [^{n}Bu$_4$N][GeCl$_3$] in DCM on TiN (4 mm diameter circle), at a constant potential of -1.7 V for 2 h (low and high magnification a, b) and at a nucleation potential of -1.7 V for 5 ms, and then the deposition growth was continued to complete the 2 h at -1.18 V (low and high magnification c,d).

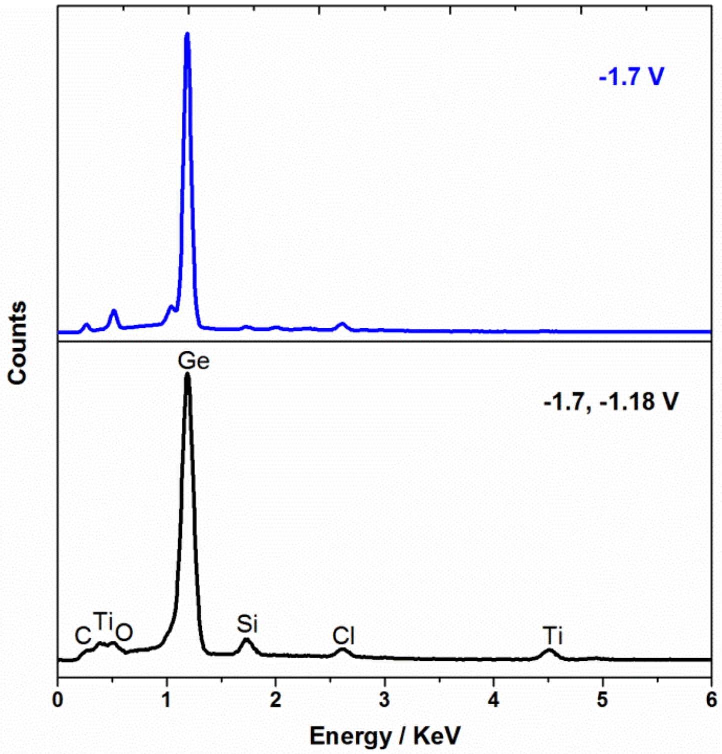

Figure 4.16 EDX spectra for Ge films deposited from dried [^{n}Bu$_4$N]Cl in DCM on TiN (4 mm diameter circle), at -1.7 V (blue) and at -1.7 for 5 ms and -1.18 V for the rest of deposition duration (black). The films were deposited for 2 h.

Generally, Ge films produces from the nucleation and growth method have surfaces consisting of deep cracks, which show thicker layers compared to the single potential derived films. Thus better adhesion is expected in the former method. EDX analysis results indicated thicker Ge layers in the case of nucleation and growth over the single potential deposition method in films produced over the same deposition time and under same conditions.

4.3.3 Ge electrodeposition using surfactants

Seeking improved adhesion between the deposit and the substrate, modifications to the Ge solution by adding the surfactants cetyl trimethyl ammonium bromide (CTAB) and oleylamine (OAm) were trialled. CTAB is a cationic surfactant, widely used in nanomaterial fabrications as a capping agent. CTAB can influence the crystallite size, reduce roughness and promote more uniform particle growth, even sometimes controlling the shape of the nanoparticles.[161-164] In electrochemistry CTAB has been used to assist the production of gold atomic clusters electrodeposited from aqueous electrolyte.[165] CTAB is also widely utilised as templating agent to produce mesoporous template structures.[39, 166, 167] Oleylamine exhibits a number of exceptional properties as a surfactant in nano-particle fabrications, the properties includes high boiling point, low cost, feasibility to form complexes at intermediate temperature which facilitate the decomposition process in nanoparticle formation, and finally OAm is liquid at room temperature.[168, 169] OAm has been used in the synthesis of crystalline Ge nanowires and nanoparticles, in the utility of reducing agent, binding ligand and solvent.[170-172]

The effect of adding the surfactants to the electrolyte was studied. Figure 4.16 shows CVs for Ge species on the glassy carbon (GC) and TiN substrates in the presence of each CTAB and OAm. The observations from the CVs on GC indicate shifts in the peak potential associated with the Ge^{+2} reduction to Ge^{0} (Figure 4.17 peak A), to less negative potentials in the presence of both CTAB and OAm. The CVs on TiN, however, show a distinction between the CTAB and OAm voltammograms, in the former the reduction peak potential is similar to what was obtained for standard Ge electrolyte composition, but in the latter a shift in the peak to more negative potential was found. This suggests that OAm binds strongly to the TiN surface. Consequently the electrodeposition is inconvenient using OAm added electrolyte, due to the requirement to use a more negative potential. The TiN CVs are completed with a nucleation loop in both cases, hence electrodeposition is expected. It can be noticed that in the CV with OAm the reduction peak with decreased intensity still remains on the subsequent scans, suggesting less Ge on the surface from the initial scan hence the passivation layer of Ge on the surface is not fully produced.

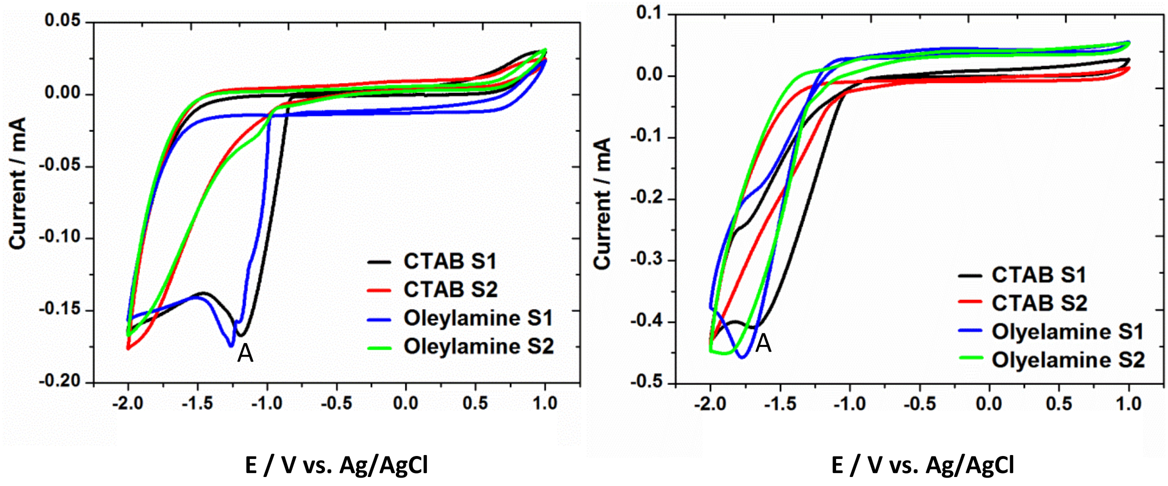

Figure 4.17 Voltammetry of 10 mmol dm^{-3} [^{n}Bu$_4$N][GeCl$_3$] containing 10 µmol dm^{-3} CTAB (black and red lines) or 15 µmol dm^{-3} oleylamine (blue and green lines) in 0.1 mol dm^{-3} [^{n}Bu$_4$N]Cl in DCM vs. Ag/AgCl reference electrode, using potential window of -2, 1 V and the scan rate of 50 mV s^{-1}on GC (left) and TiN (right) electrodes, S1 and S2 indicate scans 1 and 2.

The overpotentials employed in these experiments are selected with regards to Ge^{+2} reduction peak on the associated CV experiments. The CA trends for OAm and CTAB derived electrodepositions (Figure 4.18) share similar characteristics, the current-time transients show a gradual decay in current with time, producing a curved chronoamperogram rather than the steep line observed in the additive free experiments, in which the current decay was sharper. Total charge passed in the ED is 0.259 C in OAm added case and is 0.211 C, leading to estimated thicknesses of ~1.45 and ~1.19 µm respectively.

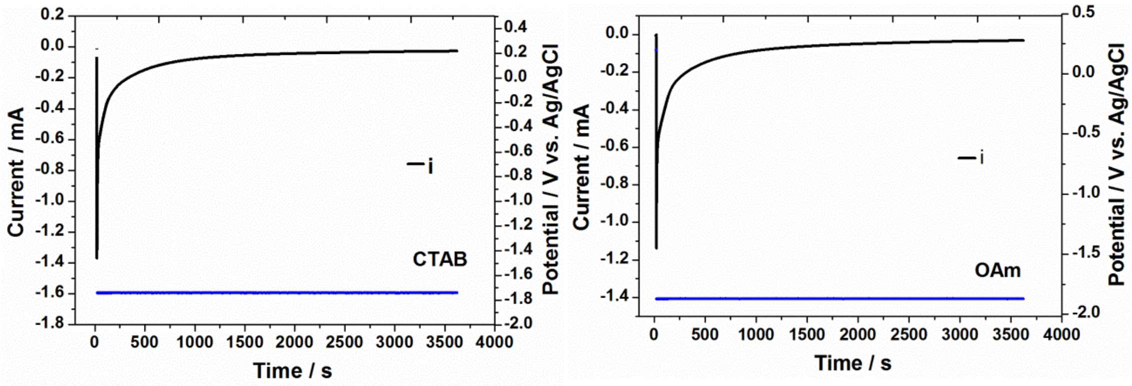

Figure 4.18 Chronoamperometric plot for Ge deposited from [^{n}Bu$_4$N][GeCl$_3$] in DCM on TiN (4 mm diameter circle), using dried [^{n}Bu$_4$N]Cl at -1.72 V, CTAB added to the electrolyte (left) and -1.87 V with oleylamine added to the electrolyte (right), the deposition duration was 1 h. The black line is the current response and the blue line is the potential applied in the deposition.

SEM images (Figure 4.19) show cracked and peeled surfaces for the films, indicating that the adhesion force between the deposit and the substrate is not increased by using surfactants. The films deposited from OAm, appear less thick compared to the CTAB derived ones. It exhibits a bubbly surface, this may be due to electrolyte decomposition, owing to the more negative potential necessary for the deposition.

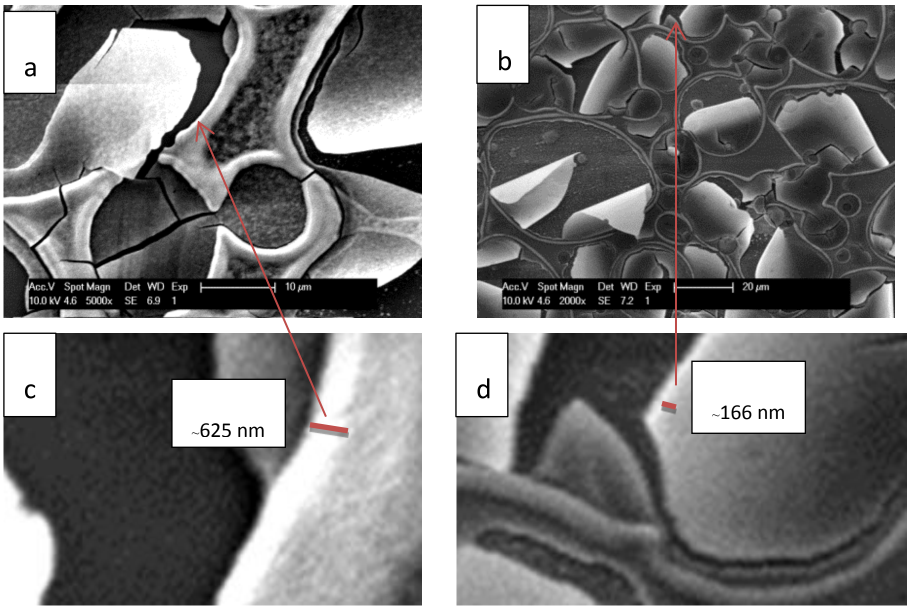

Figure 4.19 SEM images for Ge films deposited from [^{n}Bu$_4$N][GeCl$_3$] in DCM on TiN (4 mm diameter circle), (a) at -1.72 V from CTAB added electrolyte, (b) at -1.87 V from olyelamine added electrolyte, estimated thickness of peeling layer from an expanded region of a (c), and the estimated thickness of peeling layer from an expanded region of b (d).

The morphology of Ge produced with CTAB contained cracks in the place of peeled patches, indicating layer thickening. An estimation of the thickness of the peeled layer on the SEM micrographs was done by zooming in the cracks shown in Figure 4.19 c and d, the thicknesses were found to be roughly 625 and 166 nm peeled layers on the surface of CTAB and OAm derived Ge respectively. This outcome confirms the possibility that some of the charge passed in the process is utilised in processes other than Ge reduction.

4.3.4 Ge electrodeposition on TiN foil and pre-heated silica sputtered TiN on silicon substrates

The surface of the TiN substrates used in this work is smooth due to the PVD process used to produce them. A rougher surface was obtained by heating titanium metal foil in ammonia at 1100 °C. The voltammogram on these flag-shaped TiN electrodes is missing any reduction peak, but a nucleation loop observed in every CV recorded on this type of electrode (Figure 4.20 a). On the basis of these CVs the reduction of Ge ions will occur at a very cathodic overpotential, so to avoid electrolyte breakdown, a nucleation and growth approach was followed using a high nucleation overpotential for 5 ms, and then shifting the potential to a value around the onset potential for Ge reduction on the CV to continue the film growth. Although both sides of the TiN foil were exposed to the electrolyte, most Ge deposition has occurred on the side facing the reference and the counter electrodes. The current -time transient shows continuous Ge deposition at a steady rate, similar to the experiments with as-purchased [^{n}Bu$_4$N]Cl, thus the deposition was accompanied by a rapid drop in current to a steady state of small current of a value close to zero (Figure 4.20 b).

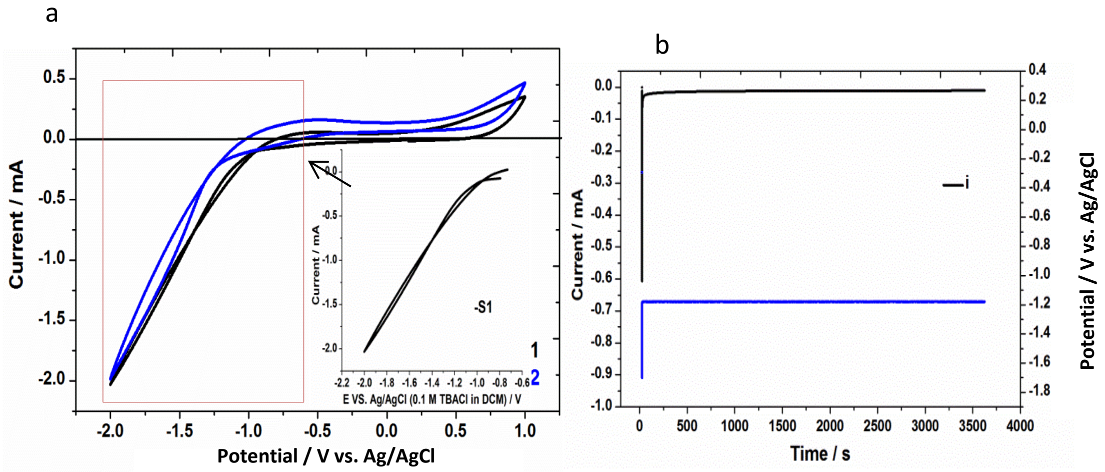

Figure 4.20 Voltammograms and chronoamperograms of 10 mmol dm^{-3} [^{n}Bu$_4$N][GeCl$_3$] in 0.1 mol dm^{-3} [^{n}Bu$_4$N]Cl in DCM on flag shaped TiN foil (1 cm^2) (a) is the CV with the cathodic scan on scan 1 showing a nucleation loop and (b) is the current-time transient at the potential -1.95 V for 5 ms then followed y -1.2 V for 1 h. The black line is the current response and the blue line is the potential applied in the deposition.

Adhesion of the deposit on the substrates surface is one of the issues associated with Ge electrodeposition on TiN substrates. Deposition on TiN foil which exhibit a rougher surface compared to the smooth TiN surface used over the chapter has resulted in better adhered and thicker film, determined from the SEM and EDX analysis, which will be covered in the following sections. Exchanging the TiN substrate by TiN foil demonstrates that changing the nature of the substrate is one of the key parameters in the process. As a significant enhancement in adhesion between the deposit and the substrate has been developed in Ge ED process on TiN foil, determined from the SEM examination on the produced Ge on the TiN foil (Figure 4.22 a, b).

Forming a very thin layer of oxidised TiN may provide a TiN surface with better nucleation sites for Ge, and hence better adhesion. Accordingly to obtain surface oxide, the substrate silica sputtered TiN (SSTiN) on silicon were heated in air. Heat treatment on similar TiN electrode surface has been done by Robertson et al. during the process of surfactant removal from mesoporous SiO$_2$ template grown on TiN substrate. [173] In their work TiN was heat treated at various temperatures and tested for the uncompensated solution resistivity and charge transfer resistance, the result from their study has revealed the rise of surface conductivity problems if the films are heated at temperatures exceeding 375 °C.[173] Comparably, the TiN electrodes in this work were heated in air at 350 °C prior the electrodeposition process. Increased dielectric property on the TiN surface by forming an oxide layer is recognised by other researchers too.[174]

CV experiments on the pre-heated silica sputtered TiN on silicon electrodes (Figure 4.21 a) under the same electrochemical condition, as in the previous experiments, exhibit a reduction peak

(Figure 4.21 a peak A) for Ge^{+2} ion at a remarkably smaller cathodic potential of -1.47 V compared to the untreated SSTiN on Si which always have been around -1.6 V. Thus the ED is expected to be easier. Figure 4.21 b, shows the current-time transient for Ge deposited on pre-heated SSTiN on silicon. From the CV, it was allowed to obtain the ED at relatively low cathodic potential, thus a fixed potential of -1.5 V was selected in the deposition. The current-time transient has a shape fairly similar to that recorded the ED on TiN foil, having the characteristic of sharp reduction in current with time. The charge passed in the Ge electrodeposited on TiN foil and pre-heated SSTiN on silicon was 0.839 and 0.0638 C suggesting thicknesses around 2.15 µm and 359 nm (table 1)for the Ge on TiN foil and pre-heated TiN on silica respectively.

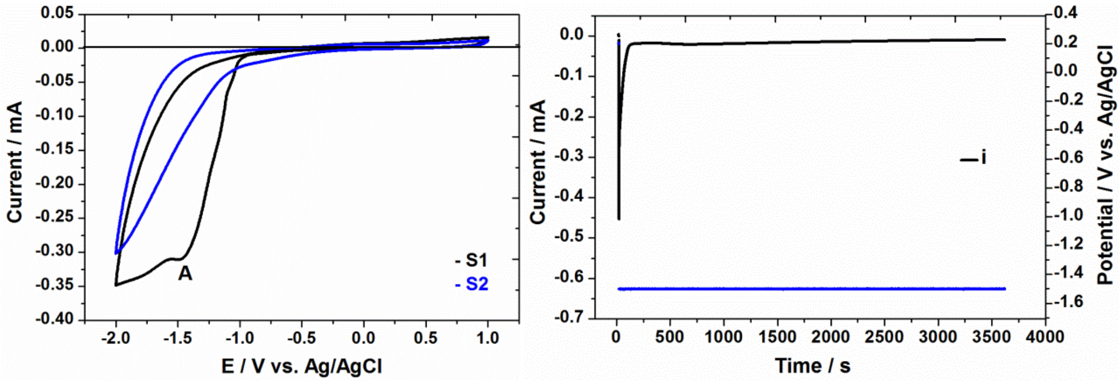

Figure 4.21 Voltammograms and chronoamperograms of 10 mmol dm^{-3} $[^nBu_4N][GeCl_3]$ in 0.1 mol dm^{-3} $[^nBu_4N]Cl$ in DCM (a) is the CV on pre-heated SSTiN on silicon electrode (4 mm diameter circle), and (b) is the current-time transient on the pre-heated SSTiN on silicon electrode (4 mm diameter circle), at -1.5 V for 1 h. The black line is the current response and the blue line is the potential applied in the deposition.

The morphology of Ge on TiN foil and on the heated SSTiN on silicon was examined by SEM (Figure 4.22), uniform relatively thick films were obtained in the both cases. The Ge film on the TiN foil showed a thick flaky deposition. From the SEM on Ge deposited on pre-heated SSTiN on silicon substrate, circular islands, likely to be related to the formation of bubbles during the ED process, are a characteristic of the film surface. This feature is shared in most of Ge films in this system, barring in this distinct film the surface is free from any peelings besides the appearance of cracks, the adhesion to the substrate is in good condition. EDX spectra collected for the deposits (Figure 4.23), show stronger Ge signal from the Ge deposited on TiN foil with respect to the substrate, with obvious lower Cl content, however the Si:Ge atomic percentage ratio the film on heated TiN foil is 0.22:1 and by referring to the plot in Figure 4.7, the thickness of the film is expected to be around 300 nm. As for the TiN foil Ge this ratio is not possible, hence we only rely on the Ge At% from the EDX which is 41.24. Comparing Ge EDX intensity with the sampling depth estimation from Castaing's formula and altogether with the plot in Figure 4.7, the thickness for Ge in here and in the previous studied Ge films always show values of orders of half the sampling depth.

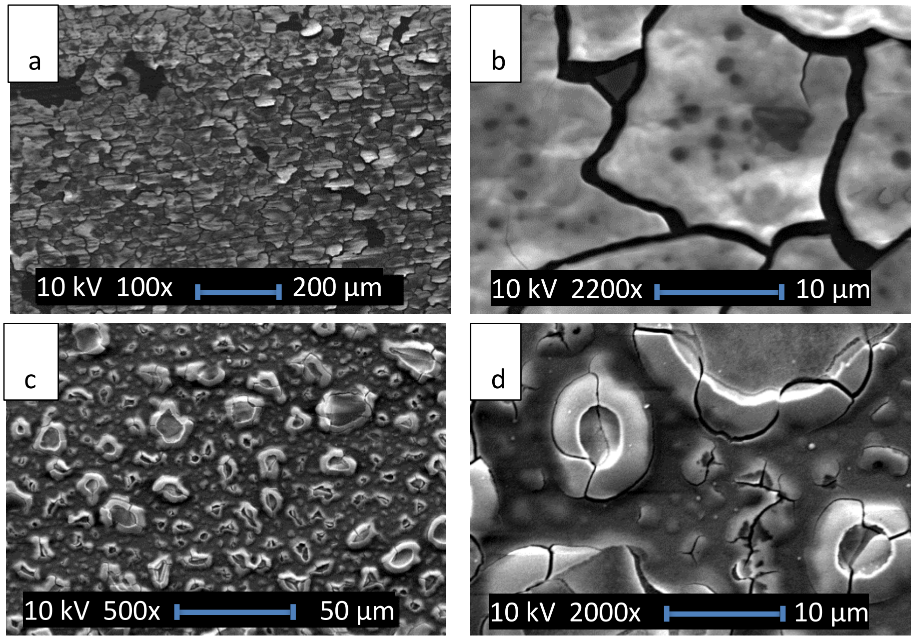

Figure 4.22 SEM images for Ge films deposited from [^{n}Bu$_4$N][GeCl$_3$] in DCM on flag shaped TiN (1 cm^2) electrode at the nucleation potential -1.95 V for 5 ms and growth potential -0.94 V, low resolution (a) and high resolution (b), and at -1.5 V on pre-heated SSTiN substrate on silicon (4 mm diameter circle) low resolution (c) and high resolution (d). The deposition duration was 1 h for the two films.

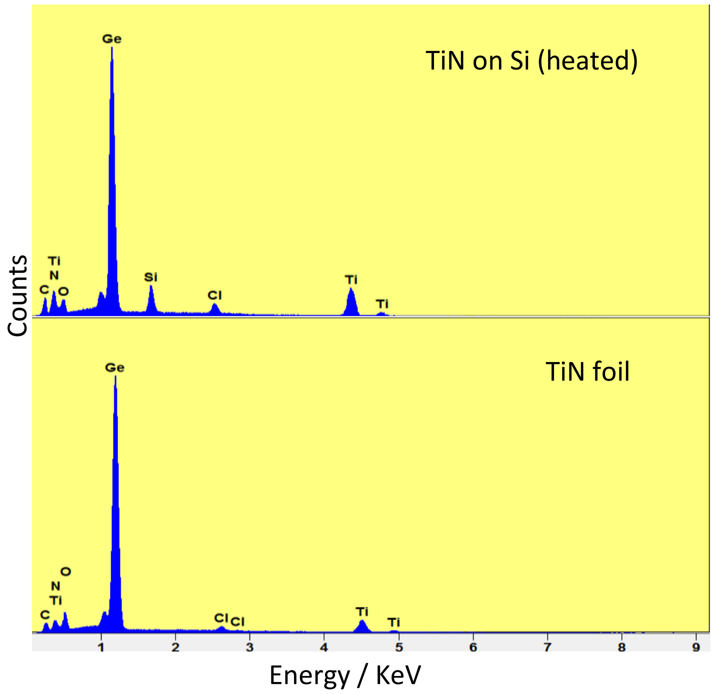

Figure 4.23 EDX spectra for Ge films deposited from [^{n}Bu$_4$N][GeCl$_3$] in DCM on pre-heated TiN (4 mm diameter circle) at -1.5 V for 1 h (top spectra), and on TiN foil (1 cm^2) at the nucleation potential -1.95 V for 5 ms and growth potential -0.94 V for 1 h.

From the examinations we deduce a significant enhancement in the thickness, morphology and adhesion of Ge when deposited on TiN foil. Presumably the ammonia calcined TiN surface performs as a better growth surface for Ge deposition compared to the SSTiN on silicon. Thicker, more uniform and highly adhered Ge deposit was achieved by pre heating the substrate at 350 °C in air. Thus oxides may make good substrates for Ge electrodeposition in future.

4.3.5 Crystallisation by annealing, SEM, EDX, XRD and XPS analysis

The electrodeposited Ge films are amorphous as deposited, Figure 4.24 shows the grazing incidence XRD pattern collected for an as-deposited Ge film, the broad features in the pattern indicates the amorphous structure or may be a mixture of amorphous and some nanocrystalline Ge. To obtain crystalline films, which allow us to further study the microstructure of the deposits, some were annealed in an inert atmosphere. Initially the annealing process was under vacuum and annealing temperatures between 500 - 800 ° C were tested. After annealing films showed no sign of crystalline Ge phase and visually most of the material had fallen off, hence the same process under Ar atmosphere was tested. The films were characterised using SEM, EDX, XRD and XPS.

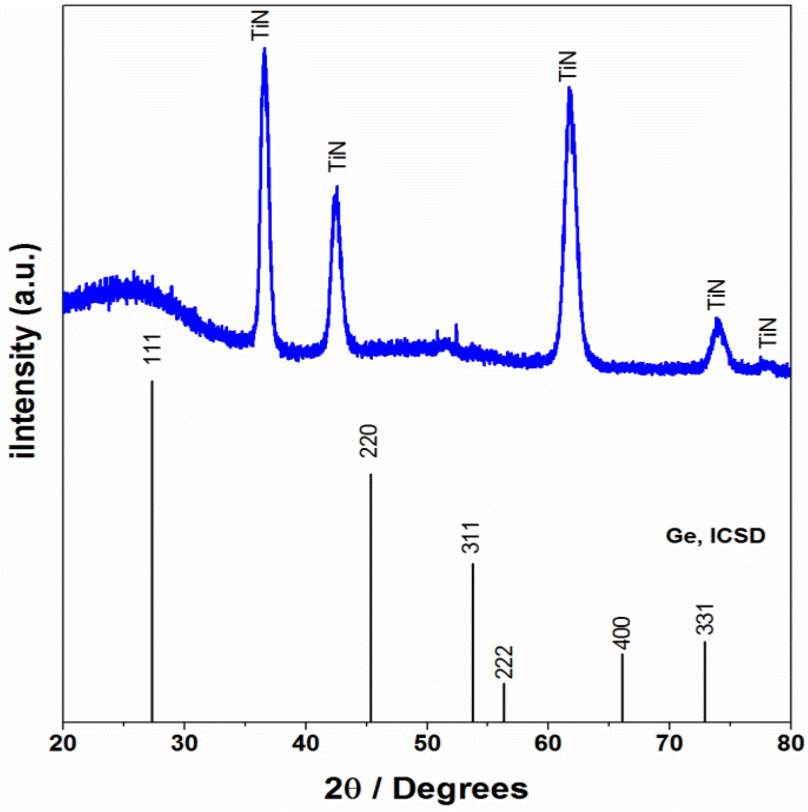

Figure 4.24 XRD pattern of 1° grazing incidence angle for as-deposited Ge electrodeposited on TiN from as-supplied electrolyte at -1.76 V for 20 min (b).

SEM images (Figure 4.25) for annealed Ge films obtained from as-supplied electrolyte indicate almost no Ge on the surface, grey spots on the surface are possibly Ge particles. The films shown in Figure 26, obtained from dried electrolyte exhibit patches of material on the surface, which are likely to be the crystalline form of Ge. The oleylamine derived Ge had peeled surface which appear to be the TiN surface after the Ge is fallen from and the TiN layer delaminated. In the case of Ge films produced with CTAB a larger part of the surface is covered with patches of the deposit compared to Ge from dried electrolyte, and the patches appear to be thicker. The area covered with the deposits remaining, and the thickness of the layer, are better in the film electrodeposited on the pre-heated TiN. TiN foil offered a good adhesion of the deposit to the substrate, the SEM image for the film after the annealing indicates a homogeneous layer on the surface relative to the Ge on the other TiN surfaces or from the electrolyte modified experiments (Figure 4.27). EDX spectra on some of the films show similar results to the observations from the SEM images, Figure 4.28 is the EDX of some of the films in Figure 4.25-4.27. No Ge was observed in the film from as-supplied electrolyte and a small amount of Ge (1.01 At. %) in the film from dried electrolyte. EDX results on the films from CTAB added electrolyte and on the pre-heated TiN substrate exhibit Ge peaks, the intensity of the peak and the quantitative results indicates higher Ge on the CTAB added film (2.43 At. %) compared to the one on the heated substrate (1.34 At. %). This result is unlike the SEM micrograph on the same film in which larger deposit is observed on the surface, the low Ge from EDX may indicates a thinner layer of Ge on the surface compared to the CTAB derived film.

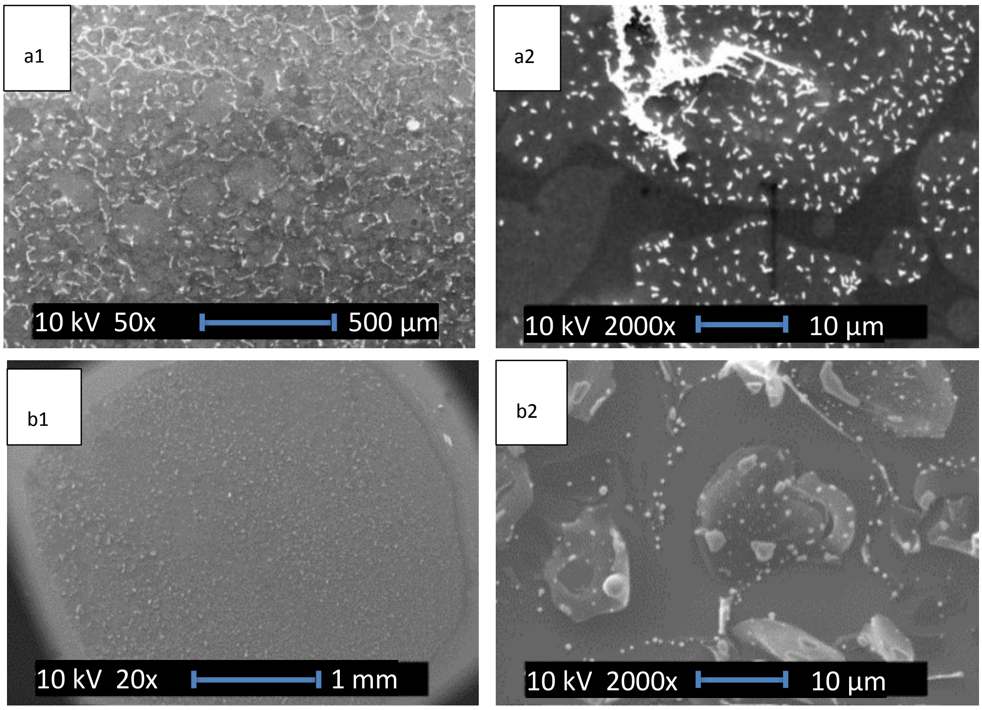

Figure 4.25 SEM on annealed Ge films at low (left) and high (right) magnification. The samples are Ge at -1.65 V, -1.12 V for 2 h from as-supplied [^{n}Bu$_4$N]Cl (a), Ge at -1.75, -1.2 V for 2h, from dried [^{n}Bu$_4$N]Cl (b).

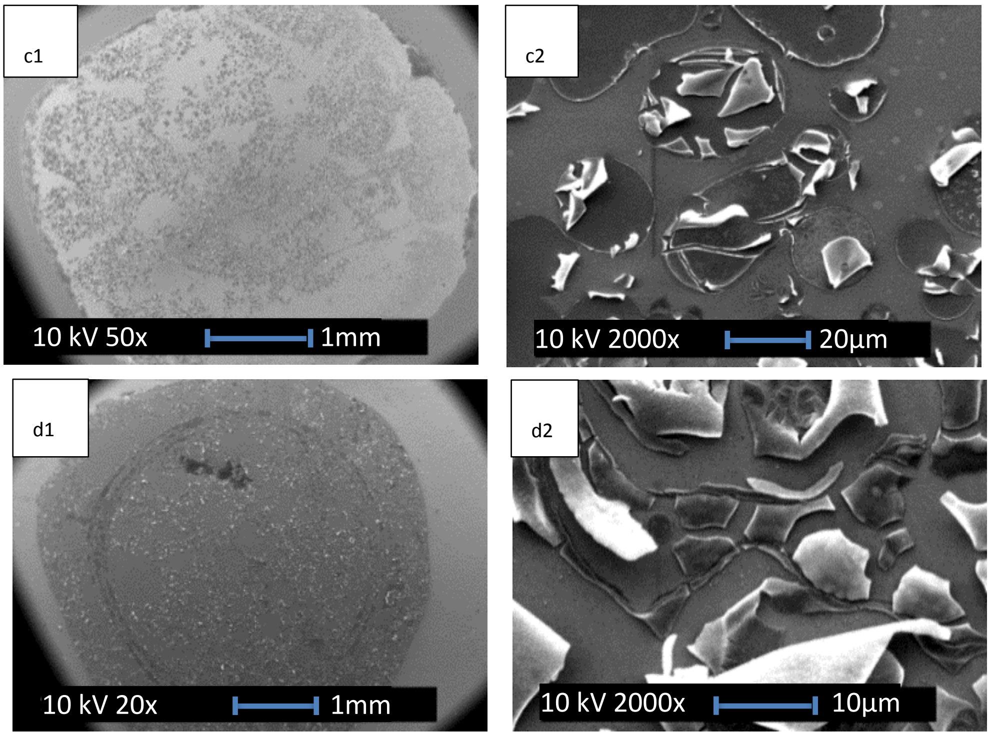

Figure 4.26SEM on annealed Ge films at low (left) and high (right) magnification. Ge at -1.74 V from oleylamine added [^{n}Bu$_4$N]Cl for 1 h (c), Ge at -1.7 V from CTAB added [^{n}Bu$_4$N]Cl for 2 h (d).

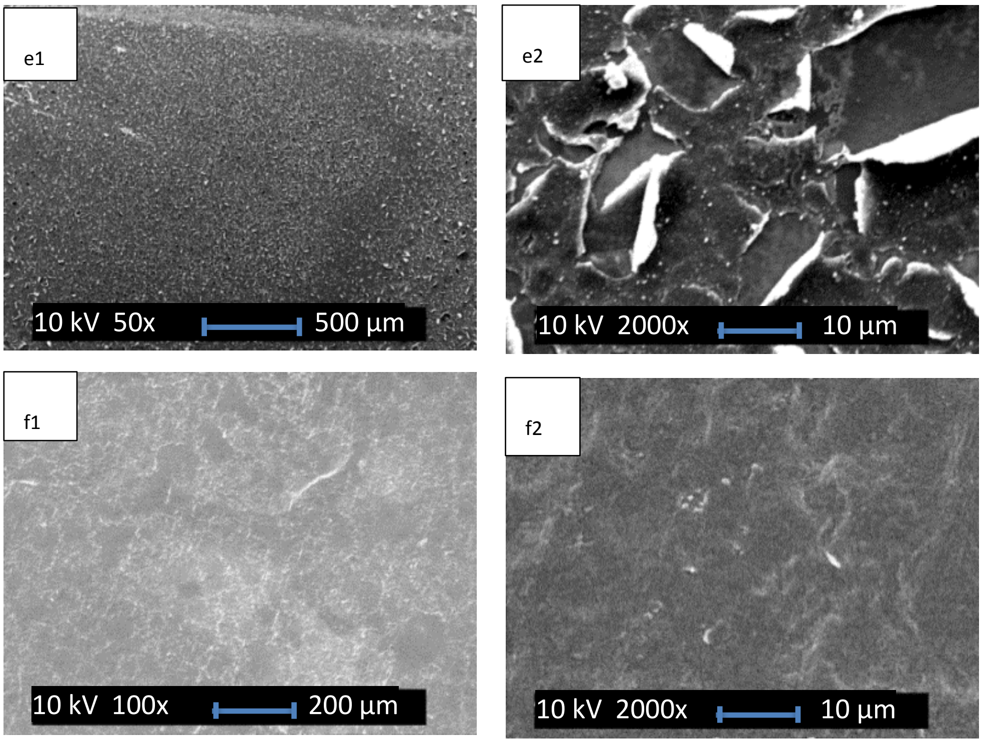

Figure 4.27 SEM on annealed Ge films at low (left) and high (right) magnification. Ge on pre-heated TiN at -1.5 V for 2 h (e) and Ge on TiN foil (1.1 cm^{-2}) at -1.95 V for 5 ms and growth potential -0.94 V for 1 h (f). The films were annealed at 700 °C, under Ar atmosphere for 1 h.

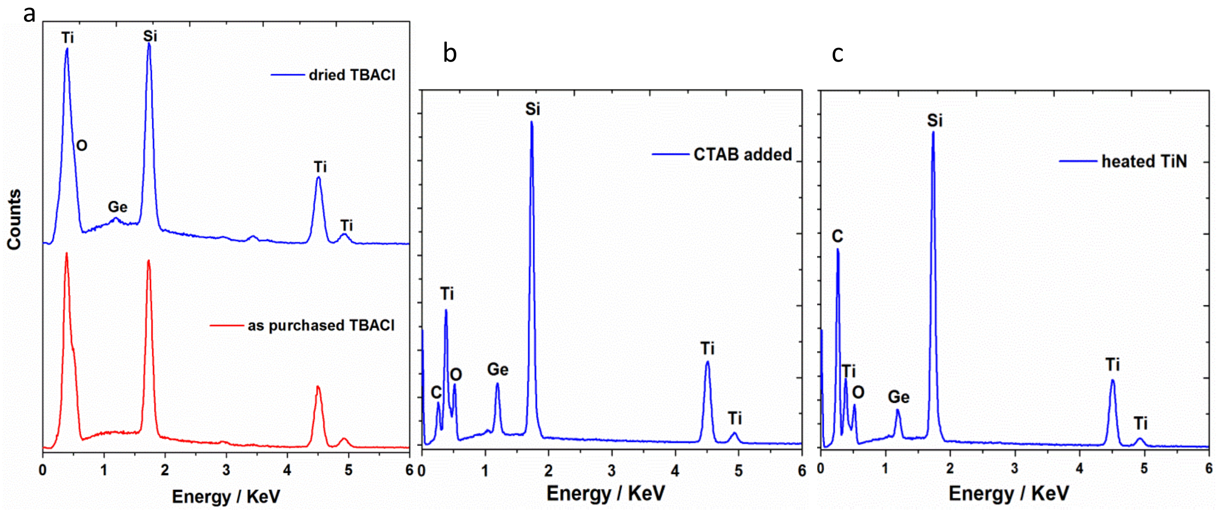

Figure 4.28 (a) EDX spectra for Ge after annealing at 700 °C in Ar, red pattern is for Ge obtained from as-supplied [^{n}Bu$_4$N]Cl at -1.65V , -1.12 V for 2 h and the blue pattern is for Ge obtained from dried [^{n}Bu$_4$N]Cl at -1.75, -1.2 V for 2h (b), Ge obtained from CTAB added dried [^{n}Bu$_4$N]Cl at -1.7 V for 2 h and (c) is Ge obtained from dried [^{n}Bu$_4$N]Cl on pre-heated TiN at -1.5, -1.2 V for 2 h.

In order to obtain best analysis for the peaks in the XRD patterns on the Ge films as-deposited and annealed, XRD patterns were collected on the SSTiN on silicon substrate used in the work, annealed and non-annealed (Figure 4.29, a), peaks associated with the TiN substrate are indicated on the patterns, and peaks at 54° and 56° 2 theta angles matching the positions for Si 310 and Si 311 diffraction peaks respectively, Si 310 is a forbidden reflection for Si and not indicated on the standard patterns of Si found in ICSD, but because the Si substrate used in here is a single crystalline Si, these reflections are seen in the XRD patterns. In face centred cubic (fcc) crystal, the XRD reflection is forbidden if the Miller indices (h,k and l) are a mixture of even and odd numbers, while the reflections with Miller indices (h, k and l) all even or all odd numbers are allowed reflections.[175] The XRD collection geometry of 1° grazing incidence scan in 2 θ range of 20-80° used in this collection was applied in all the other XRD experiments on Ge films. The annealing condition applied to the substrate was at 700 °C in Ar for 1 h.

From the experiments results 700 °C in Ar makes an ideal crystallisation temperature, annealing temperatures below and over 700 °C were applied on the Ge films. Crystalline Ge was not obtainable at up to 650 °C (Figure 4.30), similarly at temperatures above 700 °C crystalline Ge was not observed on the XRD patterns, possibly at those temperatures severe delamination occurred in the films, similar annealing temperature to crystallize Ge was used by others.[176] XRD on the films from as-supplied electrolyte and with oleylamine added electrolytes contain no Ge peaks. While the CTAB added electrolyte has successfully resulted in crystalline Ge at annealing temperature of 700 °C, annealing of Ge layer obtained from a 2 scan CV on TiN in CTAB added electrolyte has resulted in crystalline Ge phase (Figure 4.29). Thus a combination of CTAB in electrolyte and heating the substrates in air prior to the deposition was used to obtain crystalline Ge (Figure 4.30).

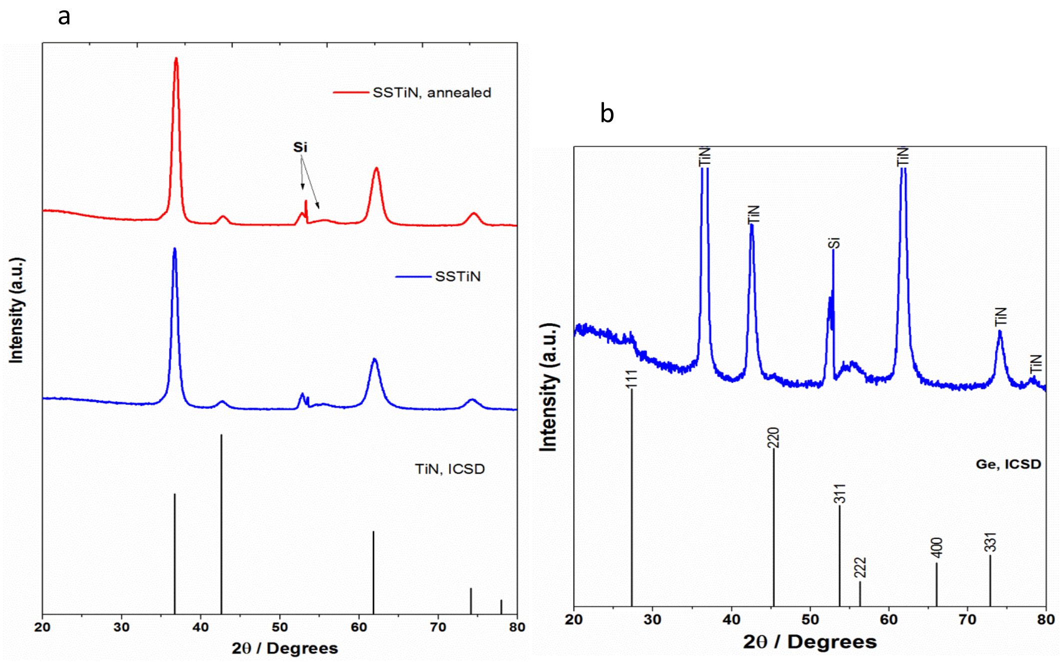

Figure 4.29 XRD pattern for 1° grazing incidence scan on the substrate (TiN) before and after annealing under conditions similar to Ge films (a), and Ge from 2 scan CV on TiN in CTAB added electrolyte, annealed at 700 °C in Ar for 1 h.

The XRD patterns for the successfully crystallised Ge films contain peaks associated with Ge 111, Ge 220 and Ge 311 diffraction peaks raised from the Ge deposit. Peaks for other phases from the TiN and Si substrates are identified on the patterns. The Si 310 and 311 peaks are usually also observed in the XRD patterns for Ge films, no signs for Si 111 reflection with the peak position of 2θ angle at ~28.5°. XRD patterns in Figure 4.29 show crystalline Ge phase in the sample obtained from 30 minute electrodeposition from the CTAB added electrolyte and on the pre-heated TiN. the samples produced from the same electrodeposition time but annealed at lower temperature didn't produce crystalline Ge (red patterns).

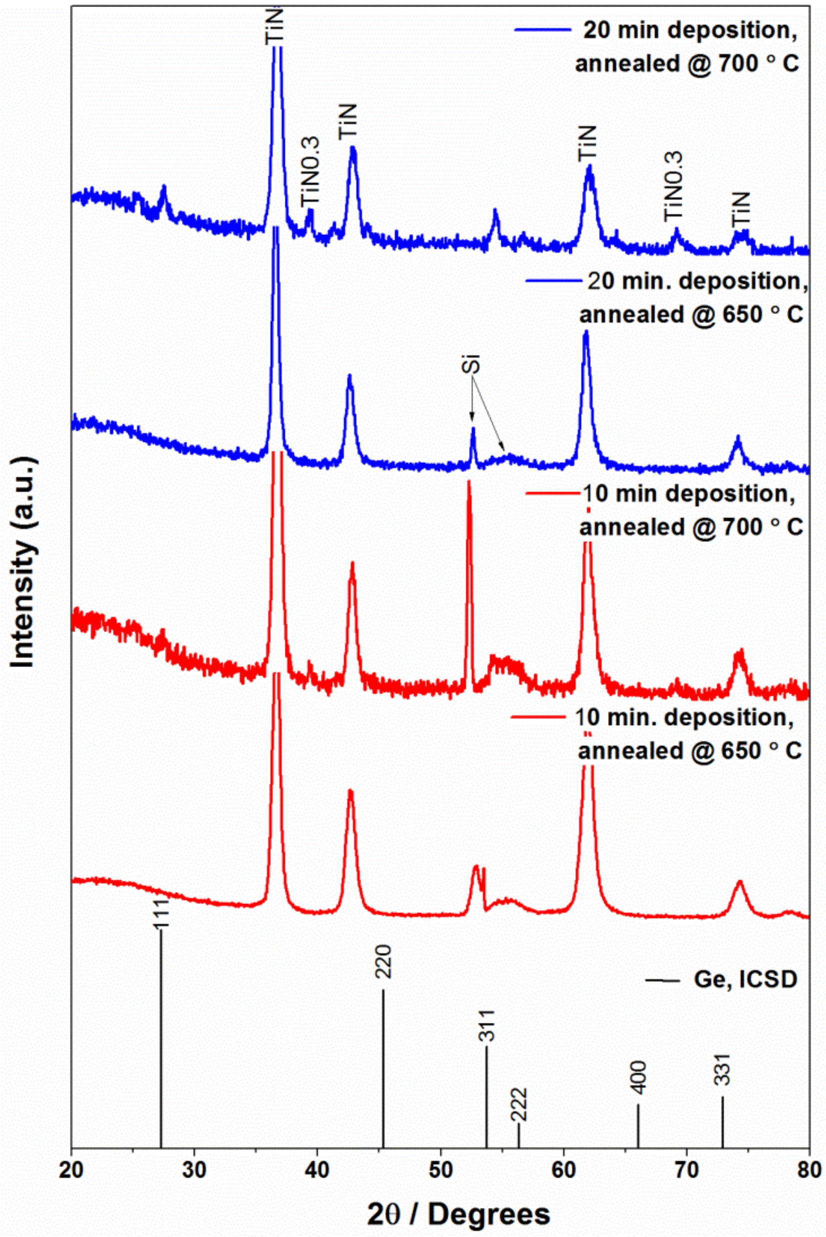

Figure 4.30 XRD on Ge films electrodeposited at -1.85 V from CTAB added [^{n}Bu$_4$N][GeCl$_3$] in DCM, and dried supporting electrolyte [^{n}Bu$_4$N]Cl was used on pre-heated SSTiN on silicon, annealed for 1 h in Ar. The red patterns are for Ge film obtained from 10 minutes deposition annealed at 650 °C (bottom) and 700 °C (top), the blue patterns are for Ge film obtained from 20 minute deposition annealed at 650 °C (bottom) and 700 °C (top).

The best Ge crystallisation was on the film electrodeposited on TiN foil, the XRD on the annealed film in Figure 4.31 exhibited wide peaks for nanocrystalline cubic Ge phase, beside the Ge phase the pattern also contain a further phase of $TiN_{0.30}$ identified using Inorganic Crystal Structure Database (ICSD).[112] This was also present before the Ge was deposited. The TiN foil results indicate that in the case of TiN substrates the adhesion was not that strong to stand high temperature annealing followed in this work. However pre-heating of the substrate at moderate temperature of 350 °C has resulted in a great improvement in the adhesion between the deposit and the substrate. Hence Ge electrodeposition in the CTAB modified electrolyte on an oxide surface would make a promising condition to obtain crystalline Ge from DCM. All the successfully crystallized samples show polycrystalline cubic Ge structure.

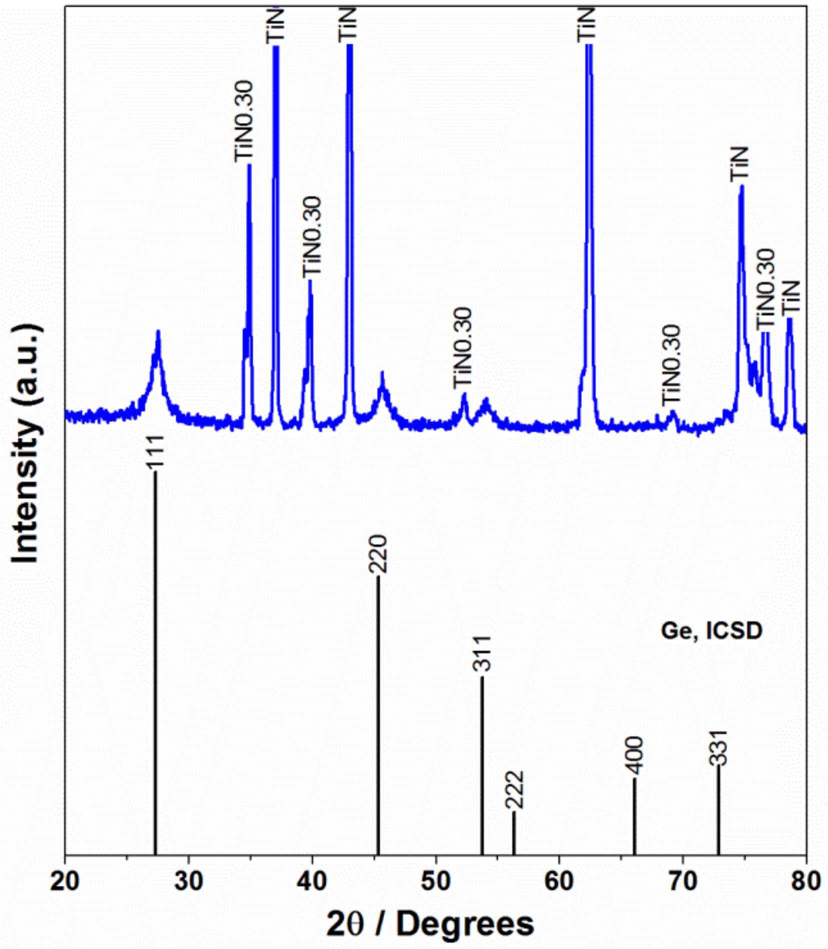

Figure 4.31 XRD pattern for Ge on TiN foil (1.1 cm^{-2}) at -1.95 V for 5 ms and growth potential -0.94 V for 1 h, annealed at 700 °C, under Ar atmosphere for 1 h.

Further characterisation on the electrodeposit was performed using X-ray photoelectron spectroscopy (XPS) to determine the chemical environment of Ge. XPS is a surface sensitive technique offering penetration depth of less than 10 nm.[74] XPS of the element exhibits shifts in the binding energy caused by different oxidation states of the element and different chemical environments.[177] Survey XPS spectra and high resolution data for Ge 3d and Ge 2p orbitals were collected for the as-deposited Ge and the annealed films. Depth profiling was applied for a short time (total etch of 20 s) to access the non-oxide layer of Ge. Although the samples were transported in a N_2 atmosphere to protect them from ambient atmosphere, they needed to be exposed to air to introduce them to the spectrometer so some oxidation could not be avoided. The Ge 3d spectral peak was fitted with an identical doublet peak of asymmetry and Gaussian shape, originated from spin orbit coupling, as the Ge 3d emission is mainly from crystal atoms below the surface.[178, 179] The peak fitting was obtained using Avantage software, doublet peak of

Ge3d spin orbit splitting with Ge 3d$_{5/2}$: Ge 3d$_{3/2}$ peak separation of (0.58 ±0.04) eV and intensity ratio of 0.67 was resolved, with the instrument's sensitivity factors of 0. 767, 0.527 and 1.294 for Ge 3d$_{5/2}$, Ge 3d$_{3/2}$ and the oxide (GeO and GeO$_2$) peaks respectively. Linear and Shirley backgrounds were applied in the fits. The Ge 2p line is the more sensitive Ge line to the maximum sample surface compared to Ge 3d line, due to the low kinetic energy (Ec = 269 eV) for the emitted photoelectrons compared to that from Ge 3d (Ec = 1457 eV).[180, 181] However herein the examined surface is a thin Ge film and the purpose was to identify the environment that Ge is present in, therefore the Ge 3d line was used in the examinations.

An example of the survey XPS is presented in Figure 4.32, the main feature is the Ge XPS peaks, which are Ge2p, Ge3d, Ge3s and Ge Auger peaks. Oxygen and Germanium oxide are observed in the spectra, XPS and Auger peaks for elemental oxygen and XPS peak for carbon element are observed in the spectra, O KLL Auger line is an indication for the degree of surface oxidation.[182] A weak peak of Si2p is identified, because XPS is effective on large area (some mm^2)[74] thus signals from the uncoated substrate region (SiO$_2$ sputtered) were detected. The two peaks at binding energies around 310 and 330 eV are not from the elements under study (unidentified).

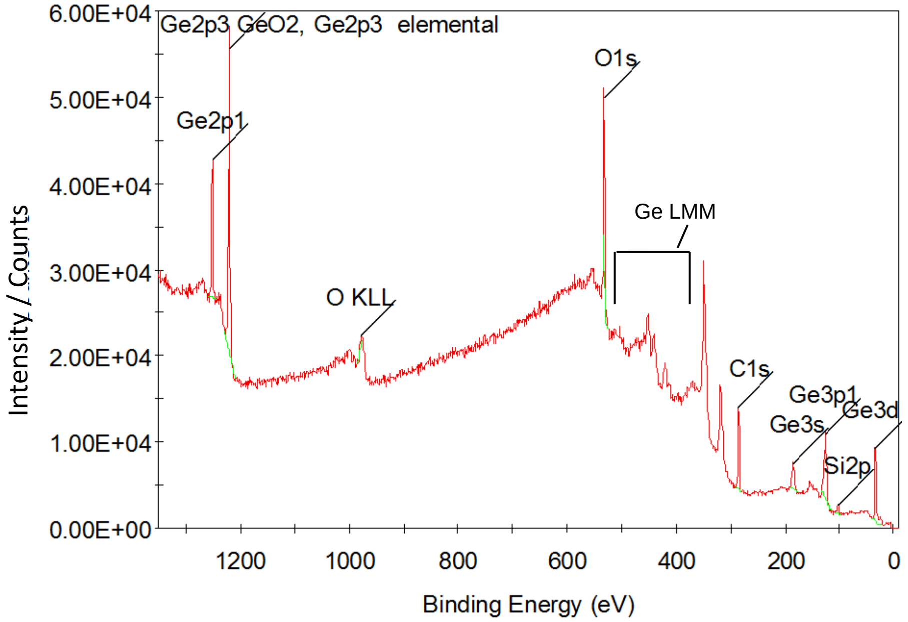

Figure 4.32 XPS survey spectra on Ge electrodeposited on TiN at -1.85 V for 1 h from CTAB added electrolyte.

Ge is a semiconductor hence a charge shift occurs during the photoionization, this charging was corrected using C 1s peak position, however this correction is not absolute. The binding energy (BE) for Ge 3d peak in Ge surface is centred at a range between 29.4 - 30.2 eV in literature.[183-186] Figure 4.33 compares high resolution XPS on Ge 3d for Ge electrodeposited from the CTAB using short and long deposition duration and also compares the spectra for the as-deposited Ge vs. the annealed sample. Ge $3d_{5/2}$ and Ge $3d_{3/2}$ peaks are centred at 28.99 and 29.57 eV in Ge obtained from 5 minutes deposition, a shift in the BE by +1.43 eV from Ge Ge $3d_{5/2}$ indicates Ge 3d line for GeO and a shift by +3.01 eV vs. Ge $3d_{5/2}$ is the Ge 3d line for GeO_2, close values of BE shifts vs. Ge were similarly denoted as germanium oxides as in here.[187, 188]

In Ge obtained from 2 h deposition (Figure 4.33) the Ge $3d_{5/2}$ and Ge $3d_{3/2}$ peaks are centred at 28.83 and 29.47 eV and the BE shifts values with respect to Ge $3d_{5/2}$ responsible for Ge 3d lines of GeO and GeO_2 are +1.38 and +3.28 respectively. GeO_x peaks are more intense compared to the elemental Ge 3d peak in the thinner (5 minutes deposit) film, while this ratio has massively altered in the thicker (2 hour deposit) one. The intensity ratios of elemental Ge $3d_{5/2}$: GeO Ge3d and elemental Ge $3d_{5/2}$: GeO_2 Ge3d peaks are 4.41:0.23 and 8.34:0.12 respectively in the thick Ge, in contrast the ratios are 1.27:0.79 and 0.74:2.12 in the thin Ge film. This determination is expected as the rate of oxidation vs. element amount gets higher as the thickness reduces and oxidation per unit area increases. The main feature in the annealed Ge obtained from 2 h deposition is the Ge dioxide Ge 3d peak at BE of 32.58 eV, a small amount of GeO is present at the BE of 30.82 eV. This result indicates that the film has undergone a great degree of oxidation during the annealing and analysis processes. Since a large amount of the material fell off of the substrate during the annealing process, a larger surface area was exposed to the atmosphere and higher proportion of the deposit oxidised.

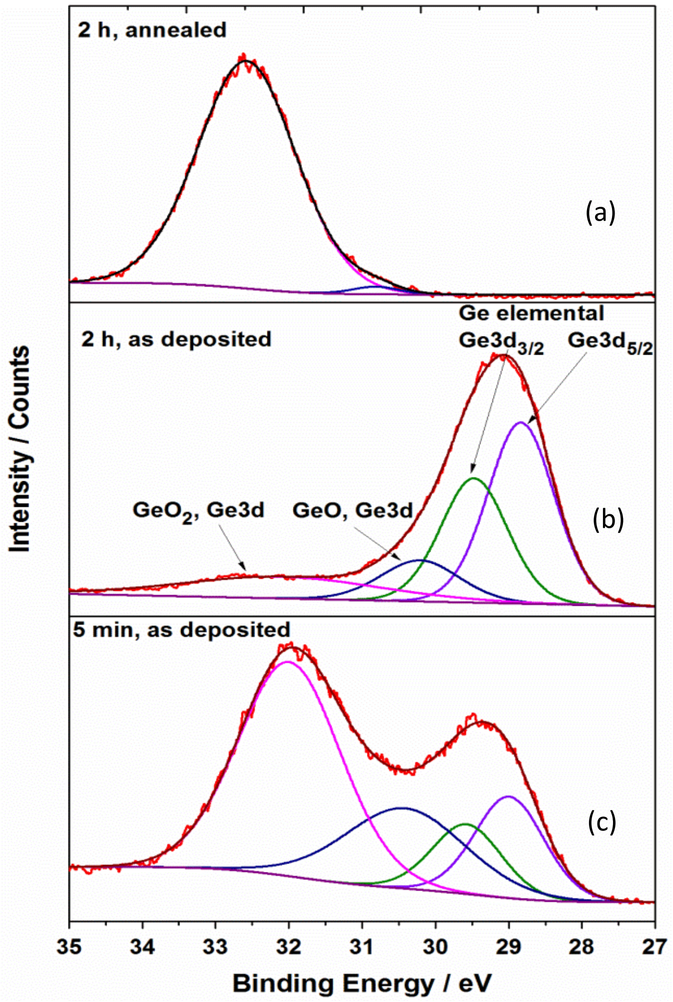

Figure 4.33 Ge3d XPS spectrum for Ge electrodeposited from CTAB added [^{n}Bu$_4$N][GeCl$_3$] in DCM on TiN (4 mm diameter circle) at -1.83V, as-deposited for 5 minutes (a) and 2 h (b) and annealed (at 700 °C for 1 h) for 2 h (c) deposition durations. The raw data (red), fitted with doublet Ge elemental (purple and green), GeO (blue) and GeO$_2$ (pink), the sum of individual peaks (black/wine). Same annotations in graph b apply in graph c.

We observed from XRD analysis that by using CTAB added Ge electrolyte in ED on pre-heated TiN substrate, good adhesion was obtained in the post-anneal films and crystalline Ge peaks were indicated in the XRD patterns. Correspondingly in the XPS analysis (Figure 4.34) a small elemental Ge signal is observed in the Ge films derived using same setup. The as-deposited Ge XPS exhibit elemental Ge 3d line fitted with doublet Ge 3d$_{5/2}$ and Ge 3d$_{3/2}$ at BE of 28.93 and 29.51 respectively, shifts in the BE vs. Ge 3d$_{5/2}$ by values of +1.39 and 3.50 eV consistent with Ge 3d lines for GeO and GeO$_2$ respectively. The XPS on same film after annealing still show a peak for the elemental Ge 3d line, fitted using doublet peak at binding energy (BE) of 29.49 and 30.07 eV for the Ge 3d$_{5/2}$ and Ge 3d$_{3/2}$ respectively, a shift in BE from Ge 3d$_{5/2}$ peak by +1.0 eV indicates Ge 3d peak for GeO.

GeO_2 XPS peaks in the Ge film with high GeO_2 content exhibit shifts by -0.2 and -0.3 eV from the literature value of shift in BE for the GeO_2 XPS peak vs. Ge elemental XPS peak, which is +3.2 eV. In the annealed Ge film deposited from CTAB on pre-heated TiN (Figure 4.34), a shift by -0.4 eV is observed from the literature value. The shifts are possibly in the elemental Ge line, due to oxide/non-oxide interface band bending, similar shifts in Ge 3d XPS origin has been reported by other researchers.[184, 185]

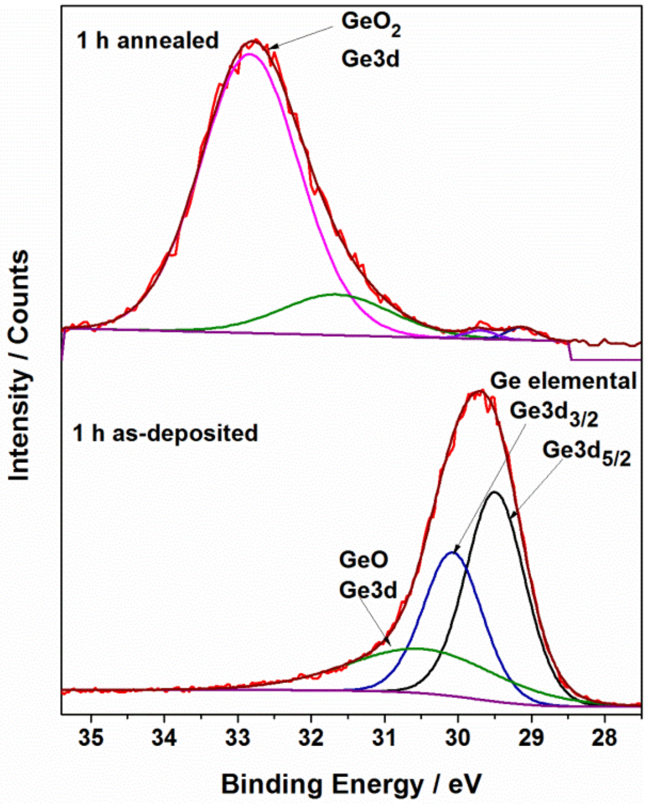

Figure 4.34 Ge3d XPS spectrum for Ge electrodeposited from CTAB added [$^nBu_4N$][$GeCl_3$] in DCM on pre-heated TiN (4 mm diameter circle), at -1.83 V for deposition durations of 1 h, as-deposited (bottom spectra) and annealed at 700° C for 1 h (top spectra). The raw data (red), fitted with doublet Ge elemental (olive and blue), GeO (green) and GeO_2 (pink), the sum of individual peaks (wine).

To examine the deposit's deeper levels, depth profiling by bombarding the surface with Ar ion beam source with the energy of 1 µA at 3 kV was performed. The profile consists of 3 levels of 0, 10 s and a final 10 s etching, resulting in 20 s final etch time. Figure 4.35 is for depth profiling for Ge 3d line on a sample obtained from 10 minute deposition time in CTAB added electrolyte fitted with a doublet originated from Ge $3d_{5/2}$ and Ge $3d_{3/2}$, and a peak corresponding to GeO at BE shifted from Ge $3d_{5/2}$ by +1.32, +1.37 and +1.82 eV in XPS collected after 0, 10 and 20 s etching. As for the GeO_2 the peak is positioned at BE shifted from Ge $3d_{5/2}$ by +2.68 and +2.76 eV the surface is free from GeO_2 after the third (20 s) etch. GeO_2 Ge3d peak as noticed in the samples in Figure 4.33 and 4.34 is shifted, and the shift by ~ 0.5 eV in the depth profiling experiment. By etching the top surface from the sample the oxide layer of GeO_2 gets less and less vs. the elemental peak (Table 2), while the peak originated from GeO gets more intense with etching levels. The peak BE positions for the Ge3d from the three environments and the Ge oxides peak intensity ratio to the elemental Ge are presented in Table 2. In the table a shift in the BE by ~ -0.2 eV with etching time in the Ge 3d line is observed.

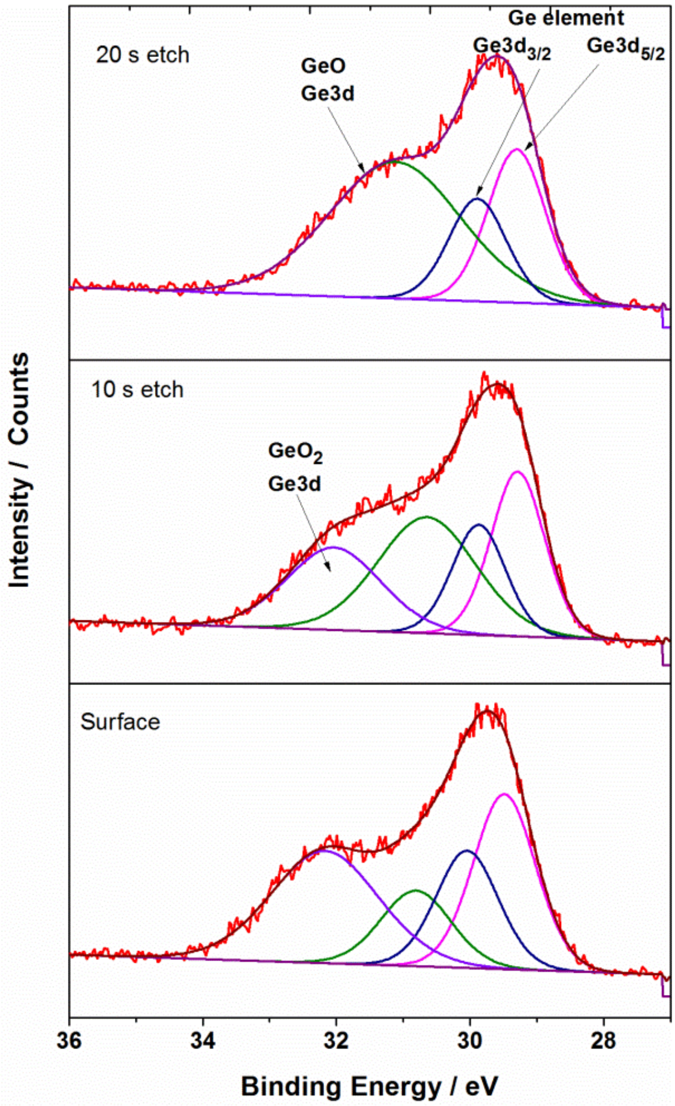

Figure 4.35 Ge3d XPS spectrum (depth profiling) for Ge electrodeposited from CTAB added $[^nBu_4N][GeCl_3]$ in DCM on TiN (4 mm diameter circle), at -1.7 V for deposition durations of 10 minutes, 2 etching levels of 20 s total etch. The raw data (red), fitted with doublet Ge elemental (pink and blue), GeO (green) and GeO_2 (purple), the sum of individual peaks (wine).

Table 2 Parameters from the fit on Ge 3d XPS lines, obtained from the depth profiling in Figure 32.

Etch time (s)	($3d_{5/2}$ / Ge $3d_{3/2}$) BE (eV)	GeO		GeO_2	
		BE (eV)	I GeO : I Ge $3d_{5/2}$	BE (eV)	I GeO2 : I Ge $3d_{5/2}$
0	29.49 / 30.04	30.81	0.30 : 0.70	32.17	0.39 : 0.61
10	29.28 / 29.87	30.65	0.41 : 0.59	32.04	0.33 : 0.67
20	29.30 / 29.89	31.12	0.47 : 0.53	-----	-----

The XPS analysis have indicated the presence of Ge^0, Ge^{+2} and Ge^{+4} on the surface of ED Ge thin films. A higher fraction of oxide was observed on the surface of the very thin (5 min ED) compared to the 2 hour ED Ge films, indicating decreased rate of oxidation by increasing the thickness of the film under such conditions of storage and analysis. The material observed on the surface after the annealing process is fully oxidised or very small proportion is maintained in the neutral oxidation state, which was in the Ge ED from CTAB added onto pre-heated TiN substrate.

The presence of Ge^0 in the XPS recorded on the as-deposited Ge films indicates that the Ge produced from the ED experiments are most likely the elemental germanium, and this is supported by the broad Ge features in some XRD patterns and the weak but sharper features in some patterns post annealing. Surface oxidations were found as a result of air exposure during the annealing and XPS experiments.

4.3.6 XRD on Ge electrodeposited from other systems

Ge thin film electrodeposited in different media from the one applied in this work were crystallized and characterised. This project was part of the supercritical fluid electrodeposition (SCFED) project. My role in this project was investigation into characterisation using XRD analysis and annealing the as-deposited amorphous and amorphous/nanocrystalline films to obtain the crystalline phase. Figure 4.36 show the XRD of Ge film as-deposited and annealed, electrodeposited on TiN (~450 nm thick films of TiN sputtered onto p-type silicon wafers) from 12 mM $[^nBu_4N][GeCl_3]$ and 60 mM $[^nBu_4N][Cl]$ from supercritical difluoromethane (sc-CH_2F_2). The ED was performed in a high pressure stainless steel cell especially designed for SCFED, details have been previously published,[132] Ge was deposited at temperature of 358 K and pressure of ~ 1.9 MPa.[189]

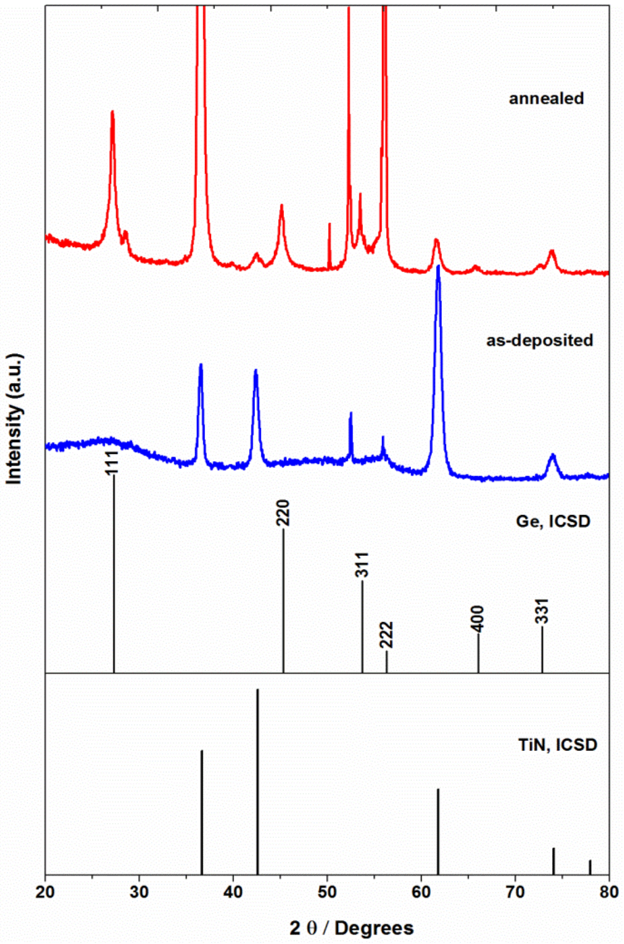

Figure 4.36 XRD pattern for a 1° grazing incidence on Ge electrodeposited on TiN, as-deposited (blue) and annealed at 700 °C under Ar for 1 h (red), from 12 mM [^{n}Bu$_4$N][GeCl$_3$] and 60 mM [^{n}Bu$_4$N][Cl] in sc-CH$_2$F$_2$ at 358 K and ~ 1.9 MPa. The deposition conditions were Epulse = -1.9 V vs. Ag|LaF$_3$ for 100 ms, Edep = -1.5 V vs. Ag|LaF$_3$ for 12000 s.

The XRD pattern for the as-deposited film (Figure 4.37), show a broad hump matching the 2θ positions of cubic Ge XRD pattern of amorphous Ge. The hump is less broad around 2θ angle of Ge 111 reflection (~ 27°), possibly indicating a mix of some nanocrystalline Ge within the amorphous structure. The peak at 2θ angle of 56° is for Si 311, it appears in some of the patterns collected on TiN on silicon substrates depending on the alignment of the sample with respect to the incident beam. Similar to the samples in this work the film was annealed at 700 °C in Ar atmosphere for 1 hour, the whole set of cubic Ge reflection peaks matching the standard Ge pattern from ICSD were detected from the XRD pattern of the annealed sample, showing a successful crystallization.

Electrodeposition of Ge film was on TiN was achieved from 1-ethyl-3-methyl imidazolium triiodogermanium [EMIM][GeI$_3$] and 1-ethyl-3-methyl imidazolium tetrafluoroborate [EMIM][BF$_4$] in sc-CH$_2$F$_2$. [190] The deposition was at temperature of 358 K and under the pressure of 19.1 MPa. The pattern for the as-deposited film contains impurities of GeI$_2$ on a broad feature for a nanocrystaline Ge. The after anneal pattern show sharp peaks in positions matching cubic Ge phase.

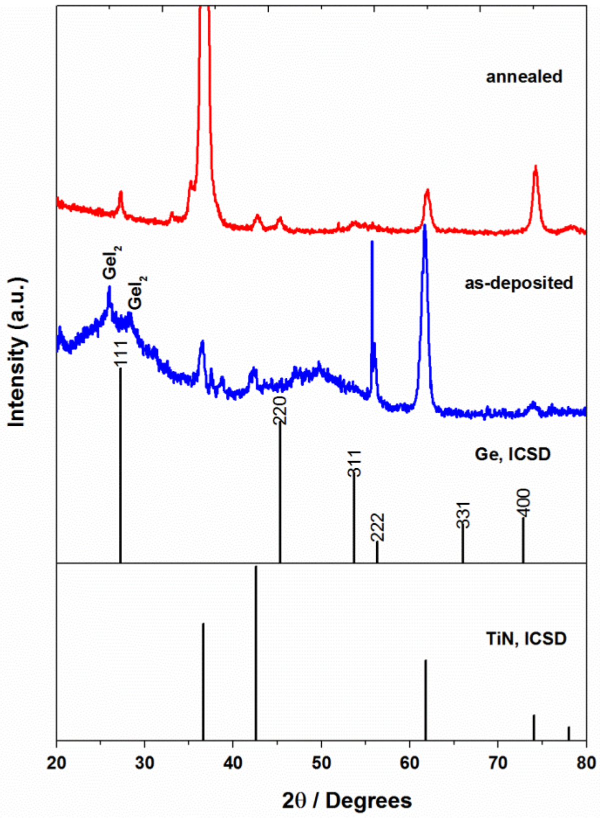

Figure 4.37 XRD patterns of an as-deposited Ge film (blue) and the same film after annealing at 700 °C in argon (red). ED from 16 mm [EMIM][GeI$_3$] and 60 mm [EMIM][BF$_4$] in sc-CH$_2$F$_2$ at 358 K and 19.1 MPa, with Edep= -1.05 V vs. Ag/LaF$_3$ for 4000 s.

Ge electrodeposited from sc-CH$_2$F$_2$ using the precursor used in our work ([^{n}Bu$_4$N][GeCl$_3$]) or [EMIM][GeI$_3$] precursor, share the same nano-crystalline Ge with the films produced in our work, indicated from the broad features on XRD patterns collected on the films as-deposited which matches the cubic Ge peak positions. While post annealing XRD patterns for the SCFD derived films show stronger Ge peaks compared to the films in this work (liquid DCM derived). This result indicates that the SCFED derived Ge films exhibit better adhesion to the TiN substrate during the high temperature annealing. Owing to the distinguished properties such as low surface tension, low viscosity and wide potential window in SCF electrolyte,[39] make it an ideal media for electrodeposition.

4.4 Conclusion

Ge thin films were deposited on TiN on silicon substrates in a potentiostatic electrochemical deposition (chronoamperometry). XRD and XPS analysis indicates that the electrodeposits are of elemental Ge. Broad features in the XRD on as-deposited films matching 2θ positions of cubic polycrystalline Ge indicated amorphous, mixed amorphous and nanocrystalline structured Ge. The high resolution XPS of Ge 3d peak has indicated the presence of elemental Ge in all as-deposited films along with the presence of oxidised Ge peaks. The ratio of oxide/element quantity estimated from the peak intensity ratios, was decreased by increasing the thickness of the Ge layer. While in the post-anneal films, Ge 3d peaks for Ge oxides were observed except in the case of CTAB added on pre-heated substrate, on which some elemental Ge 3d peak was also observed.

Seeking better adhesion especially during the crystallisation process, developments in electrolyte composition by adding surfactants and in the nature of the substrates surface were applied. The XRD on the annealed Ge ED on TiN foil (heated in ammonia) exhibited set of strong broad peaks of nanocrystalline Ge. Peaks for crystalline Ge were observed on the XRD pattern on a thin layer of Ge produced from CTAB added electrolyte using CV on TiN. Also SEM and EDX on the post annealed films, has shown improved adhesion in the CTAB derived Ge films and the films deposited on pre-heated TiN substrate. Successful crystallisation was then obtained for a set of Ge electrodeposited from CTAB added electrolyte onto pre-heated TiN substrate.

The XRD on as-deposited Ge films produced by SCFED on TiN from the same precursor in sc-CH_2F_2, exhibit broad features matching Ge cubic phase. After annealing under similar condition and the same temperature of 700 °C as applied to other films, a high degree of crystallisation was achieved and the XRD has shown strong peaks of Ge phase. SCF deposited Ge from [EMIM][GeI_3] using supporting electrolyte [EMIM][BF_4] in sc-CH_2F_2, also showed nice crystalline Ge after annealing, discovered by XRD.

Chapter 5 Electrodeposition and characterisation of Sn

5.1 Introduction

Tin is a non-toxic, highly crystalline, soft element that exhibits high stability in moisture and air. Tin exists in several allotropes depending on the temperature and pressure, the commonest are α-Sn and β-Sn, the latter is the most stable Sn form at room temperature with tetragonal crystallographic structure and is a silver white semi-metal. The α-Sn can be obtained at temperatures below 13.2 ±0.1 °C,[191] it has a grey colour and is semiconducting, having a diamond cubic crystal structure. Other high pressure phases of tin, namely γ-Sn and σ-Sn are obtainable at particular conditions of temperature and pressure.[191, 192]

Tin is widely used in oxidation and corrosion prevention coatings often replacing chromium or nickel, and is also used in decorative platings due to its silvery white colour.[193-195] Tin has been used as cheaper substitute for gold in electrical connectors in many appliances, despite the limited protection against fretting corrosion for this element, thus it is more widespread in office use electrical connectors (integrated circuits) rather in automobile connectors which face exposure to severe atmospheric and temperature conditions. The semiconductor α-tin phase has a small energy gap of -0.1 eV making it suitable for in infrared photodetector use.[196]

Many Sn alloys have been used as solder materials, and depending on the alloyed element the nature of the resultant solder will vary from a soft solder such as Pb-Sn to hard solders such as Au-Sn.[197, 198] Hard tin solders such as Au-Sn solder are desirable in the fabrication of integrated chips or for die bonding for optoelectronics and microelectronics, due to their high level of mechanical and thermal performance.[197]

Tin is used as an anode material in Li-ion batteries with measured theoretical capacity of 990 mA h g^{-1} vs. 370 mA h g^{-1} for graphite, owing to the ability of this element to form several intermetallic phases with Li.[199, 200] The cycle performance of pure tin in Li^+ batteries is limited. A noticeable improvement in cycling performance of Sn when used as anode in Li ion battery has been reported by Park *et al.* by altering the composition, nature and morphology of tin electrode, when a η-Cu_6Sn_5 phase was formed between the layers of β-Sn electrodeposited on Cu substrate.[201] This resulted a less dense Sn deposit and nodule-type morphology, caused by the high current density applied in the ED process compared to the one applied in the ED of pure tin.

Several deposition techniques have been utilized to deposit tin including electroless techniques such as immersion, dip-coating and displacement,[202-204] and high vacuum evaporation.[205] Sn can be electrodeposited from wide range of acidic and alkaline electrolytes and with low cost.[195] Tin deposits with a small negative deposition potential and can be alloyed with wide range of other elements using ED.[206]

Electrodeposition of tin mainly uses aqueous electrolytes, typically acidic solutions of stannous salts with tetrafluoroboric acid, sulphate, chlorides, methanesulfonic acid[206] or alkaline solutions of stannic ions of tin. Electrodeposition from aqueous electrolytes is limited by the narrow potential window, high surface tension and hydrogen evolution process, and these all cause energy loss and low quality of the electrodeposit.[199, 207] A number of other limitations accompany ED from acidic and alkaline electrolytes, for instance elevated temperature should be applied when an alkaline bath is used. Sn films from alkaline baths which contain $[Sn(OH)_6]^{-2}$ are determined to have a fragile morphology, due to hydrogen diffusion to inside the deposits.[201] In the case of acidic baths low current densities are obtained and stannous ions undergo oxidation.[202] Both acidic and alkaline electrolytes cause tin hydroxide precipitation during the electrodeposition. Additives of organic compounds, surfactants and oxidation inhibitors in the case of acid baths to prevent Sn^{+2} oxidation to Sn^{+4} needs to be added.[207, 208] Thus, aiming for reduced hydrogen evolution and a larger electrochemical potential window, other electrolyte systems are of interest in semiconductor electrodeposition such as the ionic liquids (ILs) and organic electrolytes. Of these the water and air stable ILs are most studied, due to properties such as wide electrochemical window, low vapour pressure, high thermal stability and the ability to dissolve metal salts.[209-211] Many publications are established on the use of ILs in tin and tin alloy ED.[199, 207, 209, 212-214] In the past Platis and Capuano have reported the ED of Al/Sn alloy from organic electrolyte based on alkyl benzenes[215], and in a recent study Santato *et al.* have deposited Sn from the organic electrolyte dimethyl sulfoxide, reporting no hydrogen evolution, improved wire morphology in tin deposits.[216]

Electrodeposition of tin and tin alloys has been studied on various metal substrates such as platinum,[212] gold,[208] copper[196, 199] and iron[217] or on metal-alloy substrates such as brass[218, 219] and steel.[206, 215] Nanostructured tin is also another area of interest, and encapsulated single crystal tin nanowire heterostructures in amorphous carbon nanotubes were obtained by Ruying *et al.* [220] Sn nanowires by electrodeposition from ILs were reported by Elbasiony *et al.*[207] using polycarbonate templates. Template free tin nanowires were electrodeposited from ILs by Deng *et al.*[221] where tin nanowires of porous morphology were electrodeposited.

We have electrodeposited thin films of tin on gold sputtered on to glass electrodes, using $[^nBu_4N][SnCl_3]$ as the tin precursor with $[^nBu_4N]Cl$ as supporting electrolyte in CH_2Cl_2. $[^nBu_4N][SnCl_3]$

is slightly moisture sensitive, therefore an anaerobic cell setup was used under flowing N_2. Sn deposition was performed at electrolyte temperatures of -78, -16, 0, 23 and 35 °C, with the aim of achieving both β-Sn and α-Sn systems. The films were examined for their morphologies, purity, crystallographic structure and texture, using SEM and XRD analysis. Anodic aluminium oxide (AAO) templated Sn nanowires were electrodeposited from the same electrolyte system and experimental setup as in the flat tin on gold. AAO templates having pore diameters of 13, 55 and 200 nm and pore heights of ~ 50 µm were sputtered with a thin layer of gold from one end to produce electrical contacts. The Sn structures were characterised using SEM, EDX, XRD and pole figure measurements. To ease the ED processes, some of the membranes were phosphonate grafted (p-grafted). The grafting changes the hydrophilic nature of the AAO membranes to hydrophobic. Thus better pore access for low polarity solvents was expected.

5.2 Experimental

The deposition method was initially tried by Dr. Peter Richardson (Chemistry, University of Southampton). The precursor $[^nBu_4N][SnCl_3]$ was synthesized by Dr. Jennifer Burt (Chemistry, University of Southampton), and the Au substrates were made by Alistair Clark (Chemistry, University of Southampton). The anodic aluminium oxide (AAO) templates were purchased from Synkera and gold sputtered for electrical contact by Zondy Webber (Physics and Astronomy, University of Southampton). The phosphonate grafted AAO membranes using diethylphenylphosphonate as grafting agent were prepared by Dr. Andrew Lodge (Chemistry, University of Southampton). Transmission electron microscopy (TEM) measurements and cross-section SEM imaging was done by Dr. Reza Kashtiban (Physics, University of Warwick).

5.2.1 Preparation of the electrolyte

0.047 g of tetrabutylammonium chlorostannate ($[^nBu_4N][SnCl_3]$) and 0.278 g of tetrabutylammonium chloride ($[^nBu_4N]Cl$; Fluka, > 99.0%) were dissolved in 10 cm^3 of dry dichloromethane (DCM). All the reagents were handled and the electrolyte preparations were performed under N_2.

5.2.2 Cyclic voltammetry experiments

The electrochemical processes were carried out in N_2-flushed 3 electrode cells containing a 1 cm^2 gold film working electrode, a Ag/AgCl reference electrode filled with 0.1 mol dm^{-3} $[^nBu_4N]Cl$ in CH_2Cl_2, and a platinum gauze counter electrode. The 200 nm gold films were sputtered on glass microscope slides with a 20 nm chromium wetting layer. The cyclic voltammetry (CV) was recorded in the potential range -2 to 1 V at a scan rate of 50 mV s^{-1}.

5.2.3 Electrochemical deposition of Sn on gold film electrodes

The deposition process was under the same conditions as the CV experiments (inside N_2 flushed cell). Various deposition temperatures (-16, 0, 23 and 35 °C), were achieved by fitting the electrochemical cell with a jacket and controlling its temperature with a Thermo-Haake K15 bath and C10 controller. For the experiments conducted at -78 °C the electrolyte was cooled with a dry ice/acetone bath. Chronoamperometry was used for the deposition, the 200 nm Au sputtered on glass with 30 nm chromium wetting layer substrate (1 cm^2) acted as the working electrode. A Pt gauze was the counter electrode and a Ag/AgCl in 0.1 mol dm^{-3} $[^nBu_4N]Cl$ in DCM reference electrode was used. A Biologics SP150 potentiostat was used for the electrochemical measurements. The samples after the deposition were taken straight out of the cell and rinsed with DCM to remove any electrolyte residues.

Sn nanowire electrodepositions were from the same electrolyte composition and experimental setup. Anodic aluminium oxide (AAO) templates of various pore diameters (13, 55, 200 nm) were sputtered with a thin layer of gold from one side to obtain electrical contact.

5.2.4 XRD, SEM and EDX experiments

The XRD patterns were collected on the Smartlab X-ray diffractometer, with Cu K_α radiation, using 2θ values in the range between 10-80°. Grazing incidence (1° incident angle) and symmetric scans were collected. Pole figure measurements were also carried out on the Smartlab using in-plane pole figure geometry. In-plane pole figures were collected on the tin in the AAO template, using the in-plane optics, 0.5° Soller slits, for the incident beam and the detector. PFs were collected on Sn 200 and 101 reflections, the detector was fixed at the 2θ position of interest and β is scanned with ϕ motion at each α angle, with the α axis controlled by a combination of 2θ and 2θχ.

Scanning electron microscopy (SEM) was carried out to examine surface morphologies and energy dispersive X-ray spectroscopy (EDX) was used to examine the presence of any impurities in Sn on Au and Sn in AAO samples. The data was collected using a JEOL JSM 6500F field emission scanning electron microscope (FEG-SEM). The SEM images and the EDX spectra were recorded at an accelerating voltage of 10 kV with EDX collections for 60 s.

5.3 Electrodeposition of tin on gold electrode

Electrodeposition of Sn onto gold disc electrodes from supercritical difluoromethane (scCH_2F_2) has been previously reported using the [^{n}Bu$_4$N][SnCl$_3$] salt with the [^{n}Bu$_4$N]Cl supporting electrolyte.[222] In the experiments in this chapter the liquid phase of the organic electrolyte dichloromethane (DCM) was utilised as solvent, and Sn was electrodeposited onto flat substrates of gold sputtered on glass at various temperatures.

5.3.1 Cyclic voltammetry experiments

Cyclic voltammetry (CV) was recorded for the Sn^{+2} species in the electrolyte on Au electrodes vs. the Ag/AgCl reference electrode. To obtain maximum compatibility in the electrochemical system and reduced contamination of the electrodeposits, the shared counter ion of [^{n}Bu$_4$N]$^+$ between the Sn precursor, the supporting electrolyte and the electrolyte used in the reference electrode was used. CVs were recorded between 1 and -2 V vs. Ag/AgCl. The cyclic voltammograms for Sn species on Au surface at various electrolyte temperatures are assembled in Figure 5.1. The electrode potential scan was started from open circuit potential (OCP) in the negative direction using scan rate of 0.05 V s^{-1}. A Sn^{+2} to Sn^0 reduction peak was observed in the CVs at a potential of -1.3 V for the CV recorded at room temperature. This peak was shifted to a more negative potential (-1.5 V) in the CV at 35 °C. Less negative Sn^{+2} / Sn^0 reduction potentials (0.75 and 0.85 V) were recorded in the CVs run at 0 °C and -16 °C. The CV at -78 °C contained a loop and an unusual peak at -1.25 V in the positive sweep scan, this showed Sn ion reduction at a lower potential established by the nucleation loop, while the peak in the positive sweep could be for Au-Sn alloying. The CVs exhibit waves in the negative scans, and are due to tin alloying with the substrate (Au). The anodic scans show stripping peaks, the peak at ~ -0.4 V is the elemental tin oxidation, and peaks at less negative potentials are for Au-Sn alloys oxidation. The CVs at 35 °C and -78 °C contain fewer waves compared to the CVs performed at other temperatures.

Hence heating the electrolyte has resulted in a more negative tin reduction potential. Although an increased mobility of the ions is expected with increased temperature of the electrolyte, in which case the reduction process would occur at a less negative potential, it seems other factors such as (nucleation, phase formation, reduction rate …..) are affected at this temperature causing reduced rate of deposition. This could be due to the increased electrolyte volume at higher temperature. The thermal expansion of DCM reduces the Sn^{+2} concentration, which could move the nucleation potential to more negative values.

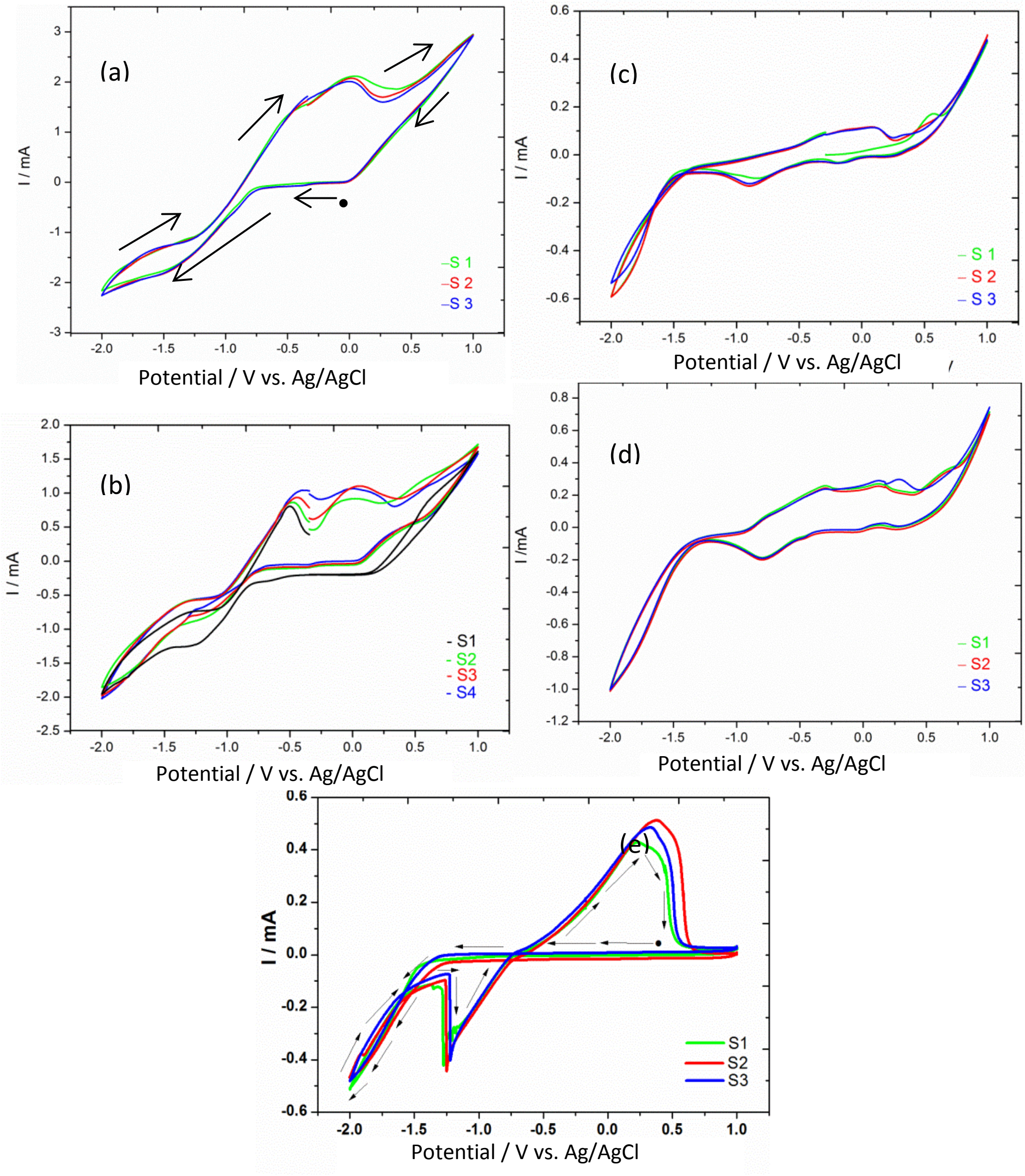

Figure 5.1 Cyclic voltammograms (50 mV s^{-1}) for 10 mmol dm^{-3} of [N^{n}Bu$_4$][SnCl$_3$] in 10 mmol dm^{-3} [N^{n}Bu$_4$]Cl in CH$_2$Cl$_2$, the working electrode was a ~1 cm^2 gold film. Bath temperatures were 35 °C (a), 23 °C (b), 0 °C (c), -16 °C (d) and -78 °C (e). S1-S4 denote scan numbers 1-4. The direction of the CVs is indicated on graphs a and e.

5.3.2 Chronoamperometry experiments

The electrodeposition was obtained by applying chronoamperometry. A fixed potential around the reduction peak potential, a potential negative to the peak (overpotential) or a potential around the onset of the reduction peak, were tested. Depending on the current response with time (current-time transient) and the quality of the deposits, the values of the potentials were chosen for the ED at different temperatures. In the experiments performed at bath temperatures of 0 °C and lower, an overpotential was applied in the long deposition durations. When these experiments were conducted at low overpotentials the current often dropped to values close to zero before the deposition time was reached.

Figure 5.2 shows examples of chronoamperograms for Sn ED at various temperatures for one hour. The choice of the deposition potentials were according to the reduction peaks observed on the CVs. ED at 35° C was achieved by applying -1.2 V, and an initial high current of ~ -2.4 mA sharply reduced to ~ -0.05 mA. The current gradually increased with time presumably as the surface roughened with the tin deposit, and reached a plateau of -0.5 mA after around 20 minutes of deposition. The high initial current in the experiment performed at room temperature is lower in value compared to the high temperature experiment, but a higher current of ~ -0.5 mA was passed in the time following the initial step, which then gradually decayed with time. The CA recorded at 0 °C show an initial current of ~ -1.0 mA, close to that observed on the CA at room temperature, reduced to ~ 0.45 mA with slight decay with time.

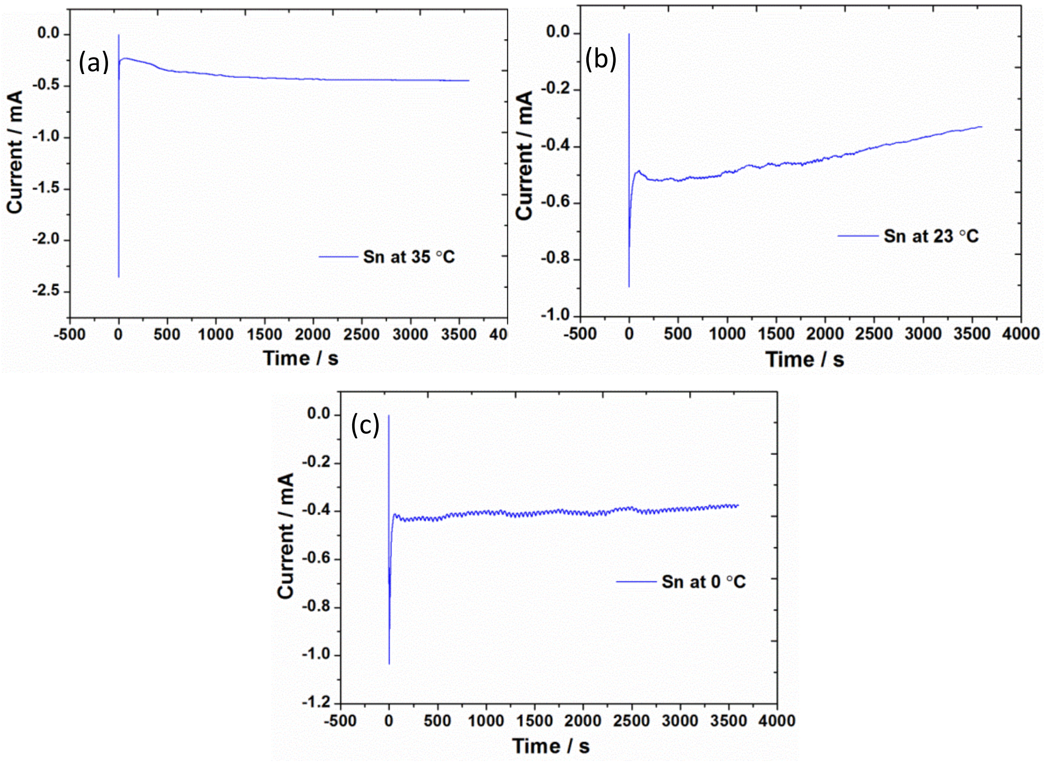

Figure 5.2 Chronoamperograms for Sn electrodeposited from 10 mmol dm^{-3} of [N^{n}Bu$_4$][SnCl$_3$] in 10 mmol dm^{-3} [N^{n}Bu$_4$]Cl in CH_2Cl_2, on a 1.1 cm^2 gold film, at -1.2 V and a bath temperature of 35 °C (a), at -1 V and 23 °C (b), and at -1.15 V and 0 °C (c).

The current passed at the three different electrolyte temperatures are found to have values of around ~ -0.5 mA. The initial decay in the current in every CA is followed by gradual reduction in the current for a limited short time, followed by gradual increase in the value until the steady current is reached.

In the EDs performed at -16 and -78 °C electrolyte temperatures (Figure 5.3), large overpotentials from the Sn^{+2} reduction peak on the CVs were applied. The current response was higher in the case of -78 °C experiment. A sharp current of -1.1 mA was passed in the start of the CA at -16 °C, and then reduced to a plateau value around -0.05 mA. The initial current in the CA at -78 has a lower value compared to the -16 °C experiment, but has decayed less sharply and the deposition has continued at -0.15 mA with slight increase in the value for the rest of the deposition time.

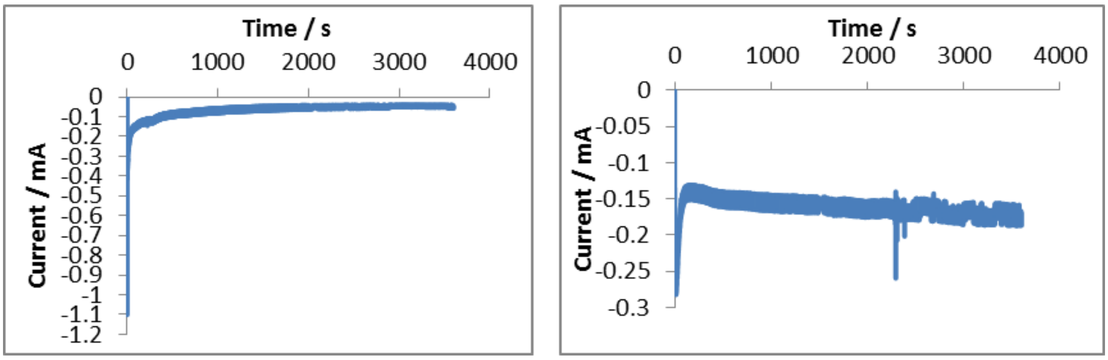

Figure 5.3 Chronoamperograms for Sn electrodeposited from 10 mmol dm^{-3} of $[N^nBu_4][SnCl_3]$ in 10 mmol dm^{-3} $[N^nBu_4]Cl$ in CH_2Cl_2, on a 1.1 cm^2 gold film, at -1.25 V and -16 °C (left) and at -1.55 V and -78 °C (right).

In the 4 hour deposition experiments, larger overpotentials compared with 1 h depositions were applied. That was to assure continuous reduction of Sn ions throughout the experiment time. With low overpotentials in longer deposition durations, the current-time response in some cases eventually dropped to zero.

5.3.3 SEM and EDX experiments

The morphology of the deposits was examined in tin films produced at various bath temperatures and for two different deposition durations. The films deposited over a period of one hour (Figure 5. 4) exhibit block shaped crystals, and the size of the blocks varies with the bath temperature. Large crystals were observed when high bath temperatures were applied, reduction in the size of the crystals was observed with lowering the bath temperature.

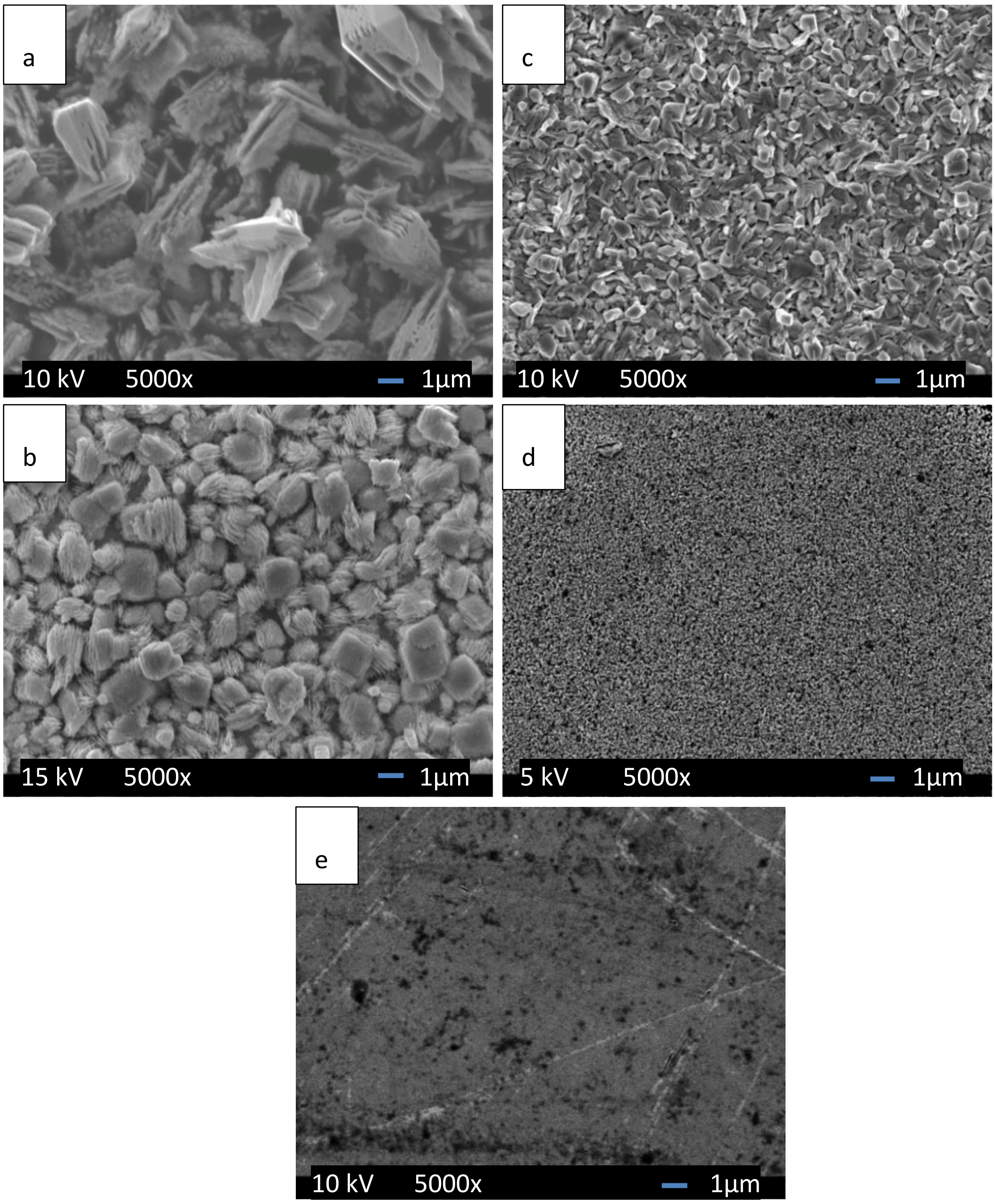

Figure 5.4 SEM micrographs for Sn electrodeposited from 10 mmol dm^{-3} of [N^{n}Bu$_4$][SnCl$_3$] in 10 mmol dm^{-3} [N^{n}Bu$_4$]Cl in CH$_2$Cl$_2$, on a 1.1 cm^2 gold film for 1 hour, at -1.0 V and bath temperatures of 35 °C (a), at -1.0 V and 23 °C (b), at -1.15 V and 0 °C (c), at -1.35 V and -16 ° C (d), and at -1.6 V and -78 ° C (e).

The size of the blocks is a few µm in the 35 °C tin, while the size is reduced to ~ 100 nm in the -16 °C tin. The blocks are formed by agglomerations of particles in the form of stacked sheets. Sn depositions at every bath temperature were extended to four hours (Figure 5.4) and the SEM results show smaller dendritic crystals at the surface grown on top of the Sn blocks. A dendritic porous tin morphology at high cathodic potential was observed previously by Walsh and Low,[193] which was grown into needle like deposits by using even higher cathodic potential. The effect was related by them to a hydrogen evolution process alongside with the element deposition. Similar morphologies were obtained here after 4 hours depositions despite the lack of hydrogen evolution from this electrolyte. The morphologies of the deposits obtained by applying higher cathodic potentials compared to the potentials used in 1 h experiments are reasonably dense (Figure 5.5). In section 5.3.2 the need to use overpotentials in the 4 h tin depositions was explained. Nanoparticles of tin are agglomerated on the surface of the tin films deposited at -16 and 0 °C bath temperatures. The tin deposited at 35 °C shows a surface morphology of cauliflower-like shaped agglomerations of particles, and the room temperature tin has grown into nanowires agglomerated in bundles of approximately 5 µm in size. Different from the other two low temperature films, the morphology of tin at -78 °C indicates blocks with sizes of ~300 nm, possibly produced from stacked nanosheets of tin.

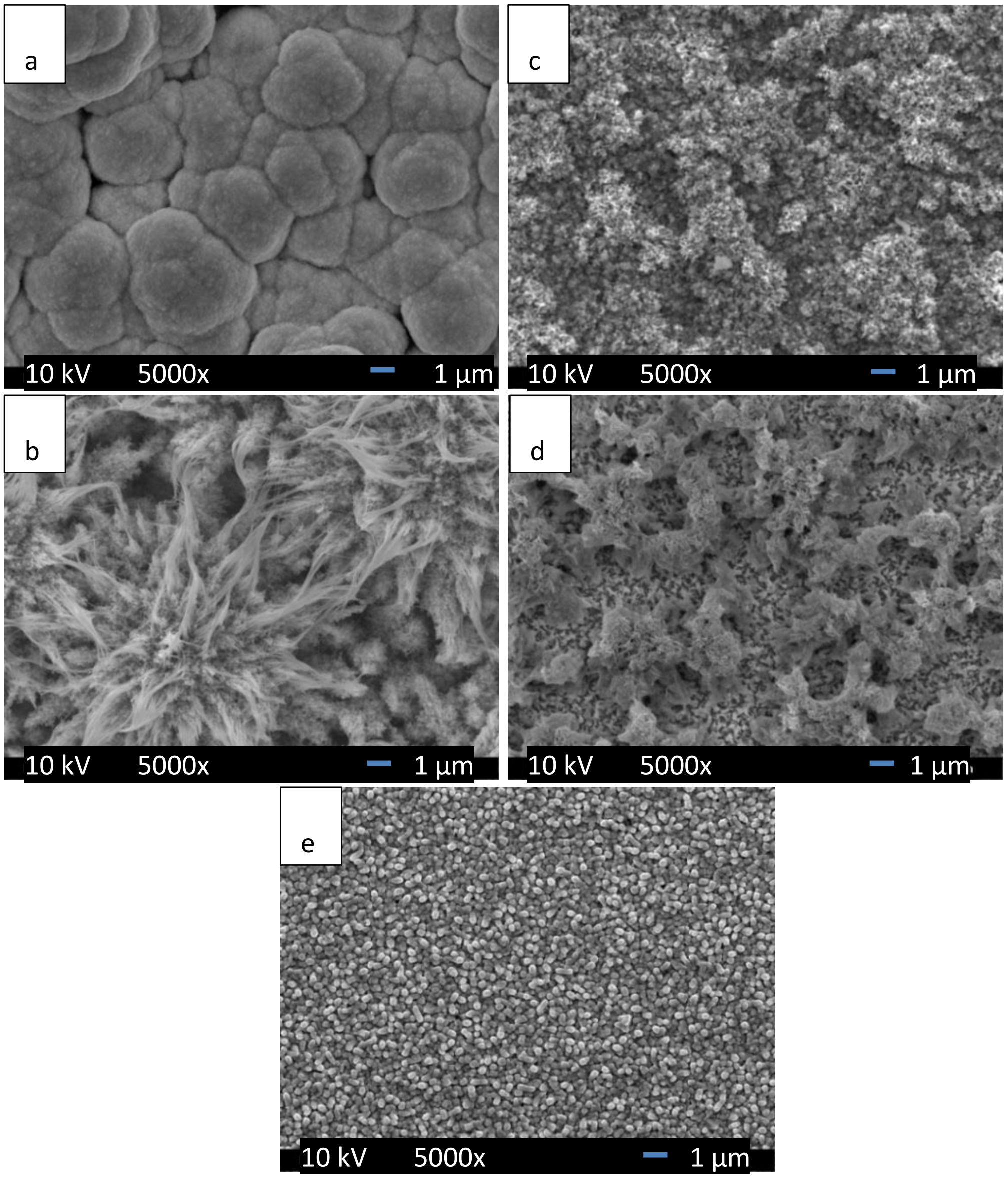

Figure 5.5 SEM micrographs for Sn electrodeposited from 10 mmol dm^{-3} of [N^{n}Bu$_4$][SnCl$_3$] in 10 mmol dm^{-3} [N^{n}Bu$_4$]Cl in CH_2Cl_2, on a 1.1 cm^2 gold film for 4 h, at -1.4 V and 35 °C (a), at -1 V and 23 °C (b), at -1.15 V and 0 °C (c), at -1.55 V and -78 ° C (d), and at -1.15 V and -16 °C (e).

To determine the composition and the level of impurities in the tin deposits, EDX analysis was applied to some of the films. Figure 5.6 is an example of EDX run on a tin film electrodeposited at room temperature for 4 h. No Au signal from the substrate is expected in these thick films. The spectra show signals from Sn and some signals around 0.5 KeV indicating some oxygen and carbon on the surface, no clear Cl peak is found in the spectrum. EDX spectrums for some of the films show Cl peak due to electrolyte residue.

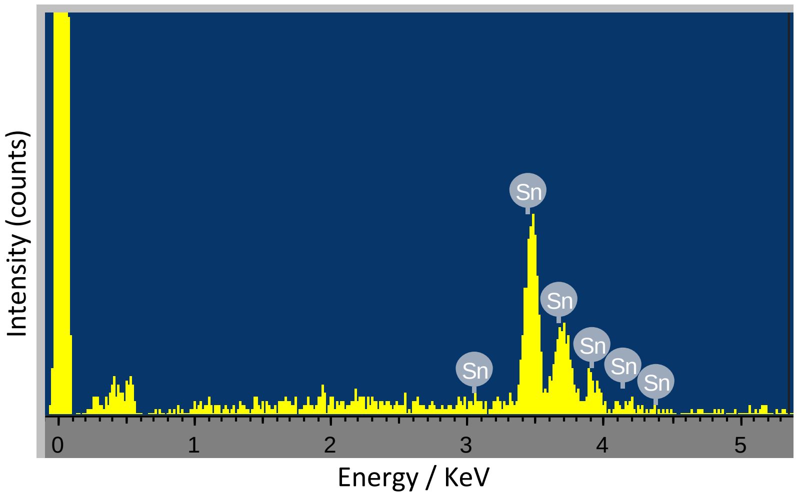

Figure 5.6 EDX analysis on Sn electrodeposited from 10 mmol dm^{-3} of [N^{n}Bu$_4$][SnCl$_3$] in 10 mmol dm^{-3} [N^{n}Bu$_4$]Cl in CH$_2$Cl$_2$, on a 1.1 cm^2 gold film, at -1.5 V and room temperature, 4 h deposition.

5.3.4 XRD experiments

The composition and the structure of the deposits were examined using grazing incidence scans and symmetric (theta/2theta) scans. Sn was electrodeposited at various temperature ranges and the X-ray diffraction experiments were performed on the fresh samples taken straight out from the cell. In Figure 5.7 (left) grazing incidence scans on tin produced after 4 hour deposition at various temperatures are shown. The Sn films in every case have tetragonal β-Sn structure even when deposited at temperatures below the Sn phase change from tetragonal β-Sn to diamond cubic α-Sn. This was despite the black colour of the deposits obtained at low temperatures. The β-Sn crystal system is tetragonal having the space group of ($I4_1/amds$) and lattice constants in the structures deposited in ICSD[112] range from a = 5.700 Å and c = 3.069 Å to a = 5.84 Å and c = 3.15 Å at room temperature. We have extracted the lattice parameters by analysing the XRD patterns of the tin deposits using the PDXL2 software, which works in association with the Smartlab X-ray diffractometer. The data shown here are for tin ED for 4 hours at every temperature. The lattice constants in every case were in the range of the literature values, and showed irregular changes with temperature. The extracted lattice constants are shown in Table 1. Accordingly α-Sn cannot be simply electrodeposited by just lowering the electrolyte temperature, a more complicated process including a control of other parameters thus is required. In a publication by Becker β-Sn was transformed to α-Sn by applying a series of rolling procedures to thin the sample, cleaning treatment and impurity additions were applied, as well as using a seeding layer of α-Sn for the growth.[191] To determine the effect of cooling a β-Sn thin film on phase transition, we have stored a tin sample, which was obtained at -78 °C, in a freezer at -18 °C for about 10 days, and then collected XRD pattern. We didn't observe any α-Sn in the XRD pattern, possibly due to the volume expansion in the metallic β-Sn when transformed to the semi-conductor α-Sn, the volume increase is measured to be by 27%,[191] thus a thin film which is strongly bonded to the gold substrate by covalent bonds will not allow this volume expansion.

Otherwise tin alloying with the gold substrate, which has produced hexagonal AuSn phase, could be responsible for the tetragonal tin deposit. The produced AuSn layer may have behaved as a seeding layer for β-Sn growth. Epitaxial growth in the initial Sn layers on the AuSn could direct the Sn phase that is deposited.

Table 1 Variations in lattice constant for Sn film produced from 4 hour electrodepositions on Au substrates at various temperatures.

Electrodeposition temperature / °C	Lattice constant (a, c) in Å
35	5.817(18), 3.199(15)
23	5.8337(18), 3.1823(18)
0	5.819(14), 3.205(13)
-16	5.816(5), 3.182(12)
-78	5.8275(15), 3.1787(14)

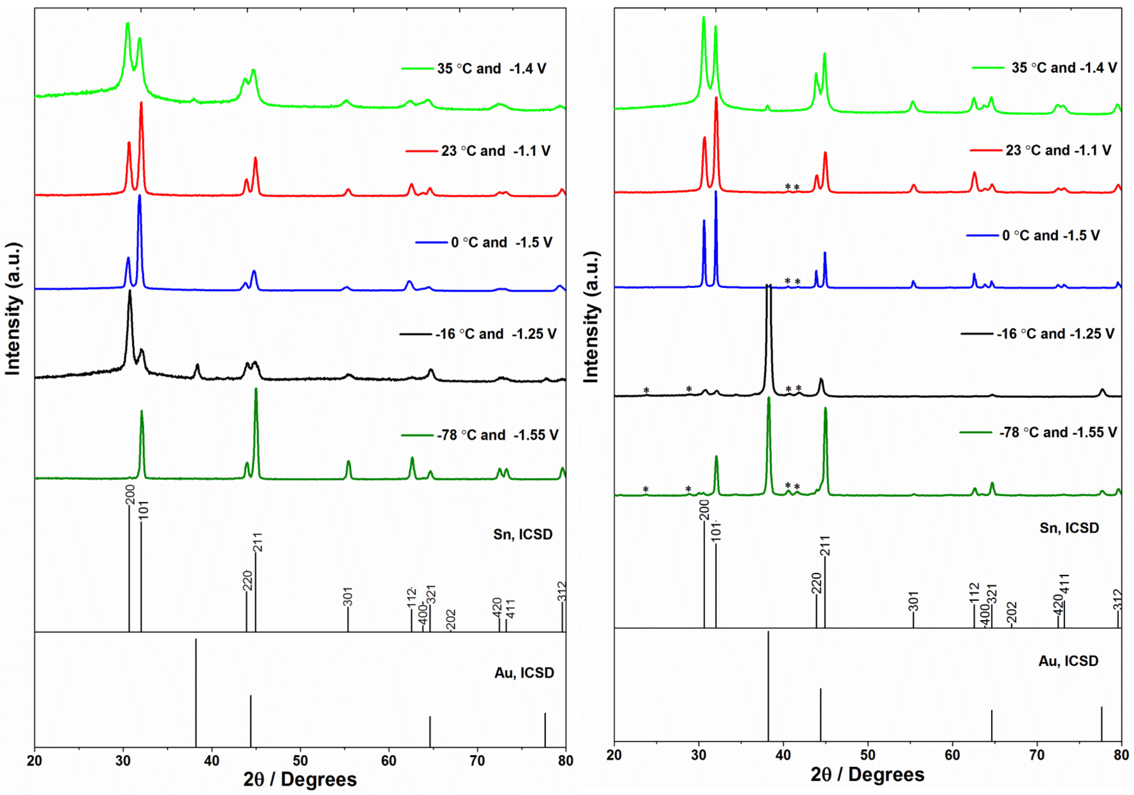

Figure 5.7 XRD patterns of 1° grazing incidence scans (left) and symmetric scans (right) on Sn electrodeposited from 10 mmol dm^{-3} of [N^{n}Bu$_4$][SnCl$_3$] in 10 mmol dm^{-3} [N^{n}Bu$_4$]Cl in CH_2Cl_2, on a 1.1 cm^2 gold film for 4 hours electrodeposition duration. The bath temperatures and deposition potentials are indicated on the patterns. Peaks marked with (*) are for the AuSn alloy phase. Stick patterns for Au and Sn standards are obtained from the ICSD site.

The grazing incidence XRD scans on tin films show some crystallographic orientation. The crystallite orientation observed from grazing incidence scans is not precise, as the diffraction vector changes its orientation during the course of the measurement. To obtain exact texture information on the tin films, symmetric (theta/2theta) X-ray diffraction patterns were collected (Figure 5.7, right), in which the incident beam and the detector angles are equal. In the symmetric scans, signals for the Sn phase in the deposit, strong signals from Au the substrate and, in the low temperature deposits, weak peaks matching the AuSn alloy, are detected. Sn alloying with the Au substrate has been reported by others in different systems,[199] and also in a system similar to this work, where main group elements were electrodeposited on Au.[136] The presence of AuSn alloy is limited to the interface, hence it's only detected in the symmetric scans for the relatively thin deposits. In the XRD on the 35 °C tin sample, AuSn was not detected, but very weak peaks for the alloy is observed on the pattern for the Sn produced at 23 °C. However the presence of a signal from the substrate in the pattern collected on the 35 °C film indicates thinner deposit compared to the 23 °C which exclude Au peaks. This may indicate that the interface alloying between Sn and

Au can be prevented when Sn ED is performed at high temperature. In a study on Au-Sn solders by Akhlaghi and Ivey, the effect of temperature on the composition of the alloy was studied, they have reported decreased Sn content in composition of the alloy by increasing the temperature to above ~35 °C,[197] this result assents with our determination from the symmetric XRD on the tin deposited at 35 °C. The XRD on tin at 35 °C shows polycrystalline structure, while the tin at room temperature and 0 °C exhibit some <101> orientation, the orientation in the tin deposited at -16 °C is hard to identify, due to low Sn signal, however is more like to exhibit some <101> orientation, the XRD pattern for the Sn ED at -78 °C show a strong <101> orientation.

5.4 Electrodeposition of tin in AAO templates

In the recent history of electrodeposition, nanostructured deposits and semi-conductors have received great interest, due to their distinctive chemical and physical properties.[223, 224] Nanowire growth in a wide range of materials has been achieved by employing templates. Controlled diameter and well defined very thin wires with high aspect ratios were reported.[224] Continuous, parallel pore structured anodic alumina membranes (AAO) are formed in acidic electrolytes by anodization of aluminium.[225] They have been utilized as templates in electrodepositions from aqueous[109, 223, 224, 226, 227] and supercritical fluid (SCF) electrolytes.[8, 40] The pore inner-walls in AAO have a hydrophilic nature, as there are hydroxyl groups lined on the surface. This nature can be changed to hydrophobic by grafting the pores using grafting agents. This process could be beneficial in reducing the surface tension, when the electrodeposition is from non-aqueous systems such as organic electrolytes and SCF electrolytes and in the cases where water sensitive reagents are used.[228]

Herein we have used AAO as supplied and phosphonate grafted AAO membranes in tin electrodeposition. Tin electrodeposition into AAO templates was from the same electrolyte and under same conditions as explained in tin ED on flat Au substrates.

5.4.1 Chronoamperometry experiments

The electrochemical experiments were performed in a Teflon cell having the capacity of 5 cm^3, especially designed to achieve contact between the electrolyte and the membrane front surface, while preventing electrolyte contact with the electrically contacted back surface. The cell consisted of a 2 cylindrical containers. The narrower part has a 4 mm diameter hole at the bottom to allow the electrolyte to contact the membrane. The internal diameter of the second cylinder is wider by 1 to 1.5 mm than the external diameter of the first one. So the first cylinder is fitted inside. The membrane with a copper sheet underneath is sandwiched between the two cylindrical fitted parts by an O-ring. The copper sheet is then connected to the working electrode using copper strip alongside the interconnect walls of the cylinders. The whole cell is then fitted inside a glass cell with water jacket surrounding used for temperature control purpose. The glass cell maintained anaerobic conditions, and was connected to a Schlenck line for the experiments to be performed under flowing N_2. Figure 5.8 shows the parts of the cell design described above.

A 3-electrode cell setup was used, in which the AAO membrane with copper current collector acted as the working electrode, the counter electrode was a Pt mesh and the reference electrode was Ag/AgCl in $[N^nBu_4]Cl$ electrolyte (0.1 M $[N^nBu_4]Cl$ in DCM). In the chronoamperometry (CA) experiments, the choice of the deposition potential was based on the CVs run for Sn on flat Au substrate (Section 5.2.1) under similar conditions. A fixed potential of -1.5 V was applied in a test experiment performed on a non-grafted 55 nm pore diameter AAO membrane. A large current responsible for the double layer charging was passed in the initial step of the CA, which then showed a sharp decrease to a value around 0.06 mA. This current value has showed a gradual decrease with time to a steady state plateau, various steady state currents were observed for different pore sized membranes. Accordingly using the value 0.06 mA the estimated amount of charge required to fill the pores with tin was calculated. The total volume of the pores was estimated from the volume of an individual pore and the number of the pores per area. Then an estimated deposition time was calculated to pass the desired charge for ED at -1.5 V deposition potential. Table 2 shows the calculated deposition times for different pore sized AAO membranes.

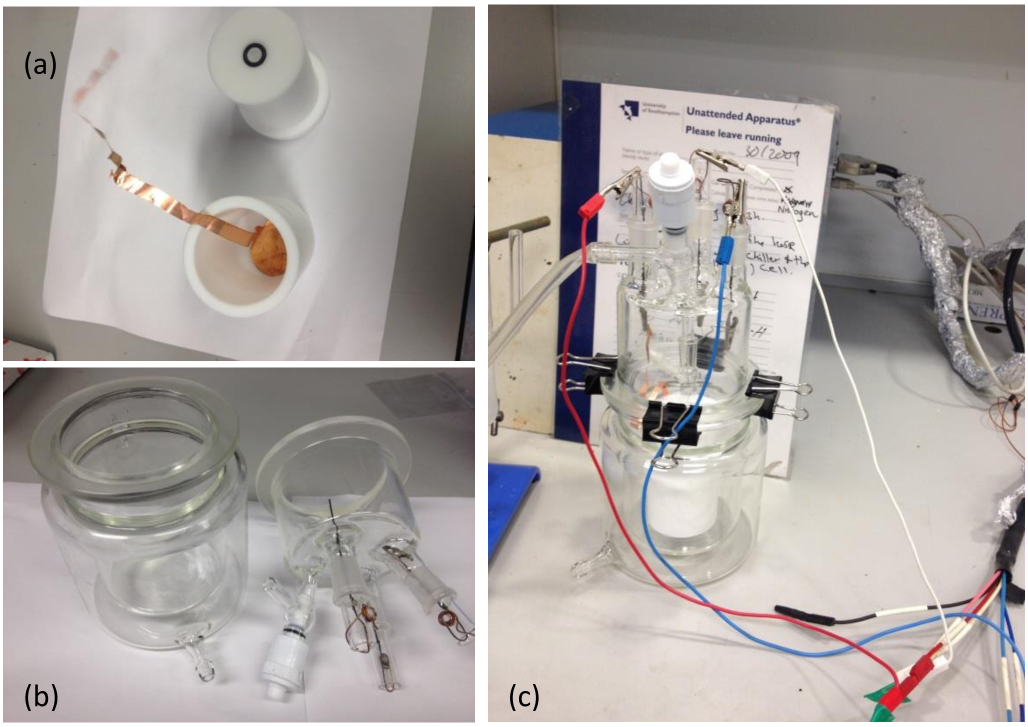

Figure 5.8 Images show the parts and the final design for the cell used in Sn nanowires electrodeposition under N_2 atmosphere. The Teflon cell parts and design (a), the outer glass cell parts (b) and the complete electrochemical cell connected to the potentiostat.

Table 2 Estimated deposition durations for different pore sized AAO.

Pore size AAO	Calculated deposition time
13 nm AAO	2 ½ h
55 nm AAO	2 h and 15 minutes
200 nm AAO	2 ½ h

The current-time transients (Figure 5.9) exhibit large initial current values due to double layer charging and initial steps of nucleation. The value of the current passed at this stage has similar values of ~ -0.14 mA for the 13 and 55 nm pore diameter membranes, but this current has a greater value in the 200 nm pore diameter membranes. This current decreased in value sharply, and followed by gradual decay over a period of ~ 200 s, which is believed to be the start of Sn nuclei formation. The following step was the plateau current for tin growing through the template, this current was varied for different pore sizes and also with hydrophobicity of the pores.

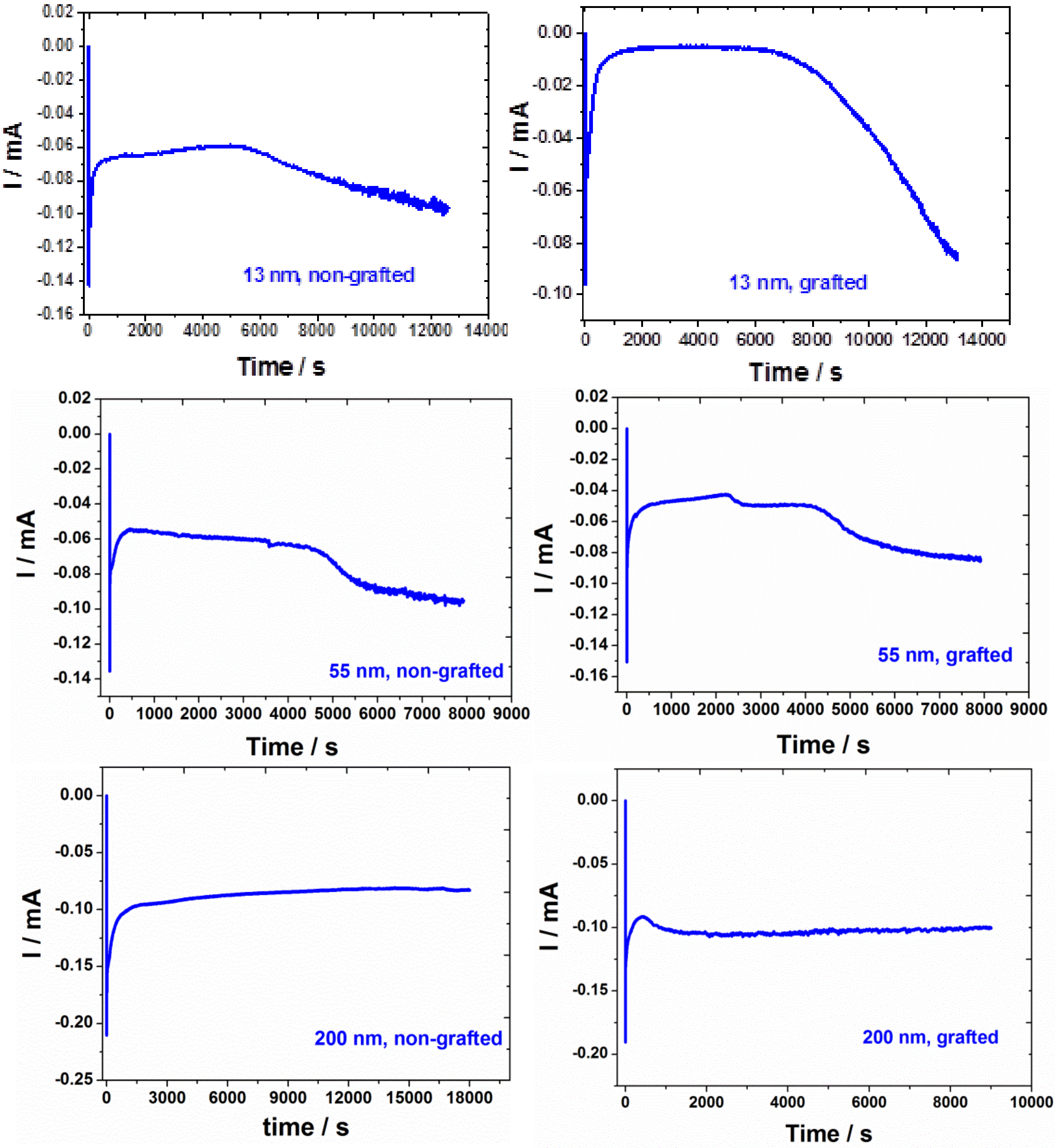

Figure 5.9 Current-time transient for the electrodeposition of Sn in AAO membranes by chronoamperometry, at deposition potential of -1.5 V, the deposition duration ranged between 2-5 h, at room temperature. The composition and the pore sizes of the individual membranes are indicated on the graphs.

In most of the cases the plateau current decreased over the deposition time, In the 55 nm pore template, in which rather unsteady plateau was observed. Several of the current-time transients show a gradual large increase in the current after a certain time of deposition, indicating filled pores and tin deposition breaking through the pores, thus the start of bulk tin deposition at the membrane surface. Smaller current was passed in the ED of tin in the grafted 13 nm pore diameter AAO membranes. In contrast larger currents were expected for these membranes, due to increased hydrophobicity of the pores which was intended to ease the access of the organic electrolyte. Pore blockage during the grafting process might be responsible for the lowered current passed or the pores volumes are possibly decreased by the presence of the grafting agent. The value of the current passed in the systems has increased in value with increasing the pore sizes. The size of the pores are not the only reason for these differences, it was noticed that in the 200 nm non-grafted and in the grafted membrane the current leaked through the pores and tin ED occurred on the back of the membrane (the gold coated face). The low thickness gold coating might resulted in non-uniform coverage of the pores and was not entirely blocked. The current passed in the membranes are listed against the pore sizes in Table 3.

Table 3 Values of the steady state current passed during the CA experiments in AAO.

AAO membrane	Value of the current passed
13 nm grafted	0.01-0.03 mA
13 nm non-grafted	0.07 mA
55 nm grafted	0.04 mA
55 nm non-grafted	0.06 mA

5.4.2 SEM, EDX and TEM experiments

The visual examination on the samples indicates full coverage of the surfaces with a layer of tin overgrown out of the pores (Figure 5.10). In the 200 nm templates, deposition was observed on the back (the gold sputtered face) of the samples, as a result of electrolyte leakage through a non-uniform rather porous gold layer sputtered on the back in the process of electric contact formation for the AAO membranes. To determine Sn presence inside the pores of AAO, EDX spectra were collected on the cross-section SEM figures of the pores.

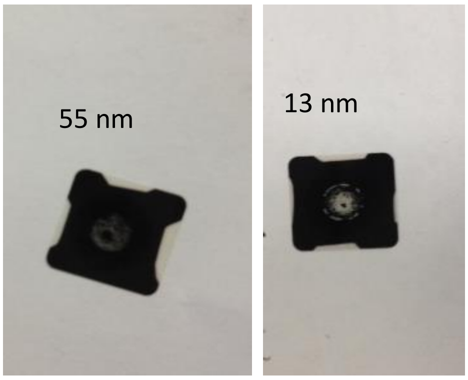

Figure 5.10 Photographs for the overgrowth of tin observed visually on the surface of the non-grafted AAO membranes.

The overgrown tin was scraped carefully from the templates using a clean sculpture knife before the EDX measurements. This process resulted in the removal of almost all the overgrowth from the surface, observed from the grazing incidence XRD scans. The presence of Sn was examined along the whole height of the pores focusing on the ends of the pores. The determinations indicate Sn inside the pores. The distribution of tin inside the pores is probably not even, as during the EDX spectra collections several areas were examined in the same sample and tin was found in some areas but not in all. These areas might be for the part of the membrane that is out of the aimed deposition, or the pores are being blocked due to surface tension. However tin was detected in every pore sized template, grafted and non-grafted. The presence of tin was checked along the pore heights, focusing on the top areas to ensure that the pores are filled to the top. The EDX spectra on Sn wires exhibit peaks for Al and O from the alumina template and C peak from the atmosphere alongside the tin peaks from the deposit. The EDX on the 13 nm pore diameter AAO from Figure 5.12 shows tin inside the pores of the un-grafted and the grafted AAO. The EDX spectrum on the un-grafted 13 nm AAO was collected on an SEM instrument conjugated with higher resolution EDX. Figure 5.13 is the EDX spectra for tin in the 55 nm AAO and shows peaks for Sn inside the pores of both the un-grafted and the grafted membranes, indicating successful deposition of tin wires. The 200 nm pores diameter AAO also indicates the presence of tin wires inside the pores, observed in the EDX spectra for the un-grafted and the grafted membranes from Figure 5.14.

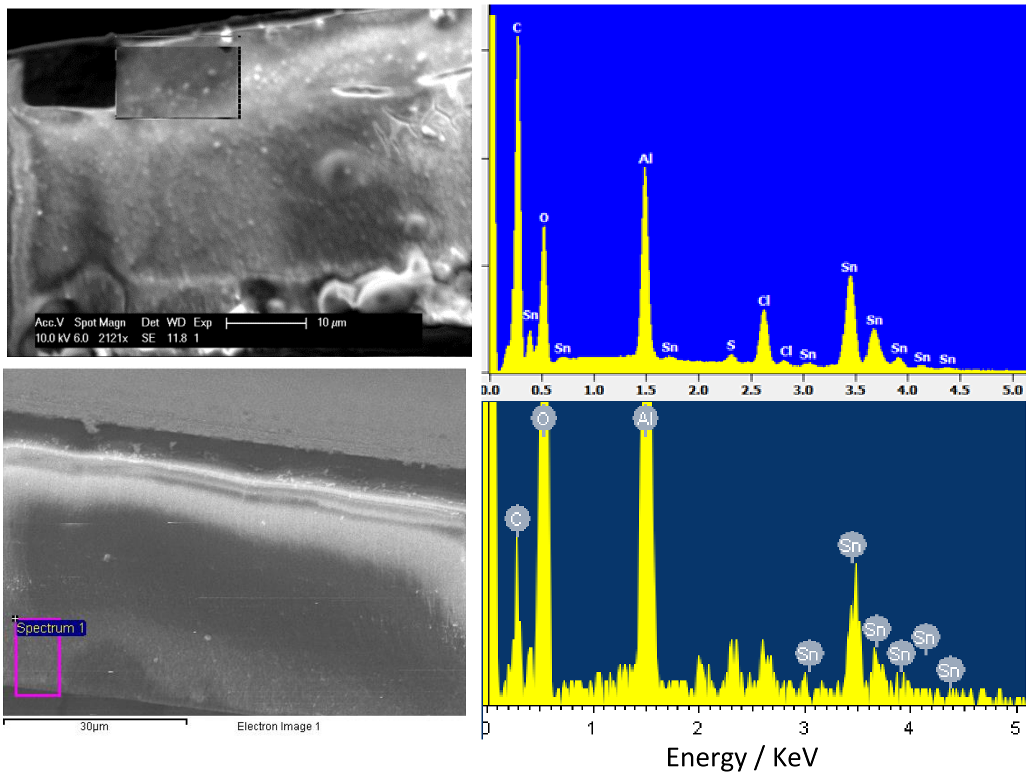

Figure 5.12 EDX on 13 nm non-grafted (top) and grafted (bottom) AAO filled with Sn.

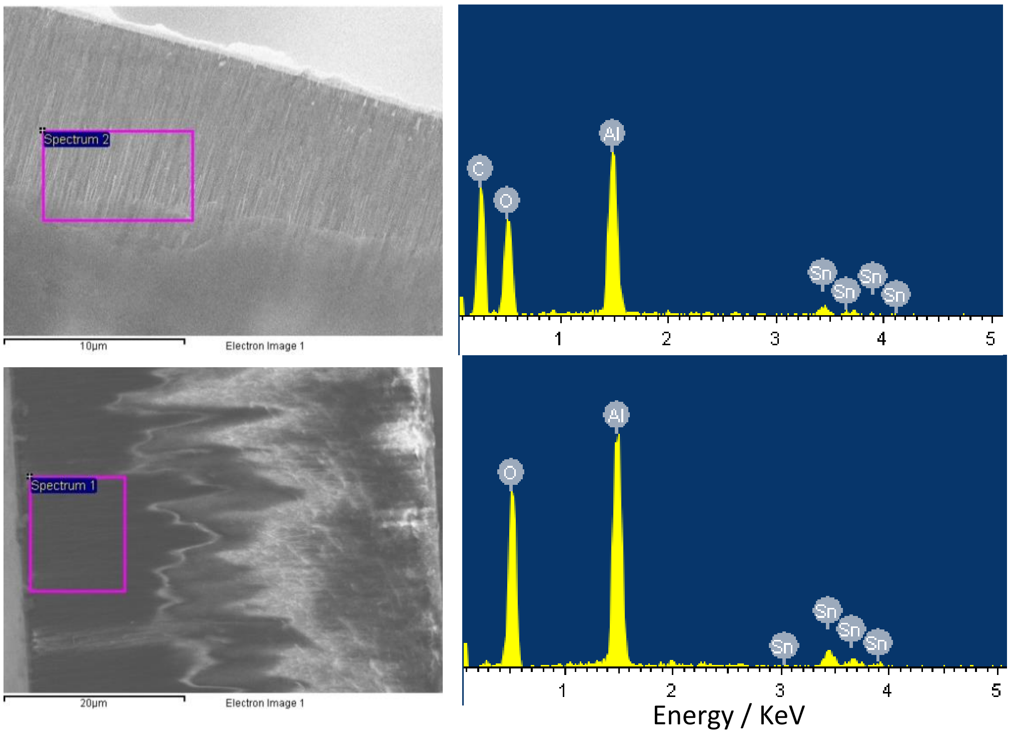

Figure 5.13 EDX on 55 nm non-grafted (top) and grafted (bottom) AAO filled with Sn.

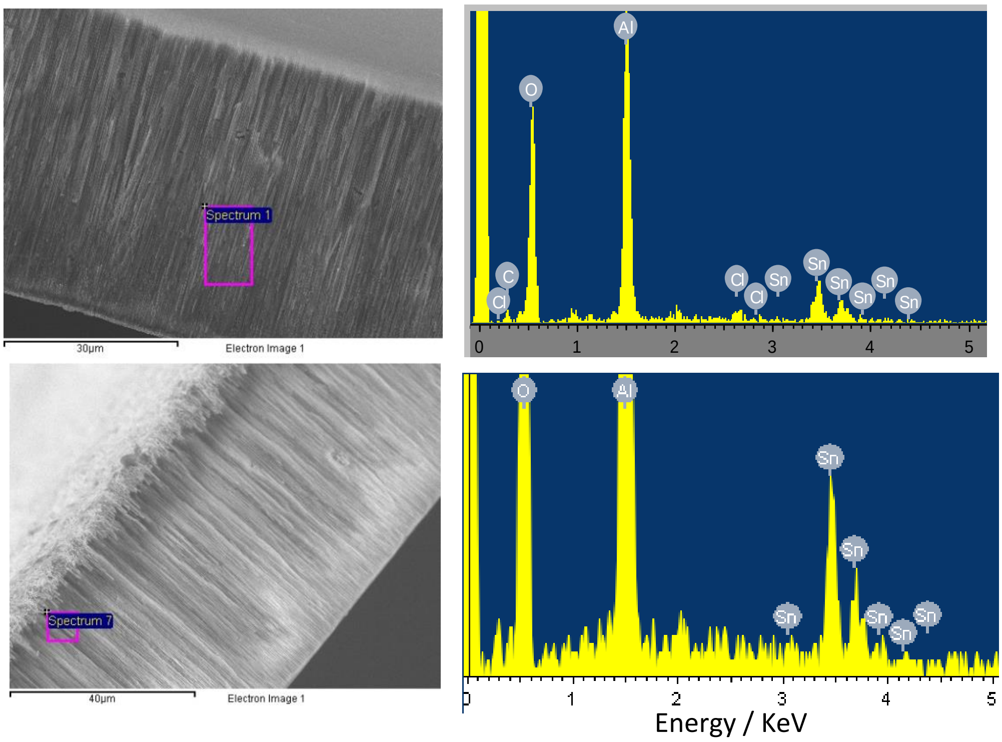

Figure 5.14 EDX on 200 nm non-grafted (top) and grafted (bottom) AAO filled with Sn.

TEM measurement on un-grafted 55 nm pore diameter AAO from Figure 5.15, shows that tin wires have been partially deposited down the pores, leaving some of the pores empty. The possible explanation is the surface tension preventing even electrolyte access into all the pores.

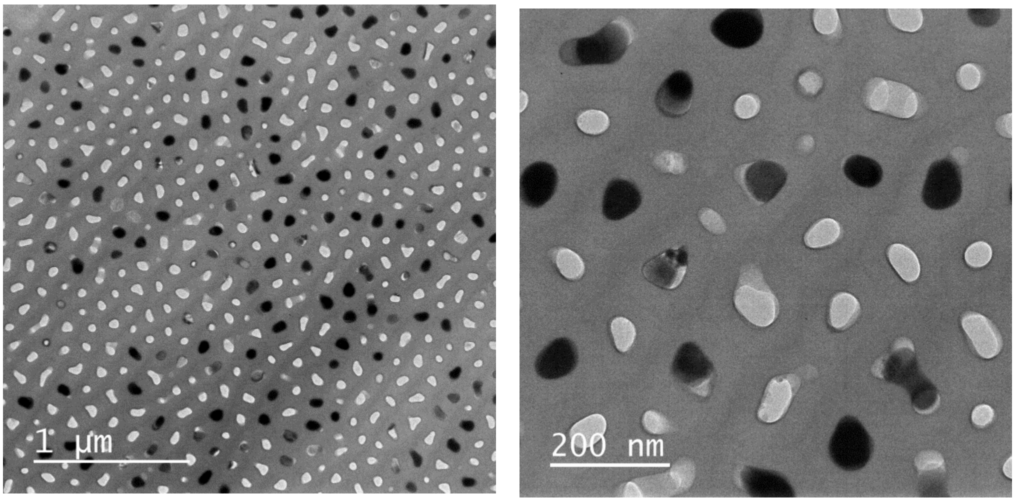

Figure 5.15 TEM image on un-grafted AAO after Sn electrodeposition. Black dots show the electrodeposited tin inside the pores.

In some cases tin wires can also be observed in the cross-section SEMs on the membranes after the ED process. Figure 5.16 is the cross-section SEM on the 55 nm membrane grafted and un-grafted. Tin nanowires were observed in some of the pores in the un-grafted AAO, in the form of white wires inside the pores. Some breakage in the wires is observed. In contrast no evidence for tin in the grafted membranes was seen. Accordingly the grafting process has increased the limitation on the numbers of filled pores. Figure 5.16 also indicates a reduction in the pore volume after the grafting process, which might explain the smaller proportion of filled pores.

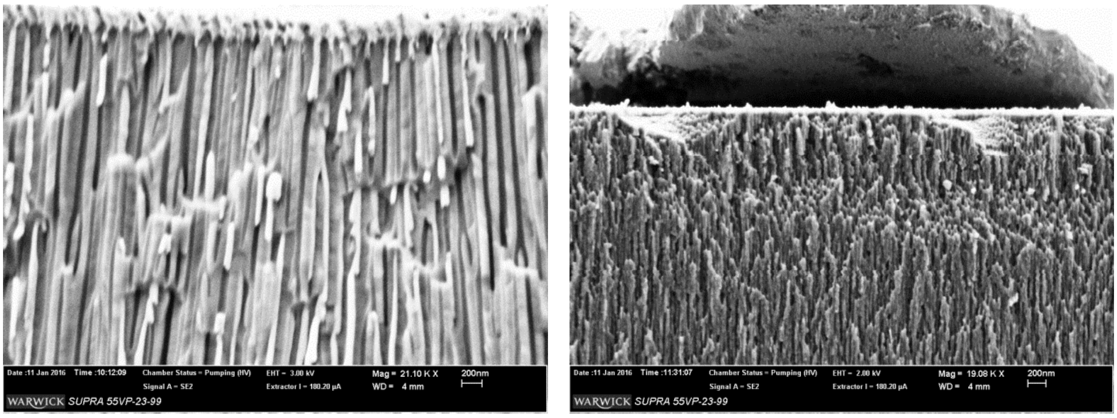

Figure 5.16 Cross-section SEM on 55 nm AAO after Sn electrodeposition, un-grafted (left) showing Sn nanowires inside the pores and grafted (right), the white coloured wires are the electrodeposited tin.

5.4.3 XRD experiments

Grazing incidence scans, using 1° incidence angle, were run on the samples before and after removing the overgrown Sn from the membrane surface. Figure 5.17 (red) shows an example of XRD collected on the overgrown tin. Subsequently symmetric XRD scans were collected on the samples on the overgrown tin and to access the tin deposits inside the pores after the overgrowth removal process. Finally to verify the crystallite orientations observed from the symmetric XRD, in-plane pole figure measurements were run on the wires inside the templates.

The symmetric scan XRD patterns on the membranes before removing the overgrowth, indicates Sn with <200> dominant texture for the overgrowth on top of the grafted membranes (Figure 5.17 blue). Symmetric XRD patterns collected after the overgrown material (if existed) was mostly removed from the top of the templates, hence accessing the inside of the pores, are shown in Figure 5.18. Tin was detected in all cases and always <200> was the dominant oriented plane. The texture observed in the symmetric XRD patterns on the overgrown material was compared to the texture for the wires inside the pores after removing the overgrowth. The consequence was the tin has overgrown with almost the same orientation as the wires inside the pores. For instance the symmetric XRD pattern in Figure 5.17 is for the 13 nm membrane in Figure 5.18 before removing the overgrowth. The two patterns show same orientation with some changes in the Sn 101/Sn 200 intensity, which has shown an increase in the pattern for the wires compared to that for the flat Sn on the surface. An elongation along Sn <101> in the grazing incidence scan pattern for the sample after the overgrowth removal, is possibly due to alignment in the sample with respect to the X-ray beam during the XRD collection.

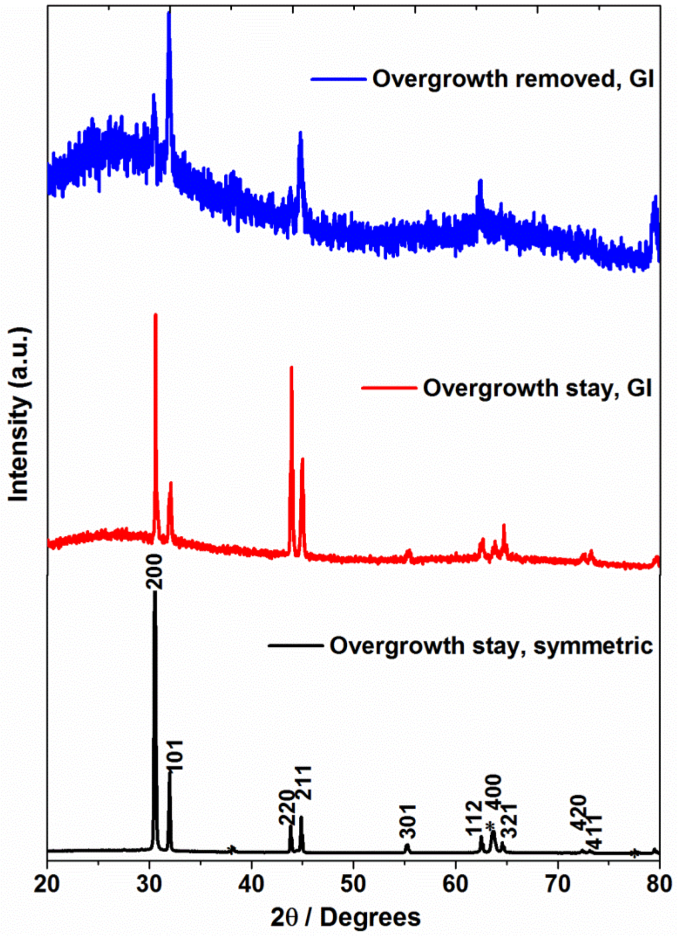

Figure 5.17 XRD patterns collected on Sn in un-grafted 13 nm diameter AAO, electrodeposited from an electrolyte containing from 10 mmol dm^{-3} of [N^{n}Bu$_4$][SnCl$_3$] and 10 mmol dm^{-3} [N^{n}Bu$_4$]Cl in CH$_2$Cl$_2$, at -1.5 V. The deposition time was 3.5 h. the patterns are for 1° grazing incidence scans, overgrowth removed (blue), 1° grazing incidence scans, overgrowth stayed (red) and symmetric scan, overgrowth left in place (black).

The XRD signal for Au from the sputtered gold layer in the bottom of the pores is detected in the 200 nm diameter pore AAO, it was previously mentioned that tin was detected on the back of these samples caused by electrolyte leakage through the membrane. Thus the templates could not be filled to the top, even after 5 h of deposition. Similarly in the case of 13 nm un-grafted templates Au signals are picked by the X-ray detector, in this case it is believed that the pores are non-uniformly filled with tin, so a number of pores are left out and the X-ray has accessed to the substrate. However overgrowth was detected on the surface, which might be due to lateral growth of tin from the filled pores and covering the neighbouring pores and blocking them from the top. Thus after the removal of the overgrown material these pores are revealed to be empty, we expect higher ratio of unfilled pores in the grafted 13 nm membrane.

Sn <200> oriented tin wires were observed in all cases. In two cases, the 13 nm un-grafted and 200 nm grafted membranes, this preferred orientation was less strong. The reason may be the incomplete removal of the overgrowth. This could also imply the presence of wires with other orientations.

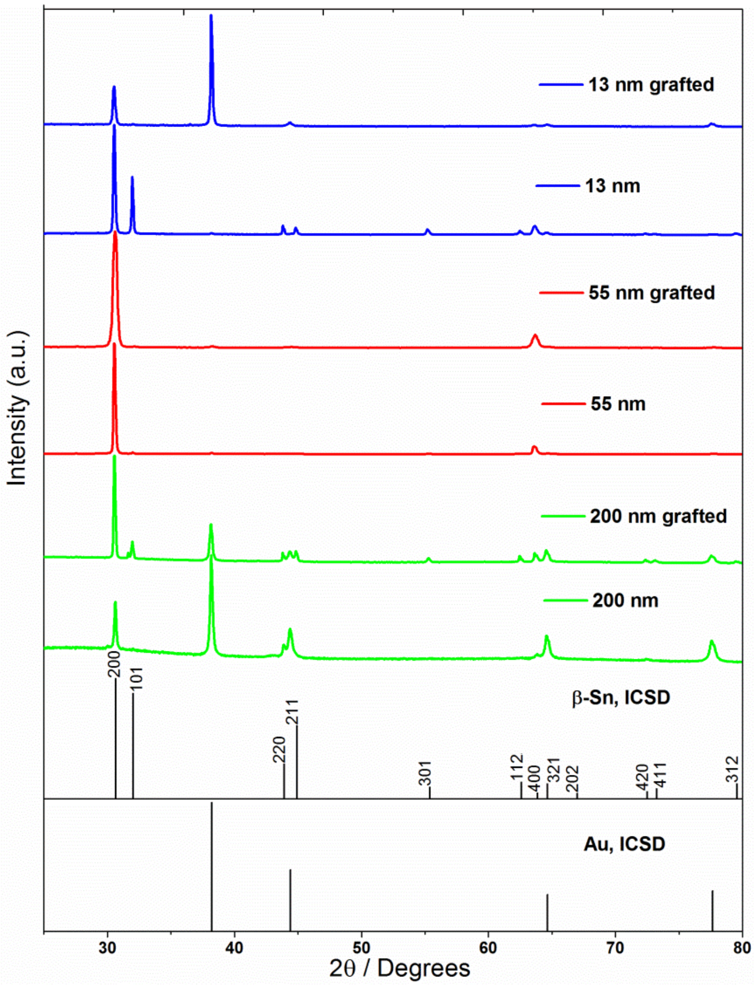

Figure 5.18 Symmetric XRD patterns on Sn electrodeposited in AAO at room temperature, from an electrolyte containing 10 mmol dm^{-3} of [N^{n}Bu$_4$][SnCl$_3$] and 10 mmol dm^{-3} [N^{n}Bu$_4$]Cl in CH_2Cl_2. The deposition potential was -1.5 V vs. Ag/AgCl and the deposition time varied for the individual experiments between 2.5 and 5 h followed by overgrowth removal. The states of the AAO templates and the pore diameters are indicated on the patterns.

Pole figure experiments were performed using the in-plane geometry, with the benefit of keeping the samples flat on the stage without any tilt movement. The use of this geometry was essential in this work, as the AAO membranes are very fragile and not easy to handle and stick to the stage. The observations from the symmetric scans show Sn <200> orientation with some times slight enhancement along Sn <101> plane. Accordingly PF measurements were performed on Sn 200 and Sn 101 diffraction peaks.

The inner-angles between the crystal planes can be calculated using the formula for the tetragonal structure.[118]

$$\cos\emptyset = \frac{\frac{h_1h_2+k_1k_2}{a^2}+\frac{l_1l_2}{c^2}}{\sqrt{\left(\frac{{h_1}^2+{k_1}^2}{a^2}+\frac{{l_1}^2}{c^2}\right)\left(\frac{{h_2}^2+{k_2}^2}{a^2}+\frac{{l_2}^2}{c^2}\right)}} \tag{22}$$

Where Ø is the angle between the planes, *(h,k,l)* are the Miller indices and *(a,c)* are the lattice constants.

PF analysis on Sn in 13 nm un-grafted AAO (Figure 5.19) show, an intense peak in the centre of the pole figure collected on Sn 200 diffraction plane, showing strong Sn <200> orientation. The Sn 101 PF on the same sample shows a dot at the centre of the pole, the peak at 90° in the cut-line pattern corresponds to the dot in the 2D projection, showing 101 axis alignments. A ring at ~31° from the pole centre, which is identical to the angle between Sn 101 and Sn 301 determined using the Ø value from Equation 1, this ring is corresponded by a peak in the cutline pattern. Hence Sn <101> and Sn <301> orientations are identified from the PF measurement. The orientation is ~ 1/6th of those with the Sn <200> orientation, measured from the intensity ratios of the peaks in the cutline patterns.

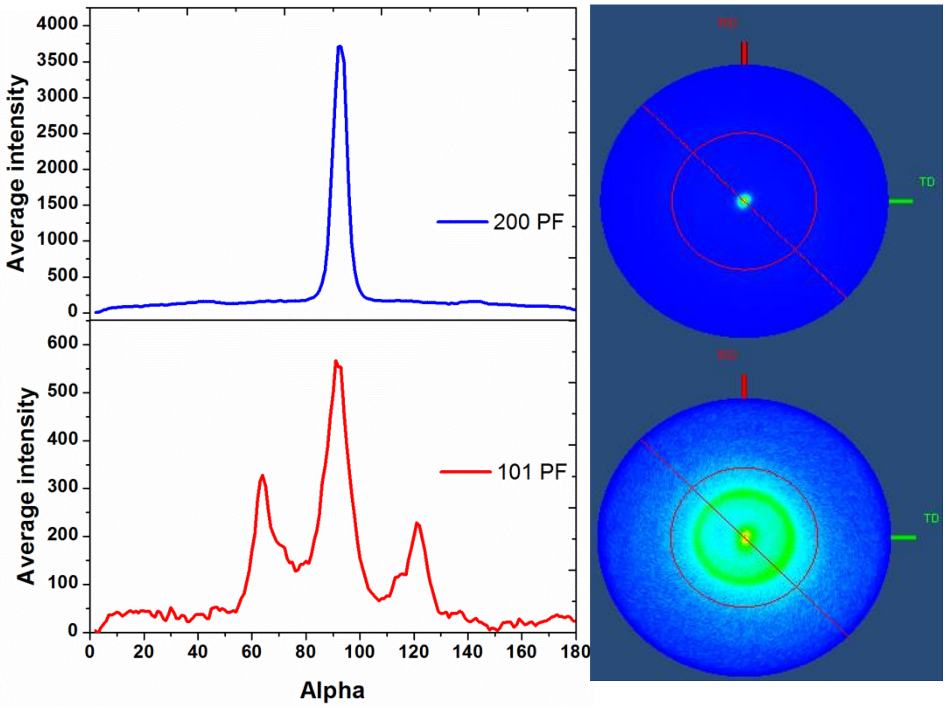

Figure 5.19 Pole figure measurement, cutline patterns (left) and 2D projections (right) on (200) and (101) planes for Sn in an un-grafted 13 nm pore diameter AAO membrane.

PF analysis on Sn in 55 nm un-grafted AAO (Figure 5.20) exhibits an intense peak at 90°, showing strong Sn <200> orientation. The Sn 101 PF on the same sample shows Sn <101> axis alignment albeit with much weaker intensity. Orientations along the Sn <200> and Sn <301>are also observed. The Sn <101> orientation is ~ 1/10th as intense as the Sn <200> and Sn <301> is very weak.

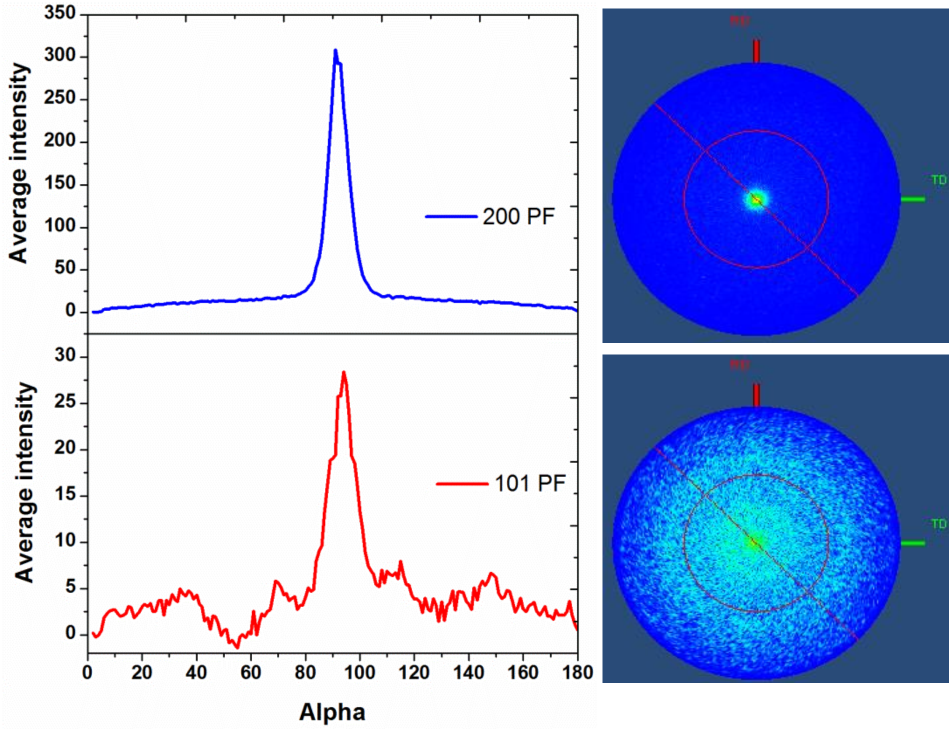

Figure 5.20 Pole figure measurement, cutline patterns (left) and 2D projections (right) on 200 and 101 planes for Sn in an un-grafted 55 nm pore diameter AAO membrane.

In the Sn 200 PF on the tin deposited inside the 200 nm un-grafted AAO (Figure 5.21), strong <200> orientation is observed. This was characterised by the dot at the centre of the pole which is also represented in the cut-line pattern by a peak at 90°. Sn 101 PF exhibits a very weak peak at centre of the pole indicating slightly Sn <101> orientation. Weak and scattered intensity on the 2D projection represented by a peak at 61° on the cut-line pattern, showing <200> orientation.

The results from the pole figure measurements confirms the predicted orientations observed from the symmetric scan, but is more sensitive to the presence of small quantities of wires with an alternative orientation. Sn <200> was the dominant oriented plane in all cases. Increased presence of Sn <101> and Sn <301> orientation is observed with decreasing the diameter of the produced wires, at 55 and 13 nm.

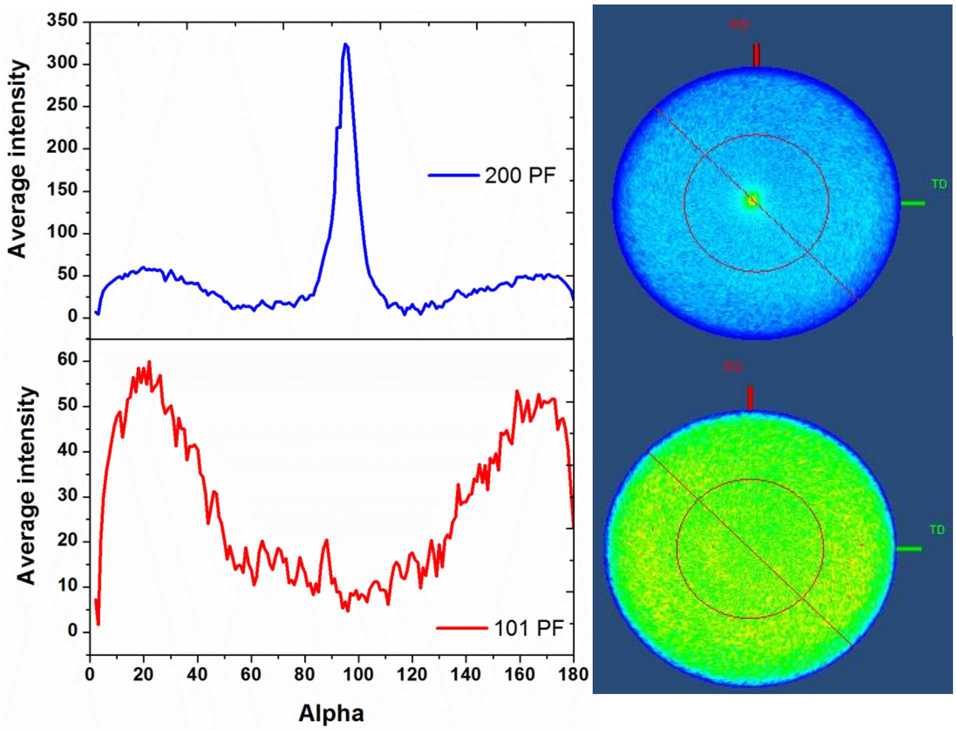

Figure 5.21 Pole figure measurement, cutline patterns (left) and 2D projections (right) on 200 and 101 planes for Sn in an un-grafted 200 nm pore diameter AAO membrane.

5.5 Sn electrodeposited from SCF

Electrodeposition of tin was worked on in a project under supercritical fluid electrodeposition (SCFED) project and I had a role in characterising the electrodeposits using X-ray diffraction based techniques. Tin electrodeposition was tested on flat titanium nitride (TiN) electrode on silicon in supercritical difluoromethane, $scCH_2F_2$, using the same reagent used in our work. The amounts used were 2 mM $[^nBu_4N][SnCl_3]$ and 50 mM $[^nBu_4N]Cl$ [P. N. Bartlett, R. Beanland, J. Burt, M. M. Hasan, A. L. Hector, R. J. Kashtiban, W. Levason, A. Lodge, S. Marks, J. Naik, A. Rind, G. Reid, P. W. Richardson, J. Sloan, D. C. Smith, submitted to Nano Letters]. The electrodeposition potential applied was -1.2 V vs. Pt, at 86 °C and under the pressure of 18.18 MPa. XRD analysis shown in Figure 5.22 on the sample has revealed a set of peaks associated with the tetragonal tin phase. The intensity distribution of the peaks indicates a polycrystalline structure. Peaks for TiN from the substrate are identified in the pattern, a further phase, observed in the pattern matches the orthorhombic TiO_2 phase. The experimental conditions associated with electrodeposition from SCF electrolytes such as specific temperature and pressure may have caused substrate oxidation.

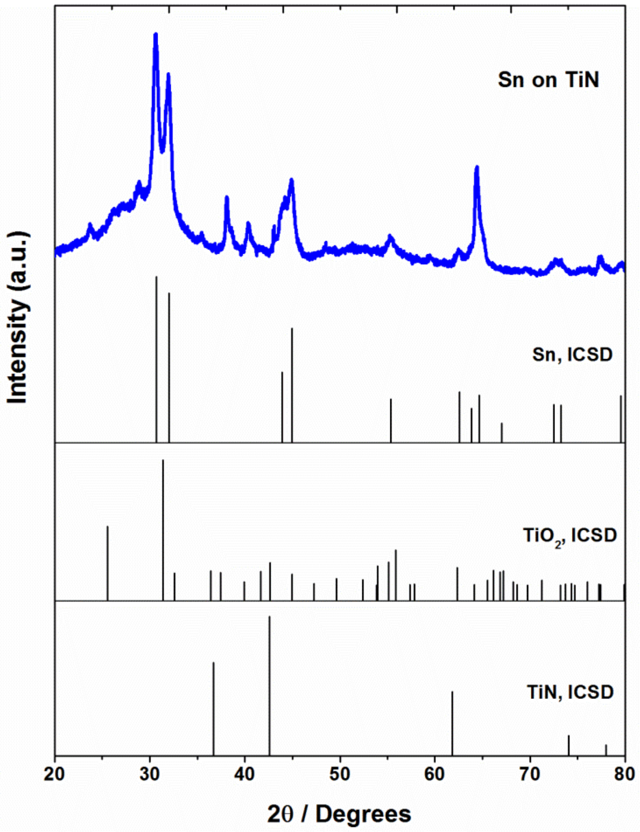

Figure 5.22 XRD pattern for 1° grazing incidence scan on Sn electrodeposited from [^{n}Bu$_4$N] [SnCl$_3$] in scCH$_2$F$_2$ on TiN substrate.

The project covers supercritical electrodeposition of tin into anodic alumina templates from an electrolyte containing 2 mM [^{n}Bu$_4$N] [SnCl$_3$] + 50 mM [^{n}Bu$_4$N]Cl in scCH$_2$F$_2$. The deposition potential applied was -2 V vs. Pt disc reference electrode, for 10000 s, the experiment was held under temperature and pressure of 85 °C and 17.9 Mpa. Symmetric XRD measurement on the wires inside the template has indicated the presence of tin inside the 55 nm pore diameter membranes (Figure 5.23). Elongation in the Sn <200> axis, similarly to the deposition from CH$_2$Cl$_2$, was observed in the pattern, suggesting Sn <200> orientation in the wires.

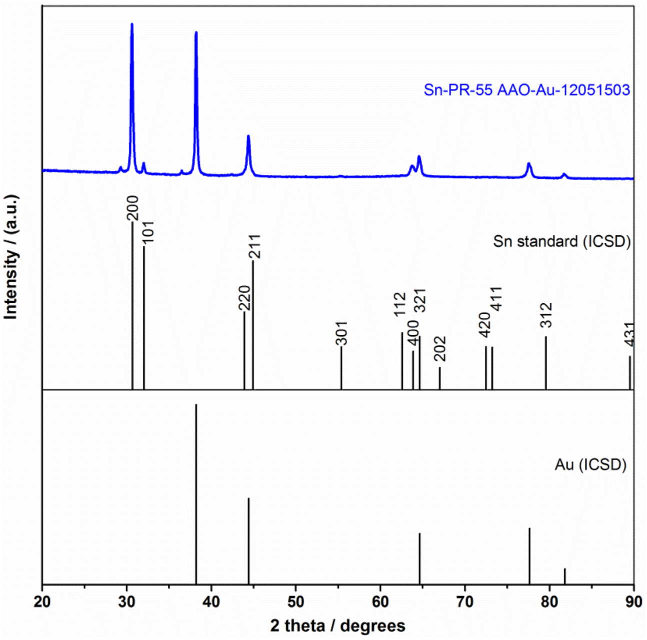

Figure 5.22 XRD pattern for symmetric scan on Sn electrodeposited into 55 nm AAO from [N^nBu_4][$SnCl_3$] in scCH_2F_2.

5.6 Conclusion

Tin was electrodeposited in the form of thin films on Au substrate and nanowires in AAO membranes. An electrolyte containing 10 mmol dm^{-3} of Sn reagent [N^nBu_4][$SnCl_3$] and 10 mmol dm^{-3} of supporting electrolyte [N^nBu_4]Cl dissolved in the dried organic solvent, CH_2Cl_2 was used. Chemical handling, electrolyte preparation and the electrochemical experiments were performed in an anaerobic atmosphere, due to air sensitivity of [N^nBu_4][$SnCl_3$]. The electrochemistry of Sn in the electrolyte on Au electrode was studied by cyclic voltammetry, and the electrodepositions were achieved by chronoamperometry. The products were examined using SEM, EDX and XRD techniques.

Electrodeposition of tin on Au was performed at various deposition temperatures, the deposition temperatures ranged between 35 °C and -78 °C. In the CVs, Sn^{+2} reduction to Sn^0 at room temperature was determined to occur at a potential of -1.3 V, this value was shifted to -1.5 V in the CVs at 35 °C. This peak has occurred at lower cathodic potentials for the CVs at 0 °C and -16 °C, and the -78 °C experiment has shown an unusual CV response, which contained a loop and a peak in the return scan.

Tin produced at low temperatures exhibited very low thicknesses when grown for only one hour, which made the characterisation experiments difficult to apply, especially the XRD. Thus a longer deposition time of four hours was applied to grow thicker tin. The morphologies of tin films obtained from 1 h deposition show blocks of agglomerated particles, the blocks have undergone reduction in their size with reducing the bath temperature. The thicker tin deposits exhibit more dendritic morphologies and generally smaller particle sizes at the surface, except in the tin obtained at -78 °C, the particles size is ~ 300 nm. The morphology of the room temperature tin was particularly different, showing nanowires agglomerated in the form of bundles. Grazing incidence scans on tin films grown for 4 hours have shown peaks associated with the tetragonal tin phase known as β-Sn. No evidence of the cubic tin (α-Sn) was found in the XRD patterns, even at electrolyte temperatures below the β-Sn/ α-Sn phase transition. Some crystallite texture was detected in the films from the symmetric XRDs, as Sn <101> orientation was observed in the deposits obtained at ambient temperature and temperatures below ambient, while the tin at 35 °C exhibited structure.

The second part of this work is tin nanowires electrodeposition into anodic alumina templates. The AAO was coated with a layer of gold from one end to produce an electrical contact. Relying on the CV results on the gold substrates in part one, constant deposition potentials were selected. The templates used included grafted and un-grafted AAO having pore diameters of 13, 55, and 200 nm. Electrodepositions were performed at room temperature, a number of experiments were processed at -16 °C, and the results were similar to those obtained at room temperature. The amount of charge needed to fill the pores was estimated using mathematical calculations. Chronoamperometry at -1.5 V was applied for deposition times calculated to be enough to fill the pores. Overgrown tin on the surfaces of the grafted and un-grafted 13 nm and 55 nm templates was observed. But the 200 nm templates have allowed the electrolyte to diffuse through the gold coating, hence electrodeposition occurred on the back of the membranes alongside the deposition inside the pores. Thus the complete filling of the pores could not be obtained even with deposition times as long as 5 hours. Symmetric XRD patterns on the templates after the overgrowth was removed have indicated Sn <200> dominant orientations in every case, with some Sn <101> alignment in some cases. The pole figure measurements also have shown Sn <200> dominant orientations with some Sn <101> and Sn <301> orientations in some of the wires.

Chapter 6 Conclusion and future works

6.1 Conclusion

In this thesis thin films of Ni, Ni-B, Ge, Sn and nanowires of Sn were produced using various electrodeposition (ED) techniques. The physical and chemical properties of these elements make them key ingredients in electronic and optoelectronic device fabrications, most interestingly in their thin film forms or as nanostructures. The focus in this study is on the factors affecting the physical and chemical properties of the deposited material. This was achieved by changing various parameters during the films EDs, such as substrate materials and nature, film compositions and thicknesses and electrolyte compositions and temperature. The deposits were then subjected to a series of characterisation techniques.

In one project Ni and Ni-B thin films were electrodeposited by chronopotentiometry from an aqueous electrolyte onto gold sputtered on glass. The samples were then characterised to examine changes in their morphology, composition, structure, texture and stress with thickness, B content and the current density variations during the film productions. In the second project thin films of Ge on TiN on silicon were produced from an organic electrolyte by chronoamperometry. The Ge films initially were amorphous and exhibited cracked and peeled morphologies. Various modification procedures were applied to improve the morphology and the adhesion in the films. In some cases high temperature annealing was applied to the films to obtain crystalline Ge. Finally a project was undertaken to electrodeposit Sn on flat Au and into anodic alumina (AAO) membranes by chronoamperometry. Sn thin films were produced on Au from an organic electrolyte at various temperatures, using long and short deposition durations. Characterisations were performed to examine the morphology, composition, structure and the texture of the produced films. Another goal in various temperature depositions was to obtain the atmosphere unstable α-Sn phase, but this was not achieved. Electrodeposition of templated Sn nanowires was carried out using the same procedure applied in flat Sn productions and wires with diameters down to 13 nm were grown.

Galvanostatic (CP) and potentiostatic (CA) techniques are employed here as the electrodeposition methods. Galvanostatic ED was often accomplished using only a 2 electrode cell, the working electrode (WE) and the counter electrode (CE), which is acting as the reference electrode (RE) and the CE, in this easy to operate system. In addition ED can be obtained at different current densities. The potentiostatic ED, often performed using a 3 electrode cell, with the advantage of controlled stoichiometry when alloy materials are electrodeposited.[229] In our work the potentiostatic ED was used in the deposition of Ge and Sn, with the benefit of varied deposition overpotentials in the film productions, and this allowed us to study the effect of overpotential variation on the properties of the electrodeposits. Ni was electrodeposited using the galvanostatic method using a 2-electrode cell, which consisted of a Ni anode and gold on glass as the cathode (the substrate). The method has allowed us to study the effect of current density variation during the ED on the quality of Ni films. Similar systems have been used for same parameter variations during Ni deposition in literature.[100, 125] In the projects accomplished using potentiostatic ED, Ge and Sn films, the method has allowed the electrochemistry of the element's reagent on the substrates to be studied using CVs. Thus the CVs were used to choose the deposition potentials. We were able to produce ED at various deposition potentials around the reduction peak observed in the CVs. This variation was useful in studying the effect of the overpotential on the morphology, composition and the crystallinity of the deposited material.

The ED experiments were investigated in a number of electrolyte phases, starting from aqueous to organic and then supercritical electrolytes. An aqueous electrolyte consisting of Watt's bath was used in the production of Ni films. This is the standard method to deposit Ni based films used industrially. The advantages of this Ni bath over the other electrolytes used in this work were that it is an easy to operate system and no air sensitive reagents were used. The disadvantages were the high number of bubbles during the deposition as a result of electrolyte electrolysis and the highly stressed films could also result from the employment of aqueous electrolyte. On the other hand the ED from the organic electrolyte of DCM has required careful treatment of drying and storage in inert atmosphere during the use. DCM is a volatile solvent with the boiling point of 39.75 °C,[230] therefore temperature variation must be done with care, it is also hazardous, therefore careful handling is needed. However DCM exhibits much lower surface tension compared to water and can be efficiently dried to be compatible with ED from air and moisture sensitive reagents. In addition a good dried organic electrolyte will allow electrodeposition from air and moisture sensitive reagents and electrodeposition of reactive elements such as germanium, which are the cases in this work.

Although some unreactive metals can be easily electrodeposited from an aqueous electrolyte, using an organic electrolyte may offer the advantages to improve particular properties within the products. No detailed study on the internal stress measurement in Ni electrodeposition from non-aqueous electrolyte is found. Employing other electrolyte phases in Ni ED was studied by others. In a paper by Neuróhr et al.,[231] Ni was deposited from several alcoholic electrolytes, the films were found to possess large internal stress, except in the case of methanol. Comparing the ED of the two metals fabricated in this work (Ni and Sn) on the same Au on glass electrode, Ni was obtained from aqueous electrolyte and Sn was from an organic electrolyte. The Ni films were found highly stressed, where the thick films mostly were peeling on the edges of the substrate. In the literature, Ni was electrodeposited from Watt's Ni bath in supercritical carbon dioxide ($scCO_2$),[232] and $scCO_2$ emulsion.[102] They have compared the internal stress in the Ni from these electrolytes to the Ni from conventional aqueous Watt's electrolyte and reported it to be higher. In our work, the stress in Sn films was not measured, as the time did not permit, but cracks or peeling were not observed in the morphology of the films, even in the ones obtained from ED over the period of 4 hours. Thus one can assume small internal stress in these films. To determine the effect of electrolyte phase on the internal stress in tin thin films, it is worthwhile to measure the stress in a sample ED from an organic electrolyte and compare to an aqueous electrolyte derived sample.

The effect of additives on the properties and the quality of the deposits was studied in the ED processes of Ni, Ni-B and Ge thin films. Adding sucrose to the composition of the Ni bath has resulted in reduced crystallite size, strain and stress in the Ni film, with the incorporation of improvements in morphology in the Ni-B films. In the Ge ED experiments the CTAB and OAm surfactants were tried and promising results were obtained in the Ge films, where growth was modified by CTAB. Better adhesion of Ge film to the TiN substrate was achieved after the high temperature thermal annealing application. Many papers describe the effects of additives on the properties of the electrodeposited materials. Influence from organic additives such as surfactants,[27] polymers,[233] saccharin[104] and pyridine[94] on a number of properties within Ni based electrodeposits is reported. Changes in morphology, preferred orientation,[84] and improvement in current efficiency and mechanical properties were observed when using organic additives in Ni based electrodepositions.[27, 111] Previous studies show small influence from inorganic additives in electrodeposited Ni.[83, 93] Oleylamine surfactant is widely employed in germanium nanoparticles and nanowire synthesis,[169, 172] it was used in our work as a modifier for the morphology and adhesion in the electrodeposited Ge thin films.

One of the key measurements in this work was the orientation in the electrodeposited crystalline samples. The crystallographic texture information on the crystallites was established from the symmetric (θ/2 θ) X-ray diffraction data and the pole figure measurements collected on the samples. The texture information obtained from PF measurements confirms the observations from the symmetric scans. Besides PF is more powerful in observing small amount of a different orientation in cases where one or more dominant orientation is identified. For instance the case of tin wire in the 13 and 55 nm AAO membranes, small fractions of the wires are found to possess orientation along the Sn <301> axes. Such information was not resolved in the symmetric XRD patterns. Similarly in the Ni-B films, texture information could not be obtained from the symmetric scan, as the Ni (111) was the only observed peak for Ni. The PF results on these films have shown characteristic information on the crystallite orientation. There are several advantages of PF over symmetric scan, for instance the preferred orientations parallel to the sample plane are not detected by symmetric XRD.[234]

6.2 Future works

This thesis covers the electrodeposition and characterisation of Ni, Ni-B, Ge and Sn thin films and nanowires of Sn. Although the electrodeposits are studied in detail using wide range of examinations, more investigation in some areas and properties is functional. The work on Ni and Ni-B deposition accomplished with deep detailed study, thus no further work required. Further works could give clearer and deeper understanding about the other projects, we will assemble them in the following list of suggestions:

1- Selecting a compatible oxide substrate in Ge electrodeposition project, a number of metal oxides to be tested for instance tin oxide (SnO_2).
2- Electrodeposition of Ge into anodic alumina substrate of different pore diameters from dichloromethane (DCM) based electrolyte, in which the ratio of post-deposition oxidation of Ge is expectedly reduced.
3- Chemical and electrochemical treatment of the Au flat substrates in tin electrodeposition pre the electrodepositions from cooled electrolyte, such as forming a seeding layer to inhibit the growth of the desired Sn phase.
4- Carry out Sn nanowire deposition at adequate high temperature to reduce the surface tension of DCM solvent and ease the pore access and prevent pore blockage during the electrodeposition process.

List of References

[1] K. Krishnaveni, T. S. N. Narayanan, S. K. Seshadri *Mater. Chem. Phys.* **2006**, 99, 300.

[2] A. M. Rashidi, A. Amadeh *J. Mater. Sci. Technol.* **2010**, 26, 82.

[3] K. Seshan, Handbook of thin film deposition processes and techniques, principles, methods, equipments and applications, Noyes publication, New York, **2002**.

[4] L. B. Freund, S. Suresh, Thin Film Materials: Stress, Defect Formation and Surface Evolution, Press syndicate of the university of Cambridge, UK, **2003**.

[5] A. R. Boccaccini, I. Zhitomirsky *Curr. Opin. Solid State Mater. Sci.* **2002**, 6, 251.

[6] I. Zhitomirsky *Adv. Colloid. Interface Sci.* **2002**, 97, 279.

[7] F. Nasirpouri, S. J. Bending, L. M. Peter, H. Fangohr *Thin Solid Films*. **2011**, 519, 8320.

[8] J. Ke, W. Su, S. M. Howdle, M. W. George, D. A. Cook, M. P. Abel, P. N. Bartlett, W. Zhang, F. Cheng, W. Levason *Proc. Natl. Acad. Sci.* **2009**, 106, 14768.

[9] S. M. Janjan, F Nasirpouri, M. G. Hosseini *Russ. J. Electrochem.* **2011**, 47, 787.

[10] P. N. Bartlett *Electrochem. Soc. Interface*. **2004**, 13, 28.

[11] D. Oloruntoba, O. Eghwubare, O. Oluwole *Leonardo El. J. Pract. Technol.* **2010**, 10, 79.

[12] Y. D. Gamburg, L. G. Zangari, Theory and practice of metal electrodeposition, Springer, London, **2011**.

[13] T. Osaka *Electrochimica Acta*. **2000**, 45, 3311.

[14] P. C. Andricacos *Electrochem. Soc. Interface*. **1999**, 8, 6.

[15] W. Schwarzacher *Electrochem. Soc. Interface*. **1999**, 8, 20.

[16] W. Schwarzacher *Electrochem. Soc. Interface.* **2006**, 15, 32.

[17] T. Liese, V. Radisch, H. U. Krebs *Rev. Scient. Instr.* **2010**, 81, 073710.

[18] P. C. P. C. Andricacos, C. Uzoh, J. O. Dukovic, J. Horkans, H. Deligianni *IBM Res. Dev.* **1998**, 42, 567.

[19] T. Onishi, T. Yoshikawa *Mater. Trans.* **2002**, 43, 1605.

[20] C. A. Ross *Annu. Rev. Mater. Sci.* **1994**, 24, 159.

[21] R. Oriňáková, K. Rošáková, A. Oriňák, M. Kupková, J. N. Audinot, H. Migeon, J. T. Andersson, K. Kovaľ *J. Solid State Electrochem.* **2011**, 15, 1159.

[22] M. Schlesinger, M. Paunovic, Modern Electroplating, John Wiley and Sons, Inc., New Jersey, **2010**.

[23] D.Y. Park, B. Yoo, S. Kelcher, N. Myung *Electrochim. Acta*. **2006**, 51, 2523.

[24] M. paunovic, M. Schlesinger, Fundamentals of electrochemical deposition, John Wiley & Sons. Inc., New Jersey, **2006**.

[25] F. Delaunois, J. P. Petitjean, P. Lienard, M. Jacob-Duliere *Surf. Coat. Tech.* **2000**, 124, 201.

[26] W. L.Tsai, P. C. Hsu, Y. Hwu, C. H. Chen *Nature*. **2002**, 417, 139.

[27] Y. C. Chuang, S. T. Chung, S. Y. Chiu, C. Y. Li, W. T. *Thin Solid Films*. **2013**, 529, 322.

[28] N. Wakeham, A. F. Bangura, Xi. Xu, J. F. Mercure, M. Greenblatt, N. E. Hussey *Nat. Commun.* . **2011**, 2, 396.

[29] G. Zangari *Coatings*. **2015**, 5, 195.

[30] A. W. Bott *Curr. Sep.* **1998**, 17, 87.

[31] G. Pulletikurthi, A. Lahiri, T. Carstens, N. Borisenko, S. Zein El Abedin, F. Endres *J. Solid State Electrochem.* **2013**, 17, 2823.

[32] J. Ristein *Science*. **2006**, 313, 1057.

[33] E. Chassaing, J. F. Guillemoles, D. Lincot *ECS Transactions*. **2009**, 19, 1.

[34] T. Seki, M. Onaka *Chem. Lett.* **2005**, 34, 262.

[35] S. P. Sawan, Supercritical fluid cleaning: fundamentals, technology and applications, Noyes publications, USA, **1998**.

[36] P. Gopaliya, P. R. Kamble, R. Kamble, C. S. Chauhan *Int. J. Pharm. Res. Rev.* **2014**, 3, 59.

[37] J. M. Blackburn, D. P. Long, A. Cabanas, J. J. Watkins *Science*. **2001**, 294, 141.

[38] I. Hwang, J. M. Kim, H. Kim *J. Electrochem. Soc.* **2011**, 159, D46.

[39] P. N. Bartlett, D. A. Cook, M. W. George, A. L. Hector, J. Ke, W. Levason, G. Reid, D. C. Smith, W. Zhang *Phys. Chem. Chem. Phys.* **2014**, 16, 9202.

[40] P. N. Bartlett, D. C. Cook, M. W. George, J. Ke, W. Levason, G. Reid, W. Su, W. Zhang *Phys. Chem. Chem. Phys.* **2011**, 13, 190.

[41] F. Scholz, Electroanalytical Methods: Guide to Experiments and Applications, Springer, Heidelberg, **2010**.

[42] A. W. Bott *Curr. Sep.* **2000**, 18, 1382.

[43] F. G. Thomas, G. Henze, Introduction to voltammetric analysis: theory and practice, Csiro Publishing, Australia, **2001**.

[44] C. G. Zoski, Handbook of electrochemistry, Elsevier, Netherlands, **2007**.

[45] J. O'M. Bockris, A. K. N. Reddy, Modern electrochemistry: an introduction to an interdisciplinary area, Plenum publishing corporation, New York, **1973**.

[46] S. I. Pyun, H. C. Shin, J. W. Lee, J. Y. Go, Electrochemistry of insertion materials for hydrogen and lithium, Springer Science & Business Media, Berlin, **2012**.

[47] D. Pletcher, A First Course in Electrode Processes, Royal Society of Chemistry, Cambridge, **2009**.

[48] G. Denault, M. V. Mirkin, A. J. Bard *J. Electroanal.Chem.* **1991**, 308, 27.

[49] R. Guinebretière, X-ray diffraction by polycrystalline materials, John Wiley & Sons, UK, **2013**.

[50] C. Hammond, Basics of Crystallography and Diffraction, Oxford University Press Oxford, GBR **2009**.

[51] J. I. Langford, D. Louer *Rep. Prog. Phys.* **1996**, 59, 131.

[52] M. Birkholz, Thin film analysis by X-ray scattering, Wiley. com, Weinheim, **2006**.

[53] M. Toru *Rigaku J.* **2009**, 25, 7.

[54] P. Dutta *Curr. Sci.* **2000**, 2000, 1478.

[55] M. Toru *Rigaku J.* **2009**, 25, 7.

[56] K. Shintaro *Rigaku J.* **2010**, 26, 3.

[57] H. M. Rietveld *J. Appl. Crystallogr.* **1969**, 2, 65.

[58] H. Putz, J. C. Schon, M. Jansen *J. Appl.Crystallogr.* **1999**, 32, 864.

[59] R. A. Young, The Rietveld Method, Oxford University Press Inc., United states, **1993**.

[60] A. C. Larson, R. B. Von Dreele *Los Alamos National Laboratory Report LAUR* **1994**, 86, 748.

[61] U. F. Kocks, C. N. Tomé, H. R. Wenk, Texture and anisotropy: preferred orientations in polycrystals and their effect on materials properties, Cambridge university press, Cambridge, **2000**.

[62] K. Nagao, E. Kagami *Rigaku J.* **2011**, 27, 6.

[63] K. N. Tu, Electronic Thin-Film Reliability, Cambridge university press, New York, **2011**.

[64] P. Russell, D. Batchelor, J. Thornton *Veeco Instruments Inc., AN46, Rev A*. **2001**, 1, 2004.

[65] S. Lampman, Characterization and Failure Analysis of Plastics, ASM International, USA, **2003**.

[66] R. Ludwing, Scanning electron microscopy: physics of image formation and microanalysis, Springer, Germany, **1998**.

[67] A. Kursheed, Scanning electron microscope optics and spectrometers, World scientific publishing Co. Pte. Ltd., Singapore, **2011**.

[68] K. Kanaya, S. Okayama *J. Phys. D: Appl. Phys.* **1972**, 5, 43.

[69] C. Lyman, D. ENewbury, J. Williams, A. Romig, J. Armstrong *J. Microsc.* **1991**, 164, 179.

[70] R. J. Ross, Microelectronics Failure Analysis: Desk Reference, ASM International, USA, **2011**.

[71] A. Naranjo, M. P. Noriega, T. Osswald, A. R-Alzate, J. D. Sierra, Plastics Testing and Characterization: Industrial Applications, Carl Hanser Verlag, Munich, **2008**.

[72] P. H. Holloway, P. N. Vaidyanathan, C. R. Brundle, C. A. Evans, Characterization of Metals and Alloys, Momentum Press LLC, New York, **2010**.

[73] R. F. Egerton, Physical Principles of Electron Microscopy: An Introduction to TEM, SEM, and AEM Springer Science+Business Media Inc., USA, **2005**.

[74] J. F. Watts in *X-ray photoelectron spectroscopy, Vol.* (Eds.: J. M. Walls, R. Smith), Elsvier Science Ltd., England, **1994**, pp.5.

[75] D. D. Sarma, P. K. Santra, S. Mukherjee, A. Nag *Chem. Mater.* **2013**, 25, 1222.

[76] A. Proctor, P. M. A. Sherwood *Anal. Chem.* **1982**, 54, 13.

[77] J. F. Watts, J. Wolstenholme, An Introduction to Surface Analysis by XPS and AES, John Wiley & Sons Ltd., England, **2003**.

[78] R. T. Haasch in *X-Ray Photoelectron Spectroscopy (XPS) and Auger Electron Spectroscopy (AES), Vol.*, Springer, New York, **2014**, pp.93.

[79] C. C. Chusuei, D. W. Goodman, Encyclopedia of Physical Science and Technology, Academic Press, San Diego, **2002**.

[80] J. M. Hollander, W. L. Jolly *Acc. Chem. Res.* **1970**, 3, 193.

[81] K. Krishnaveni, T.S.N. Narayanan, S.K. Seshadri *J. Alloys Compd.* **2009**, 480, 765.

[82] G.A. Di Bari, Electrodeposition of nickel, Wiley & Sons New Jersey, **2010**.

[83] R. Oriňáková, A. Turoňová, D. Kladeková, M. Gálová, R. M. Smith *J. Appl. Electrochem.* **2006**, 36, 957.

[84] T. Hang, M. Li, Q. Fei, D. Mao *Nanotechnology*. **2008**, 19, 035201.

[85] T. Vasilache, S. Gutt, I. Sandu, V. Vasilache, G. Gutt, M. Risca, A. V. Sandu *Recent Pat. Corr. Sci.* **2010**, 2, 1.

[86] C. Aperador , A. Williams, E. Lopez *Matéria (Rio de Janeiro)*. **2007**, 12, 583.

[87] I. Rajagopal *Bull. Mater. Sci.* **1983**, 5, 323.

[88] F. Muench, M. Oezaslan, M. Rauber, S. Kaserer, A. Fuchs, E. Mankel, J. Brötz, P. Strasser, C. Roth, W. Ensinger *J. Power Sources*. **2013**, 222, 243.

[89] S. Diplas, J. Lehrmann, S. Jørgensen, T. Våland, J. F. Watts, J. Taftø *Surf. Interface Anal.* **2005**, 37, 459.

[90] M. Bhardwaj, K. Balani, R. Balasubramaniam, S. Pandey, A. Agarwal *Surface Eng.* **2011**, 27, 642.

[91] M. Schlesinger, M. Paunovic, Modern Electroplating John Wiley & Sons, New York, **2000**.

[92] B. Pierozynski *Croat. Chem. Acta*. **2012**, 85, 1.

[93] U. S. Mohanty, B. C. Tripathy, P. Singh, S. C. Das *J. Electroanal. Chem.* **2002**, 526, 63.

[94] U. S. Mohanty, B. C. Tripathy, P. Singh, S. C. Das *J. Appl. Electrochem.* **2001**, 31, 579.

[95] G. P. Jin, Y. F. Ding, P. P. Zheng *J. Power Sources*. **2007**, 166, 80.

[96] A. Ertan, S. N. Tewari, O.Talu *J. Exp. Nanosci.* **2008**, 3, 287.

[97] M. Karolus, E. Łgiewka *J. Alloys Compd.* **2004**, 367, 235.

[98] K. S. Kumar, S. Suresh, M. F. Chisholm, J. A. Horton, P. Wang *Acta Materialia*. **2003**, 51, 387.

[99] T. F. M. Chang, T. Tasaki, C. Ishiyama, M. Sone *Microelectron. Eng.* **2011**, 88, 2225.

[100] J.K. Luo, M. Pritschow, A. J. Flewitt, S. M. Spearing, N. A. Fleck, W.I. Milne *J. Electrochem. Soc.* **2006**, 153, D155.

[101] T. F. M. Chang, M. Sone, A. Shibata, C. Ishiyama, Y. Higo *Electrochim. Acta*. **2010**, 55, 6469.

[102] T. Nagoshi, T. F. M. Chang, S. Tatsuo, M. Sone *Microelectron. Eng.* **2013**, 110, 270.

[103] M. Rahman, M. Sone, M. Eguchi, K. Ikeda, S. Miyata, T. Yamamoto *Surf. Coat. Tech.* **2006**, 201, 606.

[104] V. C. Nguyen, C. Y. Lee, L. Chang, F. J. Chen, C. S. Lin *J. Electrochem. Soc.* **2012**, 159, D393.

[105] Y. N. Bekish, S. K. Poznyak, L. S. Tsybulskaya, T. V. Gaevskaya *Electrochem. Acta*. **2010**, 55, 2223.

[106] K. M. Gorbunova, M. V. Ivanov, V. P. Moiseev *J. Electrochem. Soc.* **1973**, 120, 613.

[107] Y. C. Weng, T. C. Chou *J. Electrochem. Soc.* **2006**, 153, H127.

[108] K. H. Lee, D. Chang, S. C. Kwon *Electrochimica Acta*. **2005**, 50, 4538.

[109] S. Wen, J. A. Szpunar *Micro & Nano Letters, IET*. **2006**, 1, 89.

[110] T. Saito, E. Sato, M. Matsuoka, C. Iwakura *J. Appl. Electrochem.* **1998**, 28, 559.

[111] A. Fahami, B. N. Tabrizi, M. Rostami, R. E. Kahrizsangi *ISRN Electrochem.* **2013**, 2013, 1.

[112] ICSD *accessed via the EPSRC-funded National Chemical Database Service hosted by the Royal Society of Chemistry.*

[113] E. R. Jette, F. Foote *J. Chem. Phys.* **1935**, 3, 605.

[114] M. Saitou *Int. J. Electrochem. Sci.* **2015**, 10, 5639.

[115] S. Pathak, M. Guinard, M. G. C. Vernooij, B. Cousin, Z. Wang, J. Michler, L. Philippe *Surf. Coat. Technol.* **2011**, 205, 3651.

[116] A. Moridi, H. Ruan, L. C. Zhang, M. Liu *Int. J. Solids Structs.* **2013**, 50, 3562.

[117] M. Aguilar, A. I. Oliva, P. Quintana *Surf. Sci.* **1998**, 409, 501.

[118] M.B. Shongwe, M.J. Witcomb, L.A. Cornish, M.J. Papo *J. South. Afr. Inst. Min. Metall.* **2012**, 112, 551.

[119] S. Tamulevičius *Vacuum*. **1998**, 51, 127.

[120] J. W. Hutchinson, Stresses and failure modes in thin films and multilayers, Technical University of Denmark, Lyngby **1996**.

[121] J. J. Kelly, S. H. Goods, A. A. Talin, J. T. Hachman *J. Electrochem. Soc.* **2006**, 153, C318.

[122] H. Ogihara, K. Udagawa, T. Saji *Surf. Coat. Tech.* **2012**, 206, 2933.

[123] T. V. Gaevskaya, I. G. Novotortseva, L. S. Tsybulskaya *Met. Finish.* **1996**, 94, 100.

[124] A. Ul-Hamid, A. Quddus, H. Dafalla, H. Saricimen, L. Al-Hadhrami *J. Mater. Eng. Perform.* **2012**, 21, 213.

[125] A. M. Rashidi, A. Amadeh *Surf. Coat. Tech.* **2008**, 202, 3772.

[126] M. Wu, N. R. Brooks, S. Schaltin, K. Binnemans, J. Fransaer *Phys. Chem. Chem. Phys.* **2013**, 15, 4955.

[127] G. Gu, M. Burghard, G. T. Kim, G. S. Düsberg, P. W. Chiu, V. Krstic, S. Roth, W. Q. Han *J. Appl. Phys.* **2001**, 90, 5747.

[128] R. Al-Salman, S. Zein El Abedin, F. Endres *Phys. Chem. Chem. Phys.* **2008**, 10, 4650.

[129] M. J. Jawad, M. R. Hashim, N. K. Ali, E. P. Corcoles, M. E. Sharifabad *J. Electrochem. Soc.* **2012**, 159, D124.

[130] X. Liang, Y. G. Kim, D. K. Gebergziabiher, J. L. Stickney *Langmuir*. **2010**, 26, 2877.

[131] X. D. Meng, R. Al-Salman, J. Zhao, N. Borissenko, Y. Li, F. Endres *Angew. Chem. Int. Ed.* **2009**, 48, 2703.

[132] J. Ke, P. N. Bartlett, D. A. Cook, T. L. Easun, M. W. George, W. Levason, G. Reid, D. Smith, W. Su, W. Zhang *Phys. Chem. Chem. Phys.* **2012**, 14, 1517.

[133] E. Muthuswamy, A. S. Iskandar, M. M. Amador, S. M. Kauzlarich *Chem. Mater.* **2012**, 25, 1416.

[134] R. Al-Salman, J. Mallet, M. Molinari, P. Fricoteaux, F. Martineau, M. Troyon, S. Z. El Abedin, F. Endres *Phys. Chem. Chem. Phys.* **2008**, 10, 6233.

[135] N. Chandrasekharan, S.C. Sevov *J. Electrochem. Soc.* **2010**, 157, C140.

[136] P. N. Bartlett, D. A. Cook, C. H. de Groot, A. L. Hector, R. Huang, A. Jolleys, G. P. Kissling, W. Levason, S. J. Pearce, G. Reid *RSC Advances*. **2013**, 3, 15645.

[137] A. Lahiri, S. Zein El Abedin, F. Endres *J. Phys. Chem. C*. **2012**, 116, 17739.

[138] W. Paatsch *J. Electrochem. Soc.* **1977**, 124, 1505.

[139] G. Szekely *J. Electrochem. Soc.* **1951**, 98, 318.

[140] M. Saitou, K. Sakae, W. Oshikawa *Surf. Coat. Tech.* **2003**, 162, 101.

[141] L. K. Van Vugt, A. F. Van Driel, R. W. Tjerkstra, L. Bechger, W. L. Vos, D. Vanmaekelbergh, J. J. Kelly *Chem. Commun.* **2002**, 2054.

[142] F. Endres, S. Zein El Abedin *Phys. Chem. Chem. Phys.* **2002**, 4, 1640.

[143] E. Fahrenkrug, J. Gu, S. Jeon, P. A. Veneman, R. S. Goldman, S. Maldonado *Nano letters*. **2014**, 14, 847.

[144] C. C. Lai, Y. K. Lin, F. W. Yuan, H. Y. Tuan, Y. L. Chueh *ECS Solid State Let.* **2013**, 2, P55.

[145] F. Endres, S. Z. El Abedin *Chem. Commun.* **2002**, 892.

[146] A. Lahiri, M. Olschewski, O. Hofft, S. Z. El Abedin, F. Endres *J. Phys. Chem. C*. **2013**, 117, 1722.

[147] F. Endres *Phys. Chem. Chem. Phys.* **2001**, 3, 3165.

[148] J. S. Gu, S. M. Collins, A. I. Carim, X. G. Hao, X. G. Bartlett, S. Maldonado *Nano Letters*. **2012**, 12, 4617.

[149] M. Abidin, R. Matsumura, M. Anisuzzaman, J. H. Park, S. Muta, M. Mahmood, T. Sadoh, A. Hashim *Materials*. **2013**, 6, 5047.

[150] A. F. Khan, M. Mehmood, A. M. Rana, T. Muhammad *Appl. Surf. Sci.* **2010**, 256, 2031.

[151] E. K. Tentardini, E. Blando, R. Hübler *Nucl. Instruim. Meth. B*. **2001**, 175–177, 626.

[152] P. N. Bartlett, C. Y. Cummings, W. Levason, D. Pugh, G. Reid *Chem. Eur. J.* **2014**, 20, 5019.

[153] A. I. Galaction, L. Kloetzer, D. Cascaval *Chem. Eng. Technol.* **2011**, 34, 1341.

[154] R. J. Lesuer, C. Buttolph, W. E. Geiger *Anal. Chem.* **2004**, 76, 6395.

[155] G. A. Mabbott *J. Chem. Educ.* **1983**, 60, 697.

[156] N. Aristov, A. Habekost *World J. Chem. Educ.* **2015**, 3, 115.

[157] E. J. F. Dickinson, I Streeter, R. G. Compton *J. Phys. Chem. B*. **2008**, 112, 4059.

[158] P. Willich, R. Bethke, Microbeam and Nanobeam Analysis, Springer-Verlag/Wien, New York, **1996**.

[159] W. Dreyer, C. Guhlke, R. Muller *Phys. Chem. Chem. Phys.* **2016**, 18, 24966.

[160] E. Budevski, G. Staikov, W. J. Lorenz *Electrochimica Acta*. **2000**, 45, 2559.

[161] S. H. Wu, D. H. Chen *J. Colloid Interface Sci.* **2004**, 273, 165.

[162] A. A. Aref, L. Xiong, N. Yan, A. M. Abdulkarem, Y. Yu *Mater. Chem. Phys.* **2011**, 127, 433.

[163] A. K. Singh, G. S. Thool, S. R. Deo, R. S. Singh, A. Gupta *Res. Chem. Intermed.* **2012**, 38, 2041.

[164] Z. Niu, Q. Peng, M. Gong, H. Rong, Y. Li *Angew. Chem. Int. Ed.* **2011**, 50, 6315.

[165] C. Jeyabharathi, S. S. Kumar, G. V. M. Kiruthika, K. L. N. Phani *Angew. Chem. Int. Ed.* **2010**, 49, 2925.

[166] K. H. Kim, K. S. Kim, J. P. Kim, S. H. Baeck *Curr. Appl. Phys.* **2012**, 12, 36.

[167] X. Ren, Z. Lun *Mater. Lett.* **2012**, 68, 228.

[168] V. Mazumder, S. Sun *J. Am. Chem. Soc.* **2009**, 131, 4588.

[169] S. Mourdikoudis, L. M. Liz-Marzán *Chem. Mater.* **2013**, 25, 1465.

[170] H. Gerung, T. J. Boyle, L. J. Tribby, S. D. Bunge, C. J. Brinker, S. M. Han *J. Am. Chem. Soc.* **2006**, 128, 5244.

[171] D. D. Vaughn, J. F. Bondi, R. E. Schaak *Chem. Mater.* **2010**, 22, 6103.

[172] E. Muthuswamy, A. S. Iskandar, M. M. Amador, S. M. Kauzlarich *Chem. Mater.* **2013**, 25, 1416.

[173] C. Robertson, R. Beanland, S. A. Boden, A. L. Hector, R. J. Kashtiban, J. Sloan, D. C. Smith, A. Walcarius *Phys. Chem. Chem. Phys.* **2015**, 17, 4763.

[174] T. H. Fang, K. T. Wu *Electrochem. Commun.* **2006**, 8, 173.

[175] L. E. Smart, E. A. Moore, Solid State Chemistry, Taylor & Francis Group LLC, Boca Rotan, **2005**.

[176] M. S. Z. Abidin, R. Matsumura, M. Anisuzzaman, J. H. Park, S. Muta, M. R. Mahmood, T. Sadoh, A. M. Hashim *Materials*. **2013**, 6, 5047.

[177] A. M. Venezia *Catal. Today*. **2003**, 77, 359.

[178] D. Knapp, Doctoral dissertation, California Institute of Technology Citeseer, **2010**.

[179] B. Kiraly, R. M. Jacobberger, A. J. Mannix, G. P. Campbell, M. J. Bedzyk, M. S. Arnold, M. C. Hersam, N. P. Guisinger *Nano Lett.* **2015**, 15, 7414.

[180] D. Bodlaki, H. Yamamoto, D. H. Waldeck, E. Borguet *Surf. sci.* **2003**, 543, 63.

[181] V. Loup, P. Besson, O. Pollet, E. Martinez, E. Richard, S. Lhostis *Solid State Phenom.* **2008**, 134, 37.

[182] M. Schleberger, A. C. Simonsen, S. Tougaard, J. L. Hansen, A. N. Larsen *J. Vac. Sci. Technol. A*. **1997**, 15, 3032.

[183] V. Grossi, L. Ottaviano, S. Santucci, M. Passacantando *J. Non-Cryst. Solids*. **2010**, 356, 1988.

[184] N. Tabet, M. Faiz, N. M. Hamdan, Z. Hussain *Surf. Sci.* **2003**, 523, 68.

[185] J. S. Hovis, R. J. Hamers, C. M. Greenlief *Surf. Sci.* **1999**, 440, L815.

[186] G. A. Lungu, N. G. Apostol, L. E. Stoflea, R. M. Costescu, D. G. Popescu, C. M. Teodorescu *Materials*. **2013**, 6, 612.

[187] K. Prabhakaran, T. Ogino *Surf. Sci.* **1995**, 325, 263.

[188] Y. Oshima, Y. Sun, D. Kuzum, T. Sugawara, K. C. Saraswat, P. Pianetta, P. C. McIntyre *J. Electrochem. Soc.* **2008**, 155, G304.

[189] C. Y. Cummings, P. N. Bartlett, D. Pugh, G. Reid, W. Levason, M. M. Hasan, A. L. Hector, J. Spencer, D. Smith *J. Electrochem. Soc.* **2015**, 162, D619.

[190] C. Cummings, P. N. Bartlett, D. Pugh, G. Reid, W. Levason, M. M. Hasan, A. L. Hector, J. Spencer, D. Smith, S. Marks *ChemElectroChem*. **2016**, 3, 726.

[191] J. H. Becker *J. Appl. Phys.* **1958**, 29, 1110.

[192] A. M. Molodets, S. S. Nabatov *High Temp.* **2000**, 38, 715.

[193] F. C. Walsh, C. T. J. Low *Surf. Coat. Technol.* **2016**, 288, 79.

[194] J. Torrent-Burgués, E. Guaus *Electrochim. Acta*. **2005**, 23, 471.

[195] F. X. Xiao, X. N. Shen, F. Z. Ren, A. A. Volinsky *Int. J. Miner. Metall. Mater.* **2013**, 20, 472.

[196] Y. W. Park, T. S. N. S. Narayanan, K. Y. Lee *Wear*. **2007**, 262, 320.

[197] S. Akhlaghi, D. G. Ivey *Plat. Surf. Fnish.* **2003**, 90, 36.

[198] E. Efzan, A. Marini *Int. J. Eng. Appl. Sci.* **2012**, 1, 2305.

[199] P. Giridhar, A. M. Elbasiony, S. Zein El Abedin, F. Endres *ChemElectroChem*. **2014**, 1, 1549.

[200] R. A. Huggins *J. Power Sources*. **1999**, 81–82, 13.

[201] J. W. Park, J. Y. Eom, H. S. Kwon *Int. J. Electrochem. Sci*. **2011**, 6, 3093.

[202] Y. Fujiwara *Thin Solid Films*. **2003**, 425, 121.

[203] G. Stalnionis, L. Tamašauskaitė-Tamašiūnaitė, V. Pautienienė, A. Sudavičius, Z. Jusys *J. Solid State Electrochem.* **2004**, 8, 892.

[204] C. Longo, P. T. A. Sumodjo, F. Sanz *J. Electrochem. Soc.* **1997**, 144, 1659.

[205] S. Hishita, Z. Stryhal, I. Sakaguchi, N. Ohashi, N. Saito, H. Haneda *Thin Solid Films*. **2004**, 464–465, 146.

[206] B. Tutunaru, I. Prunaru *An. Univ. Bucharest Chemi.* **2009**, 18, 67.

[207] A. M. R. Elbasiony, S. Zein El Abedin, F. Endres *J. Solid State Electrochem.* **2014**, 18, 951.

[208] C. T. J. Low, F. C. Walsh *Electrochimica Acta*. **2008**, 53, 5280.

[209] X. H. Xu, C. L. Hussey *J. Electrochem. Soc.* **1993**, 140, 618.

[210] J. F. Huang, I. W. Sun *J. Electrochem. Soc.* **2003**, 150, E299.

[211] F. Endres *ChemPhysChem*. **2002**, 3, 144.

[212] M. Morimitsu, Y. Nakahara, Y. Iwaki, M. Matsunaga *J. Min. Metallur. B Metallur.* **2003**, 39, 59.

[213] A. P.Abbott, G. Capper, K. J. McKenzie, K. S. K. S. Ryder *J. Electroanal. Chem.* **2007**, 599, 288.

[214] N. Tachikawa, N. Serizawa, Y. Katayama, T. Miura *Electrochim. Acta*. **2008**, 53, 6530.

[215] F. S. Platis, G. A. Capuano *J. Electrochem. Soc.* **1987**, 134, 2425.

[216] C. Santato, C. M. López, K. S. Choi *Electrochem. Commun.* **2007**, 9, 1519.

[217] J. Y. Lee, J. W. Kim, B. Y. Chang, H. T. Kim, S. M. Park *J. Electrochem. Soc.* **2004**, 151, C333.

[218] A. L. Radanyi, A. Sycheva, Z. Gacsi *Arch. Metall. Mater.* **2015**, 60, 1341.

[219] E. Rudnik *Ionics*. **2013**, 19, 1047.

[220] R. Y. Li, X. C. Sun, X. R. Zhou, M. Cai, X. L. Sun *J. Phys. Chem. C*. **2007**, 111, 9130.

[221] M. J. Deng, T. I. Leong, I. W. Sun, P. Y. Chen, J. K. Chang, W. T. Tsai *Electrochem. Solid-State Lett.* **2008**, 11, D85.

[222] P. N. Bartlett, J. Burt, D. A. Cook, C. Y. Cummings, M. W. George, A. L. Hector, M. M. Hasan, J. Ke, W. Levason, D. Pugh *Chem. Eur. J.* **2016**, 22, 302.

[223] X. Zhang, Y. Hao, G. Meng, L. Zhang *J. Electrochem. Soc.* **2005**, 152, C664.

[224] G. Riveros, S. Green, A. Cortes, H. Gomez, R. E. Marotti, E. A. Dalchiele *Nanotechnology*. **2006**, 17, 561.

[225] K. H. A. Lau, H. Duran, W. Knoll *J. Phys. Chem. B*. **2009**, 113, 3179.

[226] J. Sarkar, G. G. Khan, A. Basumallick *Bull. Mater. Sci.* **2007**, 30, 271.

[227] I. Lombardi, A. I. Hochbaum, P. Yang, C. Carraro, R. Maboudian *Chem. Mater.* **2006**, 18, 988.

[228] J. Cook, Fabrication of microporous templates for use in Supercritical Fluid Electrodeposition (SCFED), University of Southampton, **2015**.

[229] S. Michel, S. Diliberto, C. Boulanger, N. Stein, J. M. Lecuire *J. Cryst. Growth*. **2005**, 277, 274.

[230] W. Liu, C. Huang, X. Jin *Nanoscale Res. Lett.* **2015**, 10, 237.

[231] K. Neuróhr, L. Pogány, B. G. Tóth, Á. Révész, I. Bakonyi, L. Péter *J. Electrochem. Soc.* **2015**, 162, D256.

[232] C. Y. Lee, M. W. Wu, V. C. Nguyen, H. W. Chuang *Int. J. Mech. Aerospace. Ind. Mechatronics. Eng.* **2013**, 7, 494.

[233] V. Vasilache, S. Gutt, G. Gutt, T. Vasilache, C. FILOTE, I. Sandu *Rev. Roum. Chim.* **2009**, 54, 243.

[234] A. Frye, G. T. Galyon, L. Palmer *IEEE Trans. Electron. Packag. Manuf.* **2007**, 30, 2.